The large-scale Structure and dynamics of the local universe

Radburn-Smith, David James

Durham University

The Large-Scale Structure and Dynamics of the Local Universe

by David James Radburn-Smith

A thesis submitted to Durham University
in accordance with the regulations for
admittance to the Degree of Doctor of Philosophy.

Department of Physics
Durham University
September 2007

The Large-Scale Structure and Dynamics of the Local Universe

by David James Radburn-Smith
PhD Thesis, September 2007

Abstract

This thesis investigates the dynamics of the local Universe with particular reference to discovering the source of the Local Group (LG) motion.

A redshift survey of the Great Attractor (GA) region, thought responsible for a significant fraction of the LG motion, is presented. Over 3053 galaxies, located in both clusters and filaments, were targeted using the 2dF on the AAT. Velocity distributions and mass estimates for nine clusters are reported. Together with redshifts from the literature, this survey reveals the dominant feature in the core of the GA to be a large filament extending from Abell S0639 ($l = 281°$, $b = +11°$) towards a point at $l \sim 5°$, $b \sim -50°$, encompassing the Cen-Crux, CIZA J1324.7–5736, Norma and Pavo II clusters.

A new model of the local velocity field out to $300h^{-1}$ Mpc is derived from the combined REFLEX, BCS and CIZA surveys: the RBC catalogue. This is the first all-sky, X-ray selected galaxy cluster sample. The reconstruction includes an intrinsic correction for the bias of clusters in tracing the total density field. The velocity fields from both this reconstruction and that of the PSCz survey are compared to the observed peculiar velocities of 98 local type Ia supernovae (SNIa). The best fits are respectively found for values of $\beta_{\rm RBC} (= \Omega_m^{0.6} / b_{\rm RBC}) = 0.39 \pm 0.20$ and $\beta_I = 0.55 \pm 0.06$. These results are found to be robust to culls of the SNIa sample by distance, host-galaxy extinction and the reference frame in which the comparison is carried out.

As the PSCz preferentially samples late-type galaxies, the derived density field undersamples the contributions from regions of greatest overdensity, precisely the regions traced by the RBC survey. When combined in the ratio 78% PSCz, 22% RBC these two complimentary reconstructions are a better fit to the peculiar velocities of the same SNIa sample than either one alone.

Compared to galaxy surveys, which only see contributions to the LG motion from structures within $\sim 60h^{-1}$ Mpc, previous cluster surveys have argued that sources at much greater distances ($\sim 150h^{-1}$ Mpc) influence local dynamics. However, the RBC reconstruction presented here shows similar contributions from the same depths as the PSCz, which is partly attributed to the intrinsic bias correction and inclusion of the Virgo cluster in the RBC. The extended GA region, defined as the volume enclosed by $250 < l < 350°$, $-45 < b < 45°$ and $2000 < cz < 6000$ km s^{-1}, is found to be responsible for 65% of the LG motion, whilst the more distant ($\sim 145h^{-1}$ Mpc) SSC only accounts for 12%.

Contents

List of Figures

List of Tables

Declaration

The work described in this thesis was undertaken between 2003 and 2007 while the author was a research student under the supervision of Dr. John Lucey in the Department of Physics at the University of Durham. This work has not been submitted for any other degree at the University of Durham or any other University.

Portions of this work have appeared in the following papers:

- Radburn-Smith, D. J.; Lucey, J. R.; Hudson, M. J., 2004, MNRAS, 355, 1378 (Chapter 3)
- Lucey, J. and Radburn-Smith, D. and Hudson, M., 2005, ASP Conf. Ser. 329, 21
- Radburn-Smith, D. J. and Lucey, J. R. and Woudt, P. A. and Kraan-Korteweg, R. C. and Watson, F. G., 2006, MNRAS, 369, 1131 (Chapter 2)

Acknowledgments

This thesis is the culmination of four years of research carried out at Durham University. The work would not have been possible without the support and advice of my family, friends and colleagues to whom I am forever indebted.

First and foremost, I must thank John Lucey; a conscientious adviser and a passionate astronomer, his guidance over the years has been invaluable. I hope this thesis stands as a testament to his dedication to teaching and his insight and knowledge of the subject. I could not have asked for a better supervisor.

I also owe a special thanks to my office mates, principally Chris Power, Jose Cruz da Angela and Tim Rawle. They were always available to help sort through any problem and to get me through writing another chapter.

Many thanks to my other friends and regular 'Friday-night crowd': Rich Bielby, Craig Booth, Tim Butterley, Rob Crain, Greg Davies, Jim Geach, Geraint Harker, John Helly, Jim Mullaney, Mark Norris, Nic Ross, John Stott and Dave Wake. They helped make my time at Durham an extremely enjoyable and unforgettable one.

I extend my thanks to all members of the department, who together are an unrivaled source of collective knowledge. They helped answer all the questions that arose during the writing of this thesis and provided many an interesting discussion over tea. I must particularly thank Alan Lotts and Lydia Heck for keeping the department ticking over with their support of the computers and network.

Finally, this thesis is dedicated to my brothers and sisters and especially to my parents. From the very start, they helped foster my scientific curiousity and would always approve of yet another 'experiment', even after I set fire to the living-room carpet. The support and encouragement from my family over the years has been incredible and for that I can never be thankful enough.

1

Introduction

1.1 The Evolution of Structure and Dynamics

The present day view of the Universe consists of a sponge-like distribution of galaxies; far from the picture of a homogeneous system of galaxy clusters popular until the early 80s (see Fairall 1998 for a review of the literature). Around the massive voids, galaxies group into clusters, which in turn are interconnected by a rich network of filaments. This structure has been highlighted by recent deep redshift surveys such as the Sloan Digital Sky Survey (SDSS, York et al. 2000) and the 2dF Galaxy Redshift Survey (2dFGRS, Colless et al. 2001a, see Fig. 1.1).

Comparatively, we are able to directly observe the primordial density field as temperature fluctuations frozen into the Cosmic Microwave Background (CMB) when matter and photons decoupled at the time of recombination. Observations by balloon and satellite borne instruments have charted these anisotropies with ever increasing resolution, revealing the initial temperature, and therefore density fluctuations to be as small as one part in 100,000. Fig. 1.2 shows the most recent CMB map from the Wilkinson Microwave Anisotropy Probe (*WMAP*) satellite (Hinshaw et al. 2007).

In the current paradigm, these initial small-scale perturbations are believed to have grown into the structure we see today through gravitational instability (GI). The regions that were

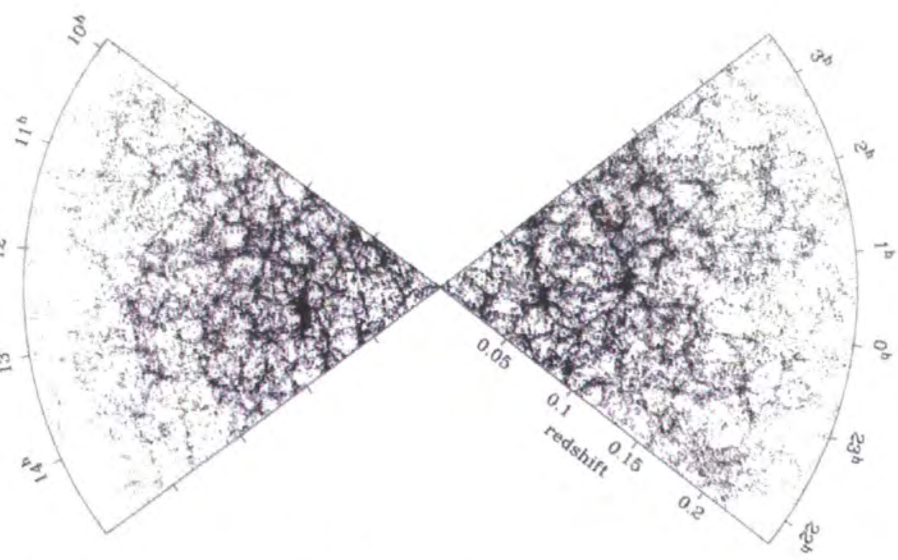

FIGURE 1.1: The present-day distribution of galaxies as seen from the 2dFGRS (Colless et al. 2001). Comprising some 250,000 galaxies, this approximately 10° thick slice highlights the cellular structure of our Universe.

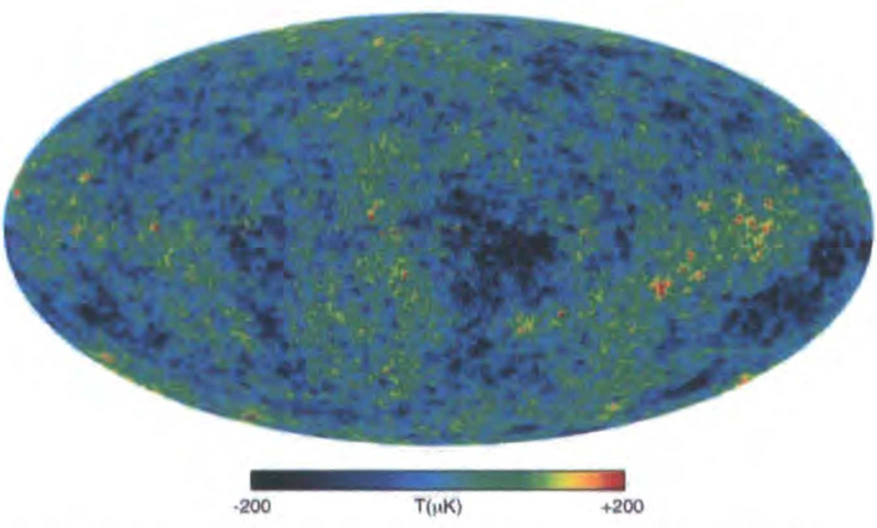

FIGURE 1.2: The density distribution at z~1100 as seen by *WMAP* from temperature fluctuations in the CMB (from Figure 9 of Hinshaw et al. 2006). This 'Internal Linear Combination' map combines *WMAP* observations at different frequencies in such a way as to remove foreground emissions from our own galaxy whilst preserving the CMB signal. The Doppler induced dipole due to the motion of the *WMAP* satellite relative to the CMB has also been removed. The typical amplitude of the remaining contrast is only 1×10^{-5} of the signal.

slightly overdense compared to their immediate surroundings accreted more matter than average. This in turn led to an even larger gravitational potential, fuelling the amplification of the initial density contrast. Over time, stars and galaxies condensed out of the gas accumulated in the overdensities.

Under GI, the motion of galaxies may be attributed to two components: the Hubble expansion, due to the overall growth of the Universe, and the infall onto overdense regions under the influence of gravity, known as a galaxy's peculiar velocity. The expansion component was first noted by Hubble (1929) as an increase in radial velocity with distance, which, when ignoring peculiar motions, is simply expressed by:

$$cz = H_0 d, \tag{1.1}$$

where the combination of the speed of light (c) and the observed redshift (the shift in observed spectral wavelength, $z = [\lambda_{\mathrm{observed}} - \lambda_{\mathrm{emitted}}]/\lambda_{\mathrm{emitted}}$) is the object's recessional velocity, H_0 is the Hubble constant (with units $\mathrm{km\,s^{-1}\,Mpc^{-1}}$) and d is a measure of the distance to the source.

Although galactic peculiar motions may be up to several hundred $\mathrm{km\,s^{-1}}$, they account for only a small fraction of the combined velocity for distances $\gtrsim 50$ Mpc ($\lesssim 10\%$). Hence, as a first approximation, equation 1.1 may be used to infer distances directly from redshifts. In this case, distances are often quoted in units of h^{-1} Mpc, where $100 \times h = H_0$, thus negating the uncertainty in the value of H_0[1].

Alternatively, the inverse of equation 1.1 may be used to directly measure H_0. However, whilst the radial velocity of a galaxy can be determined to a high degree of accuracy, measurements of distance carry a large uncertainty (see Section 1.3). Together with inaccurate peculiar velocities, this uncertainty in distance has yielded a wide range of estimates for H_0. To date, the most accurate determination of H_0 is quoted by the 'Hubble Space Telescope (HST) Key Project to measure H_0'. By using Cepheid variables to measure distances to 31 nearby galaxies, Freedman et al. (2001) have been able to calibrate 78 distances from secondary indicators covering the range 60-400h^{-1} Mpc. Amalgamating the sample they find $H_0 = 72 \pm 8\ \mathrm{km\,s^{-1}}$.

An alternative derivation may be found by combining *WMAP* observations of the CMB anisotropies with clustering analysis from the 2dFGRS. Assuming a Lambda-Cold Dark Matter (ΛCDM) cosmology yields $H_0 = 73.2^{+1.8}_{-2.5}\ \mathrm{km\,s^{-1}\,Mpc^{-1}}$ (Spergel et al. 2007), which is

[1] Unless otherwise indicated by a subscript number, H_0 is taken as 100 $\mathrm{km\,s^{-1}\,Mpc^{-1}}$ throughout this thesis.

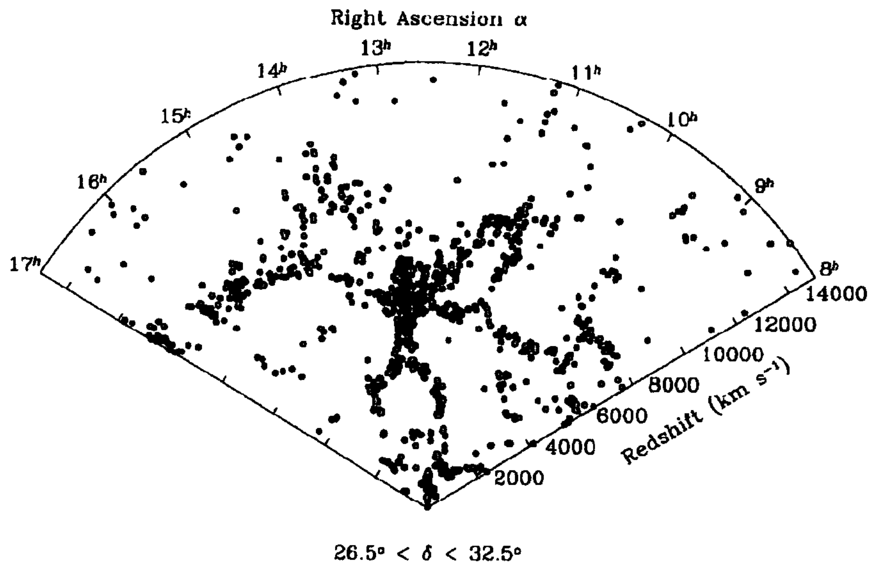

FIGURE 1.3: A 6° × 117° slice through the Coma cluster using data from the extended CfA survey (de Lapparent, Geller & Huchra 1986). The walls marking the edges of the voids are clearly visible.

in excellent agreement with the HST Key Project result.

1.2 Mapping the Universe: Redshift Surveys

The exploitation of redshift surveys to measure galaxy distances and map large-scale structure began in the late 1970s (Gregory & Thompson 1978, 1984; Gregory et al. 1981). These early pencil beam surveys were only able to drill out small regions in the direction of nearby clusters. However, shallower surveys of much larger areas of the sky followed soon after. Of these, the Center for Astrophysics (CfA) redshift survey (Huchra et al. 1983), which includes redshifts from several sources in the literature, is notable for first highlighting the cellular structure of the global galaxy distribution (see Fig. 1.3).

Early surveys relied on images of the sky taken in optical bands to identify targets for spectroscopic follow up. However, due to stellar contamination and foreground extinction from our own galaxy, a band of sky defined by the plane of the Milky Way ($b \lesssim 15°$) is effectively unobservable in the optical. This region, known as the Zone of Avoidance (ZoA), is less severely affected by Galactic extinction in the infrared. Therefore, target catalogues extracted from the Infrared Astronomical Satellite (*IRAS*) Point Source Catalogue (PSC, Beichman et al. 1988) have now been extensively used for all-sky redshift surveys.

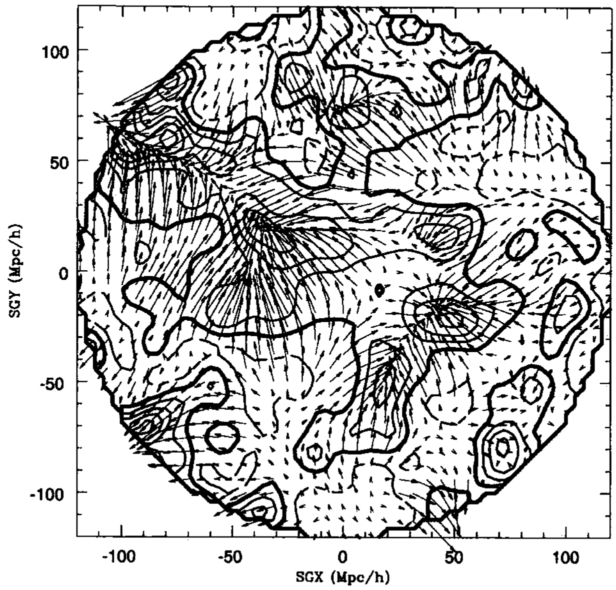

FIGURE 1.4: The density and velocity fields in the supergalactic SGX/SGY plane out to $120h^{-1}$ Mpc from the PSCz (Figure 12 from Branchini et al. 1999). The fields have been smoothed with a Gaussian Kernel of radius $6h^{-1}$ Mpc. Density contours are plotted at $\delta_g = 0.5$ intervals and velocities are arbitrarily scaled. The heavy solid contour marks the $\delta_g = 0$ boundary.

The first two major *IRAS* redshift surveys were the IRAS-1.2 Jy survey of 5339 galaxies at a median redshift of 5800 km s^{-1} (Fisher et al. 1995a) and the sparser, but deeper, QDOT survey with 2184 galaxies and a median redshift of 8400 km s^{-1} (Rowan-Robinson et al. 1990). From these surveys, the benefits of a statistically complete redshift survey drawn from the entire PSC soon became clear. The resulting Point Source Catalogue Redshift (PSCz) survey includes 15,411 *IRAS* galaxies with a median redshift of 8500 km s^{-1} and is the deepest all-sky survey to date (Saunders et al. 2000b). The smoothed PSCz galaxy density field is shown in Fig. 1.4. As detailed in Section 1.5 and Chapter 3, the peculiar velocities of the galaxies have been taken into account to reveal the realspace distribution of the structures. Fig. 1.5 shows the equivalent map from the recently published 2-Micron All Sky Survey (2MASS) Redshift Survey (2MRS) (Huchra et al. 2005; Erdoğdu et al. 2006b). So far, the 2MRS has measured redshifts for ~ 24,000 targets taken from the ground based infrared 2MASS catalogue (Jarrett et al. 2000). Although this is a much higher density than the PSCz, the median redshift is significantly closer at ~ 6000 km s^{-1}.

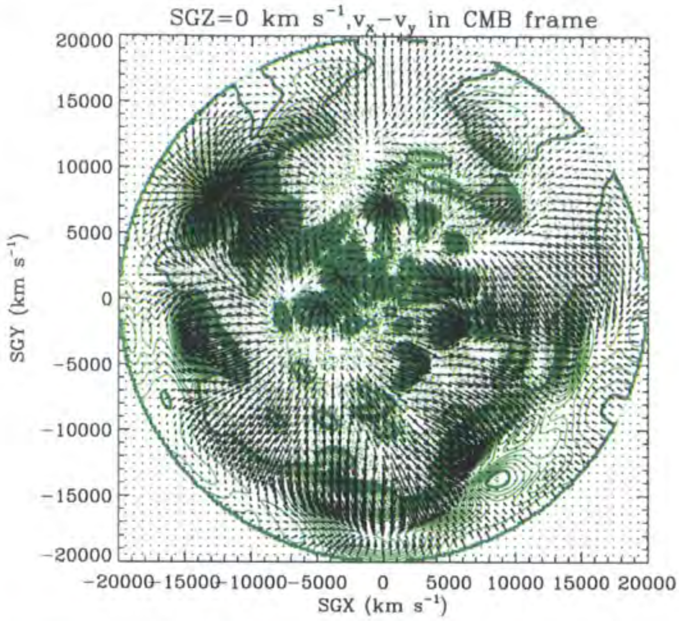

FIGURE 1.5: The same supergalactic plane as in Fig. 1.4 but as seen from the 2MRS (Figure 19 from Erdoğdu et al. 2006b) out to $200h^{-1}$ Mpc. The reconstructed density contours are plotted at $\delta_g = 0.1$ intervals (with the heavy green contour indicating $\delta_g = 0$) and velocities are approximately 300 km s^{-1} per cell.

1.2.1 Cosmography

At Mpc scales, galaxy clusters group together to define even larger structures that make up the cosmic web seen in Fig. 1.1. Our own galaxy, the Milky Way, resides on the outskirts of a supercluster known as the Virgo Supercluster. This system appears considerably flattened forming a natural plane, as first hinted at in observations by William Herschel in the 18th century. However, the true extragalactic origin of the supergalactic plane (SGP) was only realised some 200 years later by de Vaucouleurs (1953) who used the plane to define the supergalactic coordinate system (de Vaucouleurs et al. 1976). The extent of the SGP is still debated; however, many of the large scale structures situated beyond the Virgo Supercluster are all known to be associated with this plane. Notably, Lahav et al. (2000) were able to identify an overdensity of galaxy filaments lying on the SGP out to $\sim 80h^{-1}$ Mpc.

Fig. 1.4 and 1.5 plot the SGP as seen in the PSCz and 2MRS. The Milky Way sits at the centre of the map, embedded in the Virgo supercluster. The core of this structure is the Virgo cluster located at (SGX, SGY)~(-3, 12)h^{-1} Mpc. The Virgo cluster itself is an unrelaxed system composed of three separate infalling clumps centred on the galaxies M87, M86 and M49 (Binggeli et al. 1987, 1993; Böhringer et al. 1994). Beyond Virgo lies the Coma supercluster at (0, 65)h^{-1} Mpc. This system is primarily composed of the two very rich clusters:

Abell 1656 (Coma) and Abell 1367. With the applied smoothing lengths in both Fig. 1.4 and 1.5, this supercluster appears isolated from other structures. However, it forms part of the Virgo-Coma 'Great Wall', the first large-scale wall of galaxies to be identified (Geller & Huchra 1989).

The most striking feature in these maps however, is the apparent connection between the Perseus-Pisces supercluster (PP) at (50,–15), The Great Attractor (GA) at (-45,0) and the Shapley Supercluster (SSC) at (-130, 75). PP lies in the plane of the map and is a remarkably dense filament embedded with many clusters (Giovanelli et al. 1986). The GA has a somewhat chequered history as explained in Section 1.4. The structure was first proposed by Dressler et al. (1987) and Lynden-Bell et al. (1988), yet the extent and composition of the GA are still unclear. This is due to the structure's location in the ZoA, which runs horizontally (SGY=0) across these maps. The SSC was first observed by Shapley (1930) but it was only much later that it was identified as a supercluster (Melnick & Moles 1987; Raychaudhury 1989). With an estimated mass of approximately $5 \times 10^{16} h^{-1}\,M_\odot$, the SSC is the largest overdensity in the local Universe.

With the advent of multi-object spectrographs, redshift surveys are now able to efficiently cover large swathes of the sky to great depths. The SDSS, still in progress, aims to map a million redshifts over a quarter of the sky, whilst the 6dF Galaxy Survey (6dFGS), which is nearing completion, has recorded approximately 150,000 redshifts with a median redshift of $\sim 16,000\ \mathrm{km\,s^{-1}}$, over almost the entire southern sky (Jones et al. 2004). These surveys promise to map the structure of the local Universe to an unprecedented level of resolution.

1.3 Distance Indicators: Measuring Peculiar Velocities

As mentioned in Section 1.1, the infall of galaxies into overdense regions causes perturbations around the smooth Hubble flow described by equation 1.1. These peculiar velocities are included in the redshift measurements of galaxies. However, the amplitude of the motion is dependent on the reference frame in which the redshift is recorded.

Redshift measurements from Earth (or near Earth orbit) will include contributions from our orbit around the Sun ($\sim 30\ \mathrm{km\,s^{-1}}$) and the Sun's own orbit around our Galaxy ($\sim 220\ \mathrm{km\,s^{-1}}$). However, the Milky Way and our nearest neighbour, the Andromeda galaxy, are moving towards each other at $\sim 100\ \mathrm{km\,s^{-1}}$. Together, the Milky Way and Andromeda, along with over 40 smaller galaxies, form the Local Group (LG) and, as described in Section 1.4, this group itself takes part in a larger flow of galaxies. Hence several frames of reference exist including the heliocentric and LG frame. However, if the cosmic origin of the CMB holds true, this background signal offers us an absolute reference frame for the entire Universe.

In all frames a positive peculiar motion infers that the galaxy is moving away from the rest observer. Hence, for example in the LG frame, the recessional velocity measured will be a combination of the Hubble expansion, as given by equation 1.1, and the peculiar motion ($\boldsymbol{V}_{\rm pec}$):

$$cz = H_0 d + \hat{\boldsymbol{r}} \cdot [\boldsymbol{V}_{\rm pec} - \boldsymbol{V}(0)] \tag{1.2}$$

where $\hat{\boldsymbol{r}}$ is the unit direction vector of the galaxy and $\boldsymbol{V}(0)$ the motion of the LG.

Clearly, peculiar velocities carry information about the underlying mass density field, which we are unable to observe directly. Techniques such as strong and weak gravitational lensing often allow us to reveal the hidden mass in overdensities such as clusters as well as the broad distribution of matter in the largest-scale structures. However, only peculiar velocities are able to reliably map the total matter distribution on galaxy scales in the local Universe. Unfortunately the accuracy with which we can calculate a given galaxy's peculiar velocity is governed by the uncertainty of the distance (d) to that galaxy. Much work has therefore been devoted to improving and developing methods for measuring distance. These distance indicators are defined as either standard candles or standard rulers, where respectively, the absolute magnitude or physical size of the source may be inferred from a second observable. These are then compared to the apparent magnitude or angular size to calculate the distance.

Standard candles and rulers are able to reliably measure distances once they have been properly calibrated. Typically this is achieved through a process known as the distance ladder: techniques that are able to accurately measure nearby galaxy distances are used to calibrate indicators for which there may be few local targets available. In turn, these may then be used to calibrate indicators that operate over even greater distances. The most commonly used indicator for nearby galactic comparisons are Cepheid variables, which are calibrated in the Large and Small Magellanic Clouds from distance measurements using techniques such as the red clump, eclipsing binaries, RR Lyrae Stars and Mira Variables (e.g. see Westerlund 1997; Gibson 2000).

1.3.1 Cepheid Variables: $\lesssim 20h^{-1}$ Mpc

Cepheids are bright, post main-sequence stars that pulsate with a period directly correlated with their average absolute magnitude. With dispersions in this relation as small as $\sim \pm 0.1$ mag in the I band (Udalski et al. 1999), they are ideal standard candles. However, as they are often found in dusty environments there has been some concern over extinction corrections as well as the effect of metallicity on the period-luminosity relation (Freedman & Madore 1990). Furthermore, they can only reliably be used for apparent magnitudes $m_V \lesssim 26$ mag, which limits them to distances comparable to the Virgo Cluster. The 'HST Key Project to measure H_0' used Cepheids in 31 nearby (< 21 Mpc) galaxies to calibrate all their secondary distance indicators to determine H_0 (Freedman et al. 2001).

1.3.2 Tully-Fisher Relation: $\lesssim 300h^{-1}$ Mpc

First proposed by Tully & Fisher (1977) as a distance indicator, the Tully-Fisher (TF) relation correlates the observed rotational velocity of spiral galaxies with their total luminosity. A precise explanation of the underlying mechanism responsible for this universal relation remains unclear. However in a broad sense, if luminosity (L) is proportional to mass (M), then the virial relation tells us that:

$$L \propto M \propto r v^2 \tag{1.3}$$

where r is the galaxy radius and v the rotational velocity. If surface brightness ($I \propto L/r^2$) also varies little between galaxies then we find the relation

$$L \propto v^4 \tag{1.4}$$

However, the observed exponent is often closer to 3 with the precise value dependent on wavelength (e.g. Strauss & Willick 1995). The reason for these effects and the role of dark matter in the relation requires further study.

Early studies found values for the intrinsic scatter in the optical TF relation ranging from ~ 0.1 mag (Bernstein et al. 1994) to > 0.7 mag (e.g. Kannappan et al. 2002) (for a literature review see Strauss & Willick 1995). However, with greater understanding of sample selection and the use of modern CCDs, the scatter is now typically measured as ± 0.4 mag (e.g. as most recently determined by Pizagno et al. 2007). This is equivalent to a distance error of $\sim \pm 20\%$.

1.3.3 Fundamental Plane: $\lesssim 150h^{-1}$ Mpc

At the same time as the TF relation was found for spirals, a similar correlation between luminosity and velocity dispersion (σ) was discovered for ellipticals: the Faber-Jackson (FJ) relation (Faber & Jackson 1976):

$$L \propto \sigma^{\alpha} \tag{1.5}$$

where $\alpha \sim 4 \pm 1$ (Faber & Jackson 1976; Schechter 1980; Tonry & Davis 1981). The dispersion is typically 0.8 mag but it was soon realised that including surface brightness in the relation significantly improved the correlation (Djorgovski & Davis 1987; Dressler et al. 1987). Today, we define the $D_n - \sigma$ relation as:

$$D_n \propto \sigma^{\gamma} \tag{1.6}$$

where D_n is the diameter within which the mean surface brightness is equal to a given value and $\gamma = 1.2 \pm 0.1$ (Lynden-Bell et al. 1988). $D_n - \sigma$ is a variant of the more general relation between radius (r), surface brightness (I) and velocity dispersion known as the Fundamental Plane (FP) of elliptical galaxies (Djorgovski & Davis 1987; Dressler et al. 1987):

$$r \propto \sigma^{\alpha} I^{-\beta} \tag{1.7}$$

where α and β are approximately 1.3 and 0.8 respectively (e.g. Faber et al. 1987; Djorgovski & Davis 1987; Jorgensen et al. 1996). When measuring distances to clusters with this method, the scatter is typically found to be 20%.

1.3.4 Surface Brightness Fluctuations: $\lesssim 150h^{-1}$ Mpc

An individual pixel in a CCD image of a galaxy with a uniform distribution of stars (e.g. an elliptical) will contain a finite number of stars and so be subject to Poisson noise. If the average pixel contains N stars, each of mean flux f, then the total flux recorded by the pixel will be Nf. The root mean square (rms) pixel-to-pixel fluctuation will accordingly be $\sqrt{N}f$, corresponding to a variance of Nf^2. Dividing the variance by the mean pixel intensity will thus recover the flux measured from a typical star. If the luminosity of that star is know, then the distance to the galaxy may be derived. This forms the basis of the Surface Brightness Fluctuation (SBF) method extensively developed by Tonry & Schneider (1988); Tonry et al. (1997, 2000). In practise, however, the situation is complicated by the point spread function (PSF, which may cover many pixels), the telescope optics, atmospheric effects and assumptions about the stellar population.

The accuracy of SBF is significantly greater than TF or $D_n - \sigma$ with distance errors typically $\sim 8\%$ (Tonry et al. 1997). Practically, the technique may only be used with ellipticals or the dominant bulges of spirals out to ~ 60 Mpc with ground based telescopes, although the method may be applied to larger distances with the HST (e.g. Lauer et al. 1998).

1.3.5 Type Ia Supernovae: $\lesssim 1000h^{-1}$ Mpc

When a white dwarf star exceeds the Chandrasekhar mass limit of $1.4M_\odot$ (where $1M_\odot$ is the mass of our Sun) it explodes as a Type Ia supernovae (SNIa). As the progenitor will approximately always be similar in mass and composition, all SNIa detonations will exhibit similar characteristics. However, when directly using SNIa peak luminosity as a standard candle, the scatter around the Hubble flow was found to be greater than the expected errors (e.g van den Bergh & Pazder 1992). Subsequently, Phillips (1993) discovered a relation between the relative SNIa peak luminosity and the optical light curve decline rate (as first suggested by Pskovskii 1977). This decline rate is parametrised by the difference in B-band magnitude 15 days after maximum, $\Delta m_{15}(B)$. Generally, doubling $\Delta m_{15}(B)$ (i.e. narrower light curves) reduces the V-band magnitude by 2 mags. Further refinement of the technique (Hamuy et al. 1995) and the inclusion of colour information to account for intrinsic extinction, led to the Multi-Colour Light-curve Shape (MCLS) method (Riess et al. 1995). Using MCLS to correct the relative peak luminosities for a sample of 50 SNIa, Riess et al. (2001) find a decrease in the scatter around the Hubble flow from 0.44 mag to 0.15 mag.

Modern SNIa catalogues quote errors of $\sim 8\%$ in distance (~ 0.17 mag). However, more fundamentally, SNIa are able to probe vast distances. Recent studies have used HST-discovered SNIa out to $z \sim 2$ to analyse the early expansion of the Universe (e.g. Riess et al. 2004).

1.3.6 Malmquist Bias

An important error to correct for in using distance indicators to calculate peculiar velocities is Malmquist bias. Originally this term referred to the bias resulting from the mean luminosity of observable galaxies being brighter than the mean luminosity of the underlying population in a flux limited survey (Malmquist 1920). However, here and in later studies it refers to the bias inherent in using distance indicators, where the line of sight galaxy density is not constant, as first discussed in this context by Lynden-Bell et al. (1988).

If galaxies were homogeneously distributed throughout the Universe, then the number of galaxies along the line of sight in a given solid angle would increase as r^2. As distance indicators carry a significant error, galaxies observed at a given distance d will be sampled from a range of true distances (r). Given the previous statement, more galaxies are likely to scatter in from greater distances. Hence on average d will underestimate the true distance. This is commonly known as homogeneous Malmquist bias (HMB). However matters are complicated by including variations in galaxy number density. Specifically, if a density peak exists along a given sight line at r_p, then distances inferred to be $d < r_p$ will underestimate the true distance and at $d > r_p$ the distance will be overestimated. As the observed recessional velocity is not affected by this, the inferred peculiar velocities will also be biased: at $d < r_p$ the peculiar velocities will be more positive and at $d > r_p$ they will be increasingly negative. Hence this inhomogeneous Malmquist bias (IMB) will add a spurious component to the observed infall onto density peaks. Generally, IMB increases with the square of the distance indicator's error, with a 20% distance error corresponding to an additional ~ 15% IMB. Clearly, correcting peculiar velocities when using distance indicators with large uncertainties is important for the study of large-scale structure and flows (e.g. Hudson 1994a).

1.4 Peculiar Velocity Studies: Determining the LG motion

Stewart & Sciama (1967) predicted that the motion of the Sun would be observable as a Doppler induced dipole on the heliocentric CMB signal. Shortly afterwards, from early measurements of the all-sky CMB signal, both Conklin (1969) and Henry (1971) were able to measure a LG velocity in the CMB frame of ~590 $\mathrm{km\,s^{-1}}$ towards (l, b) ~ (282°, 18°). Today, the Cosmic Background Explorer satellite (*CoBE*) observes in the heliocentric frame a dipole of 3.358 ± 0.027 mK in the direction (264.4 ± 0.3, 48.4 ± 0.5), corresponding to a LG velocity of 627 ± 22 $\mathrm{km\,s^{-1}}$ towards ($276 \pm 3°$,$30 \pm 3°$) (Kogut et al. 1993) relative to the CMB.

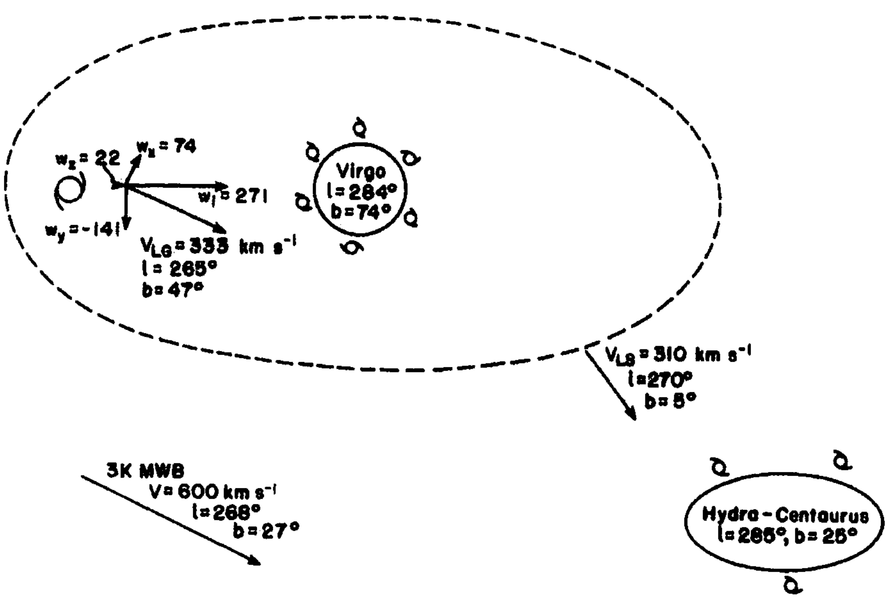

FIGURE 1.6: Figure 13 from Aaronson et al. (1986). The components of the LG motion are shown as well as the bulk motion of the local supercluster. The Virgo-centric infall is found to be comparable to the Virgo supercluster's own motion.

Early peculiar velocity studies sought to observe this motion in reflex by measuring the peculiar velocities of more distant galaxies. Initially, authors focused on the infall into the local supercluster (e.g. Peebles 1976; Yahil et al. 1980). However it was quickly realised that Virgo could only account for a fraction of the LG motion with respect to the CMB (Tammann & Sandage 1985). By observing members of 10 nearby clusters, Aaronson et al. (1986) found the local supercluster itself to be moving at (~300 – 450 $\mathrm{km\,s^{-1}}$) towards (270°, 0°), roughly coincident with the Hydra-Centaurus supercluster (see Fig. 1.6). Using TF distances for 230 nearby galaxies, Lilje et al. (1986), measured this effect locally as a shear in the local supercluster. Subsequently, Dressler et al. (1987) (now colloquially known as the Seven Samurai) used the $D_n - \sigma$ relation for a sample of 289 ellipticals to measure a local bulk flow of $599 \pm 104\ \mathrm{km\,s^{-1}}$ towards ($312 \pm 11°$, $6 \pm 10°$). Refining the distance indicator and extending their sample to 400 nearby ellipticals, the same authors found the motions to be best fit by a single attractor centred on (307°, 9°) at a distance of $4350 \pm 350\ \mathrm{km\,s^{-1}}$: the GA (Lynden-Bell et al. 1988). This overdensity was predicted to contain an excess mass of $\sim 5.4 \times 10^{16} h^{-1}\,\mathrm{M_\odot}$, comparable to the largest superclusters known. Many authors have since undertaken peculiar velocity studies attempting to verify or refute the presence of the GA with contradicting results (e.g. Lucey & Carter 1988; Dressler & Faber 1990; Mathewson et al. 1992; Tonry et al. 2000; Kolatt et al. 1995).

Direct observation of the GA is hampered by the structure's location in the ZoA. However as discussed in detail in Chapter 2, recent progress using multi-band surveys have had some success. Most notably, it has recently been proposed that the Norma cluster (Abell 3627), lying at (325°, -7°, 4848 km s^{-1}) with a mass of $\sim 1 \times 10^{15} h^{-1} M_{\odot}$ forms the core of the GA (Kraan-Korteweg et al. 1996; Woudt 1998).

Early evidence for the invalidity of the GA model was based on the lack of a clear back-side infall signal (Mathewson et al. 1992; Mathewson & Ford 1994). If the GA really is the dominant structure in the nearby Universe, then we would expect to observe the infall of galaxies on the farside of the structure towards us. However this is not generally seen (e.g. Hudson 1994a). It was therefore suggested that the more distant SSC, lying directly behind the GA, may dominate the LG motion (Melnick & Moles 1987; Raychaudhury 1989; Scaramella et al. 1989; Allen et al. 1990). Described in Chapter 2, the SSC is centred on Abell 3558 (312°, 31°, 14 500 km s^{-1}) and is comprised of galaxy clusters with a combined mass of $\sim 5 \times 10^{16} h^{-1} M_{\odot}$.

The bulk flow across our local region of space is clearly evident in Fig. 1.7. By combining peculiar velocities from several recent studies, including SNIa, SBF, FP and TF analyses, Hudson (2003) identifies a consistent bulk flow of 350 ± 80 km s^{-1} towards (l=288°, b=+8°) over $82 h^{-1}$ Mpc. However the extent to which this flow remains coherent continues to be debated. As summarised by Willick (2000), ΛCDM predicts that the Universe is homogeneous on scales $\gtrsim 60 h^{-1}$ Mpc (e.g. see Jenkins et al. 1998). Hence we should not expect to observe bulk flows over such distances. Indeed, analysis of the PSCz dipole indicates little contribution from structures beyond $140 h^{-1}$ Mpc (Rowan-Robinson et al. 2000; Schmoldt et al. 1999) and Erdoğdu et al. (2006a) find the majority of the 2MRS dipole to be in place by ~ 60 km s^{-1}. However, studies of the Abell cluster dipole (Plionis & Valdarnini 1991) together with the sparsely sampled QDOT dipole, also based on *IRAS* data, suggests significant contributions from distances beyond $\sim 150 h^{-1}$ Mpc (Plionis et al. 1993). A result confirmed by both Plionis & Valdarnini (1991) and Scaramella et al. (1991) using X-ray selected samples of Abell and ACO (Abell et al. 1989) clusters (now combined into the XBACs sample, Ebeling et al. 1996). Similarly, studies based on the combined XBACs and Clusters in the Zone of Avoidance (CIZA, Ebeling et al. 2002) surveys as well as the newly compiled REFLEX/BCS/CIZA survey (RBC, Kocevski & Ebeling 2006, detailed in Chapter 4) argue for large contributions from structures beyond $\sim 60 h^{-1}$ Mpc. The source of this discrepancy between galaxy and cluster based dipoles and the consequent implications for ΛCDM remains unclear.

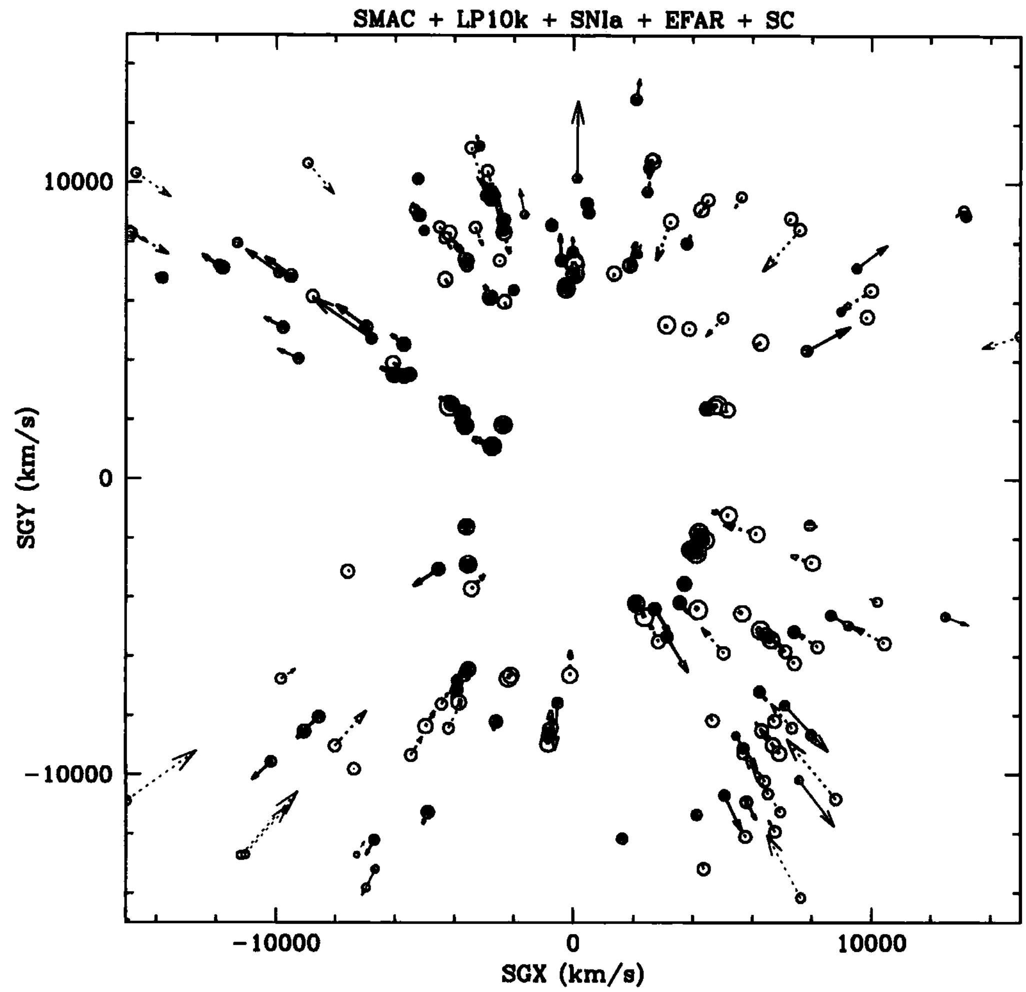

FIGURE 1.7: Figure 1 from Hudson (2003). Local peculiar velocity measurements in the supergalactic plane from the STEWS sample, combined from SMAC (Hudson et al. 1999), Tonry et al. (2003), EFAR (Colless et al. 2001b), Willick (1999) and SC (Dale et al. 1999). Larger circles indicate sources with smaller errors, whilst inflowing and outflowing measurements are labelled by open and solid circles respectively. Visually, a shear across the field can be inferred from an over abundance of inflowing objects in the lower right quadrant and outflowing objects in the upper left.

1.5 Reconstructing the All-Sky Density and Velocity Fields

To fully understand the source of the local group motion and the extent of the local bulk flow, the density field and hence the peculiar velocity field need to be mapped contiguously across the whole sky.

As detailed in Chapter 3, under GI and assuming linear theory the peculiar velocity field V_{pec} and galaxy density field δ_g can be related via the equations:

$$\nabla \cdot \boldsymbol{V}_{pec} = -a_0 H_0 \beta_g \delta_g(\boldsymbol{r}) \tag{1.8}$$

and

$$\boldsymbol{V}_{pec}(\boldsymbol{r}) = \frac{H_0 \beta_g}{4\pi} \int \delta_g(\boldsymbol{r}') \frac{(\boldsymbol{r}' - \boldsymbol{r})}{|\boldsymbol{r}' - \boldsymbol{r}|^3} d^3\boldsymbol{r}' \tag{1.9}$$

where β_g is the redshift distortion parameter defined by:

$$\beta_g = \frac{\Omega_m^{0.6}}{b_g} \tag{1.10}$$

and b_g is the linear bias between the galaxy density fluctuation and the total density fluctuation. The subscript on β and b denotes the sample used to map the density field. Generally, the bias and hence β will be different for various samples due to varying clustering amplitudes.

Using equation 1.8, density and 3D velocity fields free from bias may be inferred from observations of the radial peculiar velocities. The reconstructed density field can then be compared with measurements of the true density field from galaxy redshift surveys. Typically the POTENT method is used to reconstruct the fields and it has been extensively applied to the MARK III catalogue (Bertschinger & Dekel 1989; Dekel et al. 1990) of TF measurements. POTENT works under the assumption that the large-scale velocity field is irrotational (which is true to first order). Hence, the field may be expressed as the gradient of a potential field:

$$\boldsymbol{V}(r) = -\nabla\Phi(r) \tag{1.11}$$

This potential is calculated by simultaneously fitting all the radial peculiar velocities of a given sample. By differentiating ϕ, the full 3D velocity field can be constructed, which through equation 1.8, may be used to produce the corresponding density field. The main caveat to POTENT is that the sparse and noisy peculiar velocities need to be heavily smoothed onto a grid such that the radial component of the velocity field is defined everywhere.

Alternatively, equation 1.9 may be used to reconstruct velocity and density fields from the observed redshift space galaxy distribution. The velocities are then compared with observed peculiar motions measured using the techniques detailed in Section 1.3 . Although the galaxies are biased tracers of the density field, they are a far less noisy tracer than peculiar velocities. Several methods have been developed to exploit this strategy by mapping the galaxy distribution from redshift space to realspace. The simplest approach is to iteratively apply equation 1.9 for each galaxy in the sample, solving for the galaxy's peculiar motion at each step. Although computationally expensive, this method has been successfully applied to several surveys, e.g. the QDOT (Kaiser et al. 1991), *IRAS* (Yahil et al. 1991), PSCz (Branchini et al. 1999, see Fig. 1.4) and 2MASS (Pike & Hudson 2005) surveys. As detailed in Chapter 3, many extensions to comparisons using equation 1.9 have also been developed.

1.6 Thesis Outline

This thesis studies the local large-scale structures that influence the LG motion and investigates the differences between mappings of the LG dipole from galaxies and clusters. In Chapter 2, new redshift measurements of galaxies in the GA region will be reported and together with data from the literature, a consistent picture for the composition of the GA will be presented. In Chapter 3 the GI framework is derived and the PSCz density and velocity fields reconstructed by Branchini et al. (1999) are analysed. By comparing the predicted velocities with the observed proper motions of local SNIa, the GI framework will be tested and a new determination of β_I will be made. In Chapter 4, new velocity and density fields will be computed from the first, all-sky, X-ray selected cluster catalogue. The measured peculiar velocities of local SNIa will again be used to constrain the value of β_X. In Chapter 5, The PSCz and X-ray reconstructions will be compared and their respective dipoles will be studied in light of the model of the GA presented earlier. Finally, in Chapter 6 the key findings of the thesis will be summarised.

2

Unveiling The GA

2.1 A Hidden Supercluster

As summarised in Section 1.4, early work by Lynden-Bell et al. (1988) made the unexpected discovery of a 600 $\mathrm{km\,s^{-1}}$ outflow towards Centaurus. This led to the idea of a large, extended mass overdensity, nicknamed the Great Attractor (GA), dominating the dynamics of the local Universe. Whilst many studies have confirmed the presence of the GA (e.g. Aaronson et al. 1989), the precise mass, position and extent of the overdensity remain uncertain. Lynden-Bell et al. (1988) originally located the GA at (l, b, cz) ~ (307°, +9°, 4350 ± 350 $\mathrm{km\,s^{-1}}$) with a mass of $5.4 \times 10^{16} h^{-1} \mathrm{M_{\odot}}$. However a subsequent study by Kolatt et al. (1995) placed the GA peak at (320°, 0°, 4000 $\mathrm{km\,s^{-1}}$), whilst Tonry et al. (2000) favoured an even closer locale at (289°, +22°, 3200 ± 260 $\mathrm{km\,s^{-1}}$) and a mass approximately six times smaller (~$8 \times 10^{15} h^{-1} \mathrm{M_{\odot}}$). This range of values is partly attributed to the different models for the GA which the authors have advocated as well as the foreground extinction and high stellar contamination that has hampered studies of the underlying galaxy distribution. Recently, however, several key results have emerged.

The Norma cluster (Abell 3627), located at (325°, −7°, 4848 $\mathrm{km\,s^{-1}}$), is now recognised to be comparable in mass, richness and size to the Coma cluster (Kraan-Korteweg et al. 1996). Lying ~9° from the Kolatt et al. (1995) location of the GA, the cluster has been identified as a likely candidate for the 'core' of the overdensity (Woudt 1998). Furthermore, it has been suggested that the GA is a 'Great Wall' like structure that extends from low galactic latitudes, encompassing the Pavo II (332°, –24°, 4200 km s^{-1}, Lucey & Carter 1988) and Norma clusters before bending over and continuing towards $l \sim 290°$ (Kraan-Korteweg & Woudt 1994; Woudt et al. 1997, 2004). This connection has been labelled the Norma supercluster (Fairall et al. 1998) and constitutes the major structure in the GA region (defined here as $280° < l < 360°$, $-45° < b < +30°$, $3000 < cz < 7000$ km s^{-1}).

The richness of such connective structures in the region have been highlighted by recent blind HI surveys in the southern sky (Kraan-Korteweg et al. 2005b; Koribalski 2005; Henning et al. 2005). Because the ZoA is effectively transparent to 21 cm radiation, these surveys are able to trace the full extent of the local large-scale filaments as they pass through the plane. Notably, between galactic latitudes of –5° and +5°, Henning et al. (2005) find evidence for an extension of the Norma supercluster at $cz \sim 5000$ km s^{-1}, running from $b = 300°$ to 340°.

The X-ray selected 'Clusters In the Zone of Avoidance' (CIZA) project (described further in Chapter 4) has revealed several new X-ray clusters at low galactic latitudes (Ebeling et al. 2002; Kocevski et al. 2005). In the GA region, this survey has identified CIZA J1324.7–5736 as another potentially sizable contributor to the GA's mass. Lying at (307°, +5°, 5700 km s^{-1}) this cluster has been associated with the overdensity previously identified as the Cen-Crux cluster (Woudt 1998). X-ray measurements suggest that the structure is comparable in mass to the Norma cluster (Mullis et al. 2005).

Another important cluster in the GA region may exist around PKS 1343-601, an extremely strong radio source lying in the ZoA (Kraan-Korteweg & Woudt 1999). The host galaxy is a large E0 (Laustsen et al. 1977; West & Tarenghi 1989) located at ~ (310°, +2°, 3900 km s^{-1}). Despite the lack of an associated X-ray source (Ebeling et al. 2002), recent near-infrared surveys are consistent with the presence of an intermediate mass cluster centred on the radio source (Kraan-Korteweg et al. 2005a; Schröder et al. 2005; Nagayama et al. 2004).

Attempts to analyse the extent and mass of the GA from peculiar velocity measurements have remained inconclusive. To date, no clear sign of any backside infall has been detected (Mathewson et al. 1992; Hudson 1994a). This has been attributed to a continuing high amplitude flow, possibly due to the gravitational pull of the Shapley supercluster (SSC, Scaramella et al. 1989; Raychaudhury 1989; Branchini et al. 1999; Hudson et al. 2004). Centred on Abell 3558 (312°, 31°, 14,500 km s^{-1}), the SSC is an extremely rich concentration of galaxies. Dynamical analysis by Reisenegger et al. (2000) of the collapsing core of the SSC, indicates that the mass contained within the central 8 h^{-1} Mpc is between 2×10^{15}

and $1.3 \times 10^{16} h^{-1} M_{\odot}$. However different estimates of the SSC's mass, derived from various surveys of the region, vary significantly due to differing assessments of the extent and geometry of the structure (see Bardelli et al. 2000). Furthermore, recent analysis suggests that intercluster galaxies in the SSC may contribute twice as much mass as the galaxies within clusters, thus severely biasing previous estimates based solely on summed cluster masses (Proust et al. 2006). Accounting for all the galaxies in their 285 deg^2 survey of the SSC, Proust et al. (2006) estimate an enclosed mass of $5 \times 10^{16} h^{-1} M_{\odot}$.

This uncertainty in the relative masses of the GA and the SSC has led to much dispute over the predicted source of the bulk flow observed in the local Universe and hence the source of the Local Group's (LG) own motion. Using respectively X-ray cluster observations and reconstructions from the PSCz, Ettori et al. (1997) and Rowan-Robinson et al. (2000) estimated that the SSC was only responsible for approximately 5% of the LG's motion. However, from a dynamical analysis of the redshift distribution, Bardelli et al. (2000) placed the contribution closer to ~15% whilst others have advocated values of up to 50% (e.g Smith et al. 2000; Lucey et al. 2005; Kocevski et al. 2005).

In order to further understand the nature of the GA, and hence the role it plays in the LG's motion, we have undertaken a redshift survey with the Two-degree Field multi-fibre spectrograph (2dF, Lewis et al. 2002). Targets include five of the CIZA clusters (including the Cen-Crux cluster), the PKS 1343–601 region and over-densities located along the proposed filamentary structures.

2.2 Observations and Data Reduction

Observations were carried out in two runs on the 3.9m Anglo-Australian Telescope (AAT). The 2dF was configured using the same set up as that used for the 2dFGRS (Colless et al. 2001a). This included using the 300B gratings with the 1024×1024 24 μm pixels on the Tektronix CCDs, resulting in a dispersion of 178.8 Å mm^{-1} or 4.3 Å pixel^{-1}. At the centre of the chip, the FWHM of the focus is about 2 pixels, hence the typical spectral resolution is 9 Å. Additionally, a central wavelength of 5800 Å was chosen to cover a range of about 3650–8050 Å. The typical seeing encountered during the two runs was ~1–1.5 arcsec.

In total, we observed 25 separate fields as listed in Table 2.1. A repeat observation of one field was also taken in order to assess systematics. Field centres were chosen to maximise the number of targeted galaxies, whilst fully encompassing known clusters and noticeable overdensities. Target galaxies were taken from the 2MASS Extended Source Catalogue (2MASS XSC, Jarrett et al. 2000) and the NASA Extragalactic Database (NED). Additional

TABLE 2.1: Summary of 2dF observations. The (l, b) coordinates for each targeted field are listed. These are not necessarily identical to the coordinates of cluster centres, as small adjustments were made to maximise the number of galaxies available to fibres in each field.

Field No.	Target	l	b	Exposure length (s)	UT Date	No. Redshifts
1	Cen-Crux/CIZA J1324.7–5736 – 1	307.4	4.9	3 × 900	2004 Feb 29	46
2	Cen-Crux/CIZA J1324.7–5736 – 2	305.4	5.1	3 × 900	2004 Feb 29	51
3	Cen-Crux/CIZA J1324.7–5736 – 3	305.1	7.1	3 × 900	2004 Feb 29	40
4	Cen-Crux/CIZA J1324.7–5736 – 4	304.6	9.4	3 × 900	2005 Jun 9	87
5	PKS 1343-601	309.7	2.3	7 × 900	2004 Feb 29	5
6	Abell S0639	281.3	10.7	3 × 1200	2004 Feb 29	174
7	Triangulum-Australis/CIZA J1638.2–6420	324.7	–11.7	3 × 900	2005 Jun 8	252
8	Ara/CIZA J1653.0–5943	329.2	–9.8	3 × 900	2005 Jun 8	179
9	Cluster 1	314.3	13.9	3 × 900	2005 Jun 8	225
10	CIZA J1514.6–4558	327.3	10.2	3 × 1200	2005 Jun 7	226
11	CIZA J1410.4–4246	317.9	17.8	3 × 900	2005 Jun 8	182
12	Filament 1	296.3	9.1	4 × 900, 1 × 712	2005 Jun 8	135
13	Hydra-Antlia Extension 1	281.8	–6.2	3 × 900	2005 Jun 9	91
14	Hydra-Antlia Extension 2	280.6	–7.8	3 × 900	2005 Jun 9	126
15	Filament 2	300.4	9.0	3 × 900	2005 Jun 9	83
16	Filament 3	299.8	6.9	3 × 900	2005 Jun 9	50
17	Filament 4	312.5	5.0	4 × 900	2005 Jun 8	60
18	Filament 5	316.6	8.1	3 × 900	2005 Jun 9	70
19	Filament 6	312.9	9.0	3 × 900	2005 Jun 9	101
20	Filament 7	312.6	12.4	3 × 900	2005 Jun 8	111
21	Filament 8	351.0	–22.6	3 × 900	2005 Jun 8	146
22	Filament 9	355.3	–33.0	2 × 900	2005 Jun 8	175
23	Filament 10/RXC J1840.6-7709	317.7	–25.5	3 × 900	2005 Jun 9	156
24	Filament 11/CIZA J1407.8–5100	315.0	10.2	3 × 900	2005 Jun 9	91
25	Cluster 2	322.3	13.6	3 × 900	2005 Jun 9	155
26	Ara/CIZA J1653.0–5943 – repeat	329.2	–9.8	4 × 900	2005 Jun 9	169

targets in the Cen-Crux and PKS 1343–601 fields were identified from *J*, *H* and *Ks* observations taken with the 1.4 m InfraRed Survey Facility (IRSF, Nagayama et al. 2004, 2005) and I-band images from the Wide Field Imager (WFI) at the ESO 2.2m telescope at La Silla (Kraan-Korteweg et al. 2005a). Suitable guide stars were selected from the Tycho 2 catalogue (Høg et al. 2000). 2MASS positions were used for both targets and guide stars, with counterparts identified from the 2MASS Point Source Catalogue (Cutri et al. 2003) for sources with no equivalent 2MASS XSC position.

After acquiring each target field, a flat field and an arc exposure, using copper-argon and copper-helium lamps, were taken for fibre identification and wavelength calibration. Three 900 s exposures of the fields yielded signal to noise ratios of ~15–30. However, seven 900 s exposures of targets in the PKS 1343–601 field achieved an average S/N ratio of only ~ 5 due to high galactic extinction ($A_B \sim 10$).

The data were reduced using the 2DFDR automatic data reduction program as described in Colless et al. (2001a). The default settings were used with the exception of the use of sky flux methods for fibre throughput calibration, as no off-sky measurements were taken. Once reduced, redshifts were measured using the RUNZ program developed for the 2dFGRS (also described in Colless et al. 2001a). This program uses the Tonry & Davis (1979) technique to cross correlate nine templates with the observed spectra in order to obtain the best absorption redshift. Where available, the program also determines emission redshifts by matching O II, Hβ, O III, Hα, N II and S II features.

2.2.1 Redshifts

A total of 3053 redshifts were measured, 2603 of which were not listed in NED at the time of the original data release (July 2006). Table 2.2 lists a representative sample of the complete table which can be found in Appendix A. As of July 2006, seven galaxies were contained in neither the NED or 2MASS XSC catalogues: Two galaxies identified with the prefix KKOWA were found from ESO 2.2m WFI *I*-band observations around PKS 1343-601 (Kraan-Korteweg et al. 2005a), two galaxies, labelled NNSW, are taken from NIR IRSF observations around Cen-Crux (Nagayama et al. 2005) and a further three galaxies, labelled DJRS, are new identifications from searches of DSS images.

Emission line redshifts are reported for approximately 32% of the sample, whilst absorption line based cross correlation redshifts are available for ~96%. For the ~27% identified through both absorption and emission features, the absorption redshift is found to be larger on average by ~58 km s^{-1}. This difference, which is usually attributed to gas out-

TABLE 2.2: A representative sample of the full table listed in Appendix A. Both heliocentric absorption and emission redshifts are listed where measured. Column 1 lists the galaxy identification. The 2MASS XSC name is given first and then the equivalent NED identification.equatorial coordinates are listed as either part of the name of the target or after the colon in the first column. The 2MASS J-band magnitude ($j_{m,ext}$), extrapolated from a fit to the radial surface brightness profile, is listed in column 2 where available. Columns 3 and 4 list the heliocentric velocities (cz km s^{-1}) identified through absorption and emission features respectively. As discussed below, the uncertainty on each measurement is $\pm$ 85 km s^{-1}.

Name	J_{Ext}	cz_{ab}	cz_{em}
Field: 1 (RA:201.17° Dec:-57.68° l:307.78° b:4.90°)			
2MASX J13184671-5804502	13.00		14774
2MASX J13190643-5744311	12.38	5552	5507
2MASX J13200919-5725561	12.15	4578	
2MASX J13203723-5752421	11.57	5469	
2MASX J13211580-5827564	12.71	6155	
2MASX J13212199-5718084	14.11	6949	6835
2MASX J13220594-5728001	12.15	5706	
2MASX J13230235-5732041	12.15	5204	
2MASX J13230489-5740301	12.38	5841	5798
2MASX J13231390-5709190	12.28	5763	
2MASX J13232993-5744020	13.22	6068	
NNSW71:J13233545-5747205			32701
...	...	...	...

flows, is consistent with offsets found in other galaxy surveys (e.g. Cappi et al. 1998).

In order to assess the combined reliability of the observations and data reduction, a repeat observation of one field (Ara/CIZA J1653.0-5943) was made. The difference between these measurements (shown in the top panel of Fig. 2.1) implies an rms uncertainty on a single measurement of 81 km s^{-1}.

The lower panel of Fig. 2.1 shows the residual differences between our data and those from ZCAT (Huchra et al. 1992, , 2005 November 27 edition). Coincident galaxies between the catalogues were found through name matching and searching for separations of less than 4 arcsec. For the resulting 433 galaxies, a negligible mean offset of only +2 km s^{-1} is found. A value of $\chi^2_\nu \sim 1$ is achieved by adopting an uncertainty of 89 km s^{-1} on our values and using the quoted ZCAT errors, which in the absence of multiple measurements are taken directly from the original source. At $cz \sim 6500$ km s^{-1}, the comparison exhibits an excess of negative values (i.e. ZCAT values significantly lower than the redshifts reported here). This can be attributed to the inclusion in ZCAT of redshifts for galaxies in Abell S0639 as measured

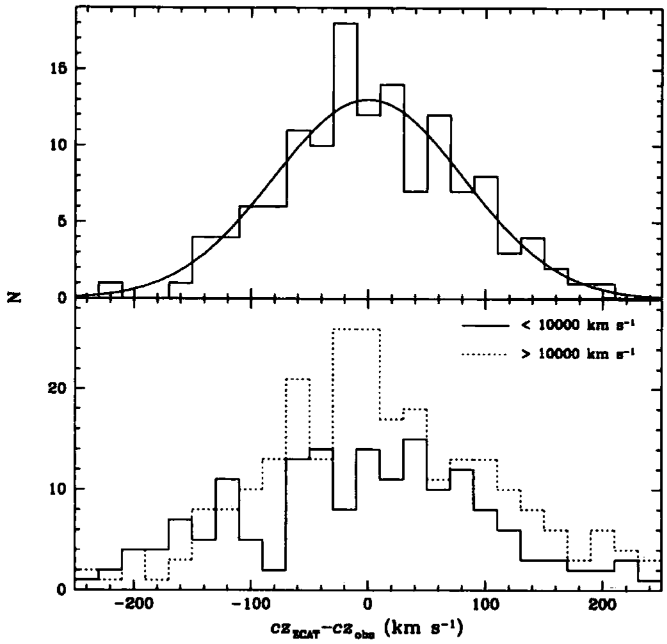

FIGURE 2.1: The top panel shows the difference between repeat observations of the same field. A Gaussian fit to the dispersion yields a value of $\sigma = 114\ \mathrm{km\,s^{-1}}$, corresponding to a single measurement rms uncertainty of 81 $\mathrm{km\,s^{-1}}$. The bottom panel plots the difference between coincident measurements from the ZCAT catalogue. Histograms are plotted separately for data within 10,000 $\mathrm{km\,s^{-1}}$ and for data beyond as coincident measurements primarily fall into two distinct velocity ranges around 6000 $\mathrm{km\,s^{-1}}$ and 15,000 $\mathrm{km\,s^{-1}}$. The mean offset of the points is +2 $\mathrm{km\,s^{-1}}$ and the scatter is consistent with an error of 89 $\mathrm{km\,s^{-1}}$ on our data points.

by Stein (1996). These measurements are offset from the rest of the ZCAT catalogue by approximately −140 $\mathrm{km\,s^{-1}}$, causing the enhancement around this value in the residual histogram that represents comparisons within 10,000 $\mathrm{km\,s^{-1}}$.

Comparison of the 221 galaxies in common with the 6dF Galaxy Survey (6dfGS 2DR, Jones et al. 2005) indicates an error of 94 $\mathrm{km\,s^{-1}}$ with a mean offset of +3 $\mathrm{km\,s^{-1}}$. While analysis of the 96 galaxies also observed by Woudt et al. (2004) yields an 89 $\mathrm{km\,s^{-1}}$ uncertainty and +19 $\mathrm{km\,s^{-1}}$ offset. Hence, as with the 2DFGRS (Colless et al. 2001a), we adopt an underlying random error of 85 $\mathrm{km\,s^{-1}}$ on all our measurements.

The completeness of the observed 2MASS galaxies as a function of the extrapolated J-band magnitude is shown in Fig. 2.2. The vast majority of targeted galaxies are found in the range $12 < J_{\mathrm{Ext}} < 16$ mag. Typically 10% of these yield no reliable redshift due to dominant stellar contamination. Hence this survey has good completeness to $J = 13$ mag, after which

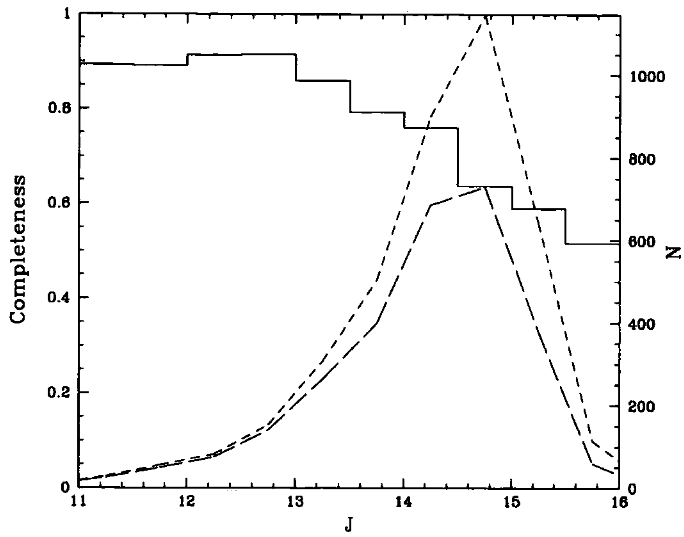

FIGURE 2.2: The completeness of targeted galaxies. The solid histogram indicates the percentage of targeted galaxies in each 0.5 mag bin for which a reliable redshift was discernible. The short and long dashed lines show respectively the total number of galaxies targeted and the number actually recorded in each corresponding bin.

a steady decline is observed down to an effective completeness of ~60% for the faintest galaxies at $J > 16$ mag. To illustrate the depth of the survey we calculate the characteristic magnitude at the distance of the GA and the SSC. By fitting a Schechter function to the combined 2dFGRS/2MASS infrared catalogue, Cole et al. (2001) find a magnitude corresponding to the characteristic luminosity $L^\star$ of $M_J^\star - 5\log h = -22.36\pm0.02$. Using this value we find an apparent magnitude of $J \sim 11$ mag at the GA ($cz \sim 4500$ km s^{-1}) and ~ 13.5 mag at the SSC ($cz \sim 14{,}500$ km s^{-1}). These values include corrections for foreground extinction, which around the Norma cluster and the SSC, is typically $A_J \sim 0.17$ and 0.05 mag respectively.

2.3 Large-Scale Structures in the GA/SSC direction

The redshift distribution for each of the surveyed fields is shown in Fig. 2.3. Immediately obvious are the large over-densities in fields 1,2 & 6–11 corresponding to the targeted clusters. The structures in which these clusters are embedded are also apparent in many of the fields as features at redshifts of around 2000–6000 km s^{-1} and ~15,000 km s^{-1}, corresponding to the GA and SSC respectively.

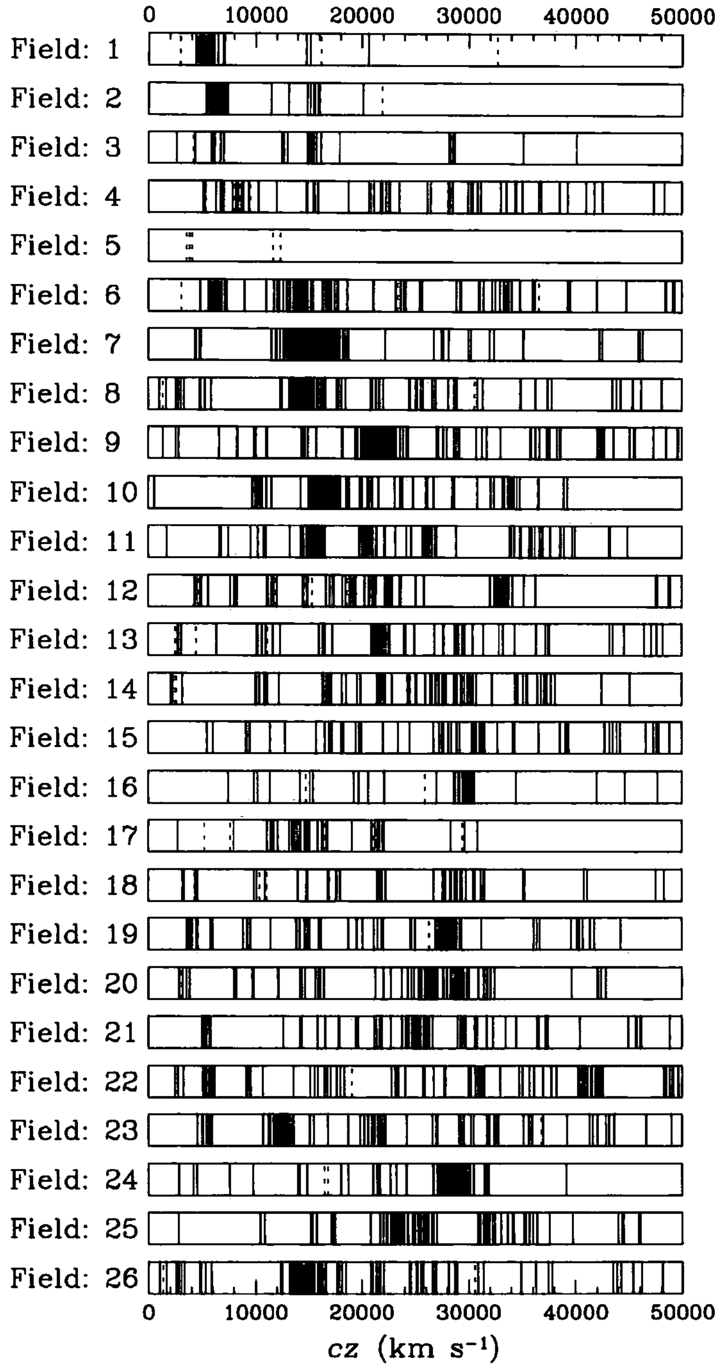

FIGURE 2.3: Distribution of radial velocities in each of the 26 targeted fields listed in Table 2.1. Dashed lines refer to redshifts derived through observed emission lines, whilst solid lines indicate measurements made via cross-correlation with template spectra. Note that field 26 is a repeat observation of field 8.

2.3.1 Review of Large-Scale Structures

The number of redshifts known in the GA and SSC region have greatly increased with the recent completion of surveys such as FLASH (Kaldare et al. 2003), 6dFGS, the SSC study of Proust et al. (2006) and the 'extragalactic large-scale structures behind the southern Milky Way' project (Kraan-Korteweg & Woudt 1994; Fairall et al. 1998; Woudt et al. 1999; Woudt et al. 2004). Together with our measurements, we use these recent surveys to assess the large-scale structures traced by the galaxies in this important region. Fig. 2.4 plots the combined projected distribution of the redshifts. The first panel identifies the 2dF fields observed by this survey. The majority of fields lie in regions outside the 6dFGS survey limit (i.e. $b < |10|°$) and predominantly near 2MASS over-densities close to the classic GA centre. Abell clusters are identified in the last two panels. whilst the remaining panels present the data in successive redshift slices, which contain the following relevant structures:

$cz \leq 2000$ km s^{-1}: In this panel, a line of galaxies crossing the Galactic plane at $l = 280°$ and extending to the centre of the Virgo Cluster (off the panel at $l = 280°$, $b = +74°$) is clearly seen. These belong to the Virgo Supercluster, which encircles the entire sky and defines the Supergalactic Plane. The smaller Fornax Wall is also seen here face-on (Fairall 1998). It appears as a filament of galaxies running from the Fornax cluster (237°, –54°) and crossing the Galactic plane at $l = 295°$. The extension of these filaments through the ZoA is traced by the HI galaxies from surveys based on the HI Parkes All-Sky Survey (HIPASS, Barnes et al. 2001), most notably the HIPASS Bright Galaxy Catalogue (Koribalski et al. 2004) and the deep HIPASS catalogue (HICAT, Meyer et al. 2004).

$2000 < cz \leq 4000$ km s^{-1}: Immediately apparent in the third panel, is the Centaurus cluster (Abell 3526) lying at (302°, +22°). Extending down from this cluster and through the galactic plane is the Centaurus Wall. This wall crosses a large part of the southern sky and is one of the most prominent features in all-sky maps of galaxies within 6000 km s^{-1} (Fairall 1998). As we lie close to the plane of the Centaurus Wall, the structure is seen edge-on (Fairall 1998).

Almost perpendicular to the Centaurus Wall is the Hydra Wall (Fairall 1998). This is seen here as a filament of galaxies reaching out from the Centaurus cluster, through the Hydra (270°, +27°) and Antlia (273°, +19°) clusters before heading on to the Puppis cluster (240°, 0°, Lahav et al. 1993) and down towards (210°, –30°).

The Hydra-Antlia extension (Kraan-Korteweg & Woudt 1994) forms a third filamentary structure in this slice. From the Hydra cluster, this feature passes through the Antlia cluster, crosses the Galactic plane at $b = 278°$ and ends in a group of galaxies at (280°, –8°).

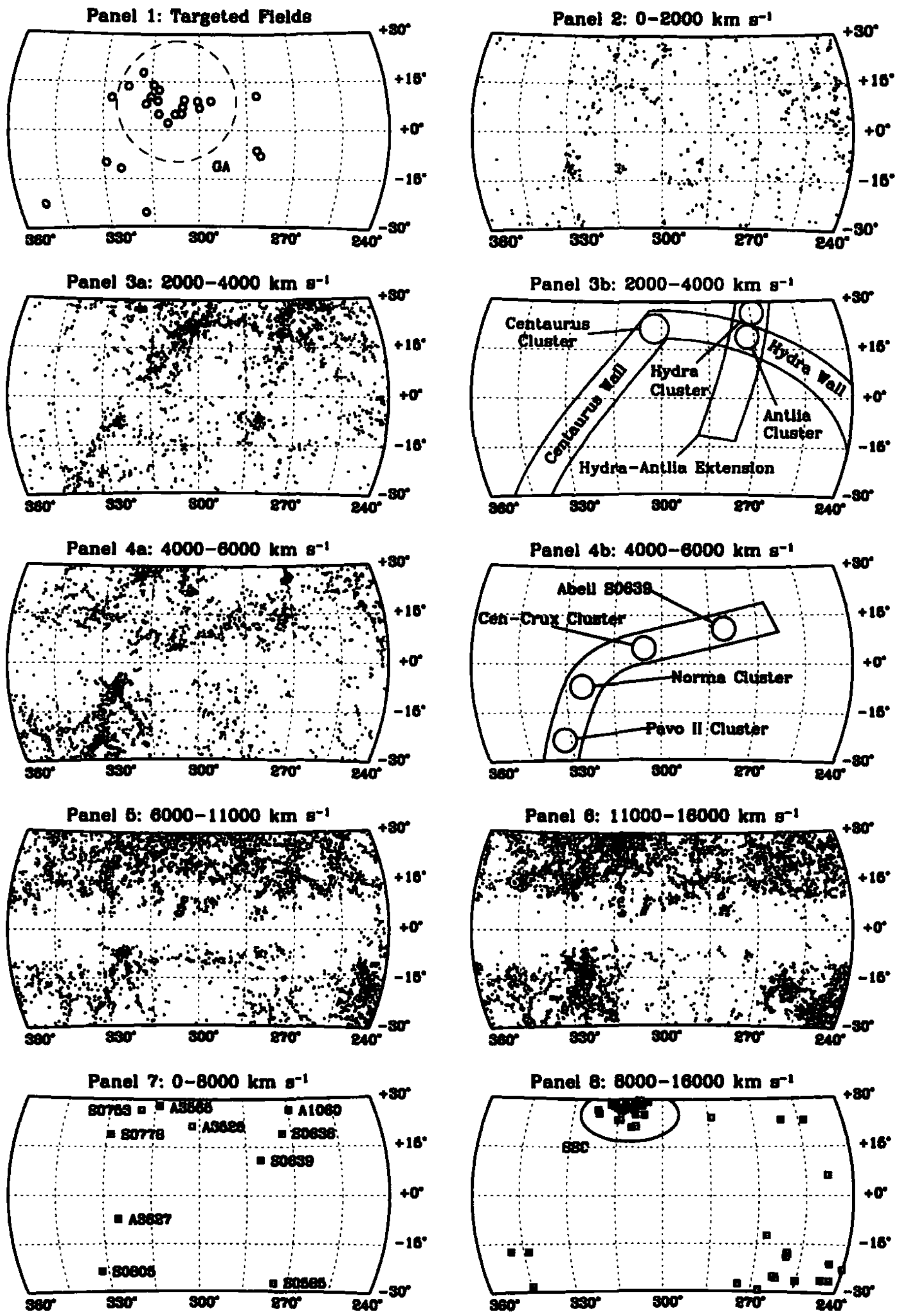

FIGURE 2.4: Aitoff projections of redshift slices containing galaxies in the range $240° < l < 360°$ and $-30° < b < +30°$ from this survey and the NED database (as of May 2007). The projected circles in the first panel represent the actual size of each 2dF target field located in the region. The dashed circle represents the core radius used in the spherical GA model of Faber & Burstein (1988) centred on (306°, +9°). Panels 3b and 4b illustrate the key features observed in the corresponding redshift slices. Abell clusters within 8000 km s^{-1} are labelled in Panel 7, whilst in panel 8, Abell clusters between 8000 and 16,000 km s^{-1} are plotted and the clusters composing the SSC are indicated.

Kraan-Korteweg & Woudt (1994) suggested that an overdensity of galaxies, named the Vela overdensity and located at (280°, +6°), formed part of the Hydra-Antlia extension. However subsequent observations of this group have revealed that it lies significantly behind the extension at $cz = 6000$ km s^{-1} (Kraan-Korteweg et al. 1995).

4000 < $cz \leq$ 6000 km s^{-1}: The fourth panel reveals the massive Norma cluster of galaxies lying at (325°, −7°). Below this and connected by a trail of galaxies is the Pavo II cluster (Abell S0805, $l = 332°$, $b = -24°$). Additionally, two smaller filaments of galaxies are seen extending down from the Norma cluster to both lower and higher galactic longitudes.

A less pronounced linear feature is also observed in this panel. Continuing from the connection between the Pavo II and Norma clusters, the structure extends across the Galactic plane and on through CIZA J1324.7–5736 (307°, +5°) and the Cen-Crux (305°, +5°) cluster before ending at Abell S0639 (281°, +11°). Collectively, this structure is known as the 'Norma supercluster' (Woudt et al. 1997) and is discussed further in Section 2.3.3.

6000 < $cz \leq$ 11,000 km s^{-1}: The Norma cluster 'finger of God' is still evident in this panel. The linear feature at $b = -10°$ that extends from this overdensity towards lower galactic latitudes, is an artificial enhancement due to the survey limit ($b \lesssim -10°$) of the combined southern Milky Way survey (Kraan-Korteweg et al. 1995; Fairall et al. 1998; Woudt et al. 1999). The Vela overdensity and continuation of the Cen-Crux structure are both seen as distinct groups at (305°, +6°) and (280°, +6°) respectively. Also present is the Ophiuchus cluster (Hasegawa et al. 2000; Wakamatsu et al. 2005) lying at the edge of the panel (360°, +9°, 8500 km s^{-1}).

11,000 < $cz \leq$ 16,000 km s^{-1}: In the last panel, the massive concentration of clusters that constitute the SSC becomes apparent around (314°, +30°). Also visible are the large Ara (329°, −10°) and Triangulum-Australis (325°, −12°) clusters (lying almost directly behind the Norma cluster), CIZA J1514.6–4558 at (327°, +10°) and CIZA J1410.4–4246 at (318°, +18°).

2.3.2 Clusters

Of great importance in studying the GA flow is an assessment of the relative masses of the rich clusters in the region. Notably, the CIZA survey has identified several new X-ray clusters in the GA direction. We targeted six of these sources, which together with noticeable overdensities in the 2MASS XSC, made up nine fields containing possible clusters.

To determine if these systems were indicative of relaxed clusters, their velocity dispersions, culled by an iterative 3-σ clipping procedure about their median, were tested for Gaussianity. With no prior on the mean or standard deviation, the Shapiro-Wilk W-statistic (Shapiro & Wilk 1965) is able to test the null hypothesis that data is indeed sampled from a normal distribution. We accept this hypothesis if the associated p-value, calculated via the analytical approach of Royston (1995), is greater than 0.05.

If the W-statistic for a sample indicates that the redshifts were taken from a normal distribution, the corresponding velocity dispersion was determined using a method that includes measurement errors on individual redshifts (Danese et al. 1980). Uncertainties on the derived values were calculated by bootstrap resampling.

The masses of the corresponding systems were calculated using the classical virial mass estimator, defined by Heisler et al. (1985) as

$$M_{\rm vir} = \frac{3\pi N}{2G} \frac{\sum_i (v_i - \bar{v})^2}{\sum_{i,j<i} R_{ij}^{-1}}$$

where

$$R_{ij} = |R_i - R_j|$$

is the projected galaxy separation. This virial method has been shown to be a reliable first order approximation to the mass of a dynamically relaxed system which is fully contained within the observed field (e.g. see Rines et al. 2003). The projected mass estimator for each cluster was also calculated:

$$M_{\rm proj} = \frac{32}{N\pi G} \sum_i R_i (v_i - \bar{v})^2.$$

Errors on both mass estimates were again assigned by bootstrap resampling. With their sample of nine clusters in the CAIRNS project, Rines et al. (2003) find that the projected mass is only 1.18 ± 0.05 times greater than the estimated virial mass. Hence, given the expected errors on the dispersions, the two estimators should be consistent.

Table 2.3 lists the mean redshift, velocity dispersion, mass estimate, W-statistic and associated p-value for the best fit to each of the observed clusters. These fits are plotted with the corresponding velocity histograms in Fig. 2.5.

TABLE 2.3: Parameters for the fits to the velocity distributions of the observed clusters as detailed in Section 2.3.2.

Cluster Name	$\bar{v}$ km s^{-1}	σ km s^{-1}	M_{Virial} $h^{-1}\,M_\odot$	$M_{Projected}$ $h^{-1}\,M_\odot$	W	N	p
CIZA J1324.7–5736	5570 ± 92	618 ± 72	$(3.5 \pm 1.0) \times 10^{14}$	$(3.9 \pm 0.7) \times 10^{14}$	0.9555	40	0.1176
Abell S0639A	6501 ± 61	405 ± 40	$(1.2 \pm 0.3) \times 10^{14}$	$(1.7 \pm 0.4) \times 10^{14}$	0.983	40	0.7987
Abell S0639B	14125 ± 66	412 ± 39	$(3.6 \pm 0.8) \times 10^{14}$	$(5.3 \pm 0.6) \times 10^{14}$	0.951	41	0.0648
Triangulum Australis	15060 ± 97	1408 ± 67	$(5.7 \pm 0.6) \times 10^{15}$	$(6.9 \pm 0.5) \times 10^{15}$	0.9855	220	0.0242
(corrected)	14898 ± 90	1246 ± 59	$(4.4 \pm 0.4) \times 10^{15}$	$(5.4 \pm 0.4) \times 10^{15}$	0.9919	210	0.2945
Ara	14634 ± 76	881 ± 48	$(2.0 \pm 0.3) \times 10^{15}$	$(2.6 \pm 0.2) \times 10^{15}$	0.9840	147	0.0850
CIZA J1514.6–4558	16715 ± 50	601 ± 35	$(1.2 \pm 0.1) \times 10^{15}$	$(1.5 \pm 0.1) \times 10^{15}$	0.9953	149	0.9145
CIZA J1410.4–4246A	15574 ± 63	497 ± 40	$(5.2 \pm 0.9) \times 10^{14}$	$(6.2 \pm 0.8) \times 10^{14}$	0.9761	66	0.2328
CIZA J1410.4–4246B	20463 ± 53	345 ± 37	$(5.3 \pm 1.3) \times 10^{14}$	$(7.5 \pm 0.8) \times 10^{14}$	0.9569	45	0.0922
Cluster 1 (Field 9)	21445 ± 78	925 ± 52	$(3.1 \pm 0.3) \times 10^{15}$	$(3.8 \pm 0.3) \times 10^{15}$	0.9851	151	0.1023
Cluster 2 (Field 25)	-	-	-	-	0.9685	85	0.0354

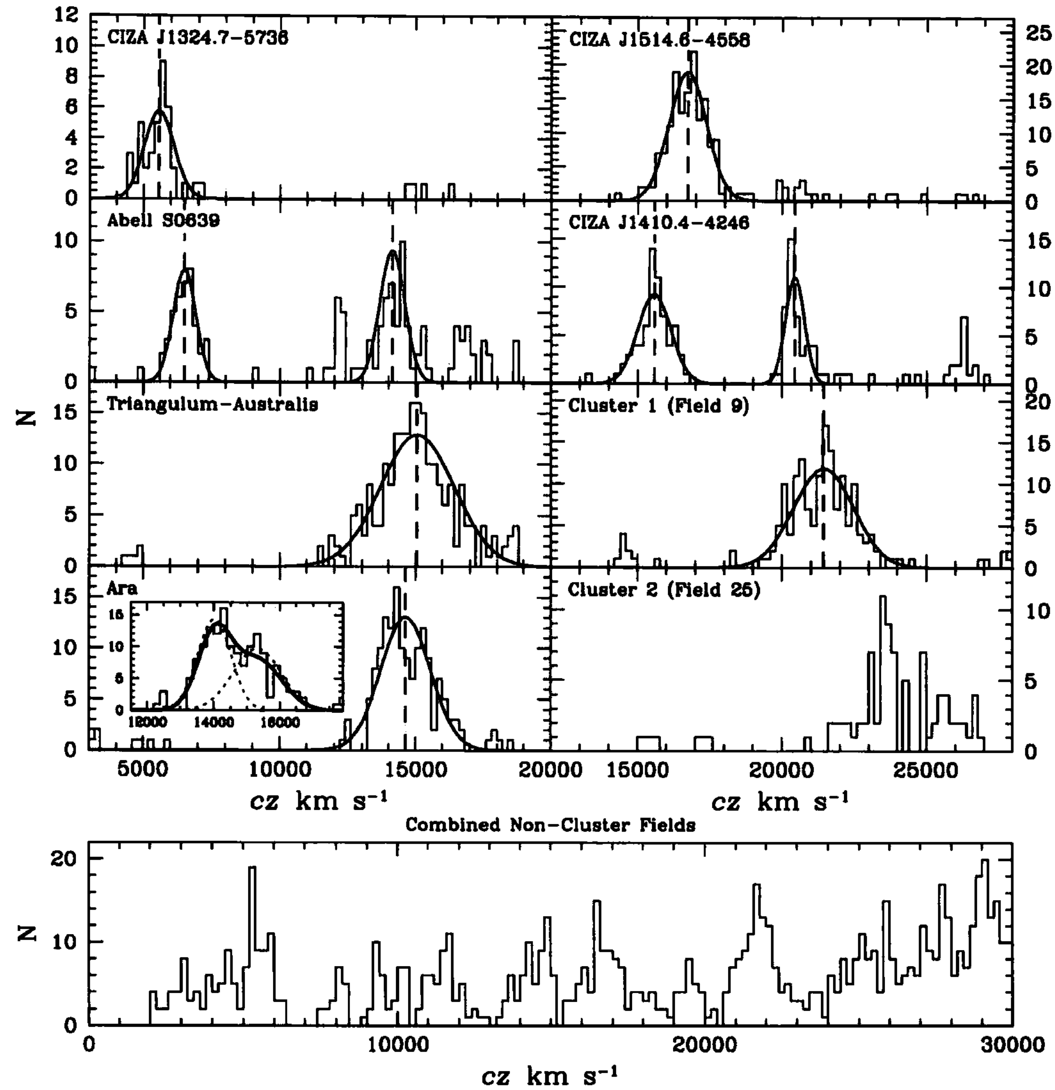

FIGURE 2.5: The radial velocity dispersions and corresponding virial fits for the observed clusters are shown in the upper panel. The corrected fit is plotted for the Triangulum-Australis cluster. The lower panel shows the combined velocity distribution for the 11 non-cluster fields.

2.3.2.1 Cen-Crux/CIZA J1324.7–5736

Multi-object spectroscopy of the GA region revealed an overdensity of galaxies at (305°, +5°, 6214 km s^{-1}), which was named the Cen-Crux cluster (Woudt 1998; Fairall et al. 1998; Woudt et al. 2004). Later, an associated X-ray cluster signature was detected by the CIZA survey at (307°, +5°). Preliminary analysis of the X-ray source (CIZA J1324.7–5736) suggested that it was comparable in mass to the Norma cluster (Ebeling et al. 2002).

We have observed one field centred on the X-ray source and three further fields targeting

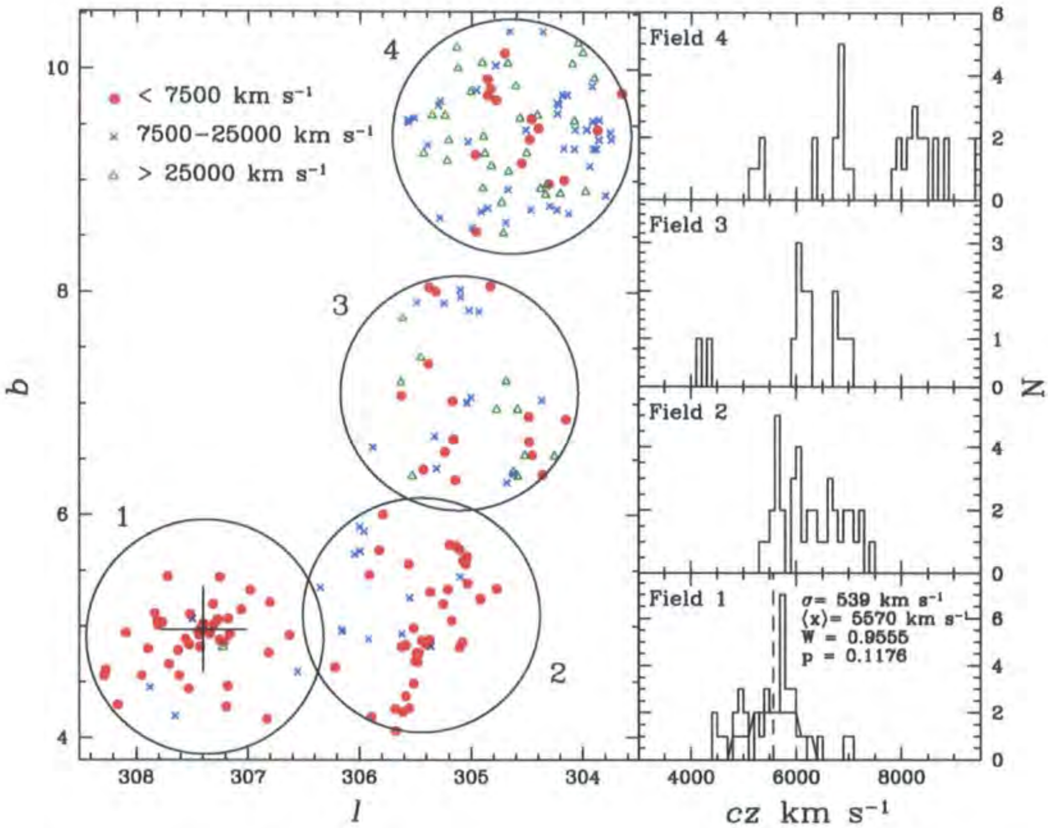

FIGURE 2.6: Galactic longitude and latitude of galaxies measured by this survey for the four denoted 2dF fields in the Cen-Crux region. The large cross marks the centre of the X-ray source CIZA J1324.7–5736. The right hand panels show the corresponding velocity histograms for each of the fields between 3000 and 9500 km s^{-1}.

the surrounding overdensities (see Fig. 2.6). Of the 223 identified redshifts in the targeted fields, 110 are within 7500 km s^{-1}. Two distinct structures are observed within these fields.

Ebeling et al. (2002) noted that the appearance of the X-ray emissions in the region and their association with the brightest cluster galaxy WKK2189 (cz = 5585 km s^{-1}), were suggestive of a dynamically relaxed cluster. 40 of the observed galaxies are found to be associated with the X-ray source. Shown in the Field 1 histogram on the right hand side of Fig. 2.6, the velocity dispersion of these galaxies is 539 ± 80 km s^{-1} centred on 5570 ± 92 km s^{-1}. The Shapiro-Wilk test on this distribution yields a p-value of 0.1176 and the estimated virial mass is $(3.5 \pm 1.0) \times 10^{14} h^{-1}\,M_\odot$. Hence the interpretation of a large relaxed cluster is supported here by the observed Gaussian velocity distribution.

Comparison with the Norma cluster velocity dispersion of 897 km s^{-1} (Kraan-Korteweg et al. 1996) suggests that CIZA J1324.7–5736 is approximately 0.3–0.5 times as massive. This is in agreement with the Mullis et al. (2005) comparison of XMM-Newton observations of CIZA J1324.7–5736 with the X-ray temperature of the Norma cluster inferred by Tamura et al. (1998). Using the mass-temperature scaling relations, they conclude that CIZA J1324.7–5736 contains about a third of the mass of the Norma cluster. A future study of the extinction-corrected K_S-band luminosity function should provide further constraints on the relative mass (Nagayama et al. 2005).

The second distinct feature observed in the fields is that of the Cen-Crux overdensity itself. This appears as a filament like trail of galaxies separated from the X-ray source both spatially on the sky and in redshift. Although no connective structure is evident between this overdensity and CIZA J1324.7–5736, their close proximity suggest that they are gravitationally bound. As the structure is not dynamically relaxed, virial theorem does not apply. However the extent of the Cen-Crux structure and the number of galaxies contained within it implies a mass similar to that of the CIZA J1324.7–5736 cluster.

2.3.2.2 PKS 1343–601

PKS 1343–601 is the second brightest extragalactic radio source in the southern sky (Mills 1952). The associated galaxy, lying at (309.7°, +1.7°, 3872 km s^{-1}, West & Tarenghi 1989), is a large elliptical galaxy (Laustsen et al. 1977; West & Tarenghi 1989), typical of those found in cluster cores. Hence it has been suggested that PKS 1343–601 may mark the centre of another highly obscured ($A_B \sim 12$) cluster (Woudt 1998; Kraan-Korteweg & Woudt 1999).

X-ray studies have yet to reveal any indication that such a hidden cluster exists. No corresponding source is seen in the CIZA survey and the point-like X-ray emissions reported by Tashiro et al. (1998) are consistent with the radio lobes of PKS 1343–601 rather than intracluster gas (Ebeling et al. 2002). However in HIPASS observations, a small overdensity around the radio galaxy has been detected (Kraan-Korteweg et al. 2005b). The nature of this overdensity has recently been examined by three near-infrared surveys (Schröder et al. 2005; Kraan-Korteweg et al. 2005a; Nagayama et al. 2004). Through radial velocity studies, simulated sky-projections and extrapolation of luminosity functions, these surveys are all consistent with the notion of a low mass group or poor cluster centred on PKS 1343–601.

Unfortunately, of the 84 targets we identified in the 2dF field, our 6300 s observation yielded only five reliable redshifts. Of these is a reconfirmation of the redshift of PKS 1343–601. At 4065 ± 85 km s^{-1}, this is in agreement with the West & Tarenghi (1989) value. Of the other four new measurements, all identified through emission lines, two are located within 500 km s^{-1} of the radio galaxy. NWN2004 45 and NWN2004 51 are both taken from the Nagayama et al. (2004) catalogue and lie at 3861 and 3571 km s^{-1} respectively. These galaxies, together with those identified both optically and in HI by Schröder et al. (2005), brings the number of galaxies with known redshifts that are associated with the PKS 1343–601 group up to 20.

2.3.2.3 Abell S0639

The Abell S0639 cluster, which lies at (281°, +11°), was first studied in detail by Stein (1994, 1997), who for 32 galaxies measured a mean velocity of 6194 ± 78 $\mathrm{km\,s^{-1}}$ and a velocity dispersion of 431 ± 52 $\mathrm{km\,s^{-1}}$. Using a sample of 40 galaxies with a mean cz = 6501 ± 61 $\mathrm{km\,s^{-1}}$, we find a similar dispersion of 409 ± 55 $\mathrm{km\,s^{-1}}$. An additional feature is located in the same field, offset from Abell S0639 by 1.5°. At 14,065 ± 69 $\mathrm{km\,s^{-1}}$, the structure lies at the same distance as the SSC and is not inconsistent with a normal distribution (p-value = 0.0648). The measured virial velocity dispersion is 597 ± 91 $\mathrm{km\,s^{-1}}$, corresponding to a mass of $(4.9 \pm 1.2) \times 10^{14} h^{-1} \mathrm{M_\odot}$.

2.3.2.4 Triangulum Australis, Ara, CIZA J1514.6–4558 & CIZA J1410.4–4246

In the extended CIZA catalogue, Kocevski et al. (2005) have identified several X-ray sources located at $z \sim 0.05$, which they suggest form an extension to the SSC. In Ebeling et al. (2002), the same authors argue that these clusters may be responsible for the observed continued flow towards a point behind the GA. Of these sources we have targeted the four largest: CIZA J1638.2–6420 (the Triangulum-Australis cluster) located at (324.5°, –11.6°, 15,060 $\mathrm{km\,s^{-1}}$), CIZA J1653.0–5943 (the Ara cluster, Woudt 1998) at (329.3°, –9.9°, 14,634 $\mathrm{km\,s^{-1}}$), CIZA J1410.4–4246 (318.0°, 17.8°, 15,574 $\mathrm{km\,s^{-1}}$) and CIZA J1514.6–5736 (327.3°, 10.0°, 16,715 $\mathrm{km\,s^{-1}}$). All four structures have clearly identified Gaussian velocity distributions from which we are able to infer virial and projected masses as listed in table 2.3. The Triangulum-Australis cluster yields a noticeably low p-value (0.0242). This is due to the overdensity seen in the right hand tail of the dispersion. Removing the 10 galaxies with cz > 18,000 $\mathrm{km\,s^{-1}}$ from the field results in a more respectable p-value of 0.2945 (listed as corrected in table 2.3). With a corresponding virial mass of $(5.7 \pm 0.6) \times 10^{15} h^{-1} \mathrm{M_\odot}$, this large cluster is similar in mass to the Norma cluster.

Despite a p-value of 0.0850, the Ara cluster appears to display a bimodal velocity distribution. Fitting two Gaussian profiles to the data results in velocity dispersions of 498 ± 68 $\mathrm{km\,s^{-1}}$ and 731 ± 112 $\mathrm{km\,s^{-1}}$ centred on 14,016 ± 84 $\mathrm{km\,s^{-1}}$ and 15,310 ± 124 $\mathrm{km\,s^{-1}}$ respectively. These fits are shown in the inset to the Ara cluster panel of Fig. 2.5. There is no discernible separation in the projected sky distribution of the two populations, hence they may be two infalling clumps collapsing along the line of sight. A 7.5 ks *ROSAT* HRI observation of the cluster supports this argument, as two distinct peaks, separated by only 4 arcmin, were observed in the elongated X-ray emissions (Ebeling et al. 2002). Summed in quadrature, the two velocity dispersions are similar to the dispersion of the overall fit (881 ± 48 km s^{-1}); hence, even though virial theorem is not strictly applicable to such a system, the mass derived from the total fit provides a likely upper limit to the combined mass of the two clumps.

The results of the Shapiro-Wilk test for CIZA J1514.6–4558 and CIZA J1410.4–4246 indicate that they are consistent with being dynamically relaxed clusters as shown in Fig. 2.5. Behind CIZA J1410.4–4246 there appears a second group with a velocity dispersion consistent with a normal distribution. However with a skewness of 0.094, the mean distance and the velocity dispersion of the feature are likely overestimated.

The Triangulum-Australis and Ara clusters are physically separated by only $\sim 13.7\ h^{-1}$ Mpc and lie in approximately the same plane as the CIZA J1514.6–4558 and CIZA J1410.4–4246 clusters. Abell 3558, the core of the SSC, lies only 38 Mpc from CIZA J1410.4–4246 and so these clusters may well form an extension to the SSC. Nevertheless the presence of such large masses in close proximity to each other has a sizable influence on the X-ray based dipole (Kocevski et al. 2004).

2.3.2.5 Additional Clusters

Examination of 2MASS maps of the GA/SSC region reveals two further overdensities centred on (314.5°, +13.7°) and (321.7°, +13.4°). These were targeted in fields 9 (314.3°, +13.9°) and 25 (322.3°, +13.6°) respectively. Recently, Kocevski et al. (2005) have reported the presence of an X-ray source, identified as CIZA J1358.7–4750, at (314.5°, +13.5°), coincident with the structure in field 9. At $cz = 21{,}445 \pm 78$ km s^{-1} this cluster is far enough removed to have little influence ($V_{LG} < 3$ km s^{-1}) on local dynamics despite the large predicted mass ($\sim 3 \times 10^{15} h^{-1} M_{\odot}$).

As evident in the lower right panel of Fig. 2.5, The galaxies between 21,000 and 27,000 km s^{-1} in field 25 are concentrated into numerous sub-clumps loosely associated in a broad distribution. The associated p-value of 0.0345 confirms that this is not consistent with a dynamically relaxed cluster and hence we do not assign it a mass.

2.3.3 The Extended Norma Supercluster

Several large clusters are now known to reside in the GA region, i.e. Norma, Pavo II, Centaurus, Hydra and CIZA J1324.7–5736. However the connections between these clusters

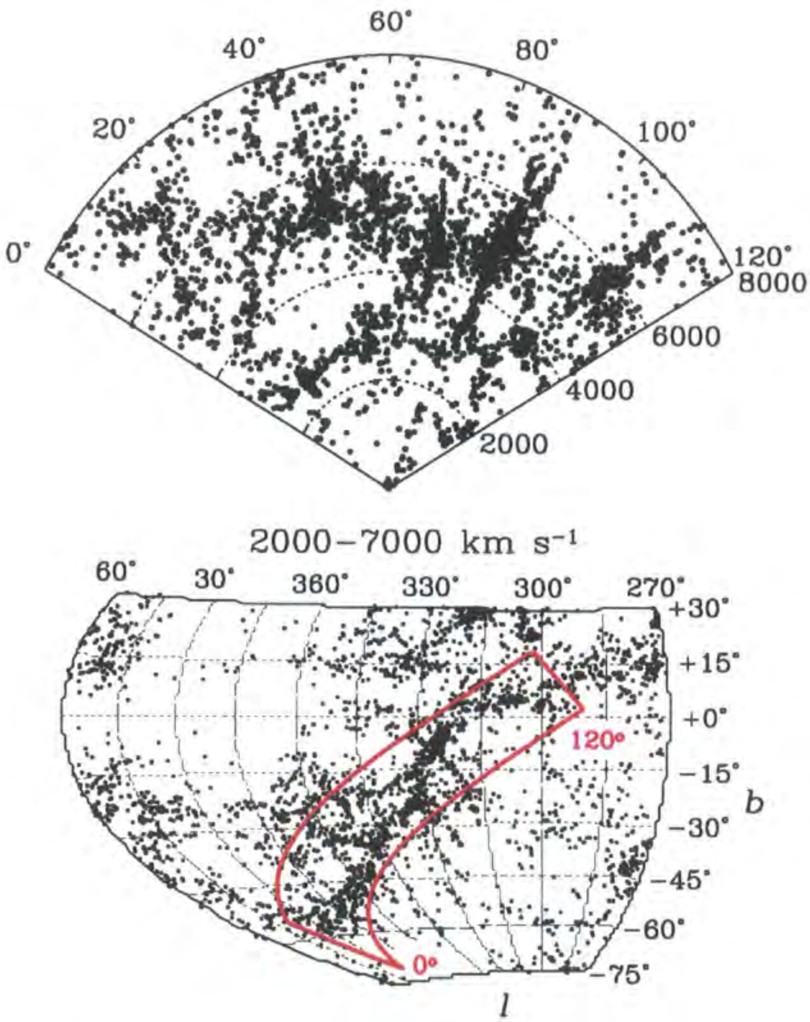

FIGURE 2.7: The pieplot represents the radial distribution of galaxies along the red projected rectangular strip shown in the lower panel. The strip covers a region 120° × 10°, orientated to lie along the filament. From the Norma cluster, lying 86° along the strip, the Norma supercluster is clearly seen as a wall of galaxies extending through the Pavo II cluster (at 71°) towards a point ~ 20° along the strip. The Centaurus Wall appears as a smaller connection of galaxies, running almost parallel to the Norma supercluster at 2600 $\mathrm{km\,s^{-1}}$. The void lying between the Norma supercluster and the Centaurus Wall is an extension of the massive Microscopium Void.

are still poorly resolved. As shown in Fig. 2.4, the Pavo II and Norma clusters are connected by a structure, which Woudt et al. (1997) have suggested extends through the ZoA towards the Cen-Crux overdensity. This connection is highlighted by the noticeable peak around 5500 $\mathrm{km\,s^{-1}}$ in the combined velocity distribution of non-cluster fields shown in the bottom panel of Fig. 2.5. To examine this feature further, Fig. 2.7 and Fig. 2.8 plot redshift slices of the filament below and above the Galactic plane.

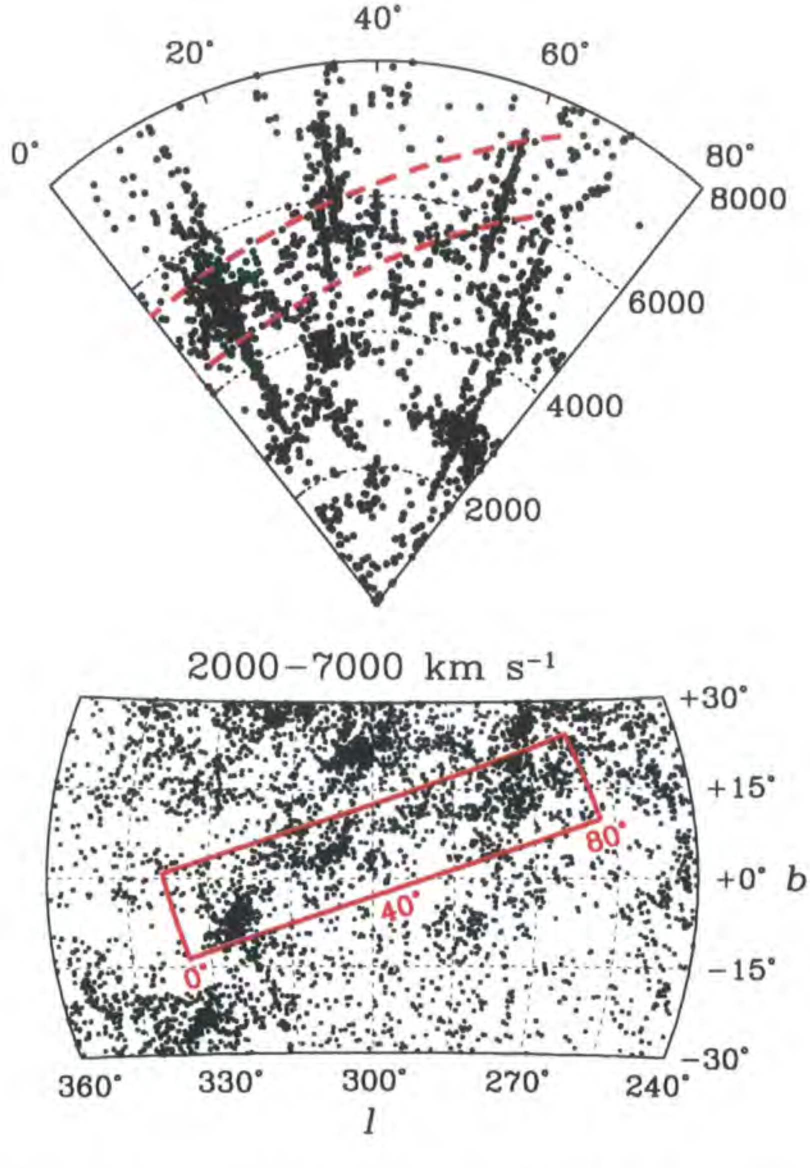

FIGURE 2.8: The pieplot contains the galaxies in the red 80° × 15° rectangular strip shown in the Aitoff projection. The proposed Norma supercluster, seen as a trail of galaxies lying between the red dashed lines, connects the 'fingers-of-God' of the Norma cluster (11°, 4500 km s^{-1}), CIZA J1324.7–5736 (31°, 5570 km s^{-1}) and Abell S0639 (58°, 6501 km s^{-1}). The overdensity at (70°, 2800 km s^{-1}) is the superposition of the Antlia cluster and the Hydra-Antlia extension seen in cross-section.

Evident in the foreground of the diagram in the upper panel of Fig. 2.7 is the Centaurus Wall. Appearing as a filament of galaxies running across the sky at $cz \sim 2600$ km s^{-1}, this structure is separated by some 2000 km s^{-1} from the Norma structure. This is in contradiction with earlier studies that have suggested the Norma cluster is a nexus between the Centaurus Wall and the Norma Supercluster (Woudt et al. 1997). The dearth of galaxies in the ZoA is clearly seen as the gap in the wall between the Norma and CIZA J1324.7–5736 clusters, which respectively appear as 'fingers-of-God' at 86° and 108° along the strip. However, below the ZoA, the extent of the structure is clearly evident as the broad wall of galaxies extends out from the Norma cluster, through the Pavo II cluster and on towards higher redshifts. In the Aitoff projection shown in the lower panel of Fig. 2.7, many additional, smaller filaments are seen branching off from the main structure, primarily at the location of the clusters. However a major branch splits off at around ~ (345°, –35°, 5000 km s^{-1}) and continues to ~ (17°, –22°, 6000 km s^{-1}). The main filament appears to disperse at ~ (5°, –50°, 5000 km s^{-1}), with apparent overdensities at greater galactic longitudes ($5° < l < 30°$, $-60° < b < -45°$) resulting from the projection along the line of sight of clumps, including galaxies in the Centaurus Wall.

Fig. 2.8 shows a possible extension of the Norma supercluster filament through the plane to higher galactic latitudes. Here the progression to higher redshifts is hinted at as the filament extends from the Norma Cluster (lying 11° along the strip), through CIZA J1324.7–5736 (at 31°) and the Cen-Crux feature (33°) and on towards Abell S0639 (58°). From this last cluster an extension towards another overdensity located off the panel at (268°, +17°, 9000 km s^{-1}) may exist, but lack of redshifts makes this difficult to discern. The Vela overdensity (280°, +6°, 6000 km s^{-1}) lies next to Abell S0639 and so forms a spur to the main filament. However, another intercluster connection from Abell S0639 appears to run at almost right angles to the Norma supercluster. This filament extends through the overdensity located at (272°, +13°, 4500 km s^{-1}), which is likely associated with Abell S0631 and Abell S0628, both of which currently have no reported redshift, before joining the Hydra cluster. As detailed in Section 2.3.1, the large Hydra cluster is connected by the Hydra Wall to the Centaurus cluster and by the Hydra-Antlia extension to the Antlia cluster and galaxies at lower galactic latitudes.

Thus, from Abell S0639 to ~(5°, –50°), there appears to exist a continuous filament of galaxies stretching across approximately 100° (i.e. ~ 120 Mpc) of the southern sky, with a velocity dispersion < 400 km s^{-1}. From studies of inter-cluster filaments in simulations, Colberg et al. (2005) find a typical overdensity along these structures of ~ 7 and cross-sectional radii of $\sim 2\,h^{-1}$ Mpc. Thus, not including the associated clusters, a filament of this size, dynamically centred at ~ (325°, –10°, 4800 km s^{-1}), might contain a mass as high as $\sim 2.5 \times 10^{15} h^{-1}\,M_{\odot}$. This is comparable to the mass of a large cluster and so represents another potentially significant component of the GA.

2.4 Summary

Using the 2dF on the AAT, we have measured 3053 redshifts in the GA/SSC region, of which 2603 are new measurements. These redshifts have helped reveal the composition of the GA, principally with the resolution of the CIZA J1324.7–5736/Cen-Crux feature. The X-ray source is revealed to be a dynamically relaxed cluster with a mass approximately 0.3–0.5 times that of the Norma Cluster, in good agreement with previous estimates.

By combining the results of this survey with redshifts from the literature, the major clusters associated with the GA are found to be joined by a possibly wall-like structure. This filament extends from Abell S0639, through the ZOA, where it meets the Norma cluster, and continues down to $\sim$ (5°, –50°, 5000 $\mathrm{km\,s^{-1}}$). Together with the Norma, Pavo II, CIZA J1324.7–5736 and Abell S0639 clusters, we can expect these structures to contribute a mass of $\sim 10^{16} h^{-1}\,\mathrm{M}_{\odot}$ towards the GA.

We have also measured the masses and composition of several other clusters behind the GA, including the Triangulum-Australis, Ara, CIZA J1514.6–4558 and CIZA J1410.4–4246 clusters. These have been proposed as possible sources to a continued flow beyond the GA. The significance of these X-ray clusters, and the implications of the GA model presented here, will be further analysed over the subsequent chapters as we study their influence on local dynamics as determined from redshift surveys.

3

The *IRAS* Gravity Field

3.1 Gravitational Instability in the Linear Regime

In order to study large-scale structure and local dynamics, we need to reconstruct from redshift surveys both the real-space density field and the real-space peculiar velocity field. The first step in this process is to construct a direct relation between the two fields. This is accomplished by restricting our analysis of the GI framework to the linear regime: i.e $V_{\rm pec} << c$ and the density contrast is defined such that

$$\delta = \frac{\rho(\boldsymbol{r}, t) - \bar{\rho}(t)}{\bar{\rho}(t)}, \tag{3.1}$$

where $\rho(\boldsymbol{r}, t)$ is the density field and $\rho\bar{(t)}$ the average density, which at the present epoch may be taken as $3H_0^2\Omega_0/8\pi G$. In this regime the present day density field is a direct scaling of the initial perturbations set in place after inflation.

We begin by expressing the pressureless fluid equations for mass continuity, force and gravity in proper coordinates:

$$\frac{\partial\rho}{\delta t} + \nabla\cdot(\rho\boldsymbol{V}) = 0, \tag{3.2}$$

$$\frac{\partial \boldsymbol{V}}{\partial t} + (\boldsymbol{V} \cdot \nabla)\boldsymbol{V} + \nabla\phi = 0, \tag{3.3}$$

$$\nabla^2\phi = 4\pi G\rho \tag{3.4}$$

where ρ is the mass density field $\rho(\boldsymbol{r}, t)$, $\boldsymbol{V}$ is the velocity field $\boldsymbol{V}(\boldsymbol{r}, t)$ which includes the Hubble expansion at $\boldsymbol{r}$ and ϕ is the gravitational potential $\phi(\boldsymbol{r}, t)$. Expanding equations 3.2 and 3.3 to first order, converting ∇ to comoving coordinates and removing the background (zeroth order) solution, yields:

$$\frac{\partial \delta}{\partial t} + \frac{1}{a}\nabla\cdot \boldsymbol{V}_{\rm pec} = 0 \tag{3.5}$$

$$\frac{\partial \boldsymbol{V}_{\rm pec}}{\partial t} + \frac{\dot{a}}{a}\boldsymbol{V}_{\rm pec} + \frac{1}{a}\nabla\phi = 0 \tag{3.6}$$

where a is the scale factor $a(t)$, an increasing function of time, and $\boldsymbol{V}_{\rm pec}$ is the peculiar velocity field as introduced in equation 1.2. Substituting the time derivative of equation 3.5 and the divergence of equation 3.6 into equation 3.4 yields:

$$\frac{\partial^2 \delta}{\partial t^2} + \frac{2\dot{a}}{a}\frac{\partial \delta}{\partial t} = 4\pi G\rho_0\delta \tag{3.7}$$

which, as a second-order partial differential equation in time alone, may be solved by separating the spatial and time dependent components as follows:

$$\delta = A(\boldsymbol{r})D_1(t) + B(\boldsymbol{r})D_2(t) \tag{3.8}$$

where D_1 and D_2 are growing and decaying modes respectively. Hence at late times the D_1 component will dominate and equation 3.5 reduces to

$$\nabla\cdot \boldsymbol{V}_{\rm pec} = -a\delta\frac{\dot{D}_1}{D_1} = -a_0 H_0 f\delta \tag{3.9}$$

since $H(t) = \dot{a}/a$ and the growth factor f is given by:

$$f \equiv \frac{1}{H_0 D_1}\frac{dD_1}{dt} = \frac{1}{H_0 D_1}\frac{dD_1}{da}\frac{da}{dt} = \frac{d\log D_1}{d\log a} \tag{3.10}$$

D_1 and so f are functions of Ω_m and Λ. Lahav et al. (1991) have shown that the present day value of f may be approximated as:

$$f(z=0) \approx \Omega_m^{0.6} + \frac{\Lambda}{70}\left(1 + \frac{1}{2}\Omega_m\right) \tag{3.11}$$

As this is only weakly dependent on Λ, f is often taken as $\Omega_m^{0.6}$ (e.g. Peebles 1980) and so:

$$\nabla \cdot \boldsymbol{V}_{\rm pec} = -a_0 H_0 \Omega_m^{0.6} \delta(\boldsymbol{r}) \tag{3.12}$$

which may be solved by the methodology of electrostatics to yield in proper coordinates the expression:

$$\boldsymbol{V}_{\rm pec}(\boldsymbol{r}) = \frac{H_0 \Omega_m^{0.6}}{4\pi} \int \delta(\boldsymbol{r}') \frac{(\boldsymbol{r}' - \boldsymbol{r})}{|\boldsymbol{r}' - \boldsymbol{r}|^3} d^3\boldsymbol{r}' \tag{3.13}$$

We are unable to observe the mass density field $\delta(\boldsymbol{r})$ directly, instead we assume that galaxies linearly trace $\delta(\boldsymbol{r})$ with a constant bias defined by b_g:

$$\delta_g(\boldsymbol{r}) = b_g \delta(\boldsymbol{r}) \tag{3.14}$$

where $\delta_g(\boldsymbol{r})$ is the observed galaxy density contrast. Using this approximation we may replace $\delta(\boldsymbol{r})$ in equations 3.12 and 3.13 with $\delta_g(\boldsymbol{r})$ provided we also replace $\Omega^{0.6}$ with the redshift distortion parameter β, defined earlier as

$$\beta = \frac{\Omega_m^{0.6}}{b_g} \tag{3.15}$$

Hence:

$$\nabla \cdot \boldsymbol{V}_{\rm pec} = -a_0 H_0 \beta \delta_g(\boldsymbol{r}) \tag{3.16}$$

and

$$V_{\rm pec}(\boldsymbol{r}) = \frac{H_0\beta}{4\pi}\int \delta_g(\boldsymbol{r}')\frac{(\boldsymbol{r}'-\boldsymbol{r})}{|\boldsymbol{r}'-\boldsymbol{r}|^3}d^3\boldsymbol{r}' \tag{3.17}$$

3.2 Application to Galaxy Catalogues

As explained in section 1.5, equations 3.16 and 3.17 offer two alternative strategies for determining the value of β. Using equation 3.16, density and 3D velocity fields may be inferred from the observed radial peculiar velocities. With equation 3.17, the fields are derived from the observed positions of the galaxies. The former approach has typically been implemented with the POTENT method (see Hendry 2001). Importantly, this technique reconstructs the density field free from any bias in the population used to trace the velocity field. However, POTENT has been shown to be particularly susceptible to errors and biases in distance estimates, thus requiring careful treatment of the data (Newsam et al. 1995).

Comparatively, many techniques beyond the simple iterative approach described in section 1.5 have been developed for solving equation 3.17. Willick et al. (1997b), for instance, have produced a maximum likelihood based code named VELMOD. This analysis uses several reconstructions with different values of β to relate the observed radial velocity with distance. It then minimises $\mathcal{L} = -2\ln P$ for each reconstruction, where P is the combined probability for each galaxy of observing either the apparent magnitude or velocity width given the corresponding TF observable and the observed radial velocity. The minimum of a fit to $\mathcal{L}(\beta)$ is taken as the best fit β.

Non–iterative techniques have also been used for mapping redshift space to real space. Most notably (Nusser & Davis 1994, ND94) have used a method based on the Zel'dovich approximation. This approximation extends linear theory by including displacements of galaxies from their initial positions as structure grows (Zel'Dovich 1970). The method employed by ND94 again assumes that the velocity field is irrotational (however this time using the redshift space derivation), such that it may be expressed as the gradient of a velocity potential field:

$$V(s) = -\nabla\Phi(s) \tag{3.18}$$

where s is the redshift space radial coordinate.

Using the Zel'dovich approximation the redshift space peculiar velocity field defined in equation 3.18 may then be directly related to the redshift space density field. Expanding the angular dependence of this expression for Φ and δ_g in spherical harmonics then yields:

$$\frac{1}{s^2}\frac{d}{ds}\left(s^2\frac{d\Phi_{lm}}{ds}\right)-\frac{1}{1+\beta}\frac{l(l_1)\Phi_{lm}}{s^2}=\frac{\beta}{1+\beta}\left(\delta_{g,lm}-\frac{1}{s}\frac{d\ln\phi}{d\ln s}\frac{d\Phi_{lm}}{ds}\right) \tag{3.19}$$

where the subscript lm denotes the spherical harmonic coefficients, s is the redshift space radial coordinate and ϕ is the selection function of the sample. The redshift space galaxy density field is then smoothed, the components of $\delta_{g,lm}$ are computed, equation 3.19 is solved for Φ_{lm} and the redshift space 3D velocity field is computed from equation 3.18. The real-space velocity field may then be inferred by using the redshift space velocity field to map the redshift space positions to real-space positions along the line of sight.

Similarly, Fisher et al. (1995b) expand the density field into orthogonal radial spherical Bessel functions, $j_l(x)$, and angular spherical harmonics, $Y_{lm}(\hat{\boldsymbol{r}})$, satisfying

$$\rho(\boldsymbol{r})=\sum_{lmn} C_{ln}\rho_{s,lmn}j_l(k_n r)Y_{lm}(\hat{\boldsymbol{r}}) \tag{3.20}$$

where C_{ln} is the spherical Bessel function normalisation and $\rho_{s,lmn}$ is the redshift space density coefficient. In this prescription, the peculiar velocities only couple to the radial component of the density field. The coupling may be described by the matrix $(\mathbf{Z}_l)_{mn'}$:

$$\rho_{s,lmn}=\sum_{n'}(\mathbf{Z}_l)_{mn'}\rho_{r,lmn'} \tag{3.21}$$

where the subscript r denotes the real-space component. The real-space density harmonics can thus be derived by inverting equation 3.21, however shot noise leads to an unstable solution. This behaviour can be suppressed by using a Wiener filter in the inversion:

$$(\rho_{r,lmn})_{\mathrm{WF}}=\sum_{n'n''}(\mathbf{S}_l[\mathbf{S}_l+\mathbf{N}_l]^{-1})_{nn'}(\mathbf{Z}_l^{-1})_{n'n''}\rho_{s,lmn''} \tag{3.22}$$

where $\mathbf{S}_l$ and $\mathbf{N}_l$ are the signal and noise matrices. The real-space velocity field may then be extracted from the harmonics of the real-space density field.

Nusser & Davis (1994) have used a similar decomposition of radial spherical Bessel functions and angular spherical harmonics to describe the real-space velocity field as measured by the inverse Tully-Fisher relation (ITF). In this method the likelihood of observing the velocity widths given the absolute magnitude (inferred from the velocity field) is maximised by adjusting the model parameters. The resulting smoothed velocity field can then be directly compared to reconstructed fields from the above methods.

Typically comparisons based on the POTENT analysis have yielded values of β_I (where the subscript I denotes comparisons using catalogues from Infrared Astronomical Satellite [*IRAS*] based data) of approximately one. Comparatively, studies based on the velocity-velocity comparison methods such as VELMOD yield values of ~ 0.5 as summarised in table 3.1. Density-density comparisons like POTENT should yield results consistent with these velocity-velocity analyses and so this marked difference in β is difficult to explain. Intriguingly, Zaroubi et al. (2002) have used an unbiased minimal variance (UMV) estimator to reconstruct both density and velocity fields from the SECat catalogue (Zaroubi 2000): a combination of peculiar velocity measurements from the SFI (Giovanelli et al. 1999) and ENEAR surveys (da Costa et al. 2000). Comparing the velocity field with the PSCz reconstruction yields a value of $\beta_I = 0.51 \pm 0.06$, similar to previous determinations. However, unlike POTENT, comparison of the two density fields results in a value of $\beta_I = 0.57^{+0.11}_{-0.13}$, consistent with the velocity-velocity comparisons. This suggest the high POTENT values may be attributed to a high noise sensitivity in the code. This principally arises through the procedures used to smooth the sparse peculiar velocity measurements to a continuous velocity field.

3.3 The PSCz Velocity Field

The PSCz survey consists of redshifts for 15,411 galaxies uniformly distributed over 84.1% of the sky with a median redshift of 8500 km s^{-1}. The survey's depth, excellent sky coverage and density allow for the reliable mapping of the distribution of galaxies in the local universe. Several independent determinations of the PSCz density and velocity fields have therefore been made; most notably by Branchini et al. (1999), Schmoldt et al. (1999) and Rowan-Robinson et al. (2000). As summarised in table 3.1, recent comparisons of these fields with peculiar velocity measurements typically yield values of β_I in the range 0.4 - 0.6 (see Zaroubi 2002).

However, a significant source of error in determining β arises from the uncertainty in the peculiar velocity measurements. As detailed in section 1.3, galaxy distance estimates from the Tully-Fisher and Fundamental Plane relations are subject to errors that are typically $\sim 20\%$ per galaxy. At depths greater than $\sim 50\ h^{-1}$ Mpc this is considerably larger than the

TABLE 3.1: The determination of β_I using several reconstruction and comparison techniques.

Reconstruction	Comparison	β	Reference
	$\delta-\delta$ Comparison		
POTENT	Various infrared TF & $D_n-\sigma$ measurements vs. *IRAS* 1.9 Jy	$1.28^{+0.75}_{-0.59}$	Dekel et al. (1993)
POTENT	MARK III vs. *IRAS* 1.2 Jy	0.89 ± 0.12	Sigad et al. (1998)
UMV	SEcat vs. PSCz	$0.57^{+0.11}_{-0.13}$	Zaroubi et al. (2002)
	v–v Comparison		
VELMOD	MARK III vs. *IRAS* 1.2 Jy	0.50 ± 0.04	Willick & Strauss (1998)
VELMOD	SFI vs. PSCz	0.42 ± 0.07	Branchini et al. (2001)
ND94 & ITF	MARK III vs. *IRAS* 1.2 Jy	0.4–0.6	Davis et al. (1996)
ND94 & ITF	SFI vs. *IRAS* 1.2 Jy	0.6 ± 0.1	da Costa et al. (1998)
ND94	SNIa vs. *IRAS* 1.2 Jy	0.40 ± 0.15	Riess et al. (1997)
ND94	SBF vs. *IRAS* 1.2 Jy	$0.42^{+0.10}_{-0.06}$	Riess et al. (1997)
UMV	SEcat vs. PSCz	0.51 ± 0.06	Zaroubi et al. (2002)

peculiar velocities of the individual galaxies. With distance errors less than 10%, Type Ia supernovae (SNIa) are less susceptible to inhomogeneous Malmquist bias (Hudson 1994a) and hence offer an important alternative probe of the local velocity field. An early attempt to use SNIa was carried out by Riess et al. (1997) who compared the peculiar velocities of 24 SNIa with the velocity fields predicted from the 1.2 Jy *IRAS* redshift survey (Fisher et al. 1995a) and the Optical Redshift Survey (Santiago et al. 1995; Baker et al. 1998). They derived $\beta_I = 0.4 \pm 0.15$ and $\beta_O = 0.3 \pm 0.1$ respectively, with the relatively large error resulting from the small sample size.

Branchini et al. (1999) used the PSCz redshift survey to determine the density and peculiar velocity fields in real space in a self-consistent way by using equation (3.17) under the assumption that mass follows the number density of *IRAS* galaxies. These fields are smoothed with a Gaussian filter of radius 5 h^{-1} Mpc. Analysis by Berlind et al. (2000) indicates that this smoothing radius should yield unbiased results for β_I. In an independent analysis, Schmoldt et al. (1999) derived the PSCz velocity and density fields by using a Fourier-Bessel approach. They found the resulting fields to be consistent with the Branchini et al. (1999) fields used here.

The integral in equation (3.17) extends over all space. The PSCz survey, however, does not extend to infinite depth, nor does it contain data in the Zone of Avoidance (ZoA). For the ZoA, Branchini et al. (1999) have implemented a similar approach to that of Yahil et al. (1991) by dividing the region ($|b| \le 8°$) into bins of 10° latitude by 1000 km s^{-1}. These bins are then populated with enough synthetic galaxies to reflect the number density of the corresponding bins at greater $|b|$. The systematic effect on the derived value of β_I due to this interpolation procedure can be estimated from the results of Hudson (1994b). He compared β values derived from an optically-selected density field with a larger ZoA ($|b| \le 12°$) using different techniques to account for the missing structure. Only an 8% difference was observed between the β value derived from the interpolated density field and that derived from a density field in which the ZOA was assumed to be at average density. Since the average density assumption is rather extreme, this result may be taken as an upper limit on the systematic uncertainty. Therefore, as the PSCz ZoA is only two-thirds the thickness of this ZoA, we might expect a systematic uncertainty on our result of the order 5%. This is considerably smaller than our random errors.

As stated previously we have truncated the PSCz velocity field at 150 h^{-1} Mpc due to increasing shot noise. Sources beyond this depth, however, may still contribute to the LG's motion. Because the statistical weight of the SNIa sample is dominated by nearby objects these external contributions can be modelled as a dipole term. For peculiar velocity comparisons in the LG frame this dipole term cancels out as the motions of the LG and SNIa are affected in the same way. LG-frame comparisons assume, however, that the LG's motion is exactly given by linear theory. In practise, the LG is expected to exhibit a nonlinear 'thermal' component to its velocity that is not well modelled by linear theory. An alternative to the LG-frame comparison is to omit the LG from the analysis entirely. This can be achieved by fitting the SNIa peculiar velocities in the CMB frame with an additional dipole component to allow for contributions not included in the PSCz density field. Ideally, analyses in both these frames should produce similar results. However, due to the larger uncertainty in the CMB analysis, we regard the LG result as a more reliable solution.

3.4 The SNIa Dataset

(Tonry et al. 2003, hereafter T03) have recently produced a homogenised compendium of 230 SNIa for constraining cosmological quantities. The release of this compendium presents a new opportunity to measure β with a significantly smaller error.

The T03 dataset is compiled from many recent studies. Most notably from the Jha (2002), Perlmutter et al. (1999), Hamuy et al. (1996), Riess et al. (1999) and Germany et al. (2004) datasets, which comprise the majority of the data. Using a variety of fitting techniques such as MLCS (Riess et al. 1998 and the work of Jha and collaborators) and dm15 (an extension of the $\Delta m_{15}(B)$ method as described by Germany 2001), T03 have re-calculated the relative SNIa distances where the original photometric data is available. The systematic offsets of each dataset were reduced by minimising the differences between all pairs of datasets where overlaps exist. The residuals of this fitting procedure are 0.02 mag or better for the majority of the samples. Table 15 of T03 lists the redshift ($\log cz$), luminosity distance ($\log dH_0$), distance error and host galaxy V-band extinction (A_V) for each SNIa.

T03 fix the zero point of nearby SNIa ($0.01 < z < 0.1$) by assuming an 'empty universe' ($\Omega_m = 0$, $\Omega_\Lambda = 0$) cosmology. For our analysis, we have converted the T03 quoted distances to a ΛCDM cosmology ($\Omega_\Lambda = 0.7$, $\Omega_m = 0.3$). However, the derived β_I is unaffected by the choice of cosmology.

In this study we only consider the 107 SNIa that lie within 150 h^{-1} Mpc as the PSCz density field is incomplete at greater distances for all galactic latitudes (Branchini et al. 1999). We further restrict the sample to SNIa with extinctions $A_V < 1.0$ mags, for reasons discussed below. These selection criteria leave 98 SNIa, which we refer to as the "default sample". The median distance error for this local SNIa sample is $\sim 8\%$.

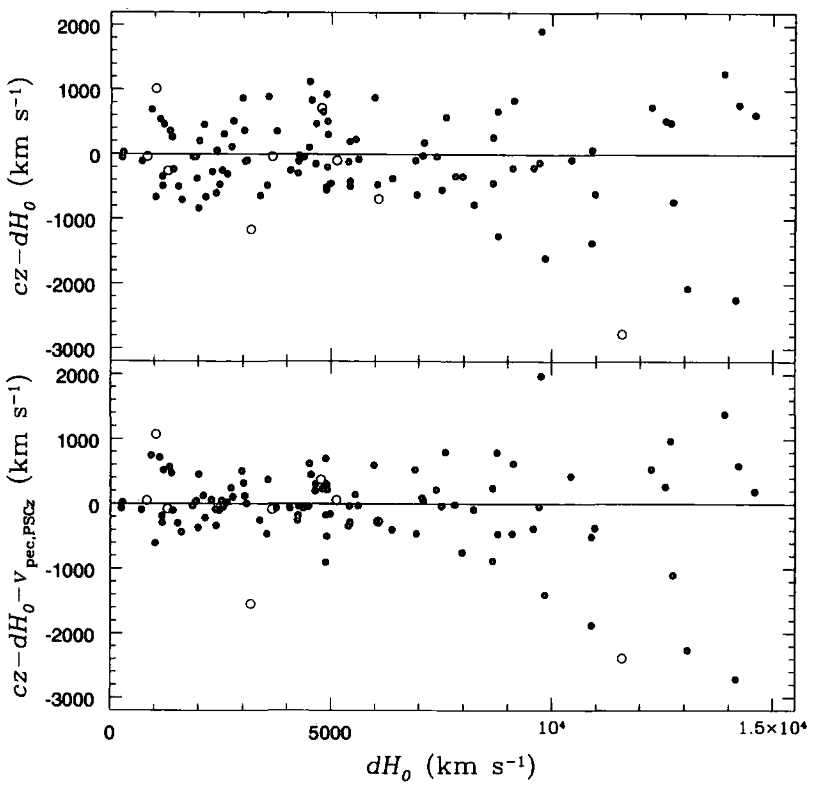

FIGURE 3.1: The Hubble flow residuals for all 107 SNIa lying within 150 h^{-1} Mpc in the LG frame. The upper panel shows the original uncorrected data whilst the lower shows the data with the predicted PSCz peculiar velocities removed. Note the reduction in scatter, particularly in the distance range 20-80 h^{-1} Mpc. SNIa with host-galaxy extinctions $A_V \geq 1.0$ are plotted as open circles whilst filled circles show the default sample used in this paper.

3.5 Determining β_I

There is a very good agreement between the peculiar velocities measured by the SNIa and predicted from the PSCz. This is shown in Fig. 3.1 where the scatter around the Hubble flow before and after the PSCz velocities for $\beta_I = 0.5$ are removed. In the range $20-80$ h^{-1} Mpc, where the majority of SNIa lie, the removal of the predicted PSCz peculiar velocities reduces the rms scatter around the Hubble flow from 490 km s^{-1} to 390 km s^{-1}. In Fig. 3.1, nine SNIa with $A_V > 1.0$ are plotted as open circles, three of which are distinct outliers. In our analysis we have chosen to exclude all objects with host galaxy extinctions greater than 1.0 as we expect that their errors are significantly underestimated.

TABLE 3.2: "Redshift error", σ_{cz}, comparison for the default sample of 98 SNIa in the LG frame. The errors have been determined from the 1σ deviation in the distribution of the medians of 1000 bootstrap re-samples.

σ^2_{cz} (km^2 s^{-2})	β_I	χ^2
150^2	0.55 ± 0.06	167
200^2	0.54 ± 0.06	131
$150^2 + \sigma^2_{cl}$ 'Trial 1'	**0.55 ± 0.06**	**98**
$200^2 + \sigma^2_{cl}$ 'Trial 1'	0.54 ± 0.06	89
150^2 'Trial 2'	0.57 ± 0.05	97
200^2 'Trial 2'	0.57 ± 0.06	88

To determine β_I in the LG frame we minimise the χ^2 relation:

$$\chi^2 = \sum_i \left(\frac{(v_{i,PSCz} - v_{i,SN})^2}{\sigma^2_{i,cz} + \sigma^2_{i,d}} \right) \tag{3.23}$$

where v_i is the radial peculiar velocity of the i^{th} supernova, $v_{i,PSCz}$ is the PSCz-predicted radial peculiar velocity which depends on β_I from (3.15), σ_d is the distance error and σ_{cz} incorporates both an estimate of the error in redshift determination as well as errors in the PSCz predictions due to shot noise or non-linear peculiar velocity contributions.

Various studies have adopted different schemes for σ_{cz}. Riess et al. (1997), adopt a value of 200 km s^{-1} for all the SNIa, whilst Blakeslee et al. (1999) use values of 150 km s^{-1} and 200 km s^{-1}. However Blakeslee et al. (1999) also account for the extra velocity dispersion of cluster galaxies using two different approaches. Their 'Trial 1' method adds in quadrature an extra factor of $\sigma_{cl}(r) = \sigma_0 / \sqrt{1 + (r/r_0)^2}$ to σ_{cz} where $\sigma_0 = 700\,(400)$ km s^{-1} and $r_0 = 2\,(1)$ Mpc for galaxies in Virgo (Fornax). Their 'Trial 2' scheme uses the standard σ_{cz} but resets the individual galaxy velocities for group members to the group-average velocities as listed in Tonry et al. (1997) for 37 separate clusters. In our analysis we extended both these techniques to account for galaxies which lie near one of the X-ray selected clusters of the NOAO fundamental plane survey (Smith et al. 2004).

Table 3.2 lists the derived β_I values for these different weightings for our default sample. The 1σ quoted errors are calculated from bootstrap re-samples of the dataset which are broadly consistent with the confidence levels defined by $\Delta\chi^2$ (e.g. as given in Numerical Recipes). If the nine $A_V > 1.0$ SNIa had not been removed, the resulting χ^2 would be larger by ~ 40.

Increasing the redshift error σ_{cz} for SNIa lying close to nearby clusters has a sizable effect on the χ^2 but appears to have no significant effect on the value of β_I. Overall, little variation from the preferred value of $\beta_I = 0.55 \pm 0.06$ is observed and β_I is effectively independent of the weighting schemes used.

In order to determine β_I in the CMB frame an extra dipole component is added as an extra free parameter in the minimisation of equation (3.23). Using the default sample with σ_{cz} given by 'Trial 1' as $\sqrt{150^2 + \sigma_{cl}^2}$, the best fit has $\beta_I = 0.48 \pm 0.09$ and $V_{\rm dipole} = 206 \pm 97$ km s^{-1} towards $l = 290° \pm 25°$, $b = 0° \pm 18°$. This extra dipole component is consistent with zero but is also consistent with the value of $V_{\rm dipole} = 372 \pm 127$ km s^{-1} towards $l = 273° \pm 17°$, $b = 6° \pm 15°$ as found by Hudson et al. (2004) for the Streaming Motions of Abell Clusters (SMAC) sample. The calculated value of β_I agrees well with the result derived in the LG frame.

The good agreement between the observed and predicted peculiar velocities in both the LG and CMB frames is shown in Fig. 3.2. If the peculiar velocities predicted by the PSCz and observed from the SNIa are in exact agreement for the chosen value of β_I, the SNIa would be expected to lie along the 1:1 line. This trend is indeed observed. The differences between the measured and predicted velocities are as expected given the errors in both distance and velocity measurements, i.e. the data is consistent with a reduced χ^2_ν of ~ 1. Thus the two datasets agree exceptionally well.

A complete list of the peculiar velocities for the 98 SNIa in the default sample can be found in table B.1 of Appendix B. This table also lists the values predicted by the PSCz in the LG and CMB reference frames for the best fit values of $\beta_I = 0.55$ and $\beta_I = 0.48$ respectively.

3.6 Robustness

To assess the robustness of the derived β_I we have examined various sub-samples of the local SNIa dataset. Unless otherwise stated all sub-samples use our default sample in the LG frame with $\sigma_{cz} = \sqrt{150^2 + \sigma_{cl}^2}$ determined using the 'Trial 1' approach. Table 3.3 lists the best fit β_I together with the associated χ^2 for each sub-sample.

Importantly, β_I is found to be independent of the distance range considered. Any derivation of β is expected to be strongly weighted by the very nearby SNIa where measurement errors are smallest. Hence we have tested the dependency of our calculations on SNIa at different distances by dividing the data into two distance ranges. The position of this division is chosen such that the bootstrap errors on each derived β_I are of similar magnitude. For a distance range of $0 - 30\ h^{-1}$ Mpc we derive a value of $\beta_I = 0.55 \pm 0.07$ and for

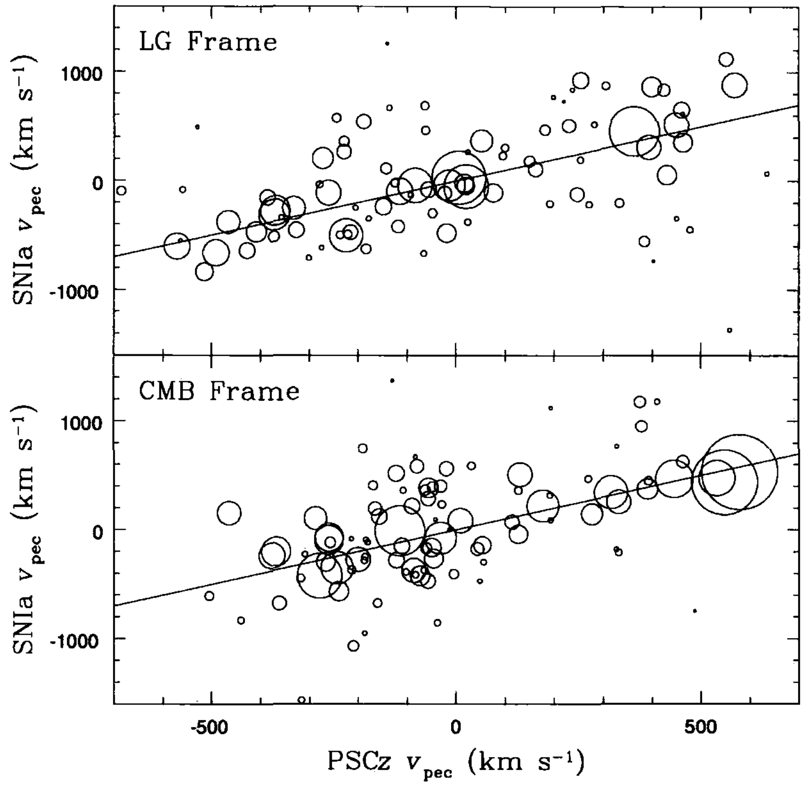

FIGURE 3.2: Comparison of SNIa peculiar velocities to PSCz predicted peculiar velocities in the range 0 h^{-1} Mpc to 150 h^{-1} Mpc with $A_V < 1.0$, $\sigma^2_{cz} = 150^2 + \sigma^2_{cl}$ and $\beta = 0.55$. The top panel shows comparisons in the LG frame, and the bottom panel shows the comparison in the CMB frame (without the extra dipole component). The size of the data point is inversely proportional to the total error ($\sigma = \sqrt{\sigma^2_d + \sigma^2_{cz}}$) on each SNIa. The smallest and largest circles correspond to values of σ = 1290 km s^{-1} and 170 km s^{-1} respectively. The lines indicate a 1:1 ratio.

TABLE 3.3: Dependency of β_I on various culls of the SNIa dataset

Sample	No. SNIa	β_I	Total χ^2_{min}
0 h^{-1} Mpc < distance < 150 h^{-1} Mpc	98	0.55 ± 0.06	98
0 h^{-1} Mpc < distance < 30 h^{-1} Mpc	31	0.55 ± 0.07	26
30 h^{-1} Mpc < distance < 150 h^{-1} Mpc	67	0.54 ± 0.10	74
20 h^{-1} Mpc < distance < 150 h^{-1} Mpc	80	0.55 ± 0.07	84
40 h^{-1} Mpc < distance < 150 h^{-1} Mpc	60	0.49 ± 0.13	67
0 h^{-1} Mpc < distance < 100 h^{-1} Mpc	85	0.58 ± 0.06	78
0 h^{-1} Mpc < distance < 125 h^{-1} Mpc	90	0.56 ± 0.06	84
No A_V cull	107	0.50 ± 0.08	141
$A_V < 0.5$	80	0.57 ± 0.06	79
$A_V < 0.3$	58	0.57 ± 0.08	57
CMB frame + dipole	98	0.48 ± 0.09	98

30 – 150 h^{-1} Mpc, $\beta_I = 0.54 \pm 0.10$. Table 3.3 also includes a variety of different distance ranges all of which yield similar values of β_I ($0.49 < \beta_I < 0.58$).

The determination of β_I is also revealed to be independent of the cull by host-galaxy extinction with β_I varying by only ± 0.05 for culls down to $A_V < 0.3$. It is found that the reduced χ^2_ν is ~ 1 for all culls of host-galaxy extinction < 1.0. Overall, for all the sub-samples considered, β_I is found to range by only 0.10.

Another source of bias which we do not account for in our analysis is inhomogeneous Malmquist bias. As described in section 1.3.6, not correcting for this effect enhances the observed infall into overdensities, thus requiring a higher value of β in the reconstruction. However, as Malmquist bias scales with the square of the distance error, the bias for the SNIa is expected to be considerably smaller (< 3%) than the random error in β_I (~ 10%).

3.7 Discussion

Table 3.1 lists a representative set of recent determinations of β_I from comparisons of predicted and observed peculiar velocities. Previously, the tightest constraints on β_I were from the merged spiral and elliptical peculiar velocity samples such as Mark III (Willick et al. 1997a) and SECat (Zaroubi 2000) as well as the SBF sample of Tonry et al. (1997). This work adds a result from local SNIa, a fourth independent data source of comparable statistical power. Recent comparisons of predicted and observed peculiar velocities ('velocity-velocity'), including the result presented here, all yield results consistent with a value of $\beta_I = 0.5$.

Some of the earliest estimates of β were obtained by matching the gravity at the LG to the measured CMB dipole. While the LG has the most accurate observed CMB-frame velocity, a weakness of this method is that one needs to integrate the density field over all space to obtain the predicted gravity at the LG. This contrasts with the velocity-velocity comparison performed above in which large-scale contributions to the predicted peculiar velocities either drop out of the analysis (if the fits are performed in the LG frame) or can be fitted independently of β (if the fits are performed in the CMB-frame). This degeneracy cannot be broken when using the LG alone as one would be attempting to fit 4 parameters (β and three components of an external dipole) to 3 degrees of freedom (the Cartesian components of the LG's CMB-frame motion). Consequently, in order to apply this method one needs either a deep, full-sky redshift survey (so that the external dipole is known to be zero) or, failing that, accurate estimates of the uncertainties arising from shot noise at large distances and from incompleteness in the ZoA. As an example of the latter, Hudson et al. (2004) have suggested, based on the "Behind the Plane" extension of the PSCz (Saunders et al. 2000a), that additional structure in the ZoA beyond 100 h^{-1} Mpc may increase the PSCz dipole by ~ (170 ± 85) km s $^{-1}$. Until these issues are fully resolved, β determinations by this method remain subject to larger systematic errors than velocity-velocity comparisons.

An alternative estimate of β_I can be obtained from other independent analyses not directly based on peculiar motion studies. One noteworthy route is via the combination of parameters: $\Omega_m^{0.6}\sigma_8$, where σ_8 is the rms amplitude of mass fluctuations (δ_m) averaged within a top-hat sphere of 8 h^{-1} Mpc radius. This combination may be related to β_I by the dependence of $\sigma_{8,I}$, the number density fluctuation of *IRAS* galaxies, on the bias parameter b_I. Since we are assuming linear biasing, the *IRAS* density field (δ_I) is equal to $b_I\delta_m$ and it follows that $\sigma_{8,I} = b_I\sigma_8$. We can thus write:

$$\beta_I = \frac{\Omega_m^{0.6}}{b_I} = \frac{\Omega_m^{0.6}\sigma_8}{\sigma_{8,I}}$$

Spergel et al. (2003) have used data from *WMAP* and other CMB and non-CMB sources to derive a value of $\Omega_m^{0.6}\sigma_8 = 0.38^{+0.04}_{-0.05}$. By directly integrating the PSCz power spectrum Hamilton & Tegmark (2002) found $\sigma_{8,I} = 0.80 \pm 0.05$. Combining these two results gives $\beta_I = 0.48 \pm 0.06$. The good agreement of the results from all these methods suggests that β_I is now known at the 10% level.

3.8 Conclusions

We have compared the measured peculiar velocities of 98 local ($< 150\ h^{-1}$ Mpc) type Ia supernovae with predictions derived from the PSCz survey. There is an excellent agreement between the two datasets with a best fit β_I of 0.55 ± 0.06. By analysing further subsets of the supernovae dataset this result is found to be robust with respect to culls by distance, host-galaxy extinction and to the choice of reference frame in which the analysis is carried out.

This independent determination of β_I is consistent with recent alternate derivations suggesting a canonical value of $\beta_I = 0.5$. This would imply that $b_I \sim 1$, suggesting that, for the most part, *IRAS* galaxies faithfully follow the underlying mass distribution. The PSCz is thus an important tool for studying large-scale motions in the local Universe.

In the next chapter we present a new reconstruction of the velocity and density fields from the first, all-sky, X-ray selected cluster catalogue. The fields derived from this survey will be complimentary to the PSCz fields discussed here. As such, in Chapter 5 we compare the reconstructions from the two surveys before combining them to investigate the source of the LG motion with respect to the CMB.

4

The X-Ray Gravity Field

4.1 An Alternate Probe

To date, the majority of reconstructions of the local density and velocity fields have been based on galaxies from the *IRAS* PSC (e.g. Yahil et al. 1991; Davis et al. 1996; Willick & Strauss 1998; Branchini et al. 1999). This is principally due to the excellent sky coverage and density of the catalogue as described in Section 3.3. However, *IRAS* preferentially samples late-type galaxies, which are less clustered than early-type galaxies (Lahav et al. 1990; Saunders et al. 1992; Strauss et al. 1992a; Peacock & Dodds 1994). Hence fields derived from the PSCz survey will underestimate contributions from the regions of greatest overdensity. Individual galaxy clusters, which trace the peaks of the density field, are therefore an important and complementary probe with which to reconstruct the real-space velocity and density fields (Bahcall et al. 1994).

All-sky galaxy cluster surveys are also able to probe much greater depths than galaxy surveys. In the optical, overdensities of galaxies at a given redshift are more readily identifiable than individual galaxies to the same statistical completeness. The characteristic depth of the combined Abell (1958) and Abell, Corwin & Olowin (1989) catalogues, which were compiled from visual scans of optical plates, is $\sim 200h^{-1}$ Mpc (Branchini & Plionis 1996). The equivalent depth for the PSCz is $\sim 90h^{-1}$ Mpc (Branchini et al. 1999).

However, optically identified galaxy clusters are unable to probe the ZoA and are subject to significant projection effects. Lucey (1983) estimates that the Abell catalogue misses between 15 and 30% of rich clusters due to contamination by foreground galaxies; whilst the population size of 15 – 25% of clusters in the catalogue are overestimated by more than a factor of two. Only with spectroscopic confirmation can some of these issues be addressed (e.g. Collins et al. 1995; Muriel et al. 2002; Smith et al. 2004). Fortunately, the hot ($\sim 10^7 - 10^8$ K), gaseous intracluster medium is very X-ray luminous and is significantly more peaked than the projected galaxy distribution. X-ray detected clusters are therefore less susceptible to projection effects as they would need to be in almost perfect alignment to be mistaken for a single source. Furthermore, the ZoA is far more transparent to X-ray wavelengths than the optical or near-IR (Ebeling et al. 2002).

Previous reconstructions have used various techniques to artificially fill in the ZoA. Typically these are based on the procedure introduced by Strauss & Davis (1988) and Yahil et al. (1991). In this method, the ZoA is split into longitudinal bins that are randomly populated with synthetic galaxies until they reproduce the densities of real galaxies observed in similar size bins lying immediately above and below the ZoA. However the majority of nearby large-scale structure lies in or close to the ZoA (see section 1.2.1). Indeed, six of the ten brightest $z < 0.06$ X-ray clusters reside at $|b| < 20°$ (Edge et al. 1990). Consequently, artificial reconstructions of the ZoA are likely to underestimate the real local mass distribution. Hence, X-ray selected clusters are a far less censored tracer of the local mass distribution.

Recently, by combining the *ROSAT*-ESO Flux Limited X-ray sample (REFLEX, Böhringer et al. 2004) from the southern hemisphere, the extended Brightest Cluster Sample (eBCS, Ebeling et al. 1998, 2000) from the north, and the Clusters in the Zone of Avoidance survey (CIZA, Ebeling et al. 2002, Kocevski et al. 2006) from the Galactic plane, Kocevski, Mullis & Ebeling (2006, hereafter K06) have compiled the first all-sky, X-ray selected, flux limited, galaxy cluster catalogue: the RBC catalogue. Using this database we here reconstruct the local mass distribution as traced by these rich clusters.

4.2 The RBC Catalogue

The *ROSAT* X-ray satellite surveyed the entire sky from August 1990 to February 1991 as part of the *ROSAT* All-Sky Survey (RASS, Trümper 1983; Voges 1992; Voges et al. 1999). Over 100,000 sources were detected in exposures ranging from 400 to 40,000 s taken in the 0.1 - 2.4 keV soft X-ray energy band covering 99.7% of the sky. As the first such survey to be taken with an imaging X-ray detector, the RASS is an ideal catalogue for compiling X-ray galaxy

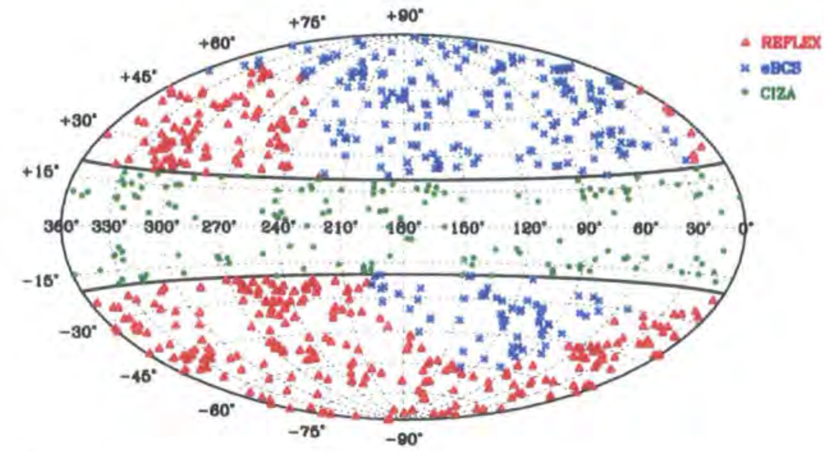

FIGURE 4.1: The sky distribution in galactic coordinates of the 755 clusters in the combined RBC catalogue with fluxes greater than $3\times10^{-12}\,\mathrm{erg\,s^{-1}\,cm^{-2}}$. The three constituent surveys are individually labelled and the ZoA is denoted by the solid thick lines at $|b| = 20°$.

cluster samples. To date, the X-ray Brightest Abell-type Clusters catalogue (XBACs Ebeling et al. 1996) is the only complete, flux-limited cluster survey to be drawn simultaneously from the entire database. However as the target clusters were selected from the optically based Abell catalogues, the survey is susceptible to the problems noted previously. In order to construct an all-sky, X-ray selected catalogue from RASS data, three key surveys need to be combined. Fig. 4.1 plots the distribution of the REFLEX, eBCS and CIZA samples, which together encompass the whole sky.

4.2.1 REFLEX

REFLEX consists of the 447 clusters within $z = 0.3$ that lie in the southern hemisphere ($\delta < 2.5°$) and outside the ZoA (i.e. $|b| > 20°$). The limiting flux is $3\times10^{-12}\,\mathrm{erg\,s^{-1}\,cm^{-2}}$ in the *ROSAT* 0.1-2.4 keV bandpass, significantly deeper than the $5\times10^{-12}\,\mathrm{erg\,s^{-1}\,cm^{-2}}$ limit of the XBACs survey. Extended sources were identified with the Growth Curve Analysis method whereby source counts are measured as a function of an increasing circular aperture (Böhringer et al. 2000). Possible clusters without existing redshift measurements were targeted in a follow-up ESO programme (Bohringer et al. 1998; Guzzo et al. 1999). With a high median count rate of 79 photons per cluster, REFLEX is expected to be ~ 90% complete (Böhringer et al. 2001).

4.2.2 eBCS

The original BCS sample surveyed clusters lying in the northern hemisphere ($\delta > 0°$), away from the galactic plane ($|b| > 20°$), within $z = 0.3$ and detected above a flux limit of $4.4 \times 10^{-12}\,\mathrm{erg\,s^{-1}\,cm^{-2}}$ in the 0.1–2.4 keV band (Ebeling et al. 1998). Cluster targets were identified by correlating the RASS with the Abell and Zwicky et al. (1961) catalogues. However to ensure that the catalogue was X-ray selected, further candidates were added by searching the RASS for extended objects. These sources were then reprocessed with a Voronoi Tessellation and Percolation (VTP) algorithm to measure an accurate count rate. Applying the VTP method to the whole survey area would allow for a 'purely' X-ray selected sample; unfortunately due to limitations in the database, the VTP procedure could only be used in areas immediately surrounding the identified sources (approximately one sixth of the total area). From these limited applications, Ebeling et al. (1998) were able to estimate that the 201 BCS clusters published were ~ 90% complete.

Ebeling et al. (2000) successfully extended the BCS to $2.8 \times 10^{-12}\,\mathrm{erg\,s^{-1}\,cm^{-2}}$ using the same detection techniques. The combined eBCS sample contains 310 clusters and is estimated to be ~ 75% complete. 68% of these are known Abell clusters, an extra 14% are recorded in the Zwicky catalogue, and 18% are listed in neither (Ebeling et al. 2000). This further highlights the importance of not relying on the optical identifications of clusters.

4.2.3 CIZA

X-ray based surveys are able to probe further into the ZoA than their optical counterparts as they are not attenuated by dust nor subject to foreground stellar confusion. The galactic plane is thus effectively transparent to hard X-rays (e.g. 2–10 keV); whilst soft X-rays, as used by the RASS, suffer from less than 2 mag of extinction due to foreground hydrogen (Ebeling et al. 2000). CIZA was thus designed to compliment previous studies by identifying X-ray clusters at $|b| < 20°$.

Targets for the survey were drawn from the RASS Bright Source Catalogue (BSC, Voges et al. 1999), which comprises 18,811 sources with count rates greater than 0.05 counts $\mathrm{s^{-1}}$. Candidates were selected based on their location in the plane, their flux limit and on a spectral hardness ratio to exclude soft, non-cluster sources. After cross-correlating with existing catalogues to remove previously known non-cluster sources, the remaining targets are optically imaged and all confirmed clusters are followed up with spectroscopic measurements of at least two cluster members. The final count rates for each cluster are measured in a fixed circular aperture of $1.5\,h_{50}^{-1}$ Mpc. Following this procedure, the CIZA survey has currently confirmed over 250 galaxy clusters, 130 of which have fluxes greater than $3 \times 10^{-12}\,\mathrm{erg\,s^{-1}\,cm^{-2}}$. Of these, approximately 80% are new identifications, not recorded in optical catalogues. Within $z = 0.075$, Kocevski et al. (2007) estimate that the sample of 130 clusters is $\sim 65\%$ complete.

4.2.4 Combining the Samples

The REFLEX, eBCS and CIZA samples are the most statistically complete galaxy cluster catalogues ever compiled in their respective regions of the sky. Each survey utilised X-ray data from the *ROSAT* X-ray observatory for target selection, used similar follow-up observations for cluster confirmation, and all three cover similar X-ray flux and luminosity ranges. However as each survey has employed a different method for determining the flux of each source, combining the samples is a non-trivial matter.

K06 have recalculated the fluxes for each survey by summing the emissions from each source within a metric 1 h^{-1} Mpc aperture located at the cluster redshift. After applying a minimum flux limit of 3×10^{-12} erg cm^{-2} s^{-1}, there are 359 REFLEX, 248 eBCS and 151 CIZA sources left in the final sample (as shown in Fig. 4.1). As previously discussed, the VTP method for serendipitously detecting clusters in the eBCS survey was only used in a limited area surrounding each pre-identified cluster. K06 estimate that 84 additional clusters would be detected if the VTP method were to be extended to the whole of the northern sky. To account for this incompleteness, each eBCS cluster is weighted by an additional factor of $w_i = 1.34$ so as to match the average comoving cluster density of the REFLEX sample. This weighting is applied uniformly to all clusters in the sample as the missing clusters are not expected to correlate with distance nor position. Similarly, to account for the missing clusters in the very centre of the ZoA ($|b| < 5°$) that are hidden by foreground hydrogen, the CIZA sample is weighted by $w_i = 1.63$. K06 repeat their analysis of the RBC dipole without these weights and find little variation in their final results.

Fig. 4.2 plots the luminosity functions from the recalculated datasets with the additional w_i weights included. All three luminosity functions agree well over the three orders of magnitude covered by the surveys. Using the simplex method, we fit the combined, unbinned luminosity function with a Schechter function of the form:

$$\Phi_X(L) = A\frac{L}{L_\star}^{-\alpha}\exp(-L/L_\star) \tag{4.1}$$

The best fit parameters are: A=$(5.67 \pm 0.68) \times 10^{-7}\, h_{100}^3$ Mpc^{-3} $(10^{44}\mathrm{erg}\,s^{-1})^{-1}$, $L_\star = (2.64 \pm$

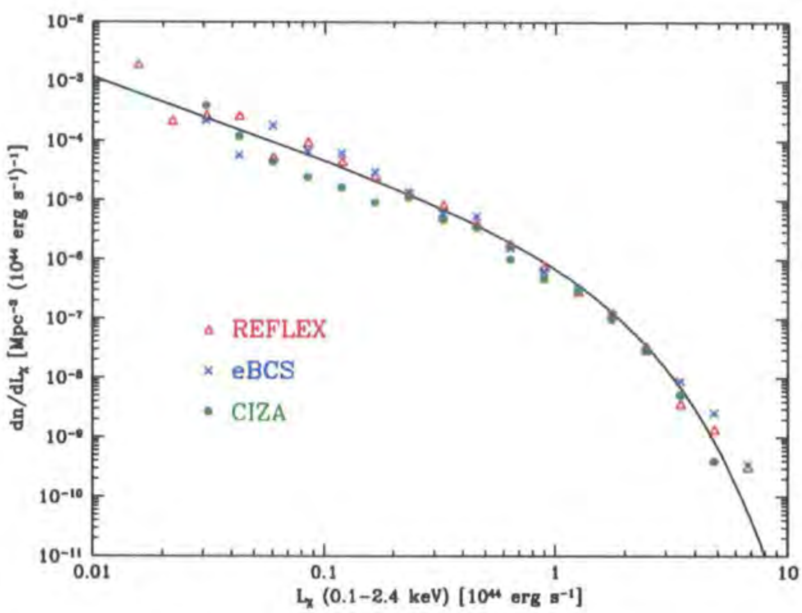

FIGURE 4.2: The separate, binned luminosity functions of the three recomputed samples, corrected for completeness. The solid line indicates the best Schechter fit to the combined sample.

0.36) $\times 10^{44}\ h_{100}^{-2}$ ergs s^{-1} and $\alpha = 1.16 \pm 0.10$, consistent with the values found by K06. 1-σ errors are assigned by subsequent fits to bootstrap resamples of the data. The best fit is shown in Fig. 4.2 as a solid line.

4.3 Real-Space Reconstruction of the RBC

By calculating the velocity of each individual cluster in the survey, the real-space position of the source and hence the real-space density and velocity fields can be computed. Following the method first implemented by Yahil et al. (1991), we iteratively solve equation 3.17 (as given in Section 3.1) for each cluster until the solution converges. In order to do so, the cluster sample first needs to be appropriately weighted and smoothed to avoid non-linear effects. The density field may then be summed over the sources contained within a distance $R_{\rm max}$, taken here as $300h^{-1}$ Mpc, rather than integrating over all space, i.e.:

$$\boldsymbol{v}(\boldsymbol{r}) = \frac{H_0\beta_{\rm RBC}}{4\pi}\left(\sum_{i=1}^{N}\left[\frac{\mathcal{W}_i S(\boldsymbol{r}_i,\boldsymbol{r})}{\bar{B}(r_i)}\frac{\boldsymbol{r}_i-\boldsymbol{r}}{|\boldsymbol{r}_i-\boldsymbol{r}|^3}\right]+\frac{4\pi\boldsymbol{r}}{3\bar{B}(r)}\right) \tag{4.2}$$

where $\beta_{\rm RBC}$ is the redshift distortion parameter for the RBC sample, $\mathcal{W}_i$ is the weight of the i^{th} cluster, S is the applied smoothing and $\bar{B}$ is an average cluster bias calculated later in Section 4.3.2. The second term after the summation accounts for using the absolute density field rather than the density contrast. This is calculated by first normalising $\mathcal{W}_i$ to ensure that the average density ($\bar{\rho}$) within R_{max} is one such that δ_g in equation 3.17 becomes simply $\mathcal{W}_i$−1. The required correction term is then:

$$\int_0^{R_{\text{max}}} \frac{-1.\,S(\boldsymbol{r},\boldsymbol{r}')}{B(r')}\frac{\boldsymbol{r}'-\boldsymbol{r}}{|\boldsymbol{r}'-\boldsymbol{r}|^3}d^3r' \tag{4.3}$$

As the smoothing has little effect on this correction, this simplifies to the expression given after the summation in equation 4.2.

4.3.1 Weighting the Clusters

The RBC catalogue is uniformly complete to a flux limit of $F_{\text{lim}} = 3\times10^{-12}$ erg s^{-1}. To account for the sources missing from a volume limited subsample, we weight each cluster by the reciprocal of the selection function, ϕ. This is defined as the probability that a cluster will be included in the sample given its distance and the distribution of cluster luminosities:

$$\phi(r,\Phi) = \begin{cases} \dfrac{\int_{4\pi r^2 F_{\text{lim}}}^{\infty} \Phi_X(L)\,dL}{\int_{L_{\text{min}}}^{\infty} \Phi_X(L)\,dL} & r \geq r_{\text{min}}, \\ 1 & \text{otherwise} \end{cases} \tag{4.4}$$

where L_{min} is a lower luminosity limit applied to the survey as the faint end of the luminosity function is poorly constrained. K06 set this limit to $1.25\times10^{42}\,h^{-2}$ ergs s^{-1}, which corresponds to a distance $r_{\text{min}} = 59h^{-1}$ Mpc within which all clusters should be detected.

Each source in the catalogue may also be weighted by the cluster's relative mass. This is inferred from the luminosity of the cluster using the empirical relation defined by Allen et al. (2003) for a value of $H_0 = 50$ km s^{-1} Mpc^{-1}:

$$M_{200} = 2^{+1.1}_{-0.5}\times10^{14}L^{0.76^{+0.16}_{-0.13}}h_{50}^{-1}M_{\odot} \tag{4.5}$$

Here, M_{200} is defined as the mass contained within the radius r_{200}, the distance at which the mean enclosed density is 200 times the critical density of the universe at the redshift of the cluster.

The proximity of the Virgo cluster precludes a reliable estimate of the flux (and so mass) of the system that is consistent with the 1 Mpc aperture technique used for the other clusters. The Virgo cluster thus has to be added in by hand. Kocevski et al. (2004) used equation 4.5 to infer a mass of $1.8 \times 10^{14} h^{-1} M_{\odot}$ from the luminosity assigned to the cluster by the eBCS survey, which we place at a redshift of 0.0036. For comparison, we also repeat the reconstruction with the X-ray luminosity inferred mass estimate of $3.5 \times 10^{14} h^{-1} M_{\odot}$ from Böhringer (1994).

Inferring mass from luminosity, however, carries a sizable uncertainty. The rms scatter in the predicted mass of the 17 clusters used to infer equation 4.5 is $\log_{10}(M) \sim 0.22$. Additionally any cooling flows present in a cluster will significantly boost the luminosity of the system (see Fabian et al. 1994). In our analysis, we thus preferentially use a number-weighted scheme, where M_i for each cluster, and so $\bar{M}$, is set to one.

The combined weight for each cluster, including an estimate of the mass M_i, is therefore taken as:

$$\mathcal{W}_i = \frac{1}{\bar{n}}\left(\frac{1}{\phi(r_i)}\frac{M_i}{\bar{M}}\right) \tag{4.6}$$

where $\bar{M}$ is the average cluster mass and the average cluster density, $\bar{n}$, is defined by:

$$\bar{n} = \frac{1}{V}\sum_{i=1}^{N}\frac{1}{\phi(r_i)}\frac{M_i}{\bar{M}} \tag{4.7}$$

The sum is over the N clusters contained within the volume V. This density does not vary much past $50h^{-1}$ Mpc but is defined here within a radius of $100h^{-1}$ Mpc so as to match the PSCz normalisation. Initially, this is found to be $4.82 \times 10^{-5} h^3$ Mpc^{-3} for the number-weighted prescription and $(8.44 \times 10^9/\bar{M}) M_{\odot} h^3$ Mpc^{-3} for the mass-weighted case.

4.3.2 Cluster Biasing

It has been shown that clusters, or more specifically the dark matter halos within which they reside, are biased tracers of mass (Mo & White 1996). Generally, larger clusters tend to be more clustered, effectively tracing the underlying mass field more faithfully. As the RBC catalogue is flux limited, the average cluster mass will increase with distance, corresponding to an increase in the average cluster bias parameter. To account for this we include an additional weight, $B(r)$, dependent on the distance to the cluster.

Several analytical approximations to this bias have been derived (e.g. Mo & White 1996; Jing 1998; Sheth et al. 2001). However by comparing the autocorrelation function of dark matter halos to that of the mass from the Millennium Simulation, Gao et al. (2005) have shown that the Mandelbaum et al. (2005) expression offers a particularly good fit to the simulations for masses ($M > 1 \times 10^{11} h^{-1} M_\odot$). This bias is defined as a function of the dimensionless parameter $\nu = \delta_{crit}/\sigma(M)$, where δ_{crit} is the critical overdensity required for collapse, taken here as 1.686 (Eke et al. 1996), and $\sigma(M)$ is the rms mass fluctuation in spheres containing an average mass M. Mandelbaum et al. (2005) define this relation as:

$$b(\nu) = 1 + \frac{\nu' - 1}{\delta_{crit}} + \frac{2p}{\delta_c(1 + \nu'^p)} \tag{4.8}$$

where $\nu' = a\nu^2$, $a = 0.73$ and $p = 0.15$. As previously stated, the cluster masses in the RBC catalogue carry a significant uncertainty. Hence rather than correcting for this bias on an individual cluster basis we infer the average bias applied at a given distance. This is achieved by integrating $b(M)$ over the mass function of the survey, taken as a Schechter function of the form in equation 4.1 with best fit values $A = (1.75 \pm 0.45) \times 10^{-21}\, h^3_{100}\, \mathrm{Mpc}^{-3}\, M_\odot^{-1}$, $M_\star = (3.24 \pm 0.30) \times 10^{14} M_\odot$ and $\alpha = 1.35 \pm 0.10$, where errors are again assigned from bootstrap resamples of the data set. Specifically the average bias applied at a given distance is calculated in the number-weighted prescription as:

$$B(r) = \frac{\int_{M_{lim}(r)}^{\infty} b(M)\Phi(M)dM}{\int_{M_{lim}(r)}^{\infty} \Phi(M)dM} \tag{4.9}$$

and in the mass-weighted prescription as:

$$B(r) = \frac{\int_{M_{lim}(r)}^{\infty} b(M)\Phi(M)M\,dM}{\int_{M_{lim}(r)}^{\infty} \Phi(M)M\,dM} \tag{4.10}$$

These relations are plotted in Fig. 4.3, where the typical correction for the number-weighted case is between two and three and for the mass-weighted case, from three to four.

A theoretical average for this bias can be calculated by comparing the two-point corre-

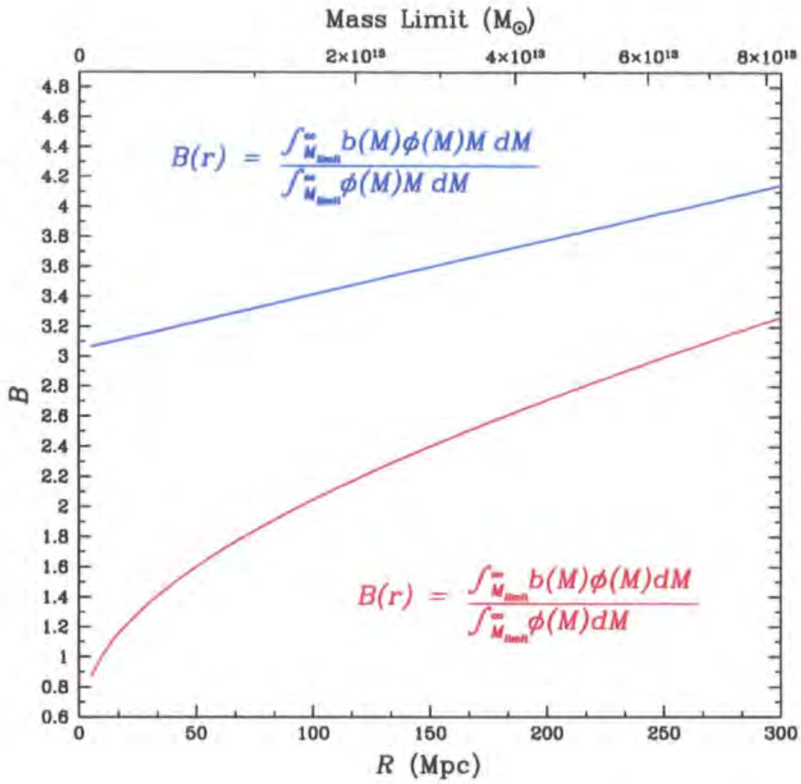

FIGURE 4.3: The average bias applied to the survey as a function of cluster distance. The number-weighted case (equation 4.9 is displayed as a red solid line, whilst the dashed blue line indicates the mass-weighted solution. The minimum cluster mass detectable, given the flux limit of the survey, is displayed on the top axis.

lation function of galaxies and clusters. As discussed in Section 3.2, the bias parameter of the *IRAS* survey has been well defined by several authors by comparing the PSCz velocity field, derived from the *IRAS* catalogue, to probes of the true velocity field. Typical $b_I \sim 0.8$–1.1, i.e. the *IRAS* galaxies trace the underlying matter structure fairly faithfully. Hamilton & Tegmark (2002) have fitted the PSCz autocorrelation function, defined over the range 0.01–$20h^{-1}$ Mpc, with a power law of the form $\xi(r) \approx (r/r_0)^{-\gamma}$ with correlation length $r_0 = 4.27h^{-1}$ Mpc and index $\gamma = 1.55$. Similarly Collins et al. (2000) have fitted the REFLEX sample with $r_0 = 18.8$ and $\gamma = 1.83$ over the range 4–$40h^{-1}$ Mpc. The relative bias between the samples is the square root of the ratio of these correlation functions. At $r = 15h^{-1}$ Mpc, comparable to the cluster separation nearby where most of the signal arises, this corresponds to a relative bias to underlying field between the RBC X-ray clusters and *IRAS* galaxies of ~ 3.3. This is equivalent to a bias to underlying field of ~ 3, comparable to the biases seen in Fig. 4.3.

4.3.3 Smoothing the Sample

To apply equation 4.2, the discrete cluster density field needs to be smoothed to avoid nonlinear effects. We smooth the field with a Gaussian kernel (S) rather than using the traditional top-hat filter so as to further dampen extreme velocities in the vicinity of each cluster.

$$S(\boldsymbol{r},\boldsymbol{r}_i) = 1 - \exp\left(\frac{-|\boldsymbol{r}_i - \boldsymbol{r}|^2}{2r_{sm}^2}\right) \tag{4.11}$$

The smoothing length, $r_{\rm sm}$, is taken as the average of the intercluster separations at $\boldsymbol{r}$ and $\boldsymbol{r}_i$. Due to the highly inhomogeneous distribution of the clusters we are unable to use density estimators to determine cluster spacing such as in Yahil et al. (1991). Instead we vary the separation from $10h^{-1}$ Mpc (at $r = 0$) to $35h^{-1}$ Mpc (at $r = 300h^{-1}$ Mpc) so as to follow the rise in mean cluster spacing observed in the catalogue. At scales below $10h^{-1}$ Mpc, the cluster velocity field is known to become non-linear (Croft & Efstathiou 1994).

4.3.4 The Iterative Procedure

The gravitational attraction of each cluster in the sample is, of course, dependent on the relative distance to that source. As we are updating the position of these sources, the peculiar velocities of the clusters need to be solved iteratively. Even though these velocities will scale linearly with $\beta_{\rm RBC}$ (as seen from equation 4.2), the best fit value will depend weakly on the input $\beta_{\rm RBC}$ used in the reconstruction. We thus use a similar technique to Pike & Hudson (2005) where the value of $\beta_{\rm RBC}$ is increased by 0.01 at each step of the reconstruction from 0 to 1. At each step, we take the peculiar motion as the average of a further five iterations for the given $\beta_{\rm RBC}$ to dampen the oscillations that occur in the procedure due to the sparse sampling.

Contributions from sources outside the RBC sample may be modelled by a simple dipole as higher order terms will be negligible given the depth of the RBC catalogue relative to the peculiar velocity surveys used to constrain $\beta_{\rm RBC}$. In the LG frame, this extra dipole will cancel out as it does not affect relative velocities. Alternatively, in the CMB frame, the LG motion may be effectively ignored by including an extra free dipole ($\boldsymbol{U}$) in the fitting. Due to the extra uncertainty in the CMB analysis we use the LG frame for our default reconstruction.

After initially assigning each cluster zero peculiar velocity, i.e. using the redshift (cz) as the real-space distance to each source, the procedure calculates the following steps at each iteration:

1. The selection function and, if required, the mass of each cluster within the RBC sample is calculated given the current distance to the source. The limiting depth of the survey is taken here as $400h^{-1}$ Mpc.

2. The average density of the weighted sample within $100h^{-1}$ Mpc, so as to match the PSCz normalisation, is computed.

3. The peculiar velocities of all clusters within $400h^{-1}$ Mpc are calculated using the sources contained within $R_{\rm max}$ (taken here as $300h^{-1}$ Mpc) and the current value of $\beta_{\rm RBC}$. The peculiar velocity adopted for each cluster is the average of a further five iterations for the given value of $\beta_{\rm RBC}$.

4. The new distance to each cluster in the sample ($r_{\rm new}$) is calculated using the updated peculiar velocity:

$$r_{\rm new} = cz - [\boldsymbol{v}(\boldsymbol{r}) - \boldsymbol{v}(0)] \cdot \frac{\boldsymbol{r}}{|\boldsymbol{r}|}$$

The final output of the program is the real-space positions and peculiar velocities for each cluster within $R_{\rm max}$ for a given value of $\beta_{\rm RBC}$ between 0 and 1.

Fig. 4.4 plots the velocity and density fields for both the number- and mass-weighted prescriptions as constructed from the real-space positions of the clusters calculated using a value of $\beta_{\rm RBC} = 0.5$. Both maps show pronounced contributions from the SSC (–120, 70)h^{-1} Mpc, the GA (–40, 0)h^{-1} Mpc and PP (45, –5)h^{-1} Mpc, all as described in Chapter 2. The mass-weighted map shows a much larger overdensity around PP than in the number-weighted prescription. Abell 426 (Perseus), the largest cluster in the PP complex, is the brightest X-ray cluster in the sky. This is due to the significant cooling flow present in the system, radiating energy in the X-ray band (Fabian et al. 1981; Boehringer et al. 1993; Fabian et al. 1994, 2000, 2003). As masses in the RBC are computed from luminosities, the cluster is likely biased. These maps will be further analysed, with comparison to the PSCz, in Section 5.2.

The shot noise in the reconstruction is calculated following Hudson (1993). Specifically:

$$\sigma^2_{\rm sn} = \left(\frac{H_0 \beta_{\rm RBC}}{4\pi}\right)^2 \sum_{i=1}^{N} \left[\frac{\mathcal{W}_i S(\boldsymbol{r}_i, \boldsymbol{r})}{\bar{B}(r_i)} \frac{\boldsymbol{r}_i - \boldsymbol{r}}{|\boldsymbol{r}_i - \boldsymbol{r}|^3}\right]^2 \tag{4.12}$$

Assuming that the shot noise along each component of the velocity vector is equal, we may take the mean one-dimensional shot noise error as $\sigma_{\rm 1d} = \sigma_{\rm sn}/\sqrt{3}$.

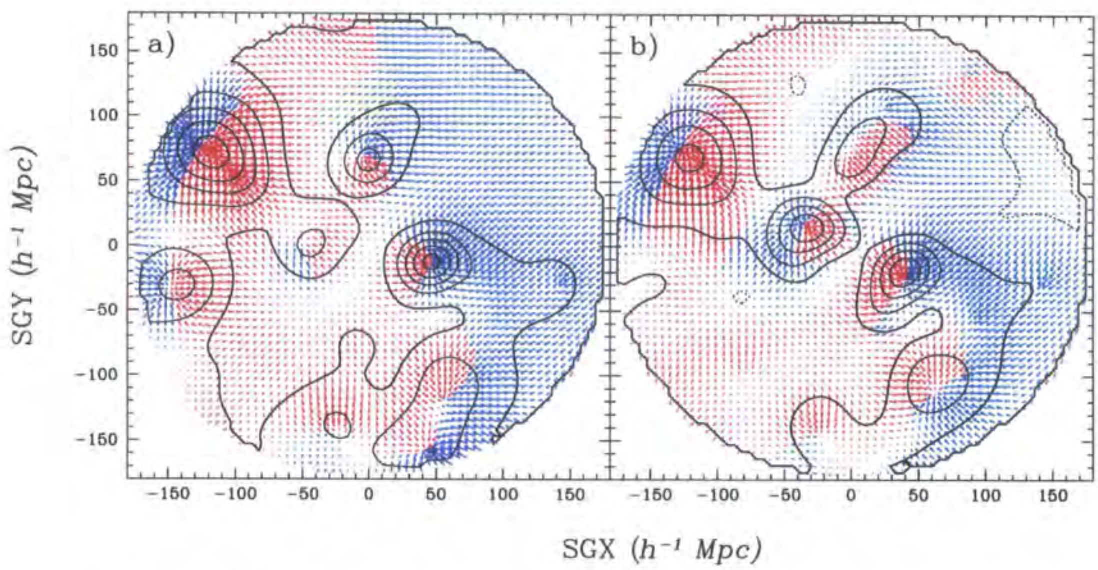

FIGURE 4.4: The velocity and density fields within $180h^{-1}$ Mpc for the mass-weighted (a) and number-weighted (b) reconstructions using a value of $\beta_{\rm RBC} = 0.5$ in the Supergalactic plane. Density contours are displayed in steps of $\delta_c = 0.5$, whilst velocities are scaled such that $1h^{-1}$ Mpc=100 km s^{-1}. Velocities that are receding from us are coloured red, whilst oncoming motions are coloured blue. The superimposed outflow, due to the correction term in equation 4.2, pushes the apparent convergence point of the velocity field around superclusters to slightly beyond the density peak. This effect increases with distance.

The shot noise corresponding to the maps in Fig. 4.4, calculated using equation 4.12, are shown in Fig. 4.5. The greater mass density contrast around the large superclusters leads to a significantly larger shot noise in the mass-weighted field, especially for PP. However, for the most part, the shot noise is observed at the level of ~100–200 km s^{-1} in both fields.

A full list of the reconstructed cluster positions and peculiar velocities is given in Appendix C for $\beta_{\rm RBC} = 0.5$. Table 4.1 presents a representative sample derived for important local clusters using several values of $\beta_{\rm RBC}$ with both the number- and mass-weighted reconstructions in the LG frame.

Clearly, the sizable shot noise, which is due to the sparseness of the RBC, represents a substantial contribution to the predicted velocities. Additionally, differences between the two weighting schemes are also apparent. Notably, the peculiar velocity of the Norma cluster, which lies at the core of the GA, is negative in the number-weighted prescription (-299 ± 221 km s^{-1}) and positive when including the calculated cluster masses (233 ± 320 km s^{-1}).

On the opposite side of the sky, the Perseus cluster shows a small negative velocity. This is in agreement with Willick (1990) who, using the TF relation, observed a majority of negative

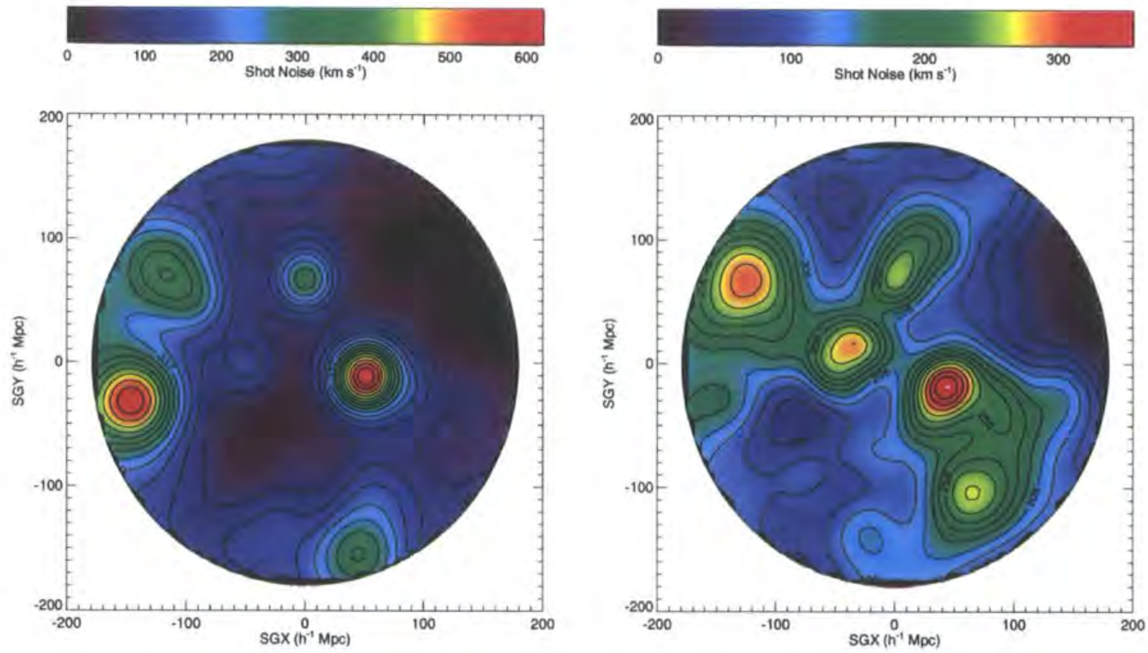

FIGURE 4.5: The shot noise within $180h^{-1}$ Mpc for the RBC mass-weighted (left panel) and number-weighted (right panel) reconstructions in the Supergalactic plane.

galactic peculiar velocities in the core of the PP structure. Similarly Han & Mould (1992) claim an average velocity of –400 km s^{-1}, although most of their TF observed galaxies lie beyond the cluster. Hudson et al. (1997) find a statistically insignificant velocity for the PP system of -60 ± 220 km s^{-1}, relative to the CMB frame.

4.4 Determining $\beta_{\rm RBC}$

To determine $\beta_{\rm RBC}$ for the reconstructed fields, we compare the radial motions predicted by the RBC to the observed motions of the same SNIa dataset discussed in Section 3.4. The default sample consists of the 98 SNIa within $150h^{-1}$ Mpc that reside in galaxies with extinctions $A_V < 1.0$. If the bias between the density field as traced by clusters and the underlying density field due to all matter has been fully corrected, we would expect a value of $\beta_{\rm RBC} \sim 0.5$ given equation 1.10 and $\Omega_m = 0.27$.

As in Pike & Hudson (2005), we determine the best fit $\beta_{\rm RBC}$ by maximising the likelihood that a SNIa at position $\boldsymbol{r}$, will have an observed radial velocity $cz_{\rm obs}$ given a model of the peculiar velocity field derived for a particular value of $\beta_{\rm RBC}$. The probability distribution of observing this velocity is given by:

TABLE 4.1: The RBC predicted real-space positions and radial proper motions of selected clusters in the CMB frame, together with an estimate of the shot noise in the reconstruction, for various values of β_{RBC}.

Cluster Name	$\beta_{\text{RBC}} = 0.25$			$\beta_{\text{RBC}} = 0.50$			$\beta_{\text{RBC}} = 0.75$		
	d (h^{-1} Mpc)	v_p (km s^{-1})	$\sigma_{1\text{d}}$ (km s^{-1})	d (h^{-1} Mpc)	v_p (km s^{-1})	$\sigma_{1\text{d}}$ (km s^{-1})	d (h^{-1} Mpc)	v_p (km s^{-1})	$\sigma_{1\text{d}}$ (km s^{-1})
Number-Weighted									
Virgo	12.9	115	108	11.8	230	226	10.7	344	361
Norma (A3627)	49.4	-150	112	50.9	-299	221	52.5	-460	333
Perseus (A0426)	53.9	-179	157	56.1	-407	305	58.3	-619	450
Coma	70.3	161	121	68.8	316	246	67.2	472	378
SSC Core (A3558)	143.7	306	154	140.4	638	306	137.5	925	462
Mass-Weighted									
Virgo	13.3	79	160	12.7	143	316	13.2	91	552
Norma (A3627)	46.7	116	166	45.6	233	320	44.8	314	489
Perseus (A0426)	54.0	-190	207	54.7	-262	347	55.6	-356	472
Coma	71.3	69	149	70.3	161	292	69.3	260	455
SSC Core (A3558)	143.6	315	274	140.5	628	506	138.3	847	739

$$P(cz_{\rm obs}) = \int_0^\infty P(cz \cap r)\, dr \tag{4.13}$$

where the joint probability is:

$$P(cz \cap r) = P(cz|r)P(r) \tag{4.14}$$

The first term is modelled by a Gaussian distribution such that:

$$P(cz|r) = \frac{1}{\sqrt{2\pi\sigma_{cz}^2}} \exp\left[\frac{(cz_{\rm obs} - cz_{\rm RBC})^2}{2\sigma_{cz}^2}\right] \tag{4.15}$$

In the CMB frame, the RBC predicted velocity $cz_{\rm RBC}$ includes a free dipole fitted for each value of $\beta_{\rm RBC}$. The error σ_{cz} is the quadratic sum of the shot noise $\sigma_{\rm SN}$ and a component σ_0 that accounts for the intrinsic error in the reconstruction procedure. We set the latter component here to 150 $\rm km\,s^{-1}$, so as to produce a reasonable χ^2_ν value as seen later in this section. As shown in Fig. 4.5, the shot noise increases dramatically in the vicinity of clusters and superclusters so suppressing the contribution to the determination of $\beta_{\rm RBC}$ from SNIa in these uncertain regions. Hence we do not include the additional error $\sigma_{\rm cl}$ around clusters as we did for the PSCz in Section 3.4, as $\sigma_{\rm SN}$ already accounts for this extra uncertainty.

As the inhomogeneous Malmquist bias correction for SNIa is small (see Section 3.6), the $P(r)$ term in equation 4.14 can be taken as a simple Gaussian of mean d (the inferred SNIa distance) and variance σ_d^2 (the distance error assigned by Tonry et al. 2003).

Finally, the probability $P(cz_{\rm obs})$ is normalised over all possible velocities (cz). The maximum likelihood is then found by minimising the quantity $\mathscr{L} = -2\sum_i \ln P(cz_i)$. As in Willick et al. (1997b) and for solutions involving fitting only one free parameter (i.e. $\beta_{\rm RBC}$), estimated 1σ errors are assigned where $\mathscr{L} = \mathscr{L}_0 + 1$. In the CMB frame, where the dipole is also fitted as a free parameter, an accurate error assessment of the maximum likelihood method is more complex. However, as shown later in this section, by repeating the CMB-frame analysis with the dipole fixed to zero we find little variation in neither $\beta_{\rm RBC}$ nor the uncertainty as assigned in both cases through $\mathscr{L} = \mathscr{L}_0 + 1$. We thus use this confidence level to assign errors for all our determinations of $\beta_{\rm RBC}$ from the maximum likelihood method.

For comparison, we also perform a χ^2 minimisation:

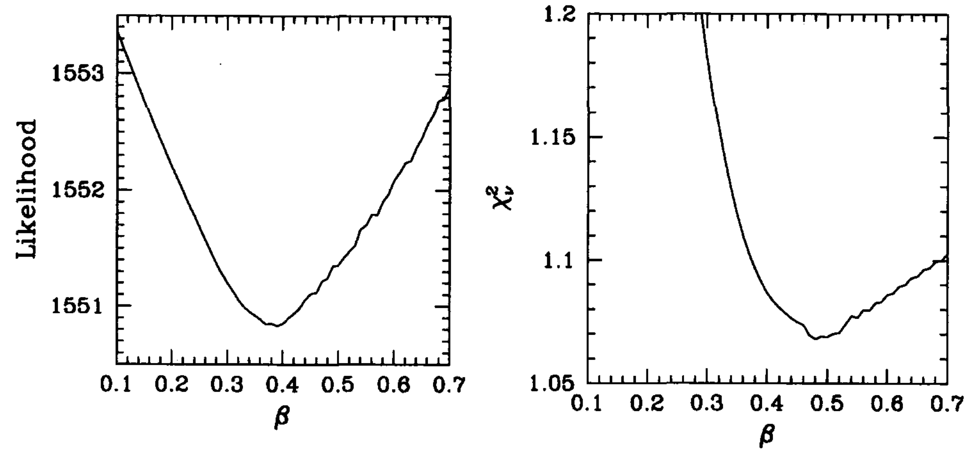

FIGURE 4.6: The value of $\mathscr{L}$ (a) and χ^2_ν (b) as a function of $\beta_{\rm RBC}$. The default sample of 98 SNIa has been used with the number-weighted RBC reconstruction in the LG frame. The best fit value is found to be $0.39^{+0.18}_{-0.15}$ for the maximum likelihood approach and 0.48 ± 0.21 using χ^2 minimisation.

$$\chi^2 = \sum_i^N \left[\frac{(\boldsymbol{v}_{\rm i,RBC} \cdot \hat{\boldsymbol{r}}_i - v_{\rm i,SNIa})^2}{\sigma^2_{\rm i,cz} + \sigma^2_{i,d}} \right] \tag{4.16}$$

where $\boldsymbol{v}_{\rm i,RBC}$ is the peculiar velocity of the ith SNIa as predicted from the RBC reconstruction, which includes the fitted dipole $\boldsymbol{U}$ in the CMB frame, σ_{cz} is the redshift error used in equation 4.15 and $v_{\rm i,SNIa}$ and $\sigma_{i,d}$ are respectively the peculiar velocity and distance error of the ith SNIa, as listed in Appendix B, from Tonry et al. (2000). A downhill simplex method is implemented to find the best fit dipole for each value of $\beta_{\rm RBC}$ in the reconstruction. 1σ errors are estimated from 100 bootstrap resamples of the 98 local SNIa.

Fig. 4.6 shows the likelihood and χ^2_ν as a function of $\beta_{\rm RBC}$ for the default SNIa sample and the RBC velocity field computed in the LG frame using the number-weighted prescription. The log likelihood is minimised at $\beta_{\rm RBC} = 0.39^{+0.18}_{-0.15}$, consistent with the χ^2 result of $\beta_{\rm RBC} = 0.48 \pm 0.21$ for which the minimum $\chi^2_\nu = 1.07$. In the CMB frame, the log likelihood is minimised at $0.51^{+0.19}_{-0.14}$ with an extra free dipole of 444 km s^{-1} towards (l,b)=(249.5°, −0.3°). Repeating the maximum likelihood analysis of the CMB-frame data with the dipole set to zero, yields $\beta_{\rm RBC} = 0.51^{+0.17}_{-0.14}$, essentially identical to the free dipole result. However as the χ^2 solution becomes unstable, oscillating between extremes, a corresponding $\beta_{\rm RBC}$ cannot be determined for either CMB-frame comparison. This unstable behaviour in χ^2 is due to the errors of the RBC reconstruction (the shot noise) scaling with $\beta_{\rm RBC}$. As $\beta_{\rm RBC}$ is increased, the errors in equation 4.16 swamp the signal. The maximum likelihood method is not susceptible to this problem due to the term in front of the exponent in equation 4.15, which divides by the reconstruction error, as well as the prior on the true distance r as imposed in equation 4.14. Overall, the LG- and CMB-frame results are fully consistent with each other and comparison between the observed and predicted radial motions, as seen in Fig. 4.7, shows remarkably good agreement given the relatively large uncertainties in the RBC reconstruction.

The peculiar velocities of the 98 SNIa as predicted from the LG- and CMB-frame, number-weighted reconstructions of the RBC are listed in full in table B.1 of Appendix B. The appropriate best-fit value of $\beta_{\rm RBC}$ and the extra free dipole for the CMB-frame reconstruction are used for these predictions.

4.5 Robustness

Table 4.2 lists the best fit $\beta_{\rm RBC}$ for various weighting prescriptions and culls of the SNIa dataset using the maximum likelihood method detailed in Section 4.4. As described above, the χ^2 minimisation technique is particularly susceptible to the large errors assigned to each measurement. It was therefore only successfully applied to the number-weighted LG case, with and without the intrinsic bias correction B. For these samples, $\beta_{\rm RBC}$ was found to be 0.48 ± 0.21 ($\chi^2_\nu = 1.07$) and 0.31 ± 0.27 ($\chi^2_\nu = 1.10$) respectively, consistent with the values found from minimising $\mathscr{L}$.

For the default sample, $\beta_{\rm RBC}$ is found to be $0.39^{+0.18}_{-0.15}$, consistent with a bias $b_{\rm RBC} = 1.2$, for $\Omega_m = 0.27$. Without the extra intrinsic bias correction (B) described in Section 4.3.2, $\beta_{\rm RBC}$ drops to $0.19^{+0.10}_{-0.05}$. This is closer to the value of 0.24 ± 0.01 quoted by K06 from their comparison of the RBC dipole in the LG frame and with 0.24 ± 0.05 from Plionis & Kolokotronis (1998) for their analysis of the XBACs dipole. This indicates that B has corrected the bias between the density field traced by the RBC clusters and the total mass field.

The comparison between observed and predicted motions will be strongly dependent on the nearby SNIa as these carry the smallest errors. However, varying the range of the culls by distance leads to only small variations in the value of $\beta_{\rm RBC}$ given the size of their uncertainties. This determination of $\beta_{\rm RBC}$ can therefore be taken as independent of the distance range from which the SNIa are drawn.

Using the mass-weighted reconstruction, a more significant uncertainty in $\beta_{\rm RBC}$ is found by solely changing the mass of the Virgo cluster. Increasing the mass from $1.8 \times 10^{14} h^{-1}\,{\rm M}_\odot$ as calculated by K06 to $3.5 \times 10^{14} h^{-1}\,{\rm M}_\odot$ as derived by Böhringer (1994) shifts $\beta_{\rm RBC}$ from $0.40^{+0.17}_{-0.20}$ to $0.11^{+0.29}_{-0.08}$, further highlighting the uncertainty in the mass-weighted reconstruc-

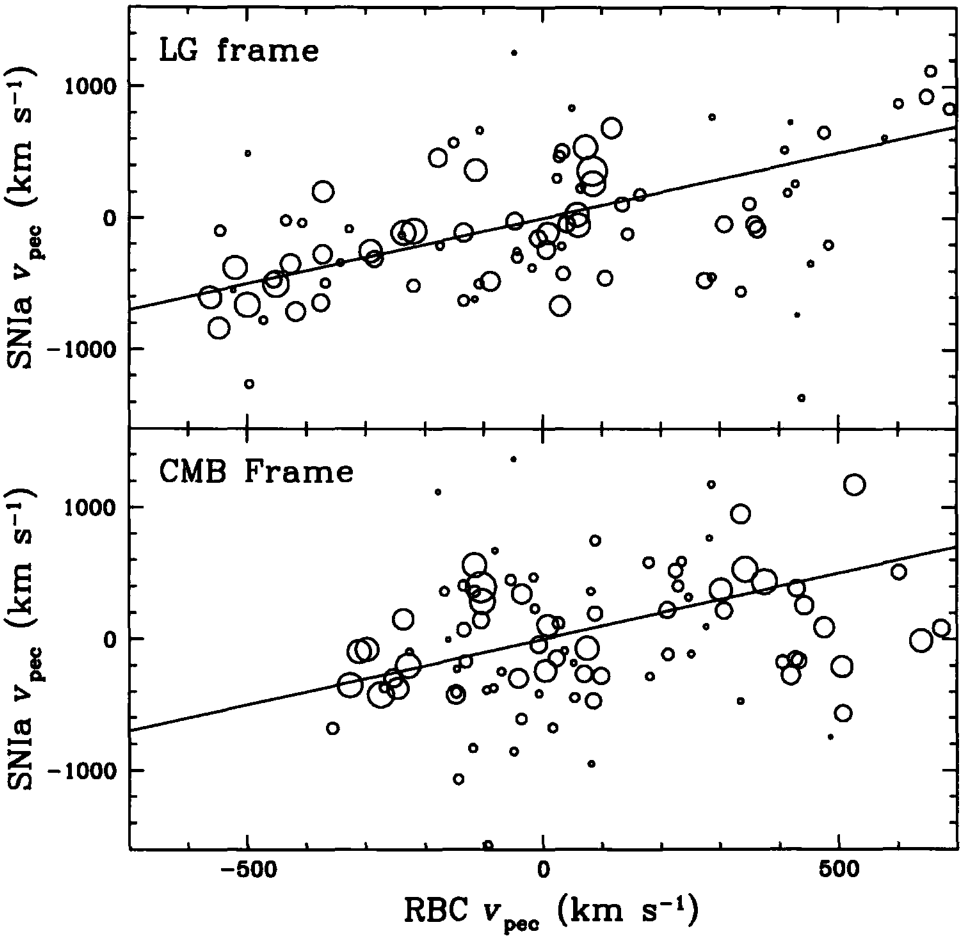

FIGURE 4.7: Comparison of the observed SNIa peculiar motions to the predicted RBC values. The top panel shows the best fit, $\beta_{RBC} = 0.39$ in the LG frame, whilst the lower is for a value $\beta_{RBC} = 0.51$ in the CMB frame. The size of the datapoint is inversely proportional to the total error ($\sigma = \sqrt{\sigma_d^2 + \sigma_{cz}^2}$) and is scaled as in Fig. 3.2, whereby the largest and smallest circles represent errors of ± 170 km s^{-1} and ± 1290 km s^{-1} respectively. The line indicates a 1:1 ratio.

TABLE 4.2: The best fit β_{RBC} for different weighting schemes and dataset culls using the maximum likelihood method.

Weighting Scheme	Cull	N	β_{RBC}	U_{dipole} (km s^{-1})	l_{dipole}	b_{dipole}	$\mathscr{L}$
Number, LG-frame	$0 < r < 150h^{-1}$ Mpc	98	$0.39^{+0.18}_{-0.15}$	–	–	–	1550.8
Number, CMB-frame	$0 < r < 150h^{-1}$ Mpc	98	$0.51^{+0.19}_{-0.14}$	444	249.5	–0.3	1552.8
Number, CMB-frame, Fixed Dipole	$0 < r < 150h^{-1}$ Mpc	98	$0.51^{+0.17}_{-0.14}$	0	–	–	1551.5
Mass, LG-frame	$0 < r < 150h^{-1}$ Mpc	98	$0.40^{+0.17}_{-0.20}$	–	–	–	1553.9
Mass, CMB-frame	$0 < r < 150h^{-1}$ Mpc	98	>1	>1000			0
Number, LG-frame	$0 < r < 125h^{-1}$ Mpc	90	$0.37^{+0.19}_{-0.19}$	–	–	–	1422.6
Number, LG-frame	$0 < r < 100h^{-1}$ Mpc	85	$0.37^{+0.21}_{-0.19}$	–	–	–	1342.8
Number, LG-frame	$20 < r < 150h^{-1}$ Mpc	80	$0.46^{+0.26}_{-0.17}$	–	–	–	1275.8
Number, LG-frame	$40 < r < 150h^{-1}$ Mpc	60	$0.57^{+0.26}_{-0.25}$	–	–	–	956.2
Number, LG-frame, No $B(r)$	$0 < r < 150h^{-1}$ Mpc	98	$0.19^{+0.10}_{-0.05}$	–	–	–	1551.0
Number, CMB-frame, No $B(r)$	$0 < r < 150h^{-1}$ Mpc	98	$0.38^{+0.12}_{-0.09}$	353	259.3	3.5	1552.4
Mass. LG-frame, $M_{Virgo} = 3.5 \times 10^{14}$	$0 < r < 150h^{-1}$ Mpc	98	$0.11^{+0.29}_{-0.08}$	–	–	–	1553.8

tion scheme. The significance of the reliance of the results on the Virgo cluster will be further explored in Chapter 5.

Given the range of values for $\beta_{\rm RBC}$ listed in Table 4.2 together with an average for the random uncertainties, we adopt a best fit $\beta_{\rm RBC} = 0.39$ (for the number-weighted, LG-frame case) with an error of $\pm\, 0.20$.

4.6 Conclusions

Using the RBC, the first all-sky, X-ray selected, galaxy cluster catalogue, we have reconstructed the real-space density and velocity fields. This reconstruction includes an intrinsic correction for the bias between the X-ray cluster density field and the underlying total mass density field.

This new map represents the contributions from the regions of greatest overdensity in the local Universe, regions that are undersampled by the PSCz. Additionally, as X-rays are able to probe the ZoA and cluster projection effects are negligible with X-ray detection, the resulting fields offer a more reliable mapping of the peaks of the density field in comparison to fields derived from optically selected cluster catalogues.

The sparse sampling of the catalogue leads to large shot noise present throughout the reconstruction. Nevertheless, comparison with the observed peculiar motions of 98 local SNIa shows good agreement with the velocities predicted from the catalogue. The best fit to the preferred dataset is $\beta_{\rm RBC} = 0.39 \pm 0.20$.

In the next chapter we use the RBC reconstruction, together with the complimentary PSCz reconstruction described in Chapter 3, to explore the source of the LG motion as well as any discrepancies between the dipole convergence depth as determined from galaxy and cluster catalogues.

5

The X-Ray and Infrared View of the Local Universe

5.1 The Cluster and Galaxy Dipoles

The source of the gravitational acceleration of the LG has been debated for nearly the past three decades. In particular, the distance to the farthest structure that significantly contributes to our motion relative to the CMB remains disputed. Various studies of galaxy and cluster samples have produced a range of values for this convergence depth. Typically, analysis of galaxy surveys have favoured values of $\sim 50h^{-1}$ Mpc. Using the *IRAS* 1.2 Jy survey, Strauss et al. (1992b) claim that the bulk of the LG motion is in place by $40h^{-1}$ Mpc. Similarly, Webster et al. (1997) also using the *IRAS* 1.2 Jy survey, Lynden-Bell et al. (1989) with an optical galaxy survey and da Costa et al. (2000) using a sample of early type galaxies, all attribute the majority of the LG motion to structures within $50h^{-1}$ Mpc. Much larger galaxy redshift surveys yield similar results. Rowan-Robinson et al. (2000) and Schmoldt et al. (1999) find little contribution to the PSCz dipole from structures beyond $140h^{-1}$ Mpc and the 2MRS dipole is found to be due to structures within $60h^{-1}$ Mpc (Erdoğdu et al. 2006a). However, studies of the dipole from rich cluster samples have argued for significant contributions from much larger distances. The convergence depth of the Abell/ACO cluster catalogues is found to be approximately $160h^{-1}$ Mpc (Scaramella et al. 1991; Plionis & Valdarnini 1991; Branchini & Plionis 1996), the same value as quoted from analysis of the

XBACs sample (Plionis & Kolokotronis 1998; Kocevski et al. 2004). Similarly, K06 find the RBC convergence depth to be $\sim 200h^{-1}$ Mpc.

If linear biasing holds true and the relative bias of both cluster and galaxy catalogues is known, then both types of survey should find similar convergence depths. The difference has thus been attributed to the limiting depth of the samples, with galaxy surveys poorly tracing structure at depths $>100h^{-1}$ Mpc. However, compared to galaxies, clusters are highly biased tracers of the total density field with $b_{\rm cluster} \sim 4$. As described in Chapter 4, we have for the first time intrinsically corrected for this bias in our real-space reconstruction of the RBC catalogue.

In this chapter we compare the dipole from the bias corrected real-space reconstruction of the RBC, with the dipole from the real-space reconstruction of the PSCz. Using these reconstructions, we can study the true effect of the limiting distance of cluster and galaxy surveys on their apparent convergence depths.

5.2 Comparison of the RBC and PSCz Reconstructions

As described in Section 3.3, Branchini et al. (1999) reconstructed the density and velocity fields from the PSCz using both an iterative method and a full spherical harmonic decomposition. Both methods produce similar fields with the bulk of the uncertainty arising from the filling-in procedure used for the ZoA (defined for the PSCz as $b \leq 8°$).

As the PSCz undersamples the cores of clusters where early-type galaxies dominate the population, the reconstructed density field is expected to differ significantly from that traced by the RBC. As the RBC samples only the peaks of the true density field, the resulting map will show a much larger density contrast. To compare the two surveys we smooth both the PSCz and RBC with a $15h^{-1}$ Mpc Gaussian kernel during the reconstructions. Fig.5.1 plots the resulting fields in arbitrarily thin slices through three Supergalactic planes within $180h^{-1}$ Mpc, beyond which shot noise dominates the PSCz. With the large smoothing length applied, the fields highlight the large-scale structures mapped by each reconstruction.

The marked difference in density contrast expected between the two catalogues is clearly evident. Although in the SGX/SGY plane the broad outline of the overdensity contours are similar, the large structures seen in common between the fields are significantly more peaked in the RBC. These include the GA at (SGX, SGY) $\sim$ (–45, 0)h^{-1} Mpc, the SSC at (130, 75)h^{-1} Mpc and the PP supercluster at (40, –20)h^{-1} Mpc. A few distinct differences

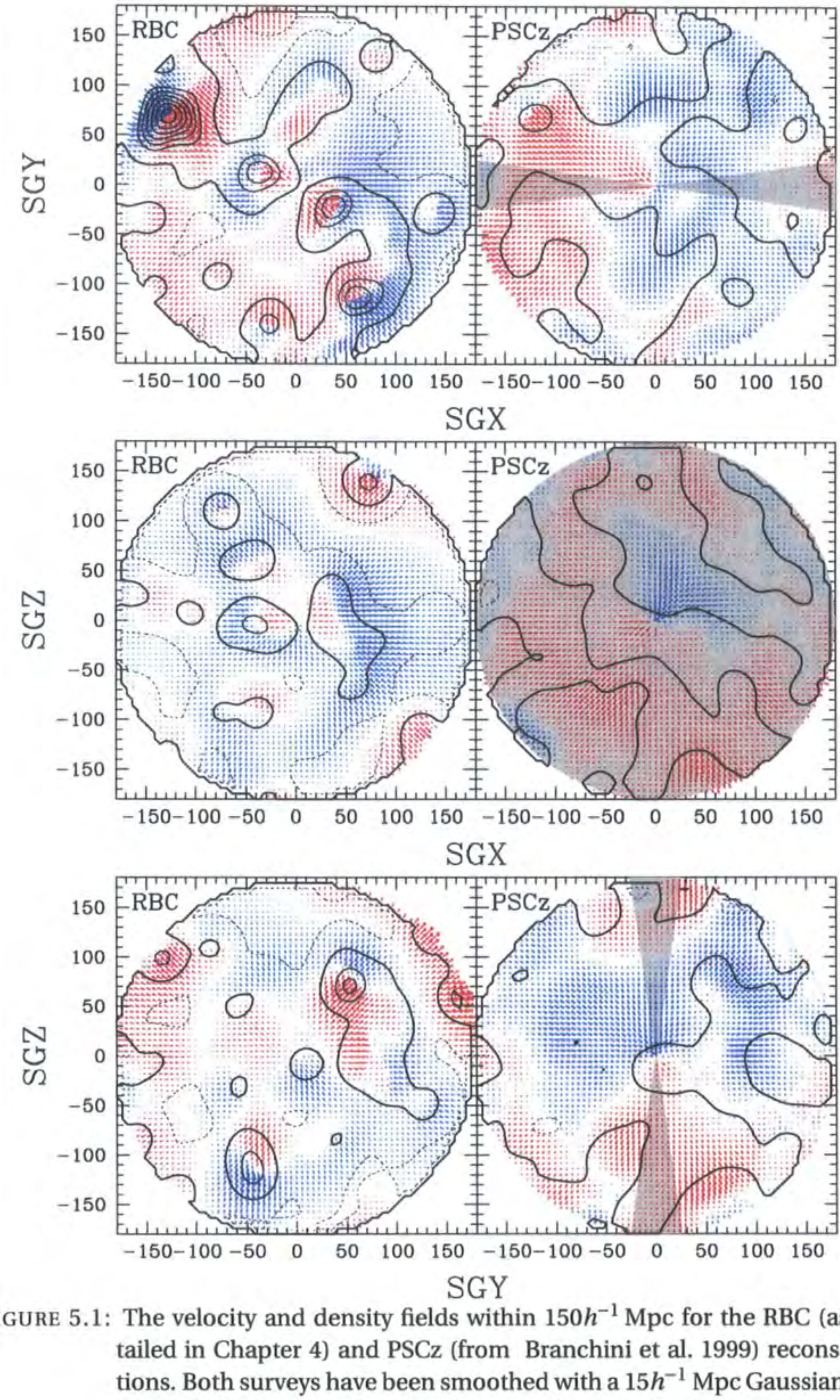

FIGURE 5.1: The velocity and density fields within $150h^{-1}$ Mpc for the RBC (as detailed in Chapter 4) and PSCz (from Branchini et al. 1999) reconstructions. Both surveys have been smoothed with a $15h^{-1}$ Mpc Gaussian kernel and plotted in arbitrarily thin slices through the three supergalactic planes. The density contrasts are plotted at intervals of $\delta = 0.5$ and the recessional velocities are scaled to $1h^{-1}$ Mpc= 100 km s^{-1}. The velocities are coloured red or blue depending on whether they are receding or advancing. The grey shaded region indicates the approximate location of the ZoA, which has been artificially filled in for the PSCz reconstruction.

are also apparent elsewhere. Absent from the PSCz is the Pisces supercluster (Einasto et al. 2001), distinct from PP, lying at (60, −110)h^{-1} Mpc. This system is composed of several Abell clusters, including the intermediate mass A119 (where the A denotes the Abell catalogue), A168 and A193 systems. The combined populations of these clusters indicate a mass comparable to that of PP. Also of note is the slight overdensity in the RBC map at (−150, −35)h^{-1} Mpc. Although not prominent in the number-weighted reconstruction, this peak represents the contributions from the Ara (CIZA J1653.0–5943) and Triangulum-Australis (CIZA J1638.2-6420) clusters. Kocevski et al. (2005) have argued that these clusters, which appear to form an extension to the SSC, are responsible for part of the continuing flow beyond the GA.

In the SGX/SGZ plane, which approximately coincides with the ZoA, the overdensities of the GA at (SGX, SGZ) ~ (−40, −5)h^{-1} Mpc and PP at (40, −10)h^{-1} Mpc are again more pronounced in the RBC. Additionally, the RBC velocity field shows an increased contribution from the Ophiuchus cluster at (−50, 60)h^{-1} Mpc. Lying at (0.56°, 9.27°, 9045 km s^{-1}), close to the Galactic bulge, this cluster has recently been studied in depth by Wakamatsu et al. (2005). They find a velocity dispersion for the cluster of 1050 ± 50 km s^{-1}, similar to that of the massive Coma cluster. Furthermore, the distribution of clumps and clusters of galaxies in the region indicates that Ophiuchus forms the core of a supercluster. Wakamatsu et al. (2005) speculate that this system may be responsible for a similar contribution to the LG acceleration as the SSC. The remaining overdensity at (70, 140)h^{-1} Mpc consists of several RBC clusters centred on A2319 (CIZA J1921.1+4357). The X-ray flux of this large system indicates a mass of ~$1.2 \times 10^{15} h^{-1} M_{\odot}$.

In the SGY/SGZ plane, the RBC field shows greater contributions from the systems at (SGY, SGZ) ~ (50,70)h^{-1} Mpc and (−45, −110)h^{-1} Mpc compared to the PSCz. The former is the Hercules supercluster, which is composed of a large primary clump centred on A2151 (the Hercules cluster) and a secondary smaller clump containing A2197 and A2199. The second system in the RBC map is a collection of six intermediate mass clusters centred on A0548, listed as supercluster SCL 67 in Einasto et al. (2001).

Despite the difference in relative contributions from the large-scale structures mentioned above, the majority of overdensities traced by the RBC out to 180h^{-1} Mpc can be seen in the PSCz, albeit at a much lower significance. The two surveys thus offer complimentary views of the local matter distribution.

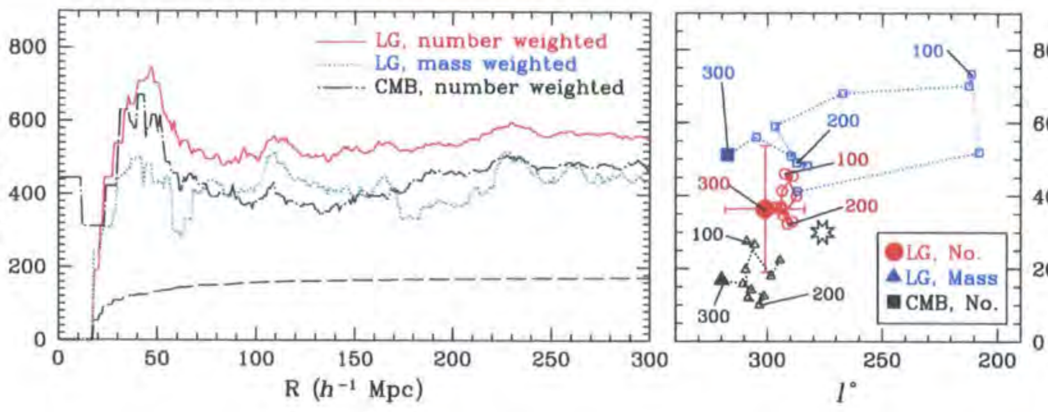

FIGURE 5.2: The real-space, cumulative RBC dipole amplitude as a function of distance for the LG-frame number-weighted (solid red line), LG-frame mass-weighted (dotted blue line) and the CMB-frame number-weighted (dot-dashed black line) reconstructions. Each dipole uses the best fit β_{RBC} listed in Table 4.2 and the CMB-frame reconstruction includes the extra free dipole of 444 $km\,s^{-1}$ towards l =250°, b =0°. The shot noise for the number-weighted reconstruction in the LG frame is shown as the black long dashed line. The right hand panel shows the shift in alignment direction for the dipoles plotted every $25h^{-1}$ Mpc. The direction of the dipole every $100h^{-1}$ Mpc is labelled with the final dipole direction, using all sources within $300h^{-1}$ Mpc, indicated by a large solid symbol. The star indicates the direction of the CMB dipole from Kogut et al. (1993).

5.3 The RBC Dipole

From the reconstruction of the RBC catalogue we are able to trace the contributions to the LG motion from distances beyond the effective depth of the PSCz. As discussed earlier, the different dipole convergence depths predicted from galaxy and cluster samples has been attributed to the greater effective depth of the cluster catalogues.

Fig. 5.2 plots the amplitude and direction of the cumulative RBC dipole from the LG- and CMB-frame reconstructions detailed in Chapter 4. Rather than matching each dipole to the ~630 $km\,s^{-1}$ motion of the LG, the reconstructions are plotted using the best fit values of $\beta_{RBC} = 0.39$ for the LG-frame case and 0.51 for the CMB-frame case as found in Section 4.4 by comparing the reconstructions with the local SNIa dataset. This provides a more reliable estimate as the fields are matched to 98 probes of the true velocity field rather than just the motion induced at the LG, where the unknown contributions from both very local structure and from sources outside the survey area are not included. The extra free dipole of 444 $km\,s^{-1}$ towards l =250°, b =0°, as found in Section 4.4, is included in the CMB-frame reconstructed dipole. This extra component causes the initial 444 $km\,s^{-1}$ motion seen in the CMB-frame, number-weighted dipole in Fig. 5.2. In the LG reference frame, the peculiar motion of structures that are aligned with the direction of the LG motion will be reduced and so their reconstructed position will be greater than their true distance. To minimise this inverse 'rocket effect' (Kaiser 1987; Kaiser & Lahav 1988), we transform the predicted velocities back into the CMB frame using the predicted LG motion. Additionally, due to the large contribution from the Virgo cluster, we fix the distance of this system at 17 Mpc as found by Tully et al. (2007).

As seen in the left hand panel of Fig. 5.2, the mass-weighted reconstruction differs from the number-weighted prescriptions in the relative contribution from sources between 60 and $200h^{-1}$ Mpc. This is attributed to the significant noise introduced by using the luminosity of the clusters to infer mass. Comparatively, the number-weighted schemes in the LG- and CMB-frame reconstructions show a similar profile with a large increase in amplitude up to $40h^{-1}$ Mpc, which is then pulled back by PP, followed by a gradual increase in amplitude out to $230h^{-1}$ Mpc. The final dipole amplitude of the preferred number-weighted, LG-frame reconstruction is 550 ± 170 km s^{-1}. Although slightly lower than the LG motion of 627 ± 22 km s^{-1} as measured by Kogut et al. (1993), the two are in agreement given the size of the uncertainty. Interestingly, in a recent study of the dynamical influence of very local ($<30h^{-1}$ Mpc) structure, Tully et al. (2007) find that 172 ± 15 km s^{-1}, i.e. 30%, of the CMB dipole can be attributed to structures within the local Supercluster. The slightly low value for the LG motion presented here may be due to these missing contributions. This would imply that estimates of β taken solely from comparison of the dipole from any cluster catalogue with the LG motion may be overestimated. Compensating for this local component, Tully et al. (2007) estimate that the value of β_{RBC} derived by K06 for the RBC would be reduced by 11%, from 0.24 for their LG-frame case to 0.21.

The direction of the dipole, plotted in the right hand panel of Fig. 5.2, shows a more significant difference. The CMB-frame reconstruction yields a dipole that shifts by ~100° between 0 and $100h^{-1}$ Mpc before being pulled back into alignment by structures lying between 100 and $300h^{-1}$ Mpc. This is due to the extra free dipole of 444 km s^{-1} towards (333.0°, -68.7°) which, acting at right angles to the LG motion, pulls the dipole out of alignment, reducing the apparent contributions to the dipole amplitude between 60 and $230h^{-1}$ Mpc as compared to the LG-frame reconstruction. The final dipole of the mass-weighted LG-frame reconstruction is pointed ~30° from the equivalent number-weighted dipole. As this misalignment is approximately constant from $17h^{-1}$ Mpc onwards, it can be attributed to the relative mass assigned to the Virgo cluster.

All three dipoles show poor agreement with the true LG acceleration vector which lies towards (276 ± 3°, 30 ± 3°, Kogut et al. 1993). As suggested by Tully et al. (2007), this is likely due to very local, small-scale structure that is not well sampled by the RBC. The effect of this missing component was demonstrated by the analysis of Basilakos & Plionis (2006), who find that excluding the local volume ($<4h^{-1}$ Mpc) from the PSCz decreases the LG motion by $\sim 200\beta_I^{-1}$ km s^{-1}and shifts the alignment of the dipole at $20h^{-1}$ Mpc by 10°.

The Virgo cluster is the closest source in the RBC catalogue and so is expected to have a sizable influence on local dynamics. Fig. 5.3 plots the amplitude and direction of the number-weighted cumulative dipole with and without Virgo as well as with and without the intrinsic bias correction. As the best fit $\beta_{\rm RBC}$ listed in Table 4.2 is used for each reconstruction, the dipoles do not necessarily converge to the ~600 km s^{-1} motion of the LG in the CMB frame. In the LG-frame reconstruction, the bias corrected value of $\beta_{\rm RBC}$ is twice as great as the non-corrected value (0.39 compared to 0.19). This lower value for the non-corrected case strongly suppresses the contribution from the Virgo cluster, which comprises a significant fraction of the dipole, as seen in panel (a) of Fig. 5.3.

Removing the Virgo cluster is found to lower the bias corrected dipole amplitude by almost a factor of two and shift the dipole direction by ~16°. However many cluster surveys, such as the Abell and ACO catalogues and so the XBACs sample as well, preclude Virgo due to the proximity of the system. Some studies of the cluster dipole have thus fitted the LG motion with the Virgo-centric infall removed (e.g. Branchini & Plionis 1996; Plionis & Kolokotronis 1998; Kocevski et al. 2004). As shown in Fig. 5.3, however, Virgo not only affects the final amplitude and direction of the dipole but the change in the cumulative amplitude and direction as a function of distance. With Virgo, the real-space dipole remains in tighter alignment, especially for the bias corrected case. This explains the apparent increase in cumulative amplitude beyond $130h^{-1}$ Mpc for the reconstruction without Virgo (Fig. 5.3, panel b), where structures at the distance of the SSC shift the dipole back to its initial alignment. It is therefore important to ensure the correct contribution from the Virgo cluster in studies of the LG motion from any cluster survey.

The intrinsic bias correction $B(r)$ increases with distance in this flux limited survey. Contributions from more distant structures are thus more heavily dampened. This effect is shown in Fig. 5.3 (panel c) where the magnitude of the contributions to the LG motion have been summed in $10h^{-1}$ Mpc bins and plotted as a percentage of the total contribution to the LG velocity. As distance increases, the fractional contribution decreases quicker for the bias corrected case. By $150h^{-1}$ Mpc, structures in the uncorrected reconstruction contribute twice as much to the total LG acceleration as for the bias corrected case. As shown in Fig. 5.3 (panel a), the amplitude of the bias corrected dipole with Virgo, exhibits little variation beyond this depth.

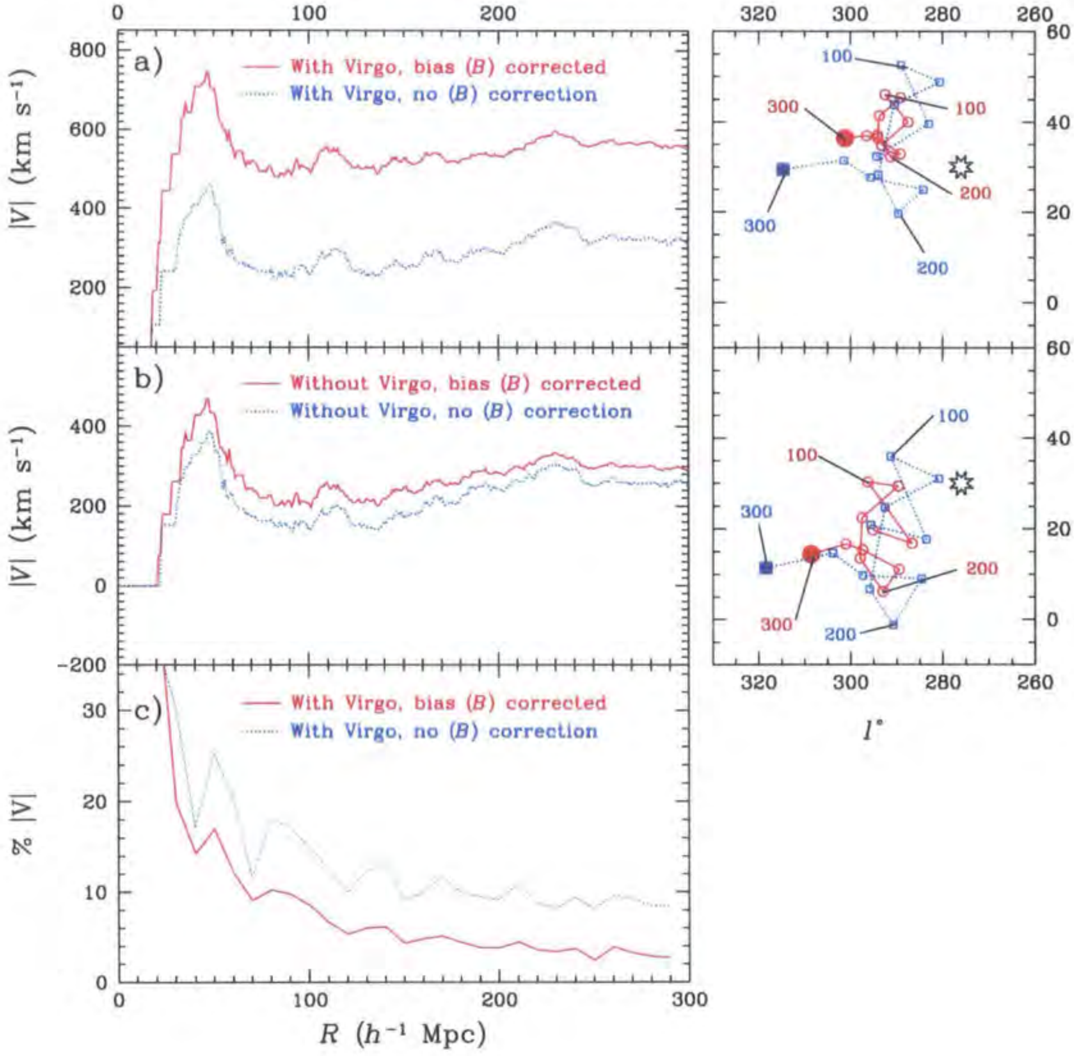

FIGURE 5.3: The real-space, number-weighted RBC dipole amplitude as a function of distance for a fixed value of $\beta_{\rm RBC} = 0.5$, reconstructed in the LG frame. The red solid line and blue dashed line show respectively the reconstruction with and without the intrinsic cluster bias correction B. The middle panel (b) shows the same dipole as in the top panel (a) but without the contribution from the Virgo cluster (note the shift of scale on the vertical axis). The right hand panels shows the shift in alignment direction for the dipoles plotted every $25h^{-1}$ Mpc. The bottom panel (c) shows the size of the projected contributions to the LG motion from successive $10h^{-1}$ Mpc bins as a percentage of the total LG velocity.

In contrast to previous cluster studies (e.g. Scaramella et al. 1991; Branchini & Plionis 1996; Plionis & Kolokotronis 1998; Kocevski et al. 2004), the majority of the bias corrected, real-space RBC dipole is due to sources within $60h^{-1}$ Mpc with structures beyond this contributing typically <100 km s^{-1}. This is partly due to a combination of the intrinsically corrected cluster bias and the inclusion of the Virgo cluster. These effects help explain the apparent difference between convergence depths as traced from galaxy (e.g. *IRAS*) based surveys and cluster samples (e.g. surveys based on the Abell/ACO catalogues).

5.4 Combining the RBC and PSCz Reconstructions

Here we combine the RBC and PSCz reconstructions of the density and velocity fields. As the RBC traces structures in regions of high overdensity, whilst the PSCz maps areas of low density, combining the two should produce a more accurate representation of the local density field.

In a dynamical study of the local void and the local supercluster, Tully et al. (2007) find that the CMB dipole can be decomposed into a large-scale component directed towards the Centaurus/SSC region, and a residual from sources within $30h^{-1}$ Mpc. This residual can be further split into a component towards Virgo and one away from the local void. Comparison with the 2MRS dipole calculated by Erdoğdu et al. (2006a) suggests that this survey traces the local structure as the dipole lies close to the reflex direction of the local void. Comparatively, the dipole of the K06 RBC dipole lies closer to the SSC direction, indicating this survey preferentially traces the larger-scale component. Although the median distance of the PSCz is greater than the 2MRS, the combined PSCz and RBC reconstruction should be more reliable over a greater distance range than either of the independent surveys.

Adopting the best fit values for β_I and $\beta_{\rm RBC}$ from Chapters 3 and 4, we sum the two fields with a variable ratio between the reconstructions. We then use the radial motions of 98 SNIa from the Tonry et al. (2003) compendium, as described in Section 3.4, to determine the best fit ratio. Fig. 5.4 plots the predicted radial motion from the combined reconstruction against the observed SNIa peculiar velocities for a range of ratios of the RBC and PSCz reconstructions. We use values of the likelihood and χ^2 (as derived in Section 4.4) as well as the rms residual scatter to assess the goodness of each fit. These are given in each panel for the different ratios.

Although the χ^2 values listed in Fig. 5.4 prefer a more even ratio between the surveys compared to the maximum likelihood analysis (χ^2_ν=0.96, $\mathscr{L}$=1549.5 at 50%/50%, χ^2_ν=0.97, $\mathscr{L}$=1549.1 at 75%/25%), they are naturally biased towards the larger errors of the RBC cat-

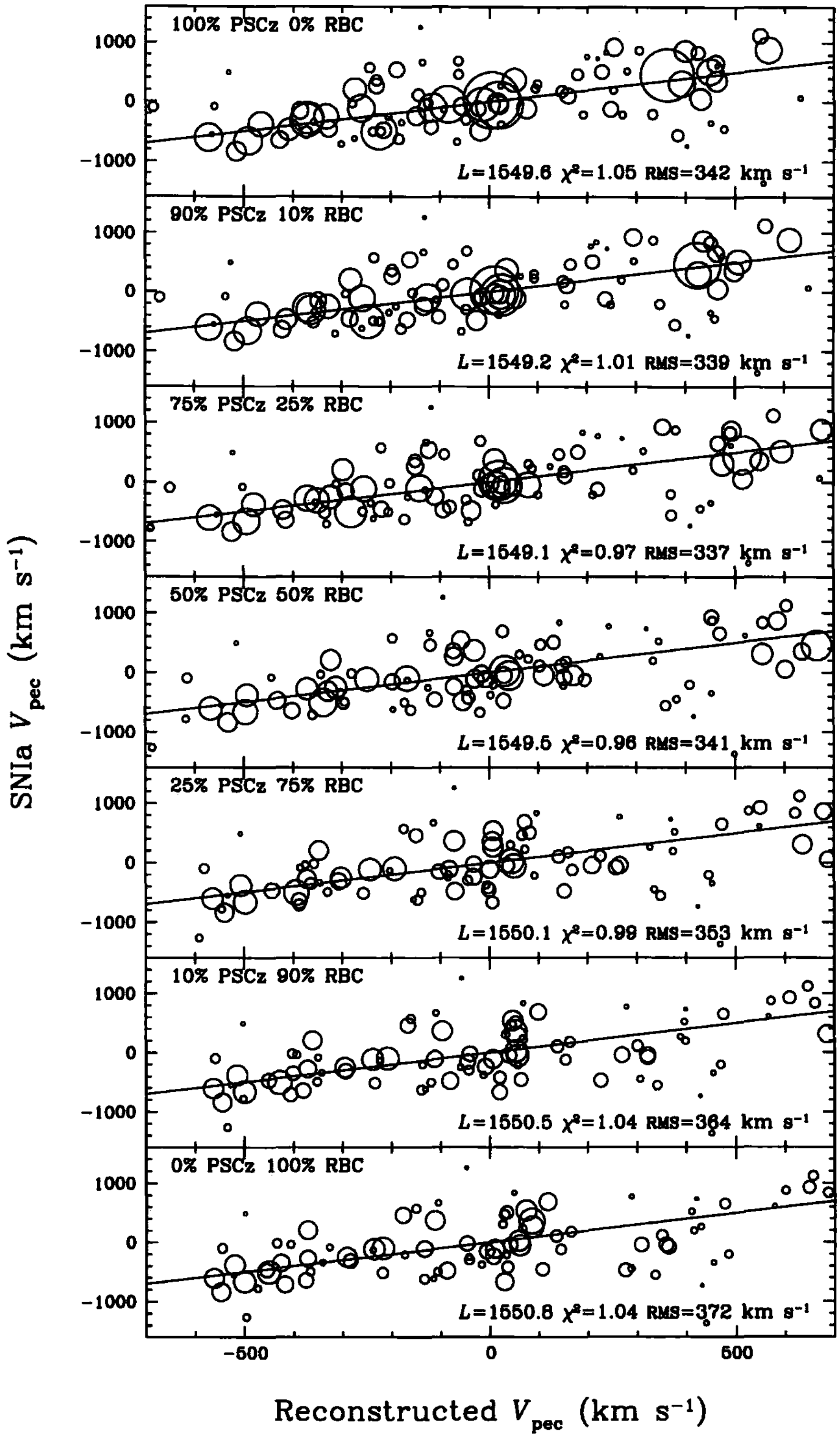

FIGURE 5.4: The observed SNIa peculiar velocities compared to predictions from the combined RBC/PSCz reconstructions for several ratios of the two catalogues. The Likelihood and reduced χ^2_ν value as well as the RMS scatter between the observed and predicted peculiar velocities for SNIa in the range $20-90h^{-1}$ Mpc are also listed for each ratio. As in Fig. 3.2. the size of the datapoint is inversely proportional to the error, with the largest ans smallest circles corresponding to combined errors of 170 km s^{-1} and 1290 km s^{-1}

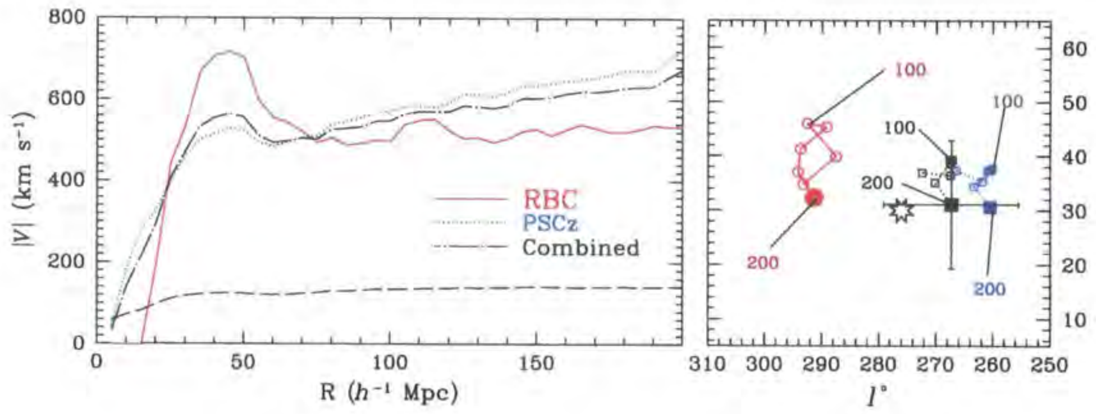

FIGURE 5.5: The cumulative amplitude and direction of the real-space LG motion from the separate RBC (red solid line) and PSCz (dotted blue line; Branchini et al. 1999) catalogues as well as from the combined sample (dot-dashed black line; 78% PSCz, 22% RBC). The dipole is sampled every $5h^{-1}$ Mpc. The combined shot noise is also indicated by the long dashed black line. The right hand panels shows the shift in alignment direction of the dipoles plotted every $25h^{-1}$ Mpc. The pointing error of the combined dipole is calculated from the uncertainty in the reconstruction due to shot noise.

alogues. This is validated by the rms values which show a slightly better fit of 337 km s^{-1} at 75%/25% compared to 341 km s^{-1} at 50%/50%. By varying the contribution from each survey we find the best fit case to be 78% PSCz and 22% RBC for the LG-frame reconstruction, with similar values of 81% PSCz, 19% RBC for the CMB-frame result. The log likelihood for the LG-frame case drops from 1549.6 and 1550.8 for the PSCz and RBC respectively to 1549.1 for the combined case. Similarly, the reduced χ^2_ν value decreases from 1.05 and 1.04 for the PSCz and RBC to 0.98. This corresponds to a decrease in the rms scatter between the observed and predicted motions from 342 km s^{-1}and 371 km s^{-1}for the PSCz and RBC to 337 km s^{-1}. Overall, the velocity field from the combined reconstruction is a better fit to the local SNIa data than the individual fields of the separate reconstructions. However, as indicated by the small decrease in χ^2, the improvement is not highly significant with the independent and combined reconstructions all providing good fits to the SNIa peculiar velocities.

A more reliable combination of the density and velocity fields from the two surveys may be found by relocating the RBC clusters to their equivalent positions in the PSCz reconstruction. This would remove the uncertainties in the RBC reconstruction due to the large shot noise, whilst including their contribution to the overall density field. A best fit ratio between the reconstructions could then be found using the same method above. However such an analysis is beyond the scope of this thesis.

5.4.1 The Combined Dipole

The amplitude and direction of the cumulative dipole from the best fit combined density and velocity fields, as well as from the individual RBC and PSCz reconstructions, is plotted in Fig. 5.5. Both the RBC and PSCz dipoles show similar profiles. A pronounced increase from 20 to $40h^{-1}$ Mpc due to structures in the foreground of the general GA region (defined later as 250< l <350°, −45< b <45°, 2000< cz <6000 km s^{-1}) is followed by a decrease between 40–$60h^{-1}$ Mpc as PP, on the opposite side of the sky, acts to retard the initial contributions. Overall, the RBC shows a larger contribution from these nearby structures than the PSCz reconstruction of Branchini et al. (1999). Conversely, from $60h^{-1}$ Mpc onwards, the RBC shows an approximately constant amplitude of ~650 km s^{-1}, whilst the PSCz shows a gradual rise from ~500 km s^{-1} at $60h^{-1}$ Mpc to ~700 km s^{-1} at $200h^{-1}$ Mpc. This increase is due to the steady growth of shot noise with distance in the PSCz catalogue as shown in Basilakos & Plionis (2006). As the limiting depth of each dipole increases, the direction of the dipoles shift by about 10°. Generally, structures between 0 and $100h^{-1}$ Mpc push the dipole away from the CMB dipole, whilst structures between 100 and $200h^{-1}$ Mpc bring it back into alignment. Although the RBC and PSCz dipoles are separated by ~30°, the combined dipole lies closer to the CMB dipole than either of the independent dipoles. This again lends credence to the work of Tully et al. (2007), who suggest that the LG motion is due to a local component, as preferentially traced by galaxy surveys, as well as a large scale component traced by cluster surveys.

5.4.2 The GA/SSC Influence

The initial discovery of the GA introduced the concept of a nearby, massive overdensity dominating local dynamics. However, as detailed in Section 2.1, subsequent studies of the region failed to detect any clear sign of backside infall into the overdensity. Several studies attribute this observation to a continuing flow towards the SSC in which the GA takes part (Scaramella et al. 1989; Allen et al. 1990; Branchini et al. 1999; Hudson et al. 2004). The size of the relative contributions to the LG motion from these two large structures remains unclear. This is principally due to their close proximity on the sky, which prevents their dynamical influence from being easily decoupled.

An overview of the GA region was presented in Chapter 2, however the precise meaning of the GA has varied significantly between authors. Fig 5.6 plots an area of the sky defined by $225 < l < 375°$, $-60 < b < 60°$ and $2000 < cz < 6000$ km s^{-1}, identifying the important structures in the region. As summarised in Section 1.4, Lynden-Bell et al. (1988) originally defined the GA as a theoretical overdensity centred at (l, b, cz)~(307°, 9°, 4350 ± 350 km s^{-1}),

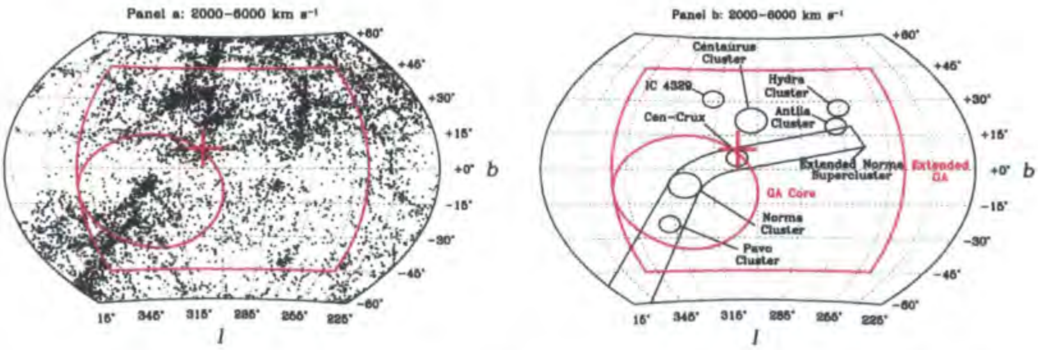

FIGURE 5.6: The position of structures in the region $225 < l < 375°$, $-60 < b < 60°$, $2000 < cz < 6000$ km s^{-1}. The left hand panel plots the galactic coordinates of galaxies from the NED database (as of August 2007). The right hand panel identifies the key clusters and structures in the region. The red circle denotes the core of the extended Norma Supercluster, whilst the red rectangle marks the extended GA region ($250 < l < 350°$, $-45 < b < 45°$, $2000 < cz < 6000$ km s^{-1}). The original Lynden-Bell et al. (1988) position of the GA is marked by a red cross.

marked in Fig. 5.6 by a red cross. This location, which is approximately coincident with the projected position of the Cen-Crux feature (yet some ~1000 km s^{-1}closer), lies along the wall of the extended Norma Supercluster, defined in Section 2.3.3 and outlined in Fig. 5.6. The red, 25° radius circle denotes the core of this structure, encompassing the massive Norma cluster as well as the Pavo II, CIZA J1324.7–5736 and Cen-Crux clusters. Alternate delineations of the GA have included the Hydra-Centaurus supercluster (Chincarini & Rood 1979), composed of the Centaurus, Hydra and Antlia clusters as well as the IC 4329 group, which are also all marked in Fig. 5.6. As highlighted in Fig. 2.4 of Chapter 2, these clusters lie some $15h^{-1}$ Mpc closer to us than the Norma cluster. We here define an extended GA as the region bounded by $250 < l < 350°$, $-45 < b < 45°$, $2000 < cz < 6000$ km s^{-1}, which encompasses all the structures in Fig 5.6 and is denoted by the red projected rectangle.

Several peculiar velocity studies have surveyed the regions surrounding the GA and the SSC. Fig. 5.7 plots the peculiar velocities of the Tonry et al. (2003) local SNIa as well as the SMAC (Hudson et al. 2004) and SCI (Giovanelli et al. 1998) cluster surveys in the direction of the core of the Norma supercluster (defined as within 25° of l = 325°, b =–10°) and the SSC (within 10° of l=310°, b=30°). Also plotted are the amplitudes of the flow from the RBC, PSCz and combined reconstructions, averaged over several sight lines in the denoted regions. As in Lucey et al. (2005), predicted peculiar motions are shown for a simple Faber & Burstein (1988) model representing LG motions due solely to a GA centred at $43.5h^{-1}$ Mpc and for a model with equal contributions from this GA and the SSC at

$145h^{-1}$ Mpc.

The top panel of Fig. 5.7 shows little effect from the core of the Norma supercluster. Although both reconstructions predict a small amount of backside infall, the amplitudes of the velocities are comparable to the uncertainties (±200 km s^{-1}). For the number-weighted reconstruction of the RBC, as plotted here, this is to be expected as the massive Norma cluster is not assigned any additional weight over any other source in the catalogue. The similar lack of amplitude from the PSCz reflects the low sampling of the survey so close to the ZoA. The clusters plotted in this region (Pavo and Pavo II, which was measured by both the SMAC and SCI surveys) show slightly positive peculiar velocities. A preliminary study of the infrared FP of the Norma cluster by Woudt et al. (2005) also reveals a small positive peculiar velocity for this system relative to the CMB. By summing contributions projected onto the CMB dipole from a sphere of radius $25h^{-1}$ Mpc (~25° at $50h^{-1}$ Mpc) centred on the Norma cluster, we find that the core of the Norma supercluster is responsible for only 46 km s^{-1} of the 580 km s^{-1} PSCz dipole, 34 km s^{-1} of the 640 km s^{-1} RBC dipole and 45 km s^{-1} of the 580 km s^{-1} combined dipole.

A coherent flow pattern, equivalent to that shown for the Norma supercluster core in Fig. 5.7, cannot be found for the extended GA due to the large volume of space which it encloses. However the effect of the structures in the region can be seen in the foreground of the SSC as shown by the lower panel of Fig. 5.7. Both the PSCz and RBC show large contributions from structures within $30h^{-1}$ Mpc. Beyond this distance, the more peaked signal from the number-weighted RBC reconstruction predicts backside infall. This effect is not observed in the equivalent PSCz prediction. The total contribution to the CMB dipole from the extended GA is found to be 379 km s^{-1} from the PSCz, 368 km s^{-1} from the RBC and 379 km s^{-1} from the combined reconstruction.

All the cluster and SNIa peculiar velocities along the line-of-sight in the lower panel of Fig. 5.7 are positive, suggestive of a continued flow towards the SSC. Summing within a sphere of $40h^{-1}$ Mpc at (310°, 30°, $145h^{-1}$ Mpc) to include the clusters within the SSC, we find contributions of 61 km s^{-1}, 83 km s^{-1} and 68 km s^{-1} for the PSCz, RBC and combined reconstructions. Repeating the analysis for the RBC reconstruction without the intrinsic bias correction B, using the corresponding value of $\beta_{\rm RBC}$=0.19 and normalising to reproduce the same LG motion, finds the relative contribution from the SSC increase by more than a factor of 2.3 from 83 km s^{-1} to 193 km s^{-1}. Comparatively, without the bias correction, the extended GA contribution increases by only 1.4 from 368 km s^{-1} to 522 km s^{-1}. Analysis of the source of the LG motion from cluster surveys uncorrected for cluster bias are therefore likely to overestimate the relative contribution from distant structures such as the SSC.

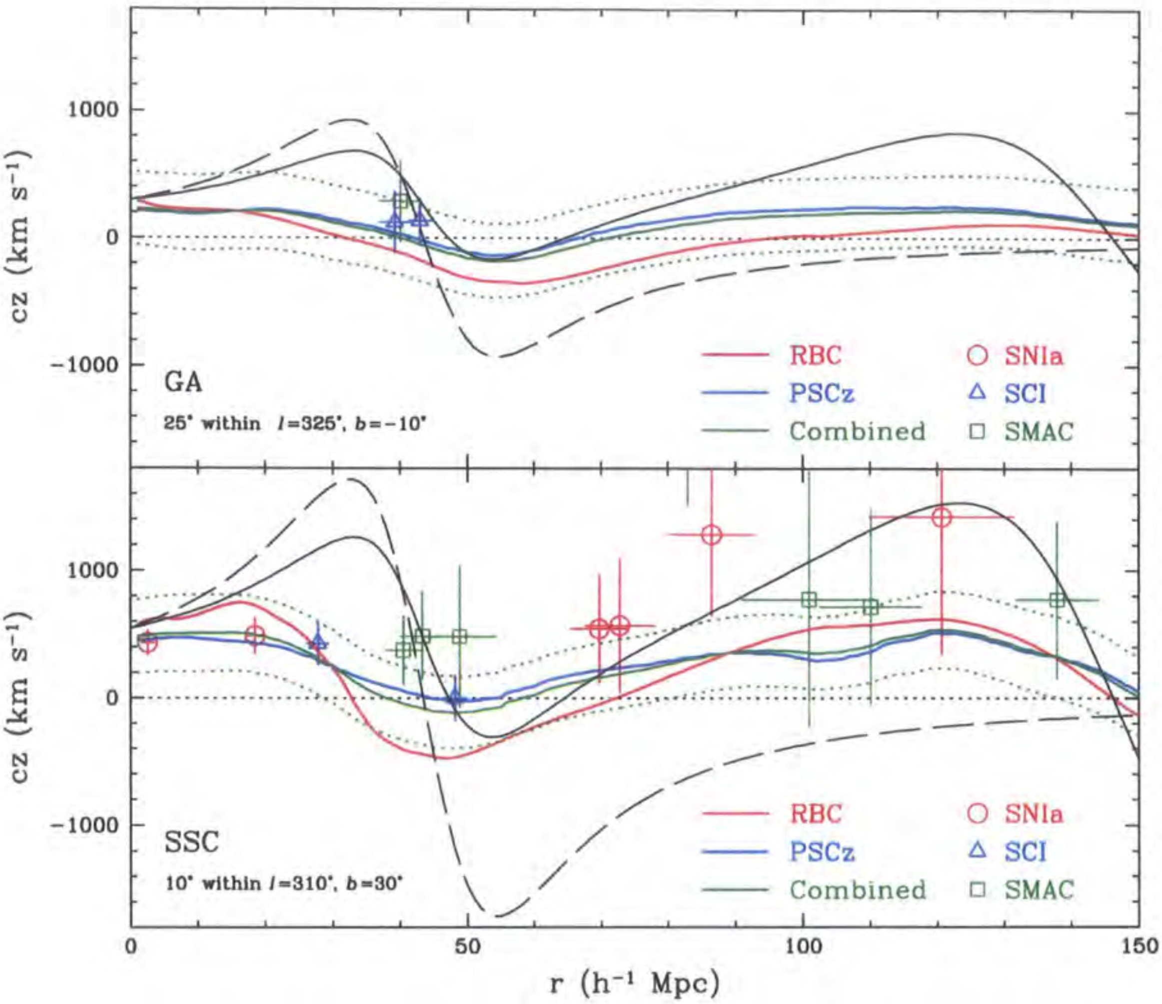

FIGURE 5.7: The proper motions averaged along several line-of-sights within 25° of the core of the Norma supercluster and 10° of the SSC. The solid red, blue and green lines are predictions from the RBC, PSCz and combined reconstructions respectively. The dashed green lines are the predicted limits of the uncertainty inferred from the sum of the shot noise and a 150 $\mathrm{km\,s^{-1}}$ component. The red datapoints are the peculiar velocities of the Tonry et al. (2003) SNIa with the errorbars indicating the σ_{cz} errors detailed in Section 3.5. Similarly, the blue and green datapoints are the motions of clusters taken from the SCI and SMAC datasets respectively. The solid black line is a Faber & Burstein (1988) model normalised to produce the CMB dipole, projected onto the line of sight, with equal contributions from a GA at $43.5h^{-1}$ Mpc and the SSC at $145h^{-1}$ Mpc. The dashed line represents a similar model but with the GA solely responsible for the dipole.

The large Triangulum-Australis (CIZA J1638.2–6420) and Ara (CIZA J1653.0–5943), lying at $(l, b, cz)\sim(324.5°, -11.6°, 15060\ \mathrm{km\,s^{-1}})$ and $(329.3°, -9.9°, 14643\ \mathrm{km\,s^{-1}})$ respectively, may form part of an extension of the SSC into the ZoA. Lying so close to the Galactic centre these structures are outside the region surveyed by the PSCz. The X-ray fluxes indicate masses of approximately $1.0\times10^{15}h^{-1}\,\mathrm{M_\odot}$ and $5.3\times10^{14}h^{-1}\,\mathrm{M_\odot}$ for these clusters respectively. As these are comparable to the mass of Coma, Kocevski et al. (2005) argue that these clusters are in part responsible for the continuing flow beyond the GA. In this number-weighted RBC reconstruction, however, they are only responsible for $<10\ \mathrm{km\,s^{-1}}$ of the LG motion. In future work, the masses of the RBC clusters may be included by using the PSCz to reconstruct the real-space RBC positions as discussed in Section 5.4.

Overall, the interplay between PP and the extended GA, which encompasses the Norma supercluster as described in Chapter 2 as well as the Hydra-Centaurus supercluster, has a $\sim 5\times$ greater affect on the CMB dipole than the SSC. The SSC does, however, influence dynamics behind the GA. The lower panel of Fig. 5.7 shows a gradual increase in the size of the flow towards the SSC from $\sim50h^{-1}$ Mpc onwards for both the PSCz and RBC. Unfortunately, as discussed in Lucey et al. (2005) for the PSCz, both of the reconstructions presented here are unable to fully account for the large positive peculiar motions of SNIa and clusters found between the GA and the SSC (also plotted in the lower panel of Fig. 5.7). This is likely due to PSCz and number-weighted RBC reconstructions used here under-sampling contributions from the massive structures in the extended GA and SSC. A more detailed study of the mass-weighted RBC catalogue, as alluded to previously, would be able to verify this assumption.

5.5 Conclusions

Using the real-space reconstruction of the RBC catalogue described in Chapter 4, we have compared the density field as traced by X-ray clusters to that mapped by *IRAS* galaxies from the PSCz reconstruction of Branchini et al. (1999). Both reconstructions have been shown to broadly trace the same structures within $180h^{-1}$ Mpc, the limiting depth of the PSCz. However the two catalogues offer complementary views of the local matter distribution. *IRAS* galaxies preferentially trace low density regions whilst the RBC clusters trace the peaks of the density fluctuations. Combining reconstructions from the two surveys has been shown to provide better estimates of the observed proper radial motions of a sample of 98 local SNIa. The best fit was found when the catalogues were combined in the ratio 78% PSCz and 22% RBC.

Importantly the separate and combined dipoles from the two reconstructions show similar relative contributions from different depths. Unlike previous studies of the cluster dipole, which find significant contributions from sources at $\sim 150h^{-1}$ Mpc (e.g. Scaramella et al. 1991; Plionis & Kolokotronis 1998; K06), we find the bulk of the LG motion is due to the structures within $60h^{-1}$ Mpc. Sources beyond this depth have little contribution (<100 km s^{-1}). This difference is partly due to a combination of the inclusion of the Virgo cluster and the intrinsic correction of the cluster bias as detailed in Chapter 4.

The separate and combined PSCz and RBC dipoles show 65% of the LG motion is due to overdensities in the extended GA region (defined previously as $250 < l < 350°$, $-45 < b < 45°$, $2000 < cz < 6000$ km s^{-1}, encompassing the core of the Norma supercluster described in Section 2.3.3, as well as the Hydra-Centaurus supercluster). Comparatively, the SSC only accounts for 12% of the LG motion. However the separate and combined reconstructions fail to account for the large positive peculiar velocities in the region between the GA and SSC. A more refined combination of the RBC and PSCz will allow for a more detailed study of the dynamical influence of the most massive clusters in the region. Together with an accurate mass estimate of the SSC, these systems may explain the apparent continuing flow on the farside of the GA.

6

Conclusions

6.1 Thesis Summary

This thesis uses the Gravitational Instability (GI) framework to investigate the influence of large-scale structures on the dynamics of the local Universe and in particular to study the source of the Local Group (LG) acceleration.

In Chapter 1 we have described the historical development of redshift and peculiar velocity surveys, which have sought to map the distribution of matter in the nearby Universe. We have also introduced the core concepts upon which this thesis is based.

In Chapter 2 we investigated the structure of the Great Attractor (GA). Originally proposed by Lynden-Bell et al. (1988) as a theoretical overdensity to explain the observed motions of nearby elliptical galaxies, this feature is believed to be responsible for a significant part of the LG motion. To further our understanding of the GA, we measured redshifts for 3053 galaxies in the region using the Two-degree Field multi-fibre spectrograph (2dF) on the Anglo-Australian Telescope (AAT). We calculated velocity dispersions for nine clusters including CIZA J1324.7–5736, now identified as a separate structure from the Cen-Crux cluster. An analysis of redshifts from this survey, in combination with those from the literature, revealed the dominant structure in the GA region to be a large filament (the extended

Norma supercluster), which appears to extend from Abell S0639 ($l = 281°$, $b = +11°$) towards a point at $l \sim 5°$, $b \sim -50°$, encompassing the Cen-Crux, CIZA J1324.7–5736, Norma and Pavo II clusters.

In Chapter 3 we described the reconstruction of the real-space PSCz peculiar velocity field made by Branchini et al. (1999) using the GI paradigm. We find this field to be in excellent agreement with the observed radial motions of a sample of 98 local type Ia supernovae (SNIa), so validating the use of the GI model. The best fit value of $\beta_I (= \Omega_m^{0.6}/b_I)$ for the PSCz reconstruction was found to be 0.55 ± 0.06. This new measurement is robust to subsequent culls of the SNIa dataset based on distance, host-galaxy extinction and the reference frame in which the comparison is carried out.

As described in Chapter 4, the PSCz survey preferentially traces late-type galaxies, so undersampling the regions of greatest overdensity. Cluster surveys, which trace the peaks of the density field, are therefore a complimentary probe of the local mass distribution. X-ray selected clusters are especially suited to this task as they are less susceptible to projection effects and are able to probe further into the Zone of Avoidance (the region of sky obscured by our own galaxy) than their optical counterparts. Hence, in Chapter 4 we reconstructed the real-space peculiar velocity and density fields from the recently compiled RBC survey: the first all-sky, X-ray selected, galaxy cluster catalogue. Unlike previous studies, this reconstruction incorporated an intrinsic correction for the bias between the cluster density field and the underlying total mass density field. Although the shot noise of the resulting velocity field was 100–200 $\mathrm{km\,s^{-1}}$, the reconstruction was found to be in good agreement with the observed peculiar velocities of the same 98 SNIa used in Chapter 3. The best fit was found for $\beta_{\mathrm{RBC}} = 0.39 \pm 0.20$.

In Chapter 5 the complimentary RBC and PSCz real-space reconstructions were compared. A combination of the two was found to be a better fit to the local 98 SNIa sample than either reconstruction alone. The best fit combination of the catalogues was found to be 78% PSCz and 22% RBC. Importantly, the two surveys were shown to produce similar contributions to the LG motion as a function of increasing distance. Previous studies based on cluster surveys have argued for significant contributions from distances of $\sim 150h^{-1}$ Mpc (e.g. Scaramella et al. 1991; Plionis & Kolokotronis 1998; K06), which are not observed in the equivalent analysis of galaxy surveys (e.g. Strauss et al. 1992b; Rowan-Robinson et al. 2000; Erdoğdu et al. 2006a). This dichotomy has in the past been attributed to the greater depths that cluster surveys are able to sample. However, in Chapter 5, sources at $150h^{-1}$ Mpc and beyond have been shown to have little influence on the LG motion in both the cluster-based RBC and galaxy-based PSCz reconstructions. This has been attributed to the intrinsic bias correction in the RBC as well as the inclusion of the Virgo cluster, which is absent from many cluster surveys.

As found from the combined RBC and PSCz surveys in Chapter 5, the majority (65%) of the LG motion is due to the extended GA, defined as the region bound by $250 < l < 350°$, $-45 < b < 45°$ and $2000 < cz < 6000$ km s^{-1}. The extended GA encompasses the core of the extended Norma Supercluster, as described in Chapter 2, as well as the Hydra-Centaurus supercluster which includes the Centaurus, Hydra and Antlia clusters as well as the IC 4329 group. Comparatively the much larger, but more distant Shapley supercluster (SSC), which lies almost directly behind the extended GA, was found to be responsible for only 12% of the LG acceleration.

6.2 Future Directions

Peculiar velocities are a direct probe of the hidden underlying mass distribution of the local Universe. As such they are able to place strong constraints on cosmological models which predict the build up of mass. On large scales, where linear theory is most applicable, the rms peculiar velocity of clusters, which as shown in Chapter 5 is due principally to superclusters, is proportional to $\sigma_8\Omega_m^{0.6}$ (Colberg et al. 2000). This same quantity can be estimated from the cluster abundancies of cosmological simulations (e.g. White et al. 1993). Comparison of the two results thus provides constraints on the cosmology assumed in the simulation (e.g. the power spectrum of the initial density field). On smaller scales, models of the peculiar velocity field can be used to correct galaxy distances as inferred from redshift measurements. This will improve the zero-point of the magnitude-distance relation for local SNIa and correct the low end of the mass and luminosity functions for galaxies in the local volume (e.g. Masters et al. 2004).

As detailed in this thesis, efforts to map the peculiar velocity field to both a higher degree of completeness and a greater level of accuracy are still ongoing. Notably, the 2MASS Tully-Fisher (2MTF, Masters 2007) survey aims to measure TF distances for all bright inclined spirals in the 2MASS Redshift Survey (2MRS). Using HI rotation widths together with 2MASS K-band magnitudes and 2MRS redshifts, the 2MTF promises to directly measure peculiar velocities with < 20% uncertainties over the majority of the sky ($|b| > 5°$) and to great depth (K_s =11.25 mag, cz <10,000 km s^{-1}). Comparably, the 6dFGS aims to measure peculiar velocities for ~15,000 early-type galaxies over the whole southern sky using FP distances (Jones et al. 2004, 2005). A study of FP distances from the SDSS in the northern sky for just 720 early-type galaxies in 36 clusters yields distance errors of ~ 8% per cluster (Vowles 2007). The results from this preliminary study are found to be in good agreement with the

SMAC and EFAR cluster surveys. Combining the 6dfGS with a more comprehensive study of FP distances from the SDSS will thus provide a significantly dense and accurate peculiar velocity catalogue for a large fraction of the sky.

These new surveys will further our understanding of the source of the LG motion. However a study of the dynamical effects of the GA and SSC masses in particular will help decouple the contributions from these two large structures. Although the masses of the RBC clusters as inferred from their X-ray luminosities carry a large uncertainty, they should at least provide better estimates of the relative contributions from the GA and SSC. To include the RBC masses in the more accurate PSCz reconstructions, each cluster could be assigned to a point in the initial PSCz redshift-space density field. As the real-space PSCz reconstruction is carried out, the RBC clusters would move with their corresponding PSCz location. The result would be positions for the real-space RBC clusters to which masses could be assigned and a flow field calculated. Alternately, more reliable cluster masses could be inferred from the summed 2MASS K-band luminosity of each source. Crook et al. (2007) have performed a similar analysis for groups in the 2MASS catalogue. By comparing the summed K-band luminosities to the projected mass estimates of each group, they were able to estimate the mass-to-light ratio and so derive a value of $\Omega_m = 0.229^{+0.016}_{-0.012}$ in good agreement with *WMAP*.

To check the predictions from the RBC reconstructions and provide yet further constraints on the relative influence of the GA and SSC, peculiar velocities of objects in and intermediate to the two structures need to be measured directly. Woudt et al. (2005) have reported early results for the proper distance to the Norma Cluster using FP analysis of member galaxies. A more detailed analysis will reveal if this structure itself takes part in a flow towards the SSC. Interestingly, an HST project (PI: J. Blakeslee) is currently underway to measure the infall onto the SSC. By obtaining SBF distances to 7 elliptical galaxies in 3 clusters lying approximately 40 Mpc in front of the SSC, this project will determine the infall velocity to an accuracy of $< 300\ \mathrm{km\,s^{-1}}$ ($< 3\%$ distance errors). The programme will also measure the distance to Abell 3558, which lies at the core of the SSC, to ensure that this system itself is at rest in the CMB frame. The local SNIa sample will be substantially improved by the many campaigns that are currently underway or that have been recently commissioned. At low redshifts ($z < 0.1$) notable programmes include: the Nearby Supernova Factory (Aldering et al. 2002), the Carnegie Supernova Project (Hamuy et al. 2006), the SDSS Supernova Survey (Sako et al. 2005), which will use the time domain study of the three-year SDSS extension: the SDSS II, and observations from the upcoming Pan-STARRS observatory (Kaiser et al. 2002). As shown in Fig. 5.7 of Section 5.4.2, current estimates of the peculiar velocities intermediate to the GA and SSC carry a large uncertainty. However, generally they are all positive indicating a large streaming motion into the SSC. The surveys described here will place a firm limit on the magnitude of this flow.

As this thesis demonstrates, peculiar velocity studies are a fundamental tool for analysing local dynamics and provide an important independent check of cosmological models. With the wealth of new data soon to become available, which promise measurements of greater accuracy over larger and deeper areas of the sky, the analysis of peculiar velocities will continue to produce significant results for the foreseeable future.

A

Appendix A

A.1 GA Redshifts

Table A.1 lists the redshifts measured for each galaxy in the 2dF observations taken during the 2004 and 2005 runs (see Chapter 2). Both heliocentric absorption and emission redshifts are listed where measured. Column 1 lists the galaxy identification. The 2MASS XSC name is given first and then the equivalent NED identification. J2000 equatorial coordinates are listed as either part of the name of the target or after the colon in the first column. The 2MASS *J*-band magnitude ($j_{\mathrm{m,ext}}$), extrapolated from a fit to the radial surface brightness profile, is listed in column 2 where available. Columns 3 and 4 list the heliocentric velocities (cz km s^{-1}) identified through absorption and emission features respectively. The uncertainty on each measurement is ± 85 km s^{-1}.

TABLE A.1: The heliocentric absorption and emission redshifts from the 2004 and 2005 2dF observations.

Galaxy ID (1)	J_{ext} mag (2)	cz_{ab} km s^{-1} (3)	cz_{em} km s^{-1} (4)	Field (5)
2MASX J13184671-5804502	13		14774	1
2MASX J13190643-5744311	12.38	5552	5507	1
2MASX J13200919-5725561	12.15	4578		1
2MASX J13203723-5752421	11.57	5469		1
2MASX J13211580-5827564	12.71	6155		1
2MASX J13212199-5718084	14.11	6949	6835	1
2MASX J13220594-5728001	12.15	5706		1
2MASX J13230235-5732041	12.15	5204		1
2MASX J13230489-5740301	12.38	5841	5798	1
2MASX J13231390-5709190	12.28	5763		1
2MASX J13232993-5744020	13.22	6068		1
NNSW 71:13233545-5747204			32701	1
2MASX J13233881-5807500	12.19	5444		1
2MASX J13234325-5731460	13.2	6433		1
2MASX J13234503-5742550	12.65	4426		1
2MASX J13235263-5723200	12.29	5967	5870	1
WKK 2178:13235366-5818428			5087	1
WKK 2182:13240144-5734210		5262		1
2MASX J13242177-5738490	13.85	5766		1
2MASX J13244117-5732569	12.51	4968		1
2MASX J13244654-5736319	10.44	5585		1
2MASX J13245486-5735398	12.42	4890		1
2MASX J13250459-5738403	12.69	4689		1
2MASX J13250572-5737143	12.51	5834		1
2MASX J13250717-5745113	12.73	5789		1
NNSW 50:13252059-5730047			16228	1
2MASX J13252907-5727053	11.86	7073		1
2MASX J13254906-5743092	13.64	4470	4365	1
2MASX J13260043-5740003	12.03	5036		1
2MASX J13261497-5806323	12.17	4967		1
2MASX J13263637-5745282	13.26	5732		1
2MASX J13263819-5705182	11.93	4823		1
2MASX J13264631-5758563	12.3	5982		1
2MASX J13272018-5752081	13.61	5339		1
2MASX J13272377-5729221	10.77		2932	1
2MASX J13272507-5820282	13.94	20638		1
2MASX J13274196-5728413	12.6		2992	1
2MASX J13274357-5730323	11.01	5756	5942	1
2MASX J13274939-5724013	12.35	5837		1
2MASX J13283697-5742188	11.35	5669		1
2MASX J13284958-5803228	14.02	14836	14933	1
2MASX J13291753-5756032	12.23	5477		1
2MASX J13295273-5732075	12.89		5705	1
2MASX J13310962-5809453	12.41	5612		1
2MASX J13313318-5750054	11.75	5955	5897	1
2MASX J13314368-5753125	11.67	4910		1
2MASX J13050567-5728451	11.55	5609		2
ESO 173-IG 005 NED01 :13061154-5733565		5942	5903	2
2MASX J13061289-5733224	11.31	6005	5924	2
2MASX J13065556-5710282	13.11	6559		2
2MASX J13065989-5724502	14.03	6325		2
2MASX J13070255-5714292	11.69	5792		2
2MASX J13070563-5713192	13.26	5390		2
2MASX J13071191-5712362	12.66	5465		2
2MASX J13072260-5706182	12.26	6230	6158	2
2MASX J13072549-5721072	13.72	13168		2
2MASX J13073500-5756199	14.15	6965		2
2MASX J13073640-5704259	11.81	6164		2
WKK 1838:13074815-5758548		6428	6574	2
2MASX J13080179-5703331	12.94	6350	6368	2
2MASX J13081287-5744181	11.9	5693		2
2MASX J13081875-5727300	11.6	6611	6541	2
2MASX J13084186-5735125	11.87	6785	6727	2
2MASX J13093047-5728160	12.31	5559	5666	2
2MASX J13094238-5757380	13.5	11497		2
2MASX J13094664-5753480	12.68	6616		2
2MASX J13100209-5755579	12.69	5675		2
2MASX J13101786-5753551	13.66	6694		2
2MASX J13103369-5800211	10.3	6815		2
2MASX J13104152-5805140	13.25	7265		2
WKK 1913:13104279-5800259			7084	2
2MASX J13104702-5746550	11.38	7438		2
2MASX J13104793-5712300	14.19	6991	6919	2
2MASX J13105161-5804479	13.55	6746		2
2MASX J13105208-5730499	14.37	20125	20167	2
2MASX J13110442-5816311	12.65		6242	2
2MASX J13112359-5755471	13.82	7120		2
2MASX J13113052-5829380	13	6034		2
2MASX J13113584-5749580	14.04		21909	2
2MASX J13114089-5822589	13.21		5645	2
2MASX J13114206-5756209	13.85	7211	7066	2
2MASX J13115832-5831276	11.39	5969		2
2MASX J13121225-5644426	12.73	5903		2
2MASX J13122869-5829295	12.61	5700		2
2MASX J13123436-5841229	12.81		5696	2
2MASX J13123816-5703449	12.86	6002	5630	2
2MASX J13132590-5716339	11.53	5507		2
2MASX J13132929-5653149	12.73	15602		2
2MASX J13134467-5650370	13.48	15932		2
2MASX J13134887-5751130	12.39	14953		2
2MASX J13135030-5703310	12.66	16001		2
2MASX J13140807-5832409	10.17	6070		2
2MASX J13141383-5705024	14.23	15551		2
2MASX J13153032-5744576	13.26	15646		2
2MASX J13153169-5745396	13.91		16099	2
2MASX J13161518-5804189	13.18		7015	2
2MASX J13163978-5721058	14.2	15217		2
2MASX J13000648-5559106	12.76	4341	4233	3
2MASX J13005400-5619006	13.53	28249		3
2MASX J13013391-5548542	12.82	12727	12558	3
2MASX J13014454-5628252	13.49	6220	6104	3
2MASX J13022290-5617338	11.95	6106	5957	3
2MASX J13022796-5557018	12.24	6212	6155	3
2MASX J13023042-5610258	13.94		6703	3
2MASX J13024707-5618083	14.72	40118		3
2MASX J13030832-5553204	13.98	28309		3
2MASX J13031885-5629193	14.19	28691		3
2MASX J13033457-5626380	13.43	28513		3
WKK 1723:13033485-5627234		13032	13122	3
2MASX J13034612-5538011	14.82		28390	3
2MASX J13040292-5632131	14.28	15296	15220	3
2MASX J13042657-5552432	14.42	28597		3
WKK 1746:13042964-5445475			6805	3
2MASX J13051416-5459342	13.04	16201		3
2MASX J13055018-5458363	13.41	15803		3
2MASX J13060232-5545294	12.9	15367		3
2MASX J13061860-5447035	13.07	14963		3
2MASX J13061878-5548255	14.35		15535	3
2MASX J13061963-5451005	12.54	15601		3
2MASX J13071466-5546353	12.02	6034		3
2MASX J13072063-5606592	11.73	6773		3
2MASX J13072237-5628572	13.35		6125	3
2MASX J13072246-5454062	13.38	15778		3
WKK 1841:13075141-5447010			6065	3
2MASX J13075558-5613271	12.05	6941		3
2MASX J13081504-5444241	13.81	2650	2470	3
2MASX J13082983-5605164	13.66	17961		3
2MASX J13083000-5622294	13.22	12492		3
WKK 1861:13083669-5525401			4170	3
WKK 1870:13090166-5452394		15749	15670	3
2MASX J13090197-5522365	14.65	35151		3
2MASX J13092252-5622009	12.93	7040	7015	3
2MASX J13095912-5500489	13.44	28319		3
2MASX J13100554-5625400	14.25	28138		3
2MASX J13102285-5535091	14.8		28402	3
2MASX J13102663-5541471	12.81	6071	5996	3
2MASX J13122797-5608355	13.01	15158		3
2MASX J12561209-5304007	13.61	6784	6691	4
2MASX J12565064-5329137	13.11	15508		4
2MASX J12565266-5325237	12.79	8266	8397	4
2MASX J12571489-5359011	14.47	10313	10241	4
2MASX J12573200-5318284	14.16		8139	4
2MASX J12573511-5329084	13.58	22610		4
2MASX J12574048-5323324	11.54	6821	6784	4
2MASX J12574464-5333574	13.32	22670		4
2MASX J12574578-5255544	14.54	31145		4
2MASX J12575441-5334043	13.12	21774		4
2MASX J12575465-5300093	13.51	22320		4
2MASX J12575566-5319073	12.54	8361		4
2MASX J12581003-5343113	14.17	18779	18731	4
2MASX J12581717-5323314	14.51	15910	15796	4
2MASX J12582365-5242084	14.18	35046		4
2MASX J12582638-5356474	15.15	42531		4
2MASX J12583902-5236413	14.56	36799		4
2MASX J12585825-5323274	13.72	15569		4
2MASX J12590005-5318494	14.56	48354		4
2MASX J12590091-5247534	15.25	28118		4
2MASX J12590259-5333504	14.59	8619	8292	4
2MASX J12592373-5304275	13.53		8496	4
2MASX J12592960-5408226	13.73		9440	4
2MASX J12593882-5304297	13.13	8410		4
2MASX J12594080-5333167	13.04	8224		4
2MASX J12594372-5350016	12.31	6857		4
2MASX J12595349-5309386	15.24	22457		4
2MASX J12595823-5357296	14.63	26417		4
2MASX J12595875-5314326	13.79	8328		4
2MASX J12595882-5308406	14.28	21929		4
WKK 1647:13001193-5405586			9542	4
WKK 1656:13003749-5403580			7986	4
WKK 1658:13003919-5351529		7030	6820	4

2MASX J13003966-5229495	14.48	23534		4
WKK 1663:13004478-5352332		34386		4
WKK 1664:13005184-5357486		47340		4
2MASX J13010923-5354273	14.82	34509		4
2MASX J13010950-5321372	13.58		5372	4
WKK 1672:13011082-5315022		28295		4
2MASX J13013373-5316277	12.44	6892	6838	4
WKK 1684:13014279-5327238		5103	4947	4
2MASX J13014757-5405321	12.79	8106	7930	4
2MASX J13015369-5335048	13.94	30196		4
2MASX J13015425-5322428	14.82	15955	15901	4
2MASX J13021353-5316137	14.81	30372		4
2MASX J13021496-5340067	13.64	6874	6823	4
2MASX J13022273-5258475	15.02	54059		4
2MASX J13023757-5228586	14.56	14795	14666	4
2MASX J13024671-5246235	14.62	38538	38415	4
2MASX J13025812-5240255	14.34	6338	6269	4
2MASX J13030084-5344460	14.56	30249		4
2MASX J13030653-5354054	13.77	21117	20908	4
WKK 1717:13032059-5411550			8031	4
2MASX J13033034-5417419	14.83	34506		4
2MASX J13033047-5247151	13.26	8220	8109	4
WKK 1720:13033161-5401019		30168		4
2MASX J13033543-5305280	11.38	6959		4
2MASX J13035274-5259072	12.93	5334		4
2MASX J13040197-5341132	15.11	41015		4
WKK 1738:13040218-5253506		5267		4
WKK 1740:13040409-5302431		6793	6697	4
2MASX J13041650-5245252	13.95	30848		4
2MASX J13042289-5403331	14.42	15734		4
2MASX J13042309-5334222	15.21	30204		4
2MASX J13042393-5325152	15.01	32986		4
2MASX J13043555-5352562	14.69	29955		4
WKK 1753:13044176-5259532		8874	8688	4
2MASX J13044754-5405243	13.78	14917		4
WKK 1756:13045861-5334199		6323	6284	4
2MASX J13050206-5300473	14.24	26154		4
2MASX J13051021-5415442	13.11	6868	6850	4
2MASX J13052075-5327332	14.37	20913		4
2MASX J13052414-5413403	14.75	9405	9366	4
2MASX J13054189-5236271	14.53	41734		4
2MASX J13054239-5247492	14.98	28496		4
2MASX J13062873-5326202	14.52	30211		4
2MASX J13063657-5312541	14.97	36598		4
2MASX J13063867-5337121	14.99	30132		4
2MASX J13065084-5304525	12.73	8662		4
WKK 1815:13065903-5307059		8803		4
2MASX J13071779-5407352	12.11	7849	7777	4
2MASX J13072254-5312184	15.03	33525		4
2MASX J13074605-5328091	12.78	7924		4
2MASX J13080154-5332380	15	39290		4
2MASX J13082592-5313044	14.86	20911		4
2MASX J13084897-5314063	14.49	20703		4
2MASX J13084929-5315173	14.04	11980	11977	4
KKOWA 22:13442561-5911539			11707	5
KKOWA 23:13442949-5949458			12402	5
PKS 1343-601:13464902-6024299			4065	5
NWN2004 45:13473600-6037041			3861	5
NWN2004 51:13482741-6011481			3571	5
2MASX J10375981-4654084	13.64	14885		6
2MASX J10380212-4701321	14.02	14546		6
2MASX J10381748-4656501	14.68		14723	6
2MASX J10382421-4655121	12.59	14583		6
2MASX J10382630-4621432	13.89	28855		6
2MASX J10384623-4712365	13.55	17721	17613	6
2MASX J10385205-4616165	14.99	6628	6532	6
2MASX J10385263-4702245	14.47	36195		6
2MASX J10385456-4614375	14.89	23195	22976	6
2MASX J10390249-4640225	14.5	12295	12115	6
2MASX J10390858-4630195	11.27	5760		6
2MASX J10391121-4608275	10.56	6122		6
2MASX J10392152-4658445	14.62	25521	25371	6
2MASX J10393158-4705066	13.85	23969	23834	6
2MASX J10394007-4617296	12.16	6623	6511	6
2MASX J10394057-4652566	12.16	6584	6491	6
2MASX J10394256-4604446	13.54	17509		6
2MASX J10394257-4612106	12.22	7076		6
2MASX J10394297-4620186	11.57	6458		6
2MASX J10394493-4632546	13.57	6733	6577	6
2MASX J10394671-4608396	14.08	6485		6
2MASX J10394697-4712376	14.08	33856	33790	6
2MASX J10395413-4631346	14.28	6899		6
2MASX J10395899-4611263	11.39	6734		6
2MASX J10400161-4609063	12.08	5835		6
2MASX J10400182-4623053	12.82	5966		6
2MASX J10400307-4605033	14.36		23396	6
2MASX J10400604-4606564	11.11	6683	6526	6
2MASX J10401088-4706274	13.3		3097	6
LEDA 101362:10401200-4620341		6014		6
2MASX J10401480-4602504	13.95	23624	23594	6
2MASX J10401706-4657344	14.12	24134	23980	6
2MASX J10402231-4625264	11.44	7301	7237	6
2MASX J10402435-4634264	13.95	7186		6
2MASX J10402524-4737554	12.36	14159		6
2MASX J10402884-4608494	14.05	6380	6218	6
2MASX J10402999-4737514	14.24	29197	29008	6
2MASX J10403318-4611274	10.61	6818	6664	6
2MASX J10403327-4610394	13.09	6392		6
2MASX J10403606-4609123	14.39		15316	6
2MASX J10403861-4619003	11.47	6901	6835	6
2MASX J10403900-4557543	15.07	23720	23675	6
2MASX J10404206-4710253	14.88	14618	14432	6
2MASX J10405189-4649454	13.86	14196	13958	6
2MASX J10405300-4605334	12.18	6725		6
2MASX J10405347-4621034	14.84	25681		6
2MASX J10405619-4724364	14.87	70676		6
2MASX J10405925-4606084	14.4	5942	5948	6
2MASX J10405955-4735474	14.16	17418		6
2MASX J10410458-4622083	12.47	6586	6511	6
2MASX J10410483-4641293	14.09	6215	6158	6
2MASX J10410803-4730503	14	13610		6
2MASX J10410981-4708133	14.19	34017		6
2MASX J10411593-4612483	12.65	15242		6
2MASX J10411708-4656463	14.85	5657	5594	6
2MASX J10412347-4624371	13.84	6000	5807	6
2MASX J10412507-4612351	14.4	16972		6
2MASX J10412669-4617141	12.17	6818		6
2MASX J10412828-4734402	14.54	34791		6
2MASX J10412886-4633542	14.87	30953		6
2MASX J10413682-4612162	13.71	7345	7267	6
2MASX J10413886-4735522	13.01	14743		6
2MASX J10414301-4736542	14.01	13865		6
2MASX J10414953-4707541	14.52	48521		6
2MASX J10415251-4608421	13.63	6140	6071	6
2MASX J10420407-4600169	13.94	6215	6188	6
2MASX J10420451-4735469	13.82	14325		6
2MASX J10420567-4742429	14.33	14469		6
2MASX J10420637-4602119	14.29	7234	7201	6
2MASX J10421122-4743369	14.58	13854		6
2MASX J10421647-4740079	14.08	14562		6
2MASX J10423070-4734209	14.28	13925		6
2MASX J10423383-4602254	14.65	15379	15400	6
2MASX J10423402-4630334	15.21	36030		6
2MASX J10423443-4738584	13.86	15335		6
2MASX J10423775-4547564	12.98	6497	6437	6
2MASX J10424010-4732434	14.31	14217		6
2MASX J10424170-4605004	12.93	6622		6
2MASX J10424726-4716495	13.37	14406		6
2MASX J10424891-4725585	14.61	44793		6
2MASX J10425136-4731445	13.89	13617	13452	6
2MASX J10425171-4551025	12.6	6725		6
DJRS J10425493-4644593		6272	6200	6
2MASX J10425937-4744495	13.42	12996	12924	6
2MASX J10430767-4612444	10.68	6284	6299	6
2MASX J10430949-4746265	13.81	14423		6
2MASX J10431062-4602324	14.68	39389		6
2MASX J10431466-4606320	12.82	16465		6
2MASX J10431781-4738480	14.3	13796		6
2MASX J10431991-4614360	14.98	33489		6
2MASX J10432155-4659521	15.57	49118		6
2MASX J10432231-4730000	14.62	13352		6
2MASX J10432525-4601261	14.39	16860		6
2MASX J10432628-4720441	12.86	9027	8907	6
2MASX J10432870-4652501	14.97	14480	14483	6
2MASX J10433217-4732381	14.32	13808		6
2MASX J10433916-4551241	15.12	39513		6
2MASX J10434768-4733551	13.29	13530		6
2MASX J10434774-4748551	12.88	13192	13029	6
2MASX J10435309-4619286	15.03	31397		6
2MASX J10435759-4548377	14	17110		6
2MASX J10440053-4618177	14.65	17184		6
2MASX J10440117-4626147	14.72	39300		6
2MASX J10440163-4606267	14.22	16894		6
2MASX J10440231-4658337	15.2	34879		6
2MASX J10440390-4720077	13.57	16363		6
2MASX J10440807-4606247	14.6	16855		6
2MASX J10441016-4749158	14.04	14429		6
2MASX J10441076-4743568	14.31	13207		6
2MASX J10441126-4559087	14.95	48399		6
2MASX J10441188-4709398	15.34	33343		6
2MASX J10441304-4737348	14.21	17518		6
2MASX J10441413-4600308	15.28	48432		6
2MASX J10441750-4741518	15.36	13305	13278	6
2MASX J10442057-4650147	14.5	13755		6
2MASX J10442102-4547517	14.4	33675		6
2MASX J10442131-4634497	14.63	15041	14891	6
2MASX J10443273-4748528	14.86	29317		6
2MASX J10443487-4732016	14.82	17799		6
2MASX J10443591-4548568	14.06	12274		6
2MASX J10444384-4552118	14.18	18624		6
2MASX J10444676-4736039	12.96	6179	6149	6
2MASX J10444679-4643229	14.34	14103		6
2MASX J10445096-4654009	12.22	14196		6
2MASX J10445119-4613489	12.23	6476	6341	6
2MASX J10445165-4637069	14.42	14091	14042	6
2MASX J10445408-4653169	14.58	14336		6
2MASX J10445475-4543449	15.34	42031	41956	6
2MASX J10445969-4626149	11.96	12004	11926	6

2MASX J10450913-4555448	13.74	15470		6
2MASX J10451424-4653035	14.15	4872	4785	6
2MASX J10451434-4635505	15.07	33260		6
2MASX J10452432-4644056	14.84	16615		6
2MASX J10453365-4642446	13.21	16765		6
2MASX J10453647-4640496	13.7	16450	16459	6
2MASX J10454123-4641396	12.82	16633		6
2MASX J10454215-4657016	14.35	21115		6
2MASX J10454298-4740196	12.44	14535		6
2MASX J10454301-4618596	14.09	15194		6
2MASX J10454410-4654446	14.5	21082		6
2MASX J10454638-4639585	14.21	25399		6
2MASX J10455219-4703301	14.77	16510	16567	6
2MASX J10455638-4628132	14.78	54401		6
2MASX J10455981-4705542	14.09	14094		6
2MASX J10460229-4723182	13.91	14274		6
2MASX J10460882-4554453	14.87	33256		6
2MASX J10461088-4701233	14.77	12265	12139	6
2MASX J10461195-4717413	13.27	14015	13931	6
2MASX J10461391-4719273	14.9	13877	13880	6
2MASX J10461893-4624373	14.84	32959		6
2MASX J10462720-4658552	15.02	31106		6
2MASX J10463291-4715148	15.24		36572	6
2MASX J10463983-4705598	14.63	16489	16357	6
2MASX J10464079-4709039	13.75	13959		6
2MASX J10465601-4726289	14.79	52668		6
2MASX J10465869-4736599	13.29	6517	6458	6
2MASX J10470054-4612279	14.6	32500		6
2MASX J10470875-4734371	14.82	14447		6
2MASX J10471092-4730528	14.98	14649	14450	6
2MASX J10471253-4603232	14.28		18695	6
2MASX J10472080-4738092	14.74		11779	6
2MASX J10472663-4616522	14.84	32254		6
2MASX J10473000-4728393	13.94	12210		6
2MASX J10473277-4731243	13.02	12061		6
2MASX J10475444-4605016	14.11	18629	18593	6
2MASX J10480377-4722467	14.7	12654		6
2MASX J10481587-4720547	13.63	12151		6
2MASX J10482162-4703247	14.56	49280		6
2MASX J10482915-4718035	14.06	11044	11011	6
2MASX J10483742-4715536	14.37	12040		6
2MASX J10483830-4718086	11.78	12019		6
2MASX J10484213-4715266	13.5	11800		6
2MASX J10484331-4717196	12.36	12010		6
2MASX J10485137-4715146	14.26	12229		6
2MASX J16302242-6432135	13.55	14255		7
2MASX J16305184-6428445	13.32	15117		7
2MASX J16312630-6404344	12.84	4929		7
2MASX J16312799-6424454	12.77	14975		7
2MASX J16321187-6427406	13.2		15628	7
2MASX J16321925-6454336	13.43	15146		7
2MASX J16322073-6431446	13.36	14928		7
2MASX J16322393-6415446	13.84	15343		7
2MASX J16322669-6447265	12.21	4560	4482	7
2MASX J16324205-6449586	12.1	4321		7
2MASX J16324222-6421365	13.74	13847		7
2MASX J16324380-6432046	14.36	55689		7
2MASX J16324676-6430516	14.53	14724		7
2MASX J16330009-6423056	13.57	14532		7
2MASX J16330840-6419456	13.29	14846		7
2MASX J16332028-6422465	12.82	14808		7
2MASX J16332341-6404035	11.87	15452		7
2MASX J16340379-6358362	12.29	14417		7
2MASX J16341346-6410212	13.16	14574		7
2MASX J16343630-6401505	11.69	14276		7
2MASX J16344621-6504005	12.85	12354	12294	7
2MASX J16344985-6402135	14.19	42548		7
2MASX J16345110-6443555	14.56	50965		7
2MASX J16345277-6418165	14.03	15045		7
2MASX J16345486-6447345	14.64	16779	16749	7
2MASX J16345588-6507585	13.43	17025		7
2MASX J16345747-6509465	14.38		15002	7
2MASX J16345826-6408075	14.56	15560		7
2MASX J16345829-6444505	14.41	18602	18527	7
2MASX J16350287-6450505	12.87	11548		7
2MASX J16351168-6343304	12.66	14937		7
2MASX J16352244-6512023	14.65	17073		7
2MASX J16352688-6437292	13.61	14069		7
2MASX J16352740-6413062	14.07	14559		7
2MASX J16352824-6425561	14.15	14189		7
2MASX J16353032-6359261	12.84	15089		7
2MASX J16353186-6455021	13.53	12744		7
2MASX J16353256-6402561	13.03	15806		7
2MASX J16354868-6410032	14.08	13023		7
2MASX J16354875-6436022	13.86	13491		7
2MASX J16355127-6415062	14.43	16180		7
2MASX J16355265-6420412	13.61	14832		7
2MASX J16355326-6422022	13.81	13997		7
2MASX J16355955-6500012	14.5	15773		7
2MASX J16360409-6403032	13.4	15077		7
2MASX J16360517-6427532	14.36	14400		7
2MASX J16360648-6417322	14.45	15008		7
2MASX J16360711-6418392	13.69	12747	12612	7
2MASX J16361138-6345372	14.45	14000		7
2MASX J16361692-6405341	13.38	12094		7
2MASX J16361882-6356354	13.32	16249		7
2MASX J16362331-6432595	13.41	11944		7
2MASX J16362516-6415446	14.6	46081		7
2MASX J16363054-6426036	12.24	11935	11947	7
2MASX J16363287-6448446	13.85	14003		7
2MASX J16363633-6351146	13.9	13056		7
2MASX J16364538-6424157	14.25	18605	18500	7
2MASX J16364851-6456277	13.68	15541	15379	7
2MASX J16365019-6415357	15.04	46297		7
2MASX J16370506-6435597	14.22	12004	11917	7
2MASX J16370547-6428277	13.33	11551		7
2MASX J16370674-6432047	14.06	13386		7
2MASX J16370677-6355037	14.62	13596		7
2MASX J16371115-6408407	12.44	12891		7
2MASX J16371406-6422036	13.04	13206		7
2MASX J16371456-6347156	14.25	14249		7
2MASX J16371511-6420056	13.65	15388		7
2MASX J16371532-6436466	14.44	13566		7
2MASX J16372963-6434236	12.94	14177		7
2MASX J16373215-6408046	14.01	16123		7
2MASX J16374098-6426126	14.83	45943		7
2MASX J16374299-6425396	14.15	14762		7
2MASX J16374315-6422136	14.19	14312		7
2MASX J16374838-6421006	13.32	14994		7
2MASX J16375253-6448486	11.82	4716	4668	7
2MASX J16375434-6412536	14.23	15727		7
2MASX J16375503-6425046	14.99	13724		7
2MASX J16375521-6342106	14.14	17889	17886	7
2MASX J16375713-6337406	14.02	12996	13065	7
2MASX J16375749-6424096	14.68	15475		7
2MASX J16375844-6426366	14.47	16965		7
2MASX J16375871-6513526	14.39	55439		7
2MASX J16380125-6429415	12.65	15208		7
2MASX J16380531-6419515	13.48	16680		7
2MASX J16380631-6402475	13.78	16348	16225	7
2MASX J16380771-6354025	14.07	18239		7
2MASX J16381375-6443246	14.43	16999		7
2MASX J16381464-6441454	14.59	50743		7
2MASX J16381571-6432484	14.46	16812		7
2MASX J16381810-6421367	10.29	14820		7
2MASX J16382152-6355023	13.77	17778		7
2MASX J16382154-6419147	14.4	17166		7
2MASX J16382418-6436218	14.11	16947	16983	7
2MASX J16382652-6425308	13.1	15553		7
2MASX J16382822-6447078	14.13	16782		7
2MASX J16382903-6422448	14.21	14664		7
2MASX J16382980-6434128	13.91	15512		7
2MASX J16383141-6404128	13.79	15586		7
2MASX J16383302-6423548	13.96	15565		7
2MASX J16383563-6441318	12.98	14357		7
2MASX J16383739-6418569	13.56	17583		7
2MASX J16383836-6450419	14.12	16190		7
2MASX J16383898-6350579	13.54	18503		7
2MASX J16384004-6414029	14.19	13683		7
2MASX J16384034-6436089	12.55	15292		7
2MASX J16384051-6348399	13.45	18755		7
2MASX J16384228-6424159	14.33	14351		7
2MASX J16384815-6420049	13.97	14510		7
2MASX J16385090-6507389	13.51	14726		7
2MASX J16385109-6334469	12.82	14895		7
2MASX J16385138-6426269	13.55	11932		7
2MASX J16385307-6416599	13.02	17514		7
2MASX J16385385-6422269	12.18	17823		7
2MASX J16385560-6444069	14.26	42469		7
2MASX J16385771-6424009	13.63	13844		7
2MASX J16385820-6432039	14.42	14031		7
2MASX J16385933-6407389	13.52	16579		7
2MASX J16390135-6414129	12.31	18755		7
2MASX J16390186-6357069	14.07	15066		7
2MASX J16390277-6505079	11.96	14642		7
2MASX J16390599-6401109	13.39	15277	15259	7
2MASX J16390794-6428488	13.02	15220		7
2MASX J16390811-6430379	13.44	15181		7
2MASX J16391143-6436018	13.57	14783		7
2MASX J16391499-6424232	13.44	17559		7
2MASX J16391842-6422393	13.94	15820		7
2MASX J16392187-6515453	12.78	14285		7
2MASX J16392192-6405533	12.6	14552		7
2MASX J16392237-6426003	13.24	15724		7
2MASX J16392426-6351453	14.12	15622		7
2MASX J16392820-6429044	13.89	13311		7
2MASX J16393023-6427384	14.11	17055		7
2MASX J16393117-6342184	13.61	15074		7
2MASX J16393282-6415484	13.78	16063		7
2MASX J16393323-6420514	13.86	12768		7
2MASX J16393402-6419174	14.96	14693		7
2MASX J16393773-6526384	14.74	35176		7
2MASX J16394030-6424015	13.74	14501		7
2MASX J16394068-6410064	14.82	16066		7
2MASX J16394428-6334325	13.56	14864		7
2MASX J16394908-6324055	13.69	18028		7
2MASX J16395239-6448565	13	14456		7
2MASX J16395779-6433284	12.34	15634		7

2MASX J16395822-6426295	12.34	15886		7
2MASX J16395878-6507344	14.24	13282		7
2MASX J16400078-6356544	13.53	18458	18437	7
2MASX J16400522-6346254	14.23	16234		7
2MASX J16400671-6426074	13.64	18404	18359	7
2MASX J16400953-6429194	13.67	16025		7
2MASX J16401045-6417274	14.32	14327		7
ESO 101-G 006:16401075-6442029		4818	4869	7
2MASX J16401123-6423124	15.21	12833		7
2MASX J16401372-6512215	12.63	15215		7
2MASX J16401501-6510515	14.14	14430		7
2MASX J16401685-6504185	14.69	42283		7
2MASX J16401931-6456555	15.06	61700		7
2MASX J16402063-6438025	14.77	13288		7
2MASX J16402107-6426115	12.8	14366		7
2MASX J16402226-6430505	13.85	13308		7
2MASX J16402364-6358025	13.99	18254		7
2MASX J16402378-6416455	12.65	13644		7
2MASX J16402671-6353496	14.45	50530		7
2MASX J16402891-6523236	14.98	54910		7
2MASX J16403359-6422586	13.93	15742		7
2MASX J16404316-6426056	14.27	14246		7
2MASX J16404330-6418506	14.22	16237		7
2MASX J16404347-6329206	13.92	16662		7
2MASX J16405032-6432586	13.96	16692	16719	7
2MASX J16405179-6502226	14.14	13970		7
2MASX J16405379-6331326	14.13	15211		7
2MASX J16405624-6406485	14.49	14525		7
2MASX J16410127-6451025	14.06	15056	15143	7
2MASX J16410800-6441304	13.85	13695		7
2MASX J16410954-6334024	14.4	17406		7
2MASX J16411277-6446375	14.81	14879		7
2MASX J16411512-6336175	14.96	16372		7
2MASX J16411625-6420403	14.98	12789		7
2MASX J16412547-6336066	13.51	15502		7
2MASX J16412812-6423056	13.89	15907	15814	7
2MASX J16413313-6407146	15.04	26757	26700	7
2MASX J16413684-6454426	13.53	14369	14339	7
2MASX J16413875-6439156	13.24	15442		7
2MASX J16414092-6423526	14.72	14774		7
2MASX J16414967-6509526	12.87	15217		7
2MASX J16415896-6517176	14.57	55103		7
2MASX J16421127-6454096	14.4	13572		7
2MASX J16421263-6337406	14.09	15742		7
2MASX J16421696-6451286	14.12	30225		7
2MASX J16422130-6419137	14.23	12672	12567	7
2MASX J16422149-6453427	12.76	13311	13200	7
2MASX J16423019-6435247	14.87	32021		7
2MASX J16423123-6340207	13.58	14088		7
2MASX J16423454-6336047	13.98	27479		7
2MASX J16423718-6440187	14.12	13932		7
2MASX J16423721-6455187	13.85	30000		7
2MASX J16424223-6419437	13.71	13922		7
2MASX J16424238-6452447	12.74	13901		7
2MASX J16424389-6508437	14.68	30207	30045	7
2MASX J16424551-6450297	13.1	14282		7
2MASX J16425047-6412407	14.19	13224		7
2MASX J16425061-6458347	13.88	14906		7
2MASX J16430569-6520305	14.76	32360	32372	7
2MASX J16430963-6439215	14.99	13985	13847	7
2MASX J16431008-6449435	13.94	15053		7
2MASX J16431193-6451525	14.85	15334	15376	7
2MASX J16432908-6442446	14.02	15214	14996	7
2MASX J16433125-6448176	13.22	14363		7
2MASX J16433871-6417046	13.39	14199		7
2MASX J16434951-6458566	14.04	15180		7
2MASX J16440342-6452085	14.71	15159		7
2MASX J16440903-6405072	14.18		15280	7
2MASX J16440927-6454422	11.73	14903		7
2MASX J16441142-6343242	14.63	35148		7
2MASX J16441506-6457302	13.15	14793		7
2MASX J16441969-6427552	13.76	15976		7
2MASX J16443025-6338313	13.39	14633		7
2MASX J16443097-6450403	14.54	14957		7
2MASX J16443616-6456522	14.46	14594		7
2MASX J16443714-6419492	14.1	15356		7
2MASX J16443748-6429403	14.95		12846	7
2MASX J16444315-6504382	15.6	28183		7
2MASX J16444523-6411062	14.3	13812		7
2MASX J16444633-6506322	13.2	15244	15169	7
2MASX J16450187-6425371	14.52		12993	7
2MASX J16450708-6422431	13.19	15904		7
2MASX J16450855-6346291	14.59	16330		7
2MASX J16450942-6442081	14.48	17868	17847	7
2MASX J16453329-6503392	14.93	13892	13829	7
2MASX J16454941-6503242	13.67	15147		7
2MASX J16460075-6432481	13.18	12966		7
2MASX J16461193-6503510	13.68	15080		7
2MASX J16461487-6433050	13.81	13044		7
2MASX J16462943-6410571	13.09	16794		7
2MASX J16464768-6413460	14.8	15976	15967	7
2MASX J16470700-6415322	14.74	14942	14966	7
2MASX J16470756-6408402	14.24	14816		7
2MASX J16471075-6449232	13.51	14786		7
2MASX J16471156-6433423	14.02	15245		7
2MASX J16472145-6411593	14.4	16342		7
2MASX J16472259-6431003	13.98	15781	15838	7
2MASX J16472312-6415523	13.89	16728		7
2MASX J16473095-6423283	14.24	15991		7
2MASX J16474214-6413573	14.65	16226		7
2MASX J16475085-6447163	14.44	16462		7
2MASX J16480144-6359404	13.56	27641		7
2MASX J16480964-6415525	14.06	27563		7
2MASX J16481432-6448245	14.63	14753	14693	7
2MASX J16484077-6410355	14.61	16755	16791	7
2MASX J16485767-6409143	15.04	14516		7
2MASX J16491562-6423124	12.77	14631		7
2MASX J16492348-6426515	13.03	15757		7
2MASX J16493504-6421185	14.29	22228		7
WKK 7356:16440046-5923240		25578	25401	8
2MASX J16440307-6018411	14.15	22023		8
2MASX J16440985-5919172	14.23	15982		8
2MASX J16441346-5938432	14.77	15949	15760	8
2MASX J16441583-6022062	13.69	20994		8
WKK 7368:16442141-5943221		15826	15868	8
WKK 7373:16442755-5921119		16540	16588	8
2MASX J16444082-5931401	14.46	15947	15955	8
WKK 7380:16444466-6018551		46165		8
2MASX J16450199-5915211	13.27	15961		8
2MASX J16450562-5923011	14.09	28930		8
WKK 7398:16451181-5905082		14375	14528	8
2MASX J16452304-5904251	14.06	28753		8
2MASX J16454092-5922287	13.94	16686		8
WKK 7410:16454551-6032211		15400	15337	8
2MASX J16454899-6028482	14.68	45428		8
2MASX J16455009-5958561	14.28	26828		8
WKK 7415:16455448-5915065		16369		8
2MASX J16461423-5914338	14.12	15913		8
2MASX J16462062-6021281	15.05	43506		8
WKK 7437:16464087-5915245			15604	8
2MASX J16464764-6027260	15.4	45347		8
2MASX J16471814-6001383	14.98	30817	30720	8
WKK 7495:16484206-5910372		36245		8
WKK 7526:16492809-5844071			13916	8
WKK 7532:16494999-5959161		15589		8
2MASX J16500868-5915398	14.75	34950		8
2MASX J16501298-5913438	14.71	28678		8
WKK 7546:16502100-5847398			13859	8
2MASX J16502941-5915087	14.33	31370		8
WKK 7555:16503804-5958473			13416	8
2MASX J16505812-6023452	15.53	14045		8
WKK 7568:16510142-6003410		14366	14300	8
WKK 7584:16511723-5954284			12552	8
WKK 7594:16513109-5915292		2713		8
2MASX J16520500-5843522	13.68	20791		8
2MASX J16520512-5921141	14.15	13922		8
WKK 7636:16523396-6006306		15347		8
2MASX J16524102-5922041	14.66	14684		8
2MASX J16530327-5944150	13.56	13781		8
2MASX J16530885-5903050	13.35	17853	17784	8
2MASX J16531557-5946041	13.02	14126		8
WKK 7676:16532688-5923002		48111		8
2MASX J16551888-6033585	15.65	62777		8
WKK 7745:16555148-5923092		26960	26906	8
2MASX J16591630-5953080	14.72	28107	28010	8
2MASX J13511382-4725138	14.48	21288		9
2MASX J13512051-4726269	14.01	11203		9
2MASX J13513856-4728579	14.42	21450	21357	9
2MASX J13513977-4741539	14.63	49553	49334	9
2MASX J13514976-4721349	15.19	47349	47187	9
2MASX J13520456-4801457	13.92	10070	9968	9
2MASX J13520615-4731179	15.03	36656	36449	9
2MASX J13521761-4758399	14.09	28933		9
2MASX J13522054-4709559	14.71	21330	21288	9
2MASX J13522862-4721119	14.96	29137		9
2MASX J13525793-4751401	13.56	14570		9
2MASX J13530963-4706200	14.67	21948	21951	9
2MASX J13532853-4802098	14.45	27177		9
2MASX J13533327-4652043	15.62	33004		9
2MASX J13533825-4703413	14.99	29023		9
2MASX J13534137-4658532	12.8	14555		9
2MASX J13534631-4646322	15.88	42113	42007	9
2MASX J13534899-4657112	15.18	21396		9
2MASX J13535705-4706066	16.34	35835	35783	9
2MASX J13540335-4722027	13.15	14735		9
2MASX J13540619-4654177	14.47	14993	14939	9
2MASX J13541059-4756387	14.79	48515		9
2MASX J13541064-4716437	14.93	9890	9863	9
2MASX J13541079-4647157	14.94	42715	42651	9
2MASX J13541949-4720257	12.94	14462		9
2MASX J13542648-4653357	14.31	20386	20329	9
2MASX J13543019-4734176	14.14	21927	21891	9
2MASX J13543975-4734019	14.35	21750		9
2MASX J13544147-4722219	14.13	20365		9
2MASX J13544754-4815134	14.55	22053	21984	9
2MASX J13550076-4646119	14.4	20522		9
2MASX J13550183-4802464	13.25	6650	6676	9
2MASX J13550625-4715238	14.35	21864	21894	9

2MASX J13550640-4706198	14.63	28687	28585	9
2MASX J13550960-4736038	14.52	21507		9
2MASX J13551386-4715098	14.59	22107		9
2MASX J13551712-4748518	13.92	21876	21912	9
2MASX J13551728-4738088	14.8	45616		9
2MASX J13552148-4700078	14.81	35891		9
2MASX J13552243-4640469	14.14	20647		9
2MASX J13552248-4721429	15.05	20083		9
2MASX J13552259-4824489	14.5	31292		9
2MASX J13552749-4638509	15.05	20606	20542	9
2MASX J13552867-4725039	14.36	20536	20494	9
2MASX J13553340-4734199	14.65	21762		9
2MASX J13553765-4757310	14.06	22317		9
2MASX J13553953-4736479	14.22	19987		9
2MASX J13553953-4735509	14.51	20899		9
2MASX J13554178-4828190	13.05	23264		9
2MASX J13554613-4729219	14.23	21456		9
2MASX J13554662-4704178	14.04	21681	21645	9
2MASX J13555029-4732408	13.43	21015		9
2MASX J13555289-4738538	14.41	20890		9
2MASX J13555439-4725478	15.04	22784	22697	9
2MASX J13555600-4731339	13.7	19666		9
2MASX J13555601-4727559	14.02	21369		9
2MASX J13555803-4741199	15.33	21987	21897	9
2MASX J13555889-4723069	14.72	42319		9
2MASX J13555979-4718459	13.49	19894		9
2MASX J13560005-4730249	14.52	22508	22409	9
2MASX J13560262-4649049	15.15	42262		9
2MASX J13560419-4731119	13.45	22227		9
2MASX J13560499-4632439	14.6	43629		9
2MASX J13560578-4727179	14.79	21078		9
2MASX J13560609-4716039	14.18	11053	11089	9
2MASX J13560885-4655209	13.8	21789		9
2MASX J13561315-4656009	14.39	21789	21777	9
2MASX J13561921-4804229	14.39	22320		9
2MASX J13562387-4739219	14.98	21402	21330	9
2MASX J13562884-4726560	14.85	21219		9
2MASX J13562982-4707348	13.88	20575	20524	9
2MASX J13563050-4651178	14.74	28880	28834	9
2MASX J13563363-4714330	14.52	20515		9
DENIS J135635.5-472127		21753	21606	9
2MASX J13564496-4756381	13.24	22583		9
2MASX J13564496-4829501	12.82	2842	2845	9
2MASX J13564622-4654131	14.65	42753		9
2MASX J13564654-4835042	14.9	31748		9
2MASX J13565037-4814422	14.44	45086		9
DENIS J135650.4-472112		20737		9
2MASX J13565832-4729231	13.12	22565		9
2MASX J13565932-4732581	14.64	20569		9
2MASX J13570098-4727191	14.73	22353		9
2MASX J13570447-4735400	13.93	22658		9
DENIS J135705.6-471502		20560	20647	9
2MASX J13570682-4732210	13.8	22598		9
2MASX J13570691-4636490	13.94	21603		9
2MASX J13570862-4646270	14.71	28931	28858	9
2MASX J13570940-4822143	15.44	45065		9
2MASX J13570985-4641330	15.06	27974	27947	9
2MASX J13571353-4751449	14.7	26996		9
2MASX J13572049-4715200	14.68	14678	14447	9
2MASX J13572077-4719190	13.42	14585		9
2MASX J13572096-4721220	14.29	14388		9
2MASX J13572215-4759180	14.41	21774		9
2MASX J13572273-4637290	14.32	38340		9
2MASX J13572616-4736570	14.65	21549		9
2MASX J13572736-4724550	14.8	20759		9
2MASX J13572774-4740570	13.98	20581		9
2MASX J13572824-4730440	14.43	21003		9
2MASX J13572883-4735360	14.44	23129		9
2MASX J13573050-4654430	14.68	21537		9
2MASX J13573208-4830543	14.06	8332	8247	9
ESO 271-G 007:13573307-4716368		1361	1424	9
2MASX J13573527-4740360	14.77	21753		9
2MASX J13574114-4746549	14.11	23138		9
2MASX J13574328-4809563	13.89	22053		9
2MASX J13574734-4721379	14.45	20416	20362	9
2MASX J13574749-4739052	15.12	22553		9
2MASX J13575210-4708453	14.79	27674		9
2MASX J13575339-4726243	14.44	20707		9
2MASX J13575367-4751093	14.42	22113		9
2MASX J13575381-4743113	14.45	20110		9
2MASX J13575383-4737543	12.23	8376	8226	9
2MASX J13575662-4732163	15.05	38481		9
2MASX J13575853-4755093	15.18	22667		9
2MASX J13575916-4743063	13.49	21042		9
2MASX J13580047-4735273	14.7	19999		9
2MASX J13580659-4737383	15.01	23054		9
2MASX J13580789-4648193	15.3	52662		9
2MASX J13580947-4745213	14.39	22463		9
2MASX J13581085-4741243	13.48	21267		9
2MASX J13581294-4748183	14.86	20026		9
2MASX J13581342-4740223	14.1	20281		9
2MASX J13581945-4737263	15.15	22913		9
2MASX J13582304-4828339	12.11	2803		9
2MASX J13582312-4739073	14.9	20776		9
2MASX J13582501-4741103	14.28	20617		9
2MASX J13582552-4724503	15.1	37337	37204	9
2MASX J13582972-4718181	15.17	42454		9
2MASX J13582979-4817060	14.81	21408		9
2MASX J13582979-4730482	13.84	21816		9
2MASX J13583199-4801390	14.4	24199	24001	9
2MASX J13583349-4736342	13.67	21666		9
2MASX J13583400-4831300	11.38	2581	2545	9
2MASX J13583466-4735402	14.71	19915		9
2MASX J13583527-4731472	14.96	42499		9
2MASX J13583615-4735022	14.97	22571		9
2MASX J13583807-4752552	14.54	23117		9
2MASX J13583839-4637282	14.4	27738		9
2MASX J13583908-4747232	13.87	19529		9
2MASX J13584085-4709242	14.87	51819		9
2MASX J13584106-4802399	14.57	24409	24241	9
2MASX J13584125-4706192	15	30702		9
2MASX J13584264-4758162	14.77	21759		9
2MASX J13584294-4756242	14.95	38619	38652	9
2MASX J13584525-4729212	15.72	100362		9
2MASX J13584534-4739472	14.85	20077		9
2MASX J13584594-4717582	14.65	20803	20827	9
2MASX J13584702-4725572	14.22		20548	9
2MASX J13584865-4804529	14.72	37606		9
2MASX J13584919-4727162	14.15	20788		9
2MASX J13584949-4731032	15.63	37375		9
2MASX J13585308-4752092	14.43	22149		9
2MASX J13585544-4742002	15.04	21270	21126	9
2MASX J13585706-4648322	15.38	55827		9
2MASX J13585809-4734492	15.45	21594		9
2MASX J13590256-4718122	14.88	45491		9
2MASX J13590734-4744311	13.7	20077		9
2MASX J13590742-4724501	14.69	20719		9
2MASX J13590806-4747531	14.81	19987		9
2MASX J13590855-4802203	14.56	11104		9
2MASX J13590858-4736571	14.19	22167		9
2MASX J13590932-4743051	14.4	20083		9
2MASX J13590933-4716361	13.63	20926		9
2MASX J13591028-4739281	14.11	20026		9
2MASX J13591330-4742282	14.36	19609		9
2MASX J13591461-4734422	14.57	37528		9
2MASX J13591806-4738293	13.4	20611		9
2MASX J13591841-4640293	14.03	28699		9
2MASX J13591961-4752293	14.47	22523		9
2MASX J13592419-4750253	13.74	21756		9
2MASX J13592459-4741553	14.76	20686		9
2MASX J13592518-4749333	14.69	22802		9
2MASX J13592519-4720263	14.23	21513	21393	9
2MASX J13592667-4755403	14.5	22194		9
2MASX J13592976-4757043	13.13	23258		9
2MASX J13592979-4657033	14.8	42544		9
2MASX J13593381-4744533	14.66	22038		9
2MASX J13593815-4739473	14.47	20191		9
2MASX J13593870-4753472	13.7	22478		9
2MASX J13594246-4748582	14.02	20224		9
2MASX J13594612-4715342	14.48	20470	20560	9
2MASX J13594797-4712552	15.16		20623	9
2MASX J13594822-4710249	14.79	20911	20857	9
2MASX J13595922-4805486	14.15	15775	15667	9
2MASX J13595964-4752350	14.94	19391	19376	9
2MASX J13595983-4809036	14.14	21204		9
2MASX J14000383-4746160	14.95	20065		9
2MASX J14000620-4803446	14.1	23630	23567	9
2MASX J14000978-4800375	14.11	22535		9
2MASX J14001166-4816115	11.24		2890	9
2MASX J14001246-4749190	14.35	20902	20875	9
2MASX J14001325-4736270	14.73	20716	20656	9
2MASX J14001356-4753440	14.16	23938		9
2MASX J14001563-4739190	14.37	20415	20428	9
2MASX J14001628-4804415	12.9	21513		9
2MASX J14001692-4812053	14.4	21360	21267	9
2MASX J14002381-4707110	14.76	36248	36035	9
2MASX J14002814-4808374	14.14	21471		9
2MASX J14002823-4812124	14.88	21552		9
2MASX J14003203-4811114	14.25	22877		9
2MASX J14003364-4712418	14.38	51504		9
2MASX J14003648-4755338	15.09	21367		9
2MASX J14004272-4804474	13.02	21615		9
2MASX J14004414-4722498	14.49	21285		9
SUMSS J140050-473147		49681	49571	9
2MASX J14010360-4749058	14.7	22709		9
2MASX J14010383-4759110	14.15	22218		9
2MASX J14011047-4718570	13.51	21582		9
2MASX J14011708-4744310	14.61	20167	20143	9
2MASX J14012205-4736491	14.73	21573		9
2MASX J14012817-4724331	14.16	22014	21921	9
2MASX J14013200-4714081	14.17	42607		9
2MASX J14013280-4722351	13.37	21882		9
2MASX J14013303-4645581	14.54	18281	18491	9
2MASX J14013861-4748420	14.33	18203	18101	9
2MASX J14015200-4720140	15.26	21030	20923	9
2MASX J14015260-4811589	15.05	21525	21468	9
2MASX J14020666-4726250	13.97	22038	21990	9
2MASX J14021992-4715160	14.24	22014	21939	9

2MASX J14022719-4737150	14.19	21597		9
2MASX J14025072-4727261	14.64	20983		9
2MASX J14025747-4740390	14.32	21558		9
2MASX J14030895-4716596	14.15	21636		9
2MASX J15092922-4511561	13.5	18018	18003	10
2MASX J15094610-4611474	14.43		36491	10
2MASX J15095136-4523214	13.62	16942		10
2MASX J15095307-4507444	14.35	17107		10
2MASX J15100336-4538404	13.78	20062	20017	10
2MASX J15100752-4556574	14.65	23129	23129	10
2MASX J15101142-4512324	13.03	10367		10
2MASX J15101697-4534493	14.88		16932	10
2MASX J15101819-4532343	13.6	16313		10
2MASX J15101824-4526343	13.38	16806		10
2MASX J15102166-4514426	13.69	10367		10
2MASX J15102888-4505436	14.34	10283		10
2MASX J15102965-4624316	14.26	20812		10
2MASX J15103402-4601166	14.19	16681		10
2MASX J15104016-4551086	15.36	34533		10
2MASX J15104065-4559386	12.95	15295		10
2MASX J15104087-4624546	14.44	20629	20638	10
2MASX J15104366-4616456	13.72	20755		10
2MASX J15104553-4515586	14.18	10577		10
2MASX J15104966-4505226	12.72	10538	10472	10
2MASX J15105537-4515286	14.83	16830	16896	10
2MASX J15110577-4508335	14.31	16740		10
2MASX J15110637-4618205	14.65	20665	20692	10
2MASX J15110812-4518515	13.43	16989		10
2MASX J15110829-4530355	14.95	9701	9635	10
2MASX J15111086-4522555	13.43	16695	16695	10
2MASX J15111305-4518045	12.89	9833	9770	10
2MASX J15111314-4540275	15.32	17001	16938	10
2MASX J15111821-4548315	14.58	34777		10
2MASX J15112124-4534105	14.36	16867		10
2MASX J15112713-4508405	13.13	10421		10
2MASX J15112811-4600294	13.79		17355	10
2MASX J15112969-4530244	14.62	34258		10
2MASX J15113091-4623304	14.38	28471		10
2MASX J15113207-4529344	13.17	16878	16782	10
2MASX J15113294-4606434	14.52	17349		10
2MASX J15113538-4457004	14.43	15769		10
2MASX J15113867-4455333	14.92	16288		10
2MASX J15114286-4536574	14	15772		10
2MASX J15114396-4550204	14.2	10007	9956	10
2MASX J15114564-4603064	15.12	34215		10
2MASX J15114680-4601074	14.07	17466		10
2MASX J15114715-4610094	13.59	17763	17643	10
2MASX J15114718-4526084	14.53	16788	16851	10
2MASX J15115115-4537434	14.01	15784		10
2MASX J15115211-4535414	13.79	16884		10
2MASX J15115358-4456274	14.46	24812		10
2MASX J15115678-4558264	13.31	17139		10
2MASX J15115755-4609034	14.21	20014	20008	10
2MASX J15115801-4521434	14.65	15974		10
2MASX J15115811-4537474	15	16309		10
2MASX J15115839-4519124	12.74	16755	16620	10
2MASX J15115954-4534004	13.66	17322		10
2MASX J15120726-4507044	14.91	16073		10
2MASX J15120787-4519474	14.25	26208	26193	10
2MASX J15120823-4608194	13.21	17652		10
2MASX J15121004-4517224	14.55	33946		10
2MASX J15121433-4522053	15.39	30861		10
2MASX J15122627-4517542	15.09	33811		10
2MASX J15122843-4526112	13.85	33942		10
2MASX J15122915-4555432	14.55	23810	23768	10
2MASX J15123084-4456132	13.36	16342	16243	10
2MASX J15123137-4532312	13.7	16228		10
2MASX J15123212-4551352	14.73	26076		10
2MASX J15123908-4535022	12.72	16492		10
2MASX J15123910-4546492	13.83	17469		10
2MASX J15123922-4558242	13.78	15424		10
2MASX J15124019-4608552	14.56	16980		10
2MASX J15124426-4617532	14.06	16752		10
2MASX J15124487-4526182	14.02	34572		10
2MASX J15124528-4534272	13.61	16510		10
2MASX J15124602-4558032	14.09	15119		10
2MASX J15124703-4544522	13.25	16998		10
2MASX J15125074-4621031	14.18	17598		10
2MASX J15125403-4606091	14.48	15898	15781	10
2MASX J15130135-4522463	15.16	16747	16668	10
2MASX J15130338-4610453	12.74	10442		10
2MASX J15130903-4632283	14.1	10637	10586	10
2MASX J15130988-4534173	14.06	16567		10
2MASX J15130989-4520063	14.66	33718		10
2MASX J15130989-4640513	14.68	59026		10
2MASX J15131093-4524393	14.52	17217	17094	10
2MASX J15131197-4540513	15.19	33217		10
2MASX J15131235-4529203	13.86	16207		10
2MASX J15131417-4643163	14.98	15295	15193	10
2MASX J15131512-4538183	14.69	33256		10
2MASX J15131892-4535213	14.56	17362		10
2MASX J15132080-4607113	13.81	19936	19918	10
2MASX J15132226-4611443	13.86	16382		10
2MASX J15132907-4545242	13.59	11536		10
2MASX J15133001-4502092	14.81	34062		10
2MASX J15133017-4615002	13.08	17619		10
2MASX J15133069-4641222	13.71	17004		10
2MASX J15133163-4559432	13.91	17580		10
2MASX J15133357-4529472	14.29	34305		10
2MASX J15133452-4647452	15.31	28645	28510	10
2MASX J15134242-4616345	14.29	16923	16836	10
2MASX J15134739-4455265	13.46	16273		10
2MASX J15134913-4515405	14.24	16896		10
2MASX J15135104-4505555	14.19	33796		10
2MASX J15135219-4559335	14.23	17433		10
2MASX J15135680-4549075	14.77	16761		10
2MASX J15135794-4546315	12.93	16336		10
2MASX J15135939-4606405	13.62	17271		10
2MASX J15135957-4550155	13.8	16647		10
2MASX J15140150-4557205	14.62	15856		10
2MASX J15140257-4506065	14.53	33412		10
2MASX J15140338-4636515	13.72	16549	16480	10
2MASX J15140478-4607565	13.83	17235		10
2MASX J15140918-4534465	13.54	10250		10
2MASX J15140949-4540125	13.22	16315		10
2MASX J15141131-4604495	14.3	16336		10
2MASX J15141156-4511365	14.53	33910		10
2MASX J15141342-4648331	8.93	566	519	10
2MASX J15141588-4557144	14.38	17187		10
2MASX J15141780-4548215	14.77	16010		10
2MASX J15142193-4610576	13.43	17211		10
2MASX J15142405-4608506	13.65	16893		10
2MASX J15142439-4624486	14.83	16972		10
2MASX J15142823-4549116	14.55	17695		10
2MASX J15143080-4603586	14.44	16135		10
2MASX J15143560-4558396	11.52	17082		10
2MASX J15143655-4551076	14.13	15098		10
2MASX J15143659-4650036	13.64	17208		10
2MASX J15143683-4548416	13.94	17505		10
2MASX J15143889-4622436	14.09	16903		10
2MASX J15144039-4554506	12.98	18566		10
2MASX J15144137-4604396	14.63	17340		10
2MASX J15144155-4559016	14.56	18740		10
2MASX J15144176-4528346	13.3	16617		10
2MASX J15144250-4516546	13.89	16713		10
2MASX J15144568-4532386	12.94	16186		10
2MASX J15144620-4519475	14.76	16519		10
2MASX J15144633-4621416	14.54	28528		10
2MASX J15144644-4558565	15.05	17194		10
2MASX J15144705-4607455	12.23	16617	16579	10
2MASX J15144720-4531575	13.54	16396		10
2MASX J15144959-4556285	14.34	16117		10
2MASX J15145143-4618195	14.94	20560	20365	10
2MASX J15145148-4532425	13.72	16507		10
2MASX J15145585-4535269	14.69	16453		10
2MASX J15150039-4629569	13.45	15787	15730	10
2MASX J15150166-4509439	14.69	16171	16225	10
2MASX J15150226-4554219	12.79	10013		10
2MASX J15150342-4549499	14.51	16555		10
2MASX J15150471-4609409	14.19	17661	17577	10
2MASX J15150929-4631170	14.91	38940	38775	10
2MASX J15151108-4549550	14.4	17512		10
2MASX J15151414-4510320	13.6	16315		10
2MASX J15151452-4538000	13.27	10322		10
2MASX J15151846-4604340	14.45	18851	18806	10
2MASX J15151900-4538470	14.76		17391	10
2MASX J15152170-4550470	14.21	16953		10
2MASX J15152444-4639579	14.64	52677		10
2MASX J15152664-4607479	13.29	18012	17823	10
2MASX J15152759-4540349	13.4	16138		10
2MASX J15152793-4551529	13.63	17937		10
2MASX J15152800-4545289	14.33	16950		10
2MASX J15153287-4602159	13.32	17304		10
2MASX J15154003-4559107	13.86	16992		10
2MASX J15154053-4500138	14.68	36615		10
2MASX J15154127-4531348	14.22	10109	10058	10
2MASX J15154204-4600018	13.99	16620		10
2MASX J15154335-4538468	13.6		16375	10
2MASX J15154673-4604588	14.35	17241		10
2MASX J15154827-4459158	13	11071		10
2MASX J15155716-4523478	14.11	17631		10
2MASX J15155897-4624598	14.26	17290		10
2MASX J15160414-4541448	13.25	9719	9650	10
2MASX J15160583-4531128	14	16342		10
2MASX J15160766-4621068	14.79	59503		10
2MASX J15160832-4639147	15.02	21015	20896	10
2MASX J15160840-4613577	14.43	19885		10
2MASX J15160885-4628497	12.22	10163	10100	10
2MASX J15161271-4610257	13.67	19849		10
2MASX J15161442-4551327	13.96	33703		10
2MASX J15161727-4641203	13.01	16944		10
2MASX J15161956-4602593	15.37		33778	10
2MASX J15162063-4624273	14.27	17400		10
2MASX J15162292-4636423	14.93	26731	26685	10
2MASX J15162553-4558554	13.08	17238		10
2MASX J15162620-4558024	13.2	17154		10
2MASX J15162650-4554134	14.52	34125		10
2MASX J15163378-4557364	13.61	16924		10

2MASX J15163446-4610444	14.9	15985		10
2MASX J15164267-4547093	14.48	16165	15958	10
2MASX J15164471-4557123	14.68	17610		10
2MASX J15165201-4632463	13.23	16552	16405	10
2MASX J15165324-4456595	13.53	14324		10
2MASX J15165749-4559156	14.32	17029		10
2MASX J15170169-4604456	13.87	15820		10
2MASX J15170425-4616566	14.68	34026		10
2MASX J15170696-4610446	13.8	23642		10
2MASX J15171109-4641007	14.63	17799		10
2MASX J15171454-4525596	14.81	16254		10
2MASX J15171817-4633116	14.08	16333	16297	10
2MASX J15171827-4631406	13.99	16606		10
2MASX J15171966-4602286	14.41	15679		10
2MASX J15172008-4535326	13.68	15541		10
2MASX J15172252-4629276	14.63	17604	17535	10
2MASX J15172556-4547546	13.81	16066	15943	10
2MASX J15172664-4641106	12.34	15967		10
2MASX J15172950-4629306	14.47	16528		10
2MASX J15173738-4525046	14.93	50605		10
2MASX J15174025-4520456	15.37	32135		10
2MASX J15174197-4615476	13.4	16042		10
2MASX J15174679-4619016	13.81	16534		10
2MASX J15175229-4621456	13.39	16875	16941	10
2MASX J15180851-4619146	14.09	16882		10
2MASX J15181654-4630222	14.06	16432		10
2MASX J15182748-4632243	14.8	16324		10
2MASX J15182768-4631083	13.84	16378		10
2MASX J15182847-4607443	12.13	15649		10
2MASX J15183242-4615423	14.19	16641		10
2MASX J15183377-4623433	14.6	16120		10
2MASX J15183544-4532063	14.82	32411		10
2MASX J15183559-4613312	14.29	17100	17031	10
2MASX J15184588-4630032	14.55	16435		10
2MASX J15184683-4524562	14.74	21580	21714	10
2MASX J15185047-4618312	14.9	15806		10
2MASX J15185555-4620092	13.64	16795		10
2MASX J15185893-4622033	14.33	17079		10
2MASX J15190696-4612583	13.32	17007		10
2MASX J15191453-4528563	14.5	20575	20494	10
2MASX J15191688-4614563	14.01	15694		10
2MASX J15194125-4528273	15.22	39285		10
2MASX J14035950-4303054	14.65	21828		11
2MASX J14040397-4238524	14.31	20080		11
2MASX J14043743-4236408	14.49	26793		11
2MASX J14045073-4313368	14.37	20098		11
2MASX J14045473-4236558	13.64	26553		11
2MASX J14045900-4239307	14.13	20165		11
2MASX J14050041-4249297	13.45	20110		11
2MASX J14050190-4257317	14.42	26094		11
2MASX J14050318-4210437	14.84	20248		11
2MASX J14050882-4231483	14.27	21099		11
2MASX J14053073-4243343	14.41	20569		11
2MASX J14053295-4221373	14.05	20440		11
2MASX J14054165-4229403	14.07	15494		11
2MASX J14054180-4301083	14.32	15950		11
2MASX J14054182-4247213	14.45	26259		11
2MASX J14054703-4200046	13.18	20290	20137	11
2MASX J14055260-4235016	13.85	20674		11
2MASX J14055339-4246526	13.38	27035	26918	11
2MASX J14055673-4304117	14.41	15805	15814	11
2MASX J14055713-4158292	15.41	97469		11
2MASX J14060682-4239447	14.48	20273		11
2MASX J14060786-4258297	14.87		21009	11
2MASX J14060990-4236396	14.29	20647	20575	11
2MASX J14061169-4300276	13.92	20209	20167	11
2MASX J14061255-4242386	13.1	20497		11
2MASX J14061390-4241056	15.09	34914		11
2MASX J14062385-4221363	14.23	20350		11
2MASX J14063195-4227484	14.46	16612		11
2MASX J14063255-4239244	12.38	20506		11
2MASX J14063502-4154048	13.89	26334		11
2MASX J14063528-4236384	13.34	21099		11
2MASX J14063999-4239334	14.29	20350		11
2MASX J14064216-4224594	15.18	19783	19672	11
2MASX J14064353-4306004	14.67	19870		11
2MASX J14064388-4217334	13.15	15113	15044	11
2MASX J14064699-4303134	14.9	20038		11
2MASX J14064945-4209474	15.4	39995		11
2MASX J14065067-4235484	15.06	26637		11
2MASX J14065362-4221224	14.54	21333		11
2MASX J14065508-4254154	14.48	20518		11
2MASX J14065760-4308194	14.86	36809		11
2MASX J14070614-4255411	14.68	15949		11
2MASX J14071521-4207431	14.8	20275		11
2MASX J14072079-4214041	14.2	20988		11
2MASX J14073021-4236261	15.54	34855	34803	11
2MASX J14073067-4152455	14.38	15054		11
2MASX J14073202-4304081	14	16147		11
2MASX J14073299-4200581	13.63	21027	20869	11
2MASX J14074049-4305125	14.53	16144	16093	11
2MASX J14074122-4341575	15.35	37696		11
2MASX J14074272-4236215	14.13	35714		11
2MASX J14074600-4231266	13.52	15727		11
2MASX J14075584-4251276	14.85	34296	34371	11
2MASX J14080203-4302366	14.61	15862		11
2MASX J14080637-4239516	13.26	15559		11
2MASX J14080776-4255016	15.14	44924		11
2MASX J14080922-4254136	14.81	15733	15715	11
2MASX J14081140-4322536	14.84	39691	39642	11
2MASX J14081226-4238546	14.2	16396		11
2MASX J14081263-4307086	14.86	15542		11
2MASX J14081537-4246015	13.29	20242		11
2MASX J14081717-4221385	14.73	15647		11
2MASX J14081981-4333308	14.75	21414	21435	11
2MASX J14082503-4257429	14.35	15616		11
2MASX J14083198-4208199	14.71	9570		11
2MASX J14083262-4243069	14.92	15616		11
2MASX J14084538-4212299	13.59	20803		11
2MASX J14084840-4152539	15.5	15515		11
2MASX J14084922-4243009	14.86	16216		11
2MASX J14085238-4234539	13.35	11005	10927	11
2MASX J14085330-4241399	14.56	15709		11
2MASX J14085720-4301269	14.15	36874		11
2MASX J14085995-4325578	15.06	60399		11
2MASX J14090558-4222489	13.9	16330		11
2MASX J14090619-4257189	13.9	15868		11
2MASX J14090753-4234599	14.88	23192		11
2MASX J14091268-4347249	14.6	60438		11
2MASX J14091323-4239219	14.96	15403		11
SUMSS J140915-422855			101345	11
2MASX J14091649-4246569	14.5	15538		11
2MASX J14091668-4208169	14.68	14795	14678	11
2MASX J14091754-4148357	15.31	26054		11
2MASX J14091858-4249129	13.82	14495		11
2MASX J14091975-4225339	14.78	16417		11
2MASX J14092431-4159317	15.08	58472		11
2MASX J14092750-4256129	14.35	14823		11
2MASX J14092890-4148568	14.93	35918		11
2MASX J14093255-4243188	13.69	15598		11
2MASX J14093694-4244315	15.28	15481		11
2MASX J14094341-4213266	13.93	15580		11
2MASX J14094566-4310236	14.6	16312		11
2MASX J14094599-4319146	14.56	22173	22101	11
2MASX J14094734-4330056	15.33	68011		11
2MASX J14094764-4248426	14.58	15421		11
2MASX J14095004-4312016	14.46	25917		11
2MASX J14095061-4304286	14.45	15349	15307	11
2MASX J14095066-4235006	12.56	16387		11
2MASX J14095318-4246026	13.52	15167		11
2MASX J14095518-4244106	13.26	6826		11
2MASX J14095644-4321556	14.25	28861	28753	11
2MASX J14095791-4245126	14.17	15739		11
2MASX J14095809-4246336	13.42	15119		11
2MASX J14100171-4231346	13.57	16402	16390	11
2MASX J14100336-4250156	14.21	14861		11
2MASX J14100624-4235306	13.19	15487		11
2MASX J14101183-4253276	14.79	16240		11
2MASX J14101212-4210516	14.64	24214		11
2MASX J14101301-4208516	14.46	24637		11
2MASX J14101589-4246525	14.8	36686		11
2MASX J14102007-4224545	15.16	14600	14507	11
2MASX J14102201-4256355	14.57		10316	11
2MASX J14102256-4211035	14.54	15764		11
2MASX J14102305-4247485	14.15	14312		11
2MASX J14102362-4328135	15.33	69393		11
2MASX J14102503-4319285	9.37	1741	1718	11
2MASX J14102653-4237395	14.91	15442	15436	11
2MASX J14102887-4246555	11.9	15322		11
2MASX J14103050-4245465	14.15	14426		11
2MASX J14103371-4218415	15.42	14987	14999	11
2MASX J14103464-4157015	14.95	20638	20683	11
2MASX J14103505-4236325	13.93	15262		11
2MASX J14103514-4242215	13.45	16426		11
2MASX J14103711-4345345	14.52	22209		11
2MASX J14103887-4148250	13.49	20212		11
2MASX J14103895-4258036	15.21	15838	15742	11
2MASX J14104313-4247315	13.56	15490		11
2MASX J14104347-4231535	13.66	15406		11
2MASX J14104379-4147090	14.7	20293		11
2MASX J14104482-4228325	13.39	10220	10133	11
2MASX J14104519-4230515	15.66	34848	34734	11
2MASX J14104730-4245185	14.95	16021	16072	11
2MASX J14105700-4229566	13.95	20155	20008	11
2MASX J14105802-4243206	13.66	15652		11
2MASX J14110249-4323537	14.4	38727	38628	11
2MASX J14110302-4329247	14.4	26388	26292	11
2MASX J14110629-4341377	14.22	25887		11
2MASX J14110726-4323027	14.84	43182	43116	11
2MASX J14110817-4248207	14.09	15313		11
2MASX J14111020-4320347	14	26211		11
2MASX J14111339-4340257	14.8	38571		11
2MASX J14111458-4346067	14.47	14630	14594	11
2MASX J14111563-4236327	15.12	15391		11
2MASX J14111938-4341197	14.86	38925		11
2MASX J14111944-4306037	13.14	14834		11
2MASX J14112089-4249207	14.85	15619		11
2MASX J14112654-4254347	15.54	54149		11

2MASX J14112871-4250527	12.77	15853		11
2MASX J14113119-4344267	15.05	26229	26145	11
2MASX J14114384-4157081	14.62	20374	20317	11
2MASX J14114444-4301211	13.72	15313	15238	11
2MASX J14114827-4300571	14.45	16129	16147	11
2MASX J14115484-4248402	13.78	15652		11
2MASX J14120300-4233232	14.37	20344		11
2MASX J14120904-4201281	13.49	20584		11
2MASX J14121338-4327251	15.35	26350		11
2MASX J14121588-4201545	14.58	20854	20878	11
2MASX J14122426-4330155	16.11	26223		11
2MASX J14123019-4258136	14.81	10793	10775	11
2MASX J14124034-4229046	12.93	20338		11
2MASX J14125711-4159018	15.23	35906		11
2MASX J14125715-4227098	14.99	20215		11
2MASX J14130836-4220568	14.66	20830	20815	11
2MASX J14130939-4203238	15.29	35727		11
2MASX J14130980-4319438	15.18	34066	34059	11
2MASX J14131379-4204299	13.81	36185		11
2MASX J14131774-4205249	14.17	33942		11
2MASX J14132021-4244039	14.35	13287	13266	11
2MASX J14132552-4230048	15.27	20392		11
2MASX J14133161-4237288	14.98	35780	35741	11
2MASX J14133477-4304115	15.08	25731	25755	11
2MASX J14133592-4331025	11.69	6661		11
2MASX J14134295-4241245	14.71	7447	7420	11
2MASX J14134558-4240335	14.84	20068	19927	11
2MASX J14134908-4321085	15.1	74984		11
2MASX J14135485-4320105	15.41	53973		11
2MASX J14135595-4319135	15.04	33990		11
2MASX J14135743-4220065	15.61	20498		11
2MASX J14135750-4210535	15.04	35948		11
2MASX J14140071-4315045	15.55	54355		11
2MASX J14140958-4313364	14.62	43263		11
2MASX J14145484-4228102	15.04	37000		11
2MASX J14151029-4239383	15.02	20032	20326	11
2MASX J12002164-5324460	14.52	33184		12
FAIRALL 0448:12002381-5317071			4653	12
2MASX J12003049-5328299	14.02	32881		12
2MASX J12003500-5332469	13.74	32816		12
2MASX J12005321-5341125	14.12	33577		12
2MASX J12010008-5324155	14.1	32414		12
2MASX J12010288-5320405	14.12	20327	20380	12
2MASX J12010299-5313545	13.45	20686		12
2MASX J12011597-5325215	11.51	4575		12
2MASX J12012005-5347555	12.33	7651		12
WKK 0540:12012052-5302053		14861		12
2MASX J12013617-5321275	12.02	4371		12
2MASX J12014264-5329505	14.68	32075		12
2MASX J12014632-5256065	12.77	11113		12
WKK 0545:12015179-5237271		11207	11155	12
2MASX J12015440-5255284	12.66	8157	8100	12
WKK 0549:12015705-5253380			19478	12
2MASX J12015713-5313064	14.39	23654	23459	12
2MASX J12020229-5334454	13.78	11297		12
2MASX J12020333-5339504	15.01	32881		12
2MASX J12021135-5342352	13.98	22865		12
2MASX J12022125-5344193	14.22	33616		12
2MASX J12022356-5321283	14.26	4380	4416	12
2MASX J12023677-5330163	15.13	48944		12
2MASX J12023883-5312263	13.91	16755	16612	12
2MASX J12024767-5350082	11.48		8313	12
WKK 0561:12024805-5331005		12070	12019	12
WKK 0567:12030701-5334390		11740	11449	12
2MASX J12031936-5251592	12.84	12052	12058	12
2MASX J12034684-5338164	14.14		4389	12
2MASX J12035905-5241544	14.27	8061		12
2MASX J12040505-5226514	14.35	18299		12
2MASX J12041698-5237559	12.97	4775	4707	12
2MASX J12042167-5331180	15.16	33470		12
2MASX J12042527-5350430	14.49	32734		12
2MASX J12042821-5356076	13.1		8112	12
2MASX J12043027-5405336	12.53	4537	4482	12
2MASX J12043774-5236490	13.15	7992	7897	12
2MASX J12044388-5228490	12.68	8040	7936	12
2MASX J12044940-5240370	13.09	8280		12
2MASX J12045878-5314109	12.92	4995	4842	12
2MASX J12050052-5349569	14.61	32632		12
WKK 0595:12050103-5340451		17133	17112	12
2MASX J12050602-5347225	13.13	33442		12
2MASX J12051015-5251585	14.87	14516		12
2MASX J12051113-5340066	14.18	17196	17052	12
2MASX J12051707-5349466	15.2	32626		12
2MASX J12051879-5333246	13.91	17430		12
WKK 0607:12052305-5321360		4799	4767	12
WKK 0613:12054181-5309382		4542	4548	12
2MASX J12054996-5218354	14.81		11923	12
2MASX J12055628-5219304	14.23		15406	12
2MASX J12060442-5331374	15.29	23546	23477	12
2MASX J12060454-5315064	14.44	66845		12
WKK 0619:12060901-5259280			4806	12
2MASX J12061173-5343084	15.08	17205		12
2MASX J12061821-5331324	13.66	20893		12
2MASX J12062099-5326434	15.69	47565		12
2MASX J12062168-5329394	13.92	20308	20239	12
2MASX J12063041-5351337	12.4	8295		12
2MASX J12063262-5326597	13.71	11560		12
WKK 0632:12063516-5335517		20734	20689	12
2MASX J12064636-5232058	13.58	18518		12
2MASX J12064850-5346068	14.27	33121		12
2MASX J12064943-5213148	12.96	4290	4296	12
2MASX J12065076-5337348	14.57	21330		12
2MASX J12065435-5333288	14.26	20689		12
2MASX J12065528-5352158	14.74	48776		12
2MASX J12070162-5352548	14.32	17403		12
2MASX J12070518-5324027	14.48	11740	11569	12
2MASX J12072025-5337302	13.49	8298		12
2MASX J12072416-5313232	12.57	11587		12
2MASX J12075324-5324592	14.63	35164		12
2MASX J12080796-5336124	14.82	22505	22320	12
2MASX J12082788-5345524	14.62	33772		12
2MASX J12083203-5341553	15.36	33721		12
2MASX J12083498-5343513	15.18	33697		12
2MASX J12083522-5405583	13.57	5624	5630	12
2MASX J12083846-5330276	13.72	22368	22206	12
2MASX J12084248-5348206	15.85	32719		12
WKK 0664:12084421-5328210			8196	12
2MASX J12084781-5235217	15.06	25072	24946	12
2MASX J12085086-5340377	14.26	33430		12
WKK 0671:12085904-5353272		15035	15032	12
2MASX J12091935-5328126	14.97	14891		12
2MASX J12092226-5239526	14.58		18647	12
2MASX J12093022-5405489	14.95	33661		12
WKK 0681:12093811-5403317		25869	25701	12
2MASX J12093949-5251158	13.2	14672		12
2MASX J12094755-5251008	12.83	14591		12
2MASX J12094800-5257328	14.05	19259	19166	12
2MASX J12094855-5250208	12.79	14663		12
2MASX J12095969-5227477	14.13		11818	12
2MASX J12100179-5231587	13.74	11752	11731	12
2MASX J12100392-5328568	14.58	21244	20955	12
2MASX J12100394-5241497	15.22	14645		12
2MASX J12100575-5222358	14.09	19271	19166	12
2MASX J12100591-5332159	14.72	20833	20767	12
2MASX J12100611-5404071	14.83	32489		12
2MASX J12100684-5328259	14.1	20809		12
2MASX J12101519-5233319	14.57	14747	14609	12
2MASX J12102672-5223110	14.35	22670		12
2MASX J12102746-5404080	14.92	32503		12
2MASX J12102879-5242570	14.35	19031	18977	12
2MASX J12102890-5221480	12.75	11563	11377	12
2MASX J12103006-5401360	13.93	32686		12
2MASX J12103403-5223080	12.92	11830		12
WKK 0705:12103818-5249242		18884		12
2MASX J12103918-5253090	14.27	14570		12
2MASX J12103962-5225370	12.25	11176		12
2MASX J12104380-5231589	12.44	11476		12
2MASX J12105232-5406424	14.06	34173		12
2MASX J12105729-5250001	15.26	47719		12
2MASX J12105923-5259381	14.28	14996	14900	12
2MASX J12110210-5405484	12.32	32935		12
2MASX J12110364-5335042	15.02	68554		12
2MASX J12110822-5402244	14.61	32659		12
2MASX J12113163-5238073	14.37	14615	14429	12
2MASX J12114074-5258484	13.07	14852		12
2MASX J12114194-5300284	15.01	22230	22113	12
2MASX J12115489-5351125	14.52	32941	33001	12
2MASX J12120168-5306355	12.6	19109		12
2MASX J12120502-5237044	14.3	23585	23468	12
2MASX J12121895-5348180	13.43	21150		12
2MASX J12122242-5300331	14.42	19283	19241	12
2MASX J12122980-5312571	14.46	21150	21036	12
2MASX J12124286-5336071	13.37	21066		12
2MASX J12125434-5319441	14.54	19448	19373	12
2MASX J12130128-5309000	14.5	23693		12
2MASX J12130520-5339074	14.84	21210		12
2MASX J12133249-5251485	14.8	36285		12
2MASX J12133525-5252265	14.27	36266		12
2MASX J12134622-5258378	14.78	20944	20952	12
WKK 0778:12140655-5308384			17082	12
2MASX J12140848-5309089	13.7	17016	16932	12
2MASX J09325692-6103091	14.19	16421		13
2MASX J09334623-6126040	13.1	16324		13
2MASX J09340924-6050079	13.66	16549		13
2MASX J09341407-6116541	11.82		2614	13
2MASX J09342965-6042063	14.13	22652		13
2MASX J09342980-6039392	14.83	29452		13
RKK 1465:09343051-6116030			2482	13
2MASX J09343962-6035473	14.31	21274		13
2MASX J09343973-6042013	14.7	21882		13
2MASX J09344668-6037123	11.76	21519		13
2MASX J09352154-6037295	14.59	24976	24931	13
2MASX J09352978-6042436	14.52	21636		13
2MASX J09360258-6021556	14.96	36317		13
2MASX J09361494-6135145	14.67	28960		13
2MASX J09361668-6041175	13.98	20976		13
2MASX J09363107-6110076	16.19	48192		13
RKK 1487:09364099-6146390			4479	13

2MASX J09370080-6055596	11.63	2818		13
2MASX J09370565-6111225	14.5	37204		13
2MASX J09371197-6136317	14.04	10283	10175	13
2MASX J09371266-6026437	13.18	16031		13
RKK 1499:09373006-6018490			3058	13
2MASX J09374130-6053439	14.8	29027		13
2MASX J09374213-6027569	13.36	16174		13
2MASX J09375292-6137099	14.15	26820	26810	13
2MASX J09375313-6012589	14.78	29635		13
2MASX J09375869-6108189	13.31	24136		13
2MASX J09375979-6021509	14.74	31445		13
2MASX J09375988-6032179	12.51	16489		13
2MASX J09380530-6031588	14.82	17280		13
2MASX J09380702-6132438	13.89	24166		13
2MASX J09382697-6039444	15.3	47613		13
2MASX J09382912-6149464	10.77	2878		13
2MASX J09383352-6144185	10.41	2728		13
2MASX J09383394-6108575	15.23	51190		13
2MASX J09383618-6148455	15.06	22580	22386	13
2MASX J09383843-6151005	13.77	22434	22314	13
2MASX J09384085-6101195	14.81	24031		13
2MASX J09385371-6152374	15.46	34332		13
2MASX J09385729-6126004	15.16	33271		13
2MASX J09385775-6042354	14.12	22035		13
2MASX J09385900-6115024	13.3	21471	21339	13
2MASX J09392020-6154542	15.17	43230		13
2MASX J09393436-6155493	14.04	22485	22478	13
2MASX J09395434-6155533	16.29	21853		13
2MASX J09400473-6153398	14.47	21675	21654	13
2MASX J09403344-6200401	14.9	46429		13
2MASX J09403520-6104011	14.89	37396		13
2MASX J09403936-6116401	15.43	62992		13
2MASX J09405494-6122270	14.87	47121		13
2MASX J09405517-6159500	14.77	44598	44621	13
2MASX J09412525-6125390	14.72		11146	13
2MASX J09413877-6126310	14.77		11203	13
2MASX J09414364-6047560	12	3072	3076	13
2MASX J09414367-6131180	13.28	10157		13
2MASX J09422294-6106423	13.35	12414		13
2MASX J09422797-6006574	13.6	10673	10502	13
2MASX J09424053-6127304	14.72	43506		13
2MASX J09425815-6046222	14	29086	28927	13
2MASX J09431144-6047553	14.52	21783		13
2MASX J09431469-6006273	14.1	27683		13
2MASX J09432471-6042213	14.9	20976		13
2MASX J09432629-6101213	14.93	28786	28594	13
2MASX J09432973-6102094	13.98	28918		13
2MASX J09434354-6045583	13.8	21153		13
2MASX J09434645-6051093	13.3	21690		13
2MASX J09440420-6051496	14.05	21753		13
2MASX J09442487-6053157	14.33	21651		13
2MASX J09442646-6121367	14.59	32890		13
2MASX J09443511-6039057	14.03	21846		13
2MASX J09451544-6058471	13.94	21351		13
2MASX J09452053-6126551	14.27	12417	12324	13
2MASX J09452115-6042261	13.82	22278	22206	13
2MASX J09454033-6036191	14.28	29038		13
2MASX J09454237-6056501	13.57	22050	21918	13
2MASX J09455670-6059401	13.6	22200	22161	13
2MASX J09461775-6031453	14.62	28723		13
2MASX J09462574-6040313	14.08	22179		13
2MASX J09462846-6056073	13.12	21699		13
2MASX J09464625-6105152	14.56	22625	22424	13
2MASX J09464786-6034212	12.97	6365		13
2MASX J09464835-6028492	14.04	11707		13
2MASX J09465055-6107172	14.89	30411		13
2MASX J09465478-6104484	14.02	22044		13
2MASX J09470596-6104035	13.73	21615		13
2MASX J09471827-6052516	13.24	21393		13
2MASX J09471868-6052186	14.69	21300		13
2MASX J09472135-6030506	14.83	29023	29023	13
2MASX J09474287-6046136	14.23	21081		13
2MASX J09474647-6037505	14.88	37639		13
2MASX J09480294-6124528	14.07	16588	16477	13
2MASX J09165943-6152271	13.97	27002		14
2MASX J09171442-6056301	14.14	16953	16992	14
2MASX J09171796-6153551	14.89	26017		14
2MASX J09173941-6128220	14.73	30183	30234	14
2MASX J09173983-6047110	14.85	27778		14
2MASX J09174122-6048530	15.5	21448	21396	14
2MASX J09174685-6203084	14.32	30307	30138	14
2MASX J09174803-6159494	14.47	27171		14
2MASX J09175441-6201165	14.85	30246		14
2MASX J09175725-6127045	15.06	30324		14
2MASX J09175852-6047015	15.44	34609		14
2MASX J09180028-6049515	14.33	27830	27806	14
IRAS 09168-6141		3184	3115	14
2MASX J09182013-6200595	14.94	26945	26816	14
2MASX J09182562-6113475	14.51	30003	29940	14
RKK 1211:09182671-6201599			3175	14
2MASX J09183769-6115314	14.06	30468		14
2MASX J09184120-6154363	14	27155		14
2MASX J09185993-6119111	14.43	17202	17046	14
2MASX J09190300-6145081	15.37	27113		14
2MASX J09190869-6117021	14.98	37714		14
2MASX J09191018-6145281	13.32	26630		14
2MASX J09191969-6126541	13.49	17077		14
2MASX J09193039-6039541	13.91	16552	16576	14
2MASX J09194874-6145411	15.25	26445		14
2MASX J09195904-6141212	13.72	26498		14
2MASX J09200035-6129322	15.16	36754		14
RKK 1239:09201089-6214089		17139	17157	14
2MASX J09201106-6103392	14.94	37238		14
2MASX J09201968-6136192	14.68	26517		14
2MASX J09204325-6159219	14.77	30729	30543	14
RKK 1244:09205407-6125448		11197	11002	14
2MASX J09205527-6131109	14.31	27213		14
2MASX J09211746-6025590	14.41	22056		14
RKK 1247:09212659-6120449		10916	10939	14
2MASX J09212782-6128579	14.74	30040		14
2MASX J09212843-6107529	13.42	35384		14
2MASX J09212899-6055539	14.58	27111		14
2MASX J09212972-6035429	14.86	27609		14
RKK 1252:09213702-6201559			24568	14
2MASX J09214043-6123291	14.74	36458	36503	14
2MASX J09222315-6120462	15.11	30016		14
2MASX J09222490-6102582	9.87	2198	2132	14
2MASX J09222600-6139362	13.9	24487		14
2MASX J09222668-6025252	14.54	21679		14
2MASX J09222883-6035391	13.55	16900		14
2MASX J09222959-6135251	12.67	10856		14
2MASX J09223968-6120190	14.93	30243	30195	14
2MASX J09233345-6032123	15.15	38146		14
2MASX J09233838-6113534	14.68	30099		14
2MASX J09234100-6115024	14.68	30169		14
2MASX J09240626-6035195	13.77	21870		14
2MASX J09241325-6025055	14.53	19631	19561	14
2MASX J09241428-6037245	13.65	22232	22170	14
2MASX J09241453-6033414	13.98	21798		14
2MASX J09241725-6035344	13.81	21867		14
2MASX J09242119-6114094	15.26	29340		14
2MASX J09242945-6110493	14.48	37300		14
2MASX J09244727-6029599	14.79	21924		14
2MASX J09245658-6039370	15.08	19580		14
2MASX J09250032-6142210	14.09	22880		14
2MASX J09251286-6030230	14.23	22008		14
2MASX J09252066-6039089	14.12	19837		14
RKK 1318:09253007-6038341		19900		14
2MASX J09253500-6219312	14.16	18180		14
2MASX J09254087-6207472	15.72	45071		14
2MASX J09255262-6038293	15.24	79149		14
2MASX J09260066-6107583	14.62	16704		14
2MASX J09260692-6119203	14.92	35552		14
2MASX J09261440-6041093	14.49	16501	16525	14
RKK 1327:09261705-6036371			2212	14
2MASX J09261936-6059592	15.42	16615		14
ESO 126-G 011:09262431-6036540		2129	2102	14
2MASX J09262586-6052282	13.67	16801		14
2MASX J09263025-6040141	13.23	16954	16863	14
2MASX J09263210-6053431	14.91	16947	16926	14
2MASX J09263567-6041412	14.44	16552		14
2MASX J09263769-6108362	14.94	29862		14
2MASX J09264089-6120212	14.25	2290	2132	14
2MASX J09264978-6215113	15.72	74555		14
2MASX J09265003-6058223	14.44	26874		14
2MASX J09265052-6111403	14.86	37054		14
2MASX J09265270-6042083	13.76	16591		14
2MASX J09270224-6212003	14.62	25072	24991	14
2MASX J09270320-6045033	14.18	24340		14
2MASX J09270381-6116153	14.28	28823		14
2MASX J09270604-6039473	14.87	21492	21519	14
2MASX J09270672-6113113	14.66	29661		14
2MASX J09270990-6138293	14.28	28663		14
RKK 1344:09271037-6051234			27041	14
2MASX J09271123-6043073	13.06	21597		14
2MASX J09271274-6043473	14.25	21859		14
RKK 1346:09271307-6046509		27926	27932	14
2MASX J09272028-6125062	14.26	10850		14
2MASX J09272168-6212162	14.91	18585	18446	14
2MASX J09272307-6041052	13.29	16570		14
2MASX J09273156-6136388	14.48	32272		14
2MASX J09273264-6046148	10.9	2168	2159	14
2MASX J09273367-6102119	14.77	30315	30153	14
RKK 1362:09275779-6043412		27272	27218	14
2MASX J09280063-6045190	15.08	27294		14
2MASX J09280409-6058350	14.46	28921	28849	14
2MASX J09280775-6204580	13.73	25188		14
2MASX J09282046-6111039	14.55	37237	37288	14
RKK 1372:09282802-6041150		10200		14
2MASX J09282841-6135444	15.42	35111		14
2MASX J09283548-6116455	14.9	10055	9911	14
2MASX J09284409-6051196	11.62	2138	2132	14
2MASX J09285504-6116456	14.41	10082	9935	14
2MASX J09285830-6157196	14.42	10387		14
2MASX J09290647-6211376	14.9	24523		14
2MASX J09291137-6055415	14.8	27734		14
2MASX J09291941-6040284	14.68		16435	14
2MASX J09292954-6131488	15.14	29440		14

RKK 1393:09294908-6206270			3199	14
2MASX J09295994-6105589	13.64	10317		14
2MASX J09300232-6212369	14.85	34404		14
2MASX J09304536-6108353	15.07	10966	10861	14
2MASX J09305059-6126023	12.84	12252	12220	14
RKK 1416:09305489-6057410			29587	14
2MASX J09310988-6130583	15.18	42463		14
2MASX J09311757-6100152	14.76	21588	21543	14
2MASX J09314183-6135385	12.48	10206		14
2MASX J09314925-6138315	14.71	28951		14
2MASX J09315258-6055525	13.48	10158		14
2MASX J09322320-6148490	14.42	37387		14
2MASX J12282497-5405249	14.53	47824		15
2MASX J12285774-5405496	13.82	19717	19885	15
WKK 1073:12293228-5400184		30591	30528	15
WKK 1074:12293306-5412076		19991	19888	15
2MASX J12294797-5421487	11.75	6050	6008	15
2MASX J12295589-5413127	14.84	19889	19882	15
2MASX J12301649-5352089	14.46	34360		15
2MASX J12302215-5311338	14.6	34362		15
2MASX J12302980-5435580	14.91	29018		15
2MASX J12302988-5439420	14.88	29191		15
2MASX J12303112-5351009	14.65	34344		15
2MASX J12305846-5438441	13.82	28940		15
WKK 1101:12314001-5302514		30441		15
2MASX J12314273-5437307	14.68	19777		15
2MASX J12314716-5406387	14.44	36596	36653	15
WKK 1107:12321399-5350578		5528	5327	15
2MASX J12323076-5257248	15.01	47776		15
2MASX J12323535-5434273	13.77	19459		15
2MASX J12323624-5424163	14.6	16588	16528	15
2MASX J12323880-5400122	14.91	24535	24493	15
2MASX J12324387-5354272	15.48	34282	34131	15
2MASX J12324878-5358307	14.21	30725		15
2MASX J12330691-5356577	14.74	30626		15
2MASX J12330892-5302326	15.06	47563		15
2MASX J12331624-5337366	13.94	12831	12861	15
2MASX J12335015-5356011	15.27	30501	30480	15
2MASX J12341839-5445212	14.49	27293		15
WKK 1149:12341944-5356427		34144	34125	15
WKK 1150:12342633-5347596			15778	15
2MASX J12342840-5246545	14.38	31281		15
2MASX J12345488-5311205	13.18	31169		15
2MASX J12351087-5259265	15.12	30551		15
WKK 1157:12351846-5322023		17206		15
2MASX J12352103-5310484	14.53	32743		15
2MASX J12353111-5316583	14.81	31577		15
2MASX J12353649-5319470	14.28	47317		15
2MASX J12355619-5423281	14.94	38563		15
WKK 1166:12360007-5343458		9138	9279	15
WKK 1167:12360233-5353337		28139	28025	15
2MASX J12361401-5327068	14.06	18315		15
2MASX J12362074-5348189	14.41	15809		15
2MASX J12362213-5447310	14.61	26748	26825	15
2MASX J12362634-5318049	13.93	11377	11332	15
2MASX J12362761-5255549	14.37	31415		15
WKK 1176:12363194-5315335		52550		15
2MASX J12363889-5415531	15.5	74733		15
2MASX J12364311-5258328	14.03	18117	18059	15
2MASX J12365475-5315217	15.18	30345		15
2MASX J12365819-5330578	14.07	17233	17142	15
WKK 1189:12370684-5412292		27495	27374	15
WKK 1190:12370821-5319181			11422	15
2MASX J12371536-5408553	14.55	39208		15
2MASX J12371826-5322489	14.9	48846	48599	15
2MASX J12373666-5332588	14.57	18237	18143	15
2MASX J12374121-5301597	14.73	27435	27293	15
2MASX J12374918-5358501	14.74	27579		15
WKK 1202:12374903-5317406		17260		15
2MASX J12375948-5312407	14.07	31043		15
WKK 1204:12380007-5304451		17265	17157	15
WKK 1207:12380334-5259013		27683	27614	15
2MASX J12381605-5418388	14.71	39257		15
2MASX J12382120-5421178	14.72	23449		15
2MASX J12382254-5326515	14.57	39096	38931	15
2MASX J12383327-5327463	14.94	39410		15
2MASX J12383918-5423126	14.73	42786	42957	15
2MASX J12384086-5409046	15.01	42736		15
WKK 1225:12390831-5328541		28148	28222	15
WKK 1226:12390967-5407268		9456	9428	15
2MASX J12391712-5422031	14.91	9360		15
2MASX J12391790-5419431	14.86	9518	9455	15
WKK 1229:12392529-5317150		22041	22002	15
2MASX J12393151-5427370	14.2	43465		15
2MASX J12394587-5319022	14.95	44163		15
2MASX J12394669-5315269	14.91	28448		15
2MASX J12395853-5330233	14.78	46600		15
2MASX J12395916-5339423	15.05	27681		15
2MASX J12400450-5319424	13.9	17011	16959	15
2MASX J12401203-5405059	15.05	30444	30474	15
2MASX J12401467-5326144	14.89	43922		15
2MASX J12401757-5324154	14.42	27639		15
2MASX J12402713-5400017	14.89	30714		15
2MASX J12404109-5321102	14.14	27657		15
2MASX J12412760-5351320	14.01	43230		15
2MASX J12225258-5625247	13.72	22133		16
2MASX J12231177-5627397	14.27	22112		16
2MASX J12232128-5541307	14.42	28774		16
2MASX J12232157-5616197	13.42	20640	20590	16
2MASX J12232326-5603347	14.65	47709		16
2MASX J12240063-5552508	14.8	28751		16
2MASX J12240681-5558218	13.8	27002	26771	16
2MASX J12241553-5609238	13.92	15187		16
2MASX J12242398-5622398	13.05	7455		16
2MASX J12244318-5623337	13.59	19286		16
2MASX J12244801-5515397	13.98	30306		16
2MASX J12245747-5519358	15.02	34494		16
2MASX J12251579-5526358	13.76	30157		16
2MASX J12251786-5642018	13.59	14262		16
2MASX J12255352-5501120	14.18	29782	29703	16
2MASX J12260591-5513090	14.1	19724	19418	16
2MASX J12261496-5543458	14.95	30021		16
WKK 1017:12262105-5546440		11386	11419	16
2MASX J12262749-5546099	14.45	29202		16
2MASX J12263131-5541509	14.65	28699		16
2MASX J12263220-5503419	13.77	29143		16
2MASX J12263615-5544019	13.29	29995		16
2MASX J12265013-5504389	14.93	29925	29985	16
2MASX J12265748-5607109	15.08	41995		16
2MASX J12265798-5454279	14.41	29075		16
2MASX J12265963-5458089	14.17	29884		16
2MASX J12270077-5543049	13.81	29887		16
2MASX J12270488-5525538	15.36	29532		16
2MASX J12270553-5520538	15.28	30160		16
2MASX J12271312-5529004	14.49	29785		16
2MASX J12272397-5628104	12.19	7503		16
2MASX J12272789-5457525	14.92	29109		16
2MASX J12273300-5507505	14.43	30112		16
2MASX J12274717-5458044	14.02	30157		16
2MASX J12275180-5456404	14.53	29997		16
2MASX J12275195-5529164	14.12	29713		16
2MASX J12280865-5456049	14.33	30541	30381	16
WKK 1055:12282362-5626373			14819	16
2MASX J12282489-5451139	14.2	29841		16
2MASX J12284090-5639518	14.64		25938	16
WKK 1087:12310034-5459564			15490	16
2MASX J12311094-5527450	14	29544		16
2MASX J12313149-5453587	15.57	15484	15526	16
2MASX J12321491-5537332	14.64	9896	10037	16
2MASX J12324225-5638512	14.57	28799		16
2MASX J12331408-5555536	14.69	10235	10097	16
2MASX J12332027-5554596	13.66	29469		16
2MASX J12334160-5502545	14.22		29739	16
2MASX J12352069-5607544	13.94	29199	29122	16
2MASX J12352189-5520204	15.31	44651		16
2MASX J13542866-5630118	13.7		11686	17
2MASX J13544127-5634147	14.32	14046		17
2MASX J13555530-5555174	13.18	16417		17
WKK 2696:13560511-5553510			16620	17
2MASX J13563264-5603463	14.41	16312	16315	17
WKK 2719:13571183-5645187		16309		17
2MASX J13571679-5711557	13.6	11141		17
WKK 2725:13572909-5609061		15899	15829	17
WKK 2732:13574089-5609500			7681	17
WKK 2731:13574212-5649005		22077	21960	17
WKK 2754:13583384-5541460		20947	20668	17
2MASX J13583630-5712088	13.31	12114	12079	17
2MASX J13585646-5651034	13.56	14704		17
2MASX J13590915-5545565	14.82	30824		17
2MASX J13590942-5634225	13.48	13683		17
WKK 2771:13591882-5633079		21685		17
WKK 2773:13592407-5622505		14882	14819	17
2MASX J13592492-5700344	13.22	21462		17
2MASX J13592811-5545184	14.02	14234		17
WKK 2778:13594145-5659283		14184		17
WKK 2782:13595239-5556510			13778	17
2MASX J13595499-5645360	12.81	13626		17
2MASX J14000170-5618250	14.05	21244		17
2MASX J14001083-5616400	14.19	29631	29643	17
WKK 2791:14001164-5631026		21908		17
2MASX J14001389-5630290	13.41	21522		17
2MASX J14001462-5720020	12.26	11602		17
2MASX J14001882-5720060	12.69	11504		17
WKK 2795:14002019-5704451		11722	11845	17
2MASX J14002453-5710309	13.27	16890	16968	17
2MASX J14004104-5647419	13.14	15056		17
2MASX J14005321-5639249	13.49	14064		17
2MASX J14005870-5650569	13.86	13457		17
WKK 2817:14010096-5543520		2777		17
2MASX J14010454-5649409	14.3	13493		17
2MASX J14011088-5649249	12.21	14046		17
2MASX J14011416-5648208	13.84	13217		17
WKK 2826:14011817-5626553			29461	17
2MASX J14012230-5721338	13.38	11458		17
2MASX J14013262-5642279	14.5	13752		17
2MASX J14015295-5651449	12.36	14228		17
2MASX J14015457-5658379	13.53	7998		17
2MASX J14020430-5653028	14.34	13769		17

2MASX J14021880-5651188	12.63	14306		17
WKK 2871:14023739-5648317		15137	15196	17
2MASX J14024769-5633178	13.03	14235		17
2MASX J14025668-5608450	13.75	19118		17
WKK 2882:14025808-5702179			21123	17
2MASX J14043253-5649349	13.83	14253		17
2MASX J14043360-5712169	12.76	11720		17
2MASX J14043603-5642120	12.61	13968		17
2MASX J14043842-5722310	14.1	16759		17
WKK 2922:14044639-5650586		14279		17
2MASX J14052360-5628217	12.92	13746		17
WKK 2955:14061118-5620038		28330	28222	17
WKK 2979:14075177-5624475		11615	11671	17
2MASX J14081215-5707363	12.97	11606		17
2MASX J14083030-5659023	12.02	11699		17
2MASX J14083925-5615432	13.01		5264	17
2MASX J14084752-5659054	13.51	11594		17
2MASX J14155196-5223115	14.65	35222		18
2MASX J14155392-5200405	11.25	4425	4371	18
2MASX J14160447-5236315	10.31	3202		18
2MASX J14160763-5212245	14.24	28322		18
2MASX J14160981-5304595	14.89	28870		18
2MASX J14161521-5238322	14.8	29781		18
2MASX J14161682-5243032	14.61	21672	21753	18
2MASX J14165185-5249233	14.08	14812		18
2MASX J14170190-5139086	14.49	26757	26885	18
2MASX J14173356-5241456	14.35	28657		18
2MASX J14173823-5305386	14.62	29172		18
2MASX J14173908-5245036	14.73	28387		18
2MASX J14174973-5256494	14.57	21738	21711	18
2MASX J14175254-5248214	14.75	27820		18
2MASX J14175891-5301454	14.12	29199		18
2MASX J14180213-5258394	14.14	28969		18
WKK 3115:14180701-5233112		3355	3217	18
2MASX J14181023-5305394	14.93	28673		18
2MASX J14181255-5304114	14.45	28340		18
2MASX J14181871-5313274	13.96	4509	4431	18
2MASX J14181942-5302034	14.81	28966		18
2MASX J14183873-5303332	14.57	31466		18
2MASX J14184672-5258392	14.71	30489		18
2MASX J14185961-5312012	14	30590		18
2MASX J14185991-5142452	13.14	17948		18
2MASX J14192710-5302446	14.68		14840	18
2MASX J14193582-5239426	13.56	14939		18
2MASX J14194401-5141146	14.65	14072	14123	18
2MASX J14195697-5205424	14.3	47485		18
2MASX J14201805-5243155	14.83	50233		18
WKK 3936:14203199-5221130		4434	4248	18
WKK 3146:14204449-5306331			11113	18
2MASX J14205460-5237492	14.89	31172		18
2MASX J14211227-5153311	14.34	9899		18
2MASX J14211879-5233449	15.33	41125		18
WKK 3148:14212431-5234509			4374	18
2MASX J14221383-5205259	14.25	22317	22116	18
2MASX J14221766-5228189	14.13	22217		18
2MASX J14222208-5305310	14.23	28408		18
2MASX J14222599-5203140	15.57	60327		18
WKK 3955:14223509-5203220		28733	28609	18
2MASX J14223791-5227219	15.35	27814		18
2MASX J14225568-5201005	15.33	35090		18
2MASX J14225768-5123266	13.18	10919	10990	18
2MASX J14230691-5241116	14.49	27749		18
2MASX J14232868-5210255	14.97	60340		18
2MASX J14233485-5322528	14.23	18030	17952	18
2MASX J14235517-5239169	14.31	31370		18
2MASX J14241010-5235389	14.1	27630		18
2MASX J14241589-5201153	14.72	27862		18
2MASX J14241742-5319444	14.77	29388		18
2MASX J14243973-5313104	14.34	27727		18
2MASX J14244371-5219534	14.69	17636		18
2MASX J14244807-5220483	13.06	17724		18
2MASX J14250228-5222554	14.44	17736		18
2MASX J14250486-5212235	15.68	48348		18
2MASX J14251293-5243085	12.16	10182		18
2MASX J14251810-5242575	13.22	10181	10100	18
2MASX J14254200-5228235	14.92	21765		18
2MASX J14255412-5304196	14.55	40807		18
2MASX J14260868-5212377	15.15	27615		18
WKK 3976:14261807-5237188		21902	21669	18
2MASX J14262385-5223426	14.83	4626	4596	18
2MASX J14262479-5228187	14.03	21487		18
2MASX J14262642-5229527	12.79	21938		18
2MASX J14263555-5244028	11.84	10143	10094	18
2MASX J14272417-5205552	14.09	16971	17091	18
2MASX J14273079-5207152	13.66	16848	16968	18
2MASX J14274936-5240171	14.48		10385	18
2MASX J14281356-5220375	13.86	10936		18
2MASX J13500076-5247434	14.46	27294		19
2MASX J13501013-5252154	14.25	18792		19
2MASX J13502826-5239385	10.65	3633	3574	19
2MASX J13502912-5256475	11.49	3936	3876	19
2MASX J13512342-5254508	12.44	3894	3873	19
2MASX J13513072-5255237	11.57	4011	3954	19
2MASX J13520368-5213277	14.32	27350		19
2MASX J13520564-5254507	14.28	27446		19
2MASX J13521447-5217206	14.34	14945	14936	19
2MASX J13521594-5225246	14.73	16010	15949	19
2MASX J13523286-5216342	13.72	28879		19
2MASX J13523580-5215393	14.23	29154		19
2MASX J13524103-5215113	14.25	16055		19
2MASX J13524114-5213433	14.16	16216		19
2MASX J13524788-5209223	14.74	29313	28987	19
WKK 3793:13525275-5211272		29111		19
2MASX J13525767-5152022	13.11	14840		19
2MASX J13525797-5304232	14.02	27122		19
2MASX J13530428-5302127	14.96	28468		19
2MASX J13530942-5221107	13.94	27615		19
2MASX J13531528-5202298	13.79	15140		19
WKK 3800:13532239-5204073		28676		19
WKK 2637:13533026-5306346		40385		19
WKK 2640:13533809-5255030			3574	19
2MASX J13534054-5304227	15.05	39587		19
2MASX J13534370-5255577	12.21	5840		19
WKK 2643:13534541-5249041		9339	9297	19
WKK 2644:13534709-5250578		9447	9276	19
2MASX J13534840-5231303	14.79	27770		19
WKK 2645:13534841-5253269		3589	3627	19
WKK 2646:13535105-5255131		9461	9225	19
2MASX J13535660-5213194	13.99	27267		19
2MASX J13541098-5239064	13.68	14664	14654	19
2MASX J13541454-5259484	14.52	40187		19
2MASX J13541877-5305004	14.91	36173		19
2MASX J13542950-5153003	14.34	14930	14777	19
2MASX J13543348-5318403	11.66	3795	3798	19
WKK 3806:13544284-5147139		28817		19
WKK 3807:13544898-5157346		28954		19
WKK 2677:13545182-5313250		9204	9177	19
2MASX J13545602-5316374	14.71	31229		19
2MASX J13551197-5325328	14.65	40660		19
2MASX J13551459-5214303	15.1	51475		19
2MASX J13551851-5213199	14.52	28259		19
2MASX J13551992-5323449	15.16	41734		19
WKK 3810:13552083-5147226		21855	21828	19
2MASX J13552368-5224189	14.81	21165	21276	19
2MASX J13552462-5209099	14.43	27824		19
2MASX J13552729-5222090	15.16	27869		19
WKK 3813:13553102-5206047		27621		19
2MASX J13553625-5215030	12.8	27474		19
2MASX J13553657-5210160	14.23	26901		19
2MASX J13553775-5146260	14.75	22017	21828	19
2MASX J13553880-5301400	13.63	14655	14558	19
2MASX J13553958-5303410	14.04	21463		19
2MASX J13554259-5139590	13.73	28240		19
2MASX J13554296-5201480	14.34	24568		19
WKK 2692:13554332-5234239		27450	27320	19
2MASX J13554529-5215489	14.79	28522		19
2MASX J13555244-5209139	14.89	28046		19
2MASX J13560893-5208068	15.73	28436	28216	19
WKK 3818:13561375-5145378		20129	19810	19
2MASX J13561686-5206549	13.81	27986		19
2MASX J13561771-5219428	14.91	28018	27866	19
2MASX J13562297-5304149	13.35	27273		19
2MASX J13563099-5213188	15.22	28270		19
WKK 2709:13563151-5245472		19589	19549	19
2MASX J13563511-5209308	14.76		26343	19
2MASX J13564312-5243021	13.5	8913	8775	19
2MASX J13564654-5257412	13.45	9555	9342	19
2MASX J13565882-5300282	14.62	36400		19
2MASX J13570184-5221362	14.42	27854	27872	19
2MASX J13570725-5308322	15.04	27099		19
2MASX J13572645-5219392	14.83	27994		19
WKK 2727:13573199-5301041			21840	19
2MASX J13573318-5206443	14.3	27483		19
2MASX J13573484-5246183	11.61	4056	4002	19
2MASX J13574469-5200563	14.89	27302		19
WKK 3825:13575589-5219451		28070	28025	19
WKK 2739:13575741-5247121		4071	3924	19
2MASX J13580203-5242033	13.5	4590	4611	19
WKK 2746:13581703-5322221			4647	19
WKK 2758:13583305-5246059		4506	4434	19
WKK 3829:13585969-5218331		4089	4017	19
2MASX J13594626-5259046	15.06	24640	24685	19
2MASX J14000084-5158476	13.57	14918		19
2MASX J14001350-5328035	14.24	3819	3723	19
2MASX J14001898-5304094	14.32	24695		19
2MASX J14002365-5303434	14.39	25023	24898	19
WKK 2807:14003461-5243192		14148	13967	19
2MASX J14010288-5148063	15.15	27974		19
WKK 2839:14013203-5301192		9488	9425	19
2MASX J14014809-5248338	14.17	41380		19
2MASX J14014839-5252158	12.89	11413	11395	19
2MASX J14020496-5222069	14.98	44244		19
2MASX J14020684-5256379	14.43	24557		19
2MASX J14021332-5241579	14.43	36628		19
2MASX J14023029-5220153	14.63	19520		19
2MASX J14023637-5305513	12.8	6006	5819	19
2MASX J14024828-5234054	14.02	13976	13922	19
2MASX J14031852-5255545	13.6	13844		19

2MASX J13433822-4937573	14.28	26277		20
2MASX J13434576-4910094	14.12	25861		20
2MASX J13440653-4858464	14.67	29361		20
2MASX J13441739-4913474	12.97	16037		20
2MASX J13442373-4855359	14.67	29995		20
2MASX J13442469-4849169	14.18	29239		20
2MASX J13442468-4850109	14.58	29532		20
2MASX J13442910-4856569	13.99	29850		20
2MASX J13445066-4951329	13.88	28061	27977	20
2MASX J13445759-4952439	14.77	28264		20
2MASX J13445866-4958519	13.33	3580	3535	20
2MASX J13450433-5004417	14.94	7992	7915	20
2MASX J13450480-4920048	14.36	12151		20
2MASX J13453244-4856108	14.46	32035		20
2MASX J13454115-4912418	14.02	26167		20
2MASX J13455741-4912198	15.03	28870		20
2MASX J13460370-5009338	14.82	25672		20
2MASX J13461097-4902098	14.57	28838		20
2MASX J13461099-5010388	13.55	26588		20
2MASX J13461764-5005138	14.36	27901	27884	20
2MASX J13461979-4923478	14.22	28414	28336	20
2MASX J13462681-5009148	14.03	27727		20
2MASX J13463308-4935551	13.98	42373		20
2MASX J13463859-5004552	14.64	26471		20
2MASX J13464216-4926322	14.5	22763	22781	20
2MASX J13464274-5005532	14.95	27570		20
2MASX J13464759-4931152	14.56	42202		20
2MASX J13470198-5009482	14.27	21279	21249	20
2MASX J13470447-4915342	14.65	25945	25920	20
2MASX J13471370-4905541	14.57	28390	28402	20
2MASX J13471504-4943232	15.12	26727	26607	20
2MASX J13471616-4915442	14.84	29596		20
2MASX J13472059-4832232	14.3	14679		20
2MASX J13472434-4937592	14.2	29241		20
2MASX J13473232-4907383	14.44	25960		20
2MASX J13473385-4900003	14.76	25339		20
2MASX J13473484-4939003	14.67	28973		20
2MASX J13473628-4920023	13.45	26137	26142	20
2MASX J13473802-4847253	14.98	25558	25491	20
2MASX J13473894-4909593	14.67	25834		20
2MASX J13474324-4921233	15.17	25960		20
2MASX J13474387-4926173	13.82	29266		20
2MASX J13480576-4928310	14.26	42079		20
2MASX J13480873-5016100	14.03	26976		20
2MASX J13481873-5025330	12.45	8145	8196	20
2MASX J13481952-4903251	14.53	29967		20
2MASX J13482125-5014191	14.67	26699		20
2MASX J13482379-4858561	11.5	9693		20
2MASX J13482637-4925590	13.78	29164		20
2MASX J13482737-4958590	13.53	16129	16114	20
2MASX J13482912-4916140	14.74	26301		20
2MASX J13482996-4924460	14.74	82657		20
2MASX J13483670-4958530	13.26	15737		20
2MASX J13483896-4830220	14.9	31524		20
2MASX J13484134-5010130	13.45	8157	8172	20
2MASX J13485500-4957003	14.43	42859		20
2MASX J13490465-5018513	13.79	15905		20
ESO 221-G 002:13490809-4837480		2956	2962	20
2MASX J13491040-4853383	13.92	24910		20
2MASX J13491049-4932443	14.51	26061		20
2MASX J13491300-4947313	14.65	23770		20
2MASX J13492856-4851543	11.17	3861		20
2MASX J13493265-4845453	14.16	24332	24208	20
2MASX J13494276-4846574	13.07	3912	3903	20
2MASX J13494347-4943164	14.23	16504		20
2MASX J13494660-4845094	11.93	2854	2866	20
2MASX J13494872-4835104	14.5	32462		20
2MASX J13495592-4931334	14.63	29481		20
2MASX J13500208-5015154	13.93	27023		20
2MASX J13501812-4838335	14.02	32125		20
ESO 221-IG 005:13501865-4854194			3040	20
2MASX J13502029-4947205	14.78	29206		20
2MASX J13502812-4958445	14.06	14243		20
2MASX J13503000-4946465	13.48	28754		20
2MASX J13503124-4849095	14.29	29042		20
2MASX J13503245-4835225	10.4	3822		20
2MASX J13503484-4940465	12.45	9813		20
2MASX J13503650-4948565	14.22	28880		20
2MASX J13503802-4846295	14.64	31671		20
2MASX J13504251-4858145	13.7	29334		20
2MASX J13504638-4859205	14.59	28948		20
2MASX J13505332-4836284	14.61	14343		20
2MASX J13505649-4955117	14.72	29268		20
2MASX J13505692-4903197	10.18	3178	3145	20
2MASX J13505739-4909037	13.69	29406		20
2MASX J13511341-4840058	14.46	29087		20
2MASX J13513415-5022427	11.61	8260		20
2MASX J13514060-4857156	14.76	28960		20
2MASX J13514587-5009366	13.89	16141		20
2MASX J13520701-4900007	14.41	31551		20
2MASX J13521030-4911217	14.75	39673		20
2MASX J13521321-5002326	14.76	27056	27035	20
2MASX J13521532-4914236	13.88	3133	3127	20
2MASX J13522529-4903442	13.52	31388		20
2MASX J13523598-4903363	14.78	31788		20
2MASX J13523781-4955193	13.35	14441	14390	20
2MASX J13525304-4924272	14.67	29559		20
2MASX J13525371-4942592	13.54	26831		20
2MASX J13525475-4852462	14.79	3598		20
2MASX J13530024-5005332	14.5	26049	26010	20
2MASX J13530605-4854267	14.25	25884	25890	20
2MASX J13531659-4958468	14.13	28546		20
2MASX J13534055-4857007	14.1	29045		20
2MASX J13534158-4859537	14.92	26272		20
2MASX J13534346-4851557	12.1	12196		20
2MASX J13534534-4900347	14.82	25863	25824	20
2MASX J13541640-4924344	14.55	27054		20
2MASX J13542325-4942494	15.08	50513		20
2MASX J13542514-4930084	14.78	24412	24472	20
2MASX J13545817-4949114	15.06	24662	24601	20
2MASX J13552285-4941039	14.01	30908		20
2MASX J19053110-4637373	14.6	19535		21
2MASX J19055978-4604063	13.95	17856		21
2MASX J19060064-4602432	14.32	17973		21
2MASX J19062734-4556095	14.96	24982	25114	21
2MASX J19063086-4655414	15.16	29470	29407	21
2MASX J19063088-4553514	15.04	30794		21
2MASX J19064098-4633584	14.96	5609	5639	21
2MASX J19071077-4608035	15.01	26406	26277	21
2MASX J19072103-4704224	14.49	29407		21
2MASX J19072307-4642104	15.2	32336	32420	21
2MASX J19072743-4638353	15.18	26088		21
2MASX J19073811-4637023	14.04	25968		21
2MASX J19074093-4657573	12.75	25765		21
2MASX J19074122-4631443	15.2	66237		21
2MASX J19074470-4627083	13.11	26056		21
2MASX J19075726-4701043	14.14	25843		21
2MASX J19075734-4543333	13.29	22722		21
2MASX J19080728-4644403	15.45	51225		21
2MASX J19080848-4610013	15.2	62756	62636	21
2MASX J19081667-4719154	13.83	24029	23825	21
2MASX J19082263-4616584	15.49	55143		21
2MASX J19083010-4559553	15.16	36437	36404	21
2MASX J19083128-4635513	15.27	25153	25186	21
2MASX J19083550-4542273	15.56	46144	45928	21
2MASX J19083574-4718203	14.36	24316	23950	21
2MASX J19083684-4701493	14.57	25960		21
2MASX J19083741-4658283	14.64	25528		21
2MASX J19083908-4659523	15.1	24728	24703	21
2MASX J19085014-4708542	14.1	24874		21
2MASX J19085014-4632452	15.17	37378	37264	21
2MASX J19085220-4620212	14.98	30617	30567	21
2MASX J19085321-4652513	14.49	25513		21
2MASX J19085333-4546553	15.12	46064		21
2MASX J19085359-4659342	13.09	25384		21
2MASX J19085437-4700462	15.06	25116		21
2MASX J19085482-4611212	14.59	45749		21
2MASX J19085563-4705102	14.5	26616	26490	21
2MASX J19085674-4638242	15.28	37421		21
2MASX J19090463-4659213	13.79	24446	24298	21
2MASX J19090511-4657242	14.64	37255		21
2MASX J19090677-4651542	14.59	25744		21
2MASX J19091007-4622062	15.07	21738		21
2MASX J19091401-4700022	13.84	25800		21
2MASX J19091547-4658132	13.77	24992	24814	21
2MASX J19091791-4623222	14.59	23755		21
2MASX J19092052-4638531	14.92	25368		21
2MASX J19092178-4659132	14.26	25288	25078	21
2MASX J19092373-4701342	13.87	25521		21
2MASX J19092541-4655452	14.45	25141		21
2MASX J19092666-4702172	15.1	37367		21
2MASX J19092894-4721252	14.51	24254		21
2MASX J19093190-4640442	14.38	21402		21
2MASX J19093240-4630372	15.43	45677		21
2MASX J19093262-4700082	14.81	25368		21
2MASX J19093383-4645092	15.24	24865	24754	21
2MASX J19093868-4719193	13.73	24157		21
2MASX J19093918-4650393	14.77	25417		21
2MASX J19094015-4643153	14.71	25485		21
2MASX J19094317-4648423	14.77	24862		21
2MASX J19094338-4701582	14.91	25471		21
2MASX J19095121-4701262	14.98	26005	25902	21
2MASX J19095478-4547232	14.42	31760	31658	21
2MASX J19100048-4706471	15.3	40451		21
2MASX J19100095-4656021	15.59	45704		21
2MASX J19101297-4635241	14.8	25441	25255	21
2MASX J19101997-4702481	14.98	25117		21
2MASX J19102142-4650021	15.41	25843	25701	21
2MASX J19102897-4702121	13.45	25267		21
2MASX J19103233-4648501	13.76	19447		21
2MASX J19103870-4725020	13.29	5112		21
2MASX J19104027-4653314	14.83	25429		21
2MASX J19104498-4602055	14.92	25222	25138	21
2MASX J19105515-4604205	13.59	5597	5630	21
2MASX J19111058-4712185	14.09	36391		21
2MASX J19111999-4622282	14.73	55552		21
2MASX J19112666-4621543	15.33	55561		21
2MASX J19112945-4548493	14.42	19655		21

2MASX J19113026-4610393	14.92	59210		21
2MASX J19113877-4703203	13.23	5553		21
2MASX J19113972-4637513	15.91	81456		21
2MASX J19115633-4722589	11.75	5055		21
2MASX J19120596-4536120	14.26	25234	25114	21
2MASX J19122633-4601030	14.34	24853	24883	21
2MASX J19122698-4555580	15.32	60693	60630	21
2MASX J19123841-4558035	13.6	21838		21
2MASX J19124311-4557475	13.57	5309	5222	21
2MASX J19124362-4640375	15.35	44973	45056	21
2MASX J19124676-4702415	14.32	5769		21
2MASX J19124777-4533565	14.45	29242		21
2MASX J19124780-4600415	11.02	5364		21
2MASX J19125683-4653445	14.63	29692		21
2MASX J19125839-4644455	12.95	5085		21
ESO 282-G 022:19130019-4545540		5531	5555	21
2MASX J19131295-4709221	14.46	29500	29440	21
2MASX J19131398-4725505	14.41	15881		21
2MASX J19131708-4707481	13.39	5148	5192	21
2MASX J19132148-4618061	14.81	25093	25039	21
2MASX J19132344-4639412	14.76	56455		21
2MASX J19133052-4533132	15.23	58046		21
2MASX J19133101-4644122	13.99	36566		21
2MASX J19133177-4703412	10.1	5466		21
2MASX J19133295-4702312	14.65	24100	24076	21
2MASX J19133949-4648572	15.29	5330		21
2MASX J19134196-4704272	14.78	14267	14276	21
2MASX J19134434-4643252	14.72	25096		21
2MASX J19134885-4610361	15.4	36574		21
2MASX J19135279-4714561	14.52	36419		21
2MASX J19135332-4705311	14.74	59815		21
2MASX J19135397-4659301	14.76	5166		21
2MASX J19135674-4650501	15.13	25030		21
2MASX J19140415-4621401	16.06	82161		21
2MASX J19140471-4533487	14.78	61128		21
2MASX J19140550-4630347	14.47	5300		21
2MASX J19141248-4624297	12.55	5786	5780	21
2MASX J19141322-4709577	15.08	29371		21
2MASX J19141431-4615227	11.26	5202		21
2MASX J19142530-4614247	12.7	14400		21
2MASX J19143113-4644127	12.22	5394	5402	21
2MASX J19143142-4710293	15.23	23834	23929	21
2MASX J19143218-4551563	15.3	61053		21
2MASX J19143468-4635454	10.46	5217	5228	21
2MASX J19143659-4657274	12.51	5291	5213	21
2MASX J19143681-4619284	15.31	26238		21
2MASX J19144132-4540164	15.21	77943	77919	21
2MASX J19144275-4633304	12.75	5282		21
2MASX J19145231-4659255	13.37	5262		21
2MASX J19151042-4622424	12.58	5682		21
2MASX J19151212-4634194	13.4	5379		21
2MASX J19153555-4555381	14.61	12660	12723	21
2MASX J19153689-4702411	15.65	48882		21
2MASX J19153749-4710101	15.4	34473	34392	21
2MASX J19153750-4606561	15.39	59018		21
2MASX J19154052-4545380	11.63	5481		21
2MASX J19154486-4647300	14.5	21199	21126	21
2MASX J19154954-4611510	13.68	21675		21
2MASX J19155458-4547573	15.41	33492		21
2MASX J19160811-4626423	15.05	16633		21
2MASX J19162111-4601523	14.62	21630	21672	21
ACSRG 0108:19163401-4630310		5318	5351	21
2MASX J19163529-4641285	12.49	5352	5300	21
2MASX J19164211-4636036	12.79	5229		21
2MASX J19171040-4645125	14.57	24682	24715	21
2MASX J19171409-4641192	11.96	5355	5270	21
2MASX J19172034-4631392	13.42	29184		21
2MASX J19172528-4636213	13.9	29021	29023	21
2MASX J19172527-4637003	14.31	29646		21
2MASX J20082452-4440095	14.74	17670	17412	22
2MASX J20085057-4446507	15.27	40892		22
ACSRG 0114:20085551-4417510		5792	5639	22
2MASX J20090739-4451247	14.26	15682	15769	22
2MASX J20090739-4449157	15.22	52869		22
2MASX J20094373-4514342	14.16	30629		22
2MASX J20094403-4409132	12.11	5744	5732	22
2MASX J20094610-4520482	15.02	57036	57071	22
2MASX J20095113-4519212	14.67	32942		22
2MASX J20095919-4457432	14.95	31308	31050	22
2MASX J20100024-4521021	15.17	30205		22
2MASX J20101168-4358310	11.98	5718		22
2MASX J20101908-4402260	14.37	5726	5573	22
2MASX J20102693-4524360	14.64	30006		22
2MASX J20103533-4410330	14.76	26744	26876	22
2MASX J20103673-4434390	15.19	42324		22
2MASX J20103979-4408590	15.22		5582	22
2MASX J20104355-4417190	14.61	34783		22
2MASX J20104437-4356392	13.81	5906	5795	22
2MASX J20104595-4508222	14.56	15884		22
2MASX J20104962-4533193	14.46	31502		22
2MASX J20105223-4357173	14.39	5903	5687	22
2MASX J20105230-4401263	14.83	48390		22
2MASX J20105420-4456143	12.96	9372	9303	22
2MASX J20105900-4353273	15.2	13580		22
2MASX J20111745-4515163	15.03		41491	22
2MASX J20111784-4434252	15.52	36958		22
2MASX J20113123-4535357	9.87	5238	5132	22
2MASX J20113440-4436178	15.78	35051		22
2MASX J20114339-4436208	15.14	37815		22
2MASX J20114375-4416078	14.78	5960	5978	22
2MASX J20114431-4410218	14.49	23340		22
2MASX J20114494-4353408	14.35	17994	18128	22
2MASX J20120185-4350426	15.18	54374		22
2MASX J20120521-4510160	15.34	55801		22
2MASX J20120728-4428430	15.13	35670	35498	22
2MASX J20121119-4402480	15.43	72952		22
2MASX J20121174-4408480	11.04	5850		22
2MASX J20122223-4534541	15.3	48764		22
2MASX J20122957-4538171	13.56	48969		22
2MASX J20123159-4544030	15.04	38083	38026	22
2MASX J20123559-4426140	15.53	59797		22
2MASX J20123857-4545330	12.22	9378		22
2MASX J20124201-4440517	15.55	42412		22
2MASX J20124279-4435137	14.21	16534		22
2MASX J20124778-4539087	14.95	18390	18275	22
2MASX J20124939-4515437	15.41	31125		22
2MASX J20125271-4514108	14.28	31259		22
2MASX J20125716-4512418	14.5	34731		22
2MASX J20125860-4453238	15.55	78743		22
2MASX J20130427-4527428	15.36	84100		22
2MASX J20130626-4415068	13.62	16537		22
2MASX J20132094-4518580	14.86	22826	22745	22
2MASX J20132359-4446460	13.17	5184	5216	22
2MASX J20132844-4456360	15.11	61755		22
2MASX J20133109-4448141	15.46	27872	27659	22
2MASX J20133371-4456261	14.28	5139	5147	22
2MASX J20133474-4540231	14.3	40846		22
2MASX J20133514-4449091	12.69	5414	5312	22
2MASX J20133672-4352161	15.49	87819		22
2MASX J20133808-4420281	13.49	5834	5813	22
2MASX J20133926-4503561	15.34	57968	58019	22
2MASX J20134181-4356381	14.91	31161		22
2MASX J20134246-4430011	15.36	72865		22
DJRS J20134796-4502414		16839	16812	22
2MASX J20135083-4409571	15.47	37769		22
2MASX J20135321-4431361	10.77	5825		22
2MASX J20135692-4445020	15.18	55150		22
2MASX J20140547-4445281	14.76	25747		22
2MASX J20141139-4441341	14.91	25849		22
2MASX J20141234-4432411	14.95	40266	40151	22
2MASX J20141253-4437231	11.67	5847		22
2MASX J20142202-4345541	15.14		42298	22
2MASX J20142455-4540181	15	40756		22
2MASX J20142993-4431571	15.22	48270		22
2MASX J20143498-4450500	14.28	10724	10763	22
2MASX J20143896-4426231	15.2	49598		22
2MASX J20143998-4532082	14.91	3262	3163	22
2MASX J20144499-4519072	14.43	30864		22
2MASX J20144516-4439272	15.56	60978		22
2MASX J20144654-4447042	13.65	6218	6164	22
2MASX J20144966-4439072	15.16	61755		22
2MASX J20144989-4422492	13.5	9278		22
2MASX J20145791-4429073	13.65	9294		22
2MASX J20145948-4538383	14.87	49107		22
2MASX J20145958-4535483	15.95	58310		22
2MASX J20150588-4540113	14.04	49005		22
2MASX J20150835-4417522	14.82	23133		22
2MASX J20151163-4518492	15.86	62161		22
2MASX J20151188-4441402	14.69	49173		22
2MASX J20151754-4527370	15.89	40958		22
2MASX J20152019-4512280	15.73	74616		22
2MASX J20152134-4431490	14.81	15185	15083	22
2MASX J20152208-4354400	14.82	42568		22
2MASX J20152504-4532270	13.49	9234	9255	22
2MASX J20152715-4524061	15.07	30861		22
2MASX J20153158-4541071	14.8	48357		22
2MASX J20153619-4456321	15.33	63554		22
2MASX J20153677-4430381	14.92	57843		22
2MASX J20153855-4520561	15.76	89932		22
2MASX J20154062-4443311	15.65	64309		22
2MASX J20154994-4356421	15.35	49673	49778	22
2MASX J20155152-4426150	13.38	9609		22
2MASX J20155444-4430130	14.37	9257		22
ESO 284-G 038:20155462-4429395		9282		22
2MASX J20155569-4418490	12.7	9294		22
2MASX J20155830-4443167	14.99	23090		22
2MASX J20160207-4541547	15.07	48501		22
2MASX J20160547-4433117	14.91	9169		22
2MASX J20160572-4412337	15.71	71987		22
2MASX J20160577-4356217	14.05	23252		22
2MASX J20160651-4425177	11.92	5417	5399	22
2MASX J20161800-4417598	10.57	5334		22
2MASX J20161942-4501217	15.48	63779		22
2MASX J20162058-4529557	14.83	27748		22
2MASX J20162312-4512367	15.39	60007		22
2MASX J20162637-4412007	15.28	73144		22
2MASX J20162682-4440497	15.7	73371		22
DJRS J20162915-4431031		30921	30657	22

2MASX J20162947-4422187	14.52	23182	23084	22
2MASX J20163659-4440318	14.95	42189		22
2MASX J20164523-4408359	14.2	23456		22
2MASX J20164554-4456349	15.17	73443		22
2MASX J20164624-4441419	13	5927	5885	22
2MASX J20164784-4438179	13.49	5822	5792	22
2MASX J20164792-4409319	14.72	31031		22
2MASX J20164893-4415519	15.58	42304	42346	22
2MASX J20165058-4428319	15.62	30867	30774	22
2MASX J20165236-4533569	15.43	42379	42436	22
2MASX J20165327-4449209	15.52	54296		22
2MASX J20165332-4538429	14.96	41179		22
2MASX J20165389-4535249	15.67	61569		22
2MASX J20165452-4401089	15.35	42388	42559	22
2MASX J20165647-4351209	15.07	29314	29401	22
2MASX J20165713-4538409	15.31	49082		22
2MASX J20165769-4448489	13.81	16624		22
2MASX J20170023-4454089	15.25	36138		22
2MASX J20170182-4446409	14.19	64219		22
2MASX J20170394-4513269	15.03	40849		22
2MASX J20170422-4426449	15.06	41975		22
2MASX J20171195-4526489	14.59	40626		22
2MASX J20171363-4442509	15.72	5843	5813	22
2MASX J20171543-4416522	15.6	73156		22
2MASX J20171708-4514322	14.45	41141	41135	22
2MASX J20171875-4504462	14.69	41579		22
2MASX J20172049-4430552	13.11	2770	2575	22
2MASX J20172577-4523043	14.58	24052		22
2MASX J20173197-4452093	14.98	40349	40325	22
2MASX J20173376-4458023	14.62	6026	5996	22
2MASX J20173563-4406073	13.81	42319		22
2MASX J20173938-4435213	15.2	41815		22
2MASX J20173973-4412063	14.73	40250		22
2MASX J20174140-4409573	15.48	40476		22
2MASX J20174412-4454523	14.14	41650		22
2MASX J20174697-4533083	15.49	41213	41120	22
2MASX J20175085-4526222	15.61	73860		22
2MASX J20175488-4528331	15.23	41431		22
2MASX J20180323-4531092	11.83	5217		22
2MASX J20180334-4414022	15.13	41935		22
2MASX J20180902-4456002	15.19	54422		22
2MASX J20181086-4429402	14.7	40332		22
2MASX J20181181-4415172	15.4	42064		22
2MASX J20181815-4448252	9.99	2512	2416	22
2MASX J20183041-4432382	14.55	41801		22
2MASX J20183245-4408312	14.62	42111		22
2MASX J20183373-4522271	15.6	62615		22
2MASX J20183390-4406291	14.22	42382		22
2MASX J20183543-4451241	13.6	16690	16719	22
2MASX J20184502-4414042	15.73	42322	42184	22
2MASX J20185622-4504482	13.14	6227	5996	22
2MASX J20191131-4423402	15.3	38274		22
2MASX J20192544-4443533	15.54	62936		22
2MASX J20193811-4447384	14.08	17095		22
2MASX J20194431-4448083	12.67	16663		22
2MASX J20194661-4431133	15.29		19127	22
2MASX J18185988-7647409	13.86	21516	21474	23
2MASX J18201407-7616219	14.45	5690	5627	23
2MASX J18202490-7615585	13.99	21162		23
2MASX J18210765-7641418	12.11	5558		23
2MASX J18212466-7634598	10.28	5589		23
2MASX J18225774-7641452	11.88	5493	5369	23
2MASX J18243261-7715031	14.03	21465	21456	23
2MASX J18251504-7704318	12.41	5657	5579	23
2MASX J18253843-7730049	14.87	29290	29350	23
2MASX J18254557-7723129	13.15	12600	12639	23
2MASX J18254872-7704079	13.97	11681		23
2MASX J18254989-7711019	15.13	43635		23
2MASX J18261682-7703490	14.96	39189	39222	23
2MASX J18261845-7653008	14.69	21917		23
2MASX J18264398-7708153	14.76	21703	21627	23
2MASX J18265622-7709274	13.61	13502	13506	23
2MASX J18265773-7651544	14.35	21258	21174	23
2MASX J18272441-7704385	12.4	12981		23
2MASX J18274180-7709105	14.94	12015		23
2MASX J18274659-7719545	14.63	13147	13188	23
2MASX J18275646-7700474	13.31	11877	11881	23
2MASX J18275699-7714084	14.75	29485		23
2MASX J18280030-7557469	15.96	67616		23
PKS 1820-774 NED01 :18280461-7727580			36758	23
2MASX J18281784-7709311	11.28	12523		23
2MASX J18282563-7729442	13.36	16840		23
2MASX J18283484-7730402	13.19	5957	5900	23
2MASX J18283655-7656243	11.85	5688		23
2MASX J18284039-7707543	14.55	13251	13275	23
2MASX J18284969-7706233	14.74	11956		23
2MASX J18285721-7553363	14.79	26921	27044	23
2MASX J18290135-7729363	15.27	29560	29392	23
2MASX J18292475-7700073	12.72	12174		23
2MASX J18293901-7719202	14.87	29128		23
2MASX J18293963-7655141	14.95	21759	21825	23
2MASX J18294221-7706043	11.68	12709		23
2MASX J18294544-7702103	14.51	30469	30519	23
2MASX J18294701-7710433	15.07	21711		23
2MASX J18300178-7709254	13.91	12312	12190	23
2MASX J18300392-7716094	15.35	43105	43011	23
2MASX J18300597-7636464	14.02	13275	13221	23
2MASX J18305154-7626185	14.99	5597	5594	23
2MASX J18305851-7739555	14.57	33142		23
2MASX J18310003-7634315	14.39	21156	21057	23
2MASX J18310747-7640594	15.33	27110	27161	23
2MASX J18310888-7705216	15.24	12594		23
2MASX J18311708-7546353	13.67	5747	5660	23
2MASX J18312945-7716539	14.45	12175	12118	23
2MASX J18314502-7712530	15.22	35114		23
2MASX J18315351-7619491	14.07	31772		23
2MASX J18315424-7732051	14.64	32500		23
2MASX J18315777-7708071	14.34	21825	21759	23
2MASX J18320279-7713241	15.34	42864		23
2MASX J18321244-7711411	13.86	12694	12537	23
2MASX J18321535-7649171	14.9	21883		23
2MASX J18322065-7652211	14.45	15197	15196	23
2MASX J18323541-7645190	13.75	21580		23
2MASX J18332656-7659522	12.74	5517		23
2MASX J18333049-7711372	15.15	13113		23
2MASX J18335940-7657152	13.13	5898	5789	23
2MASX J18340625-7552182	14.77	12591	12576	23
2MASX J18351105-7606032	14.91	18783		23
2MASX J18351694-7548222	13.99	20572		23
2MASX J18353191-7550062	12.49	11215		23
2MASX J18353580-7724042	12.54	12679		23
2MASX J18354864-7732311	14.61	32815		23
2MASX J18355260-7549501	13.39	11467	11404	23
2MASX J18360848-7702155	13.98	12862		23
2MASX J18361522-7645416	13.99	15167	15196	23
2MASX J18361959-7637528	14.96	21054	21003	23
2MASX J18362812-7633107	14.83	35912		23
2MASX J18363942-7717167	11.94	5552		23
2MASX J18370473-7646497	14.54	21645		23
2MASX J18370918-7636317	14.97	19882	19870	23
2MASX J18371645-7646482	15.3	22242		23
2MASX J18373384-7648055	14.73	22154		23
2MASX J18373860-7646426	13.99	21618		23
2MASX J18374404-7737095	14.95	37000	36985	23
2MASX J18375734-7644508	14.24	20872	20878	23
2MASX J18381754-7731469	12.03	5340	5258	23
2MASX J18382157-7635599	13.99	20985		23
2MASX J18382631-7708269	15.2	31943		23
2MASX J18383550-7610359	14.67	21207		23
2MASX J18384135-7712509	13	5388		23
2MASX J18384210-7722189	13.55	5687		23
2MASX J18384364-7556379	13.97	12069		23
2MASX J18385174-7623448	14.37	21180		23
2MASX J18385496-7711261	14.72	31946		23
2MASX J18390002-7633552	15.32	20716		23
2MASX J18390050-7552118	14.88	12552		23
2MASX J18390191-7645208	14.38	21865		23
2MASX J18390966-7631093	15.25	20983		23
2MASX J18391447-7607114	14.88	24224		23
2MASX J18391688-7640214	13.85	15230	15229	23
2MASX J18392756-7633575	14.91	20860	20605	23
2MASX J18393158-7736475	12.59	12717		23
2MASX J18393505-7708416	14.49	4620		23
2MASX J18394678-7618386	14.04	12345	12354	23
2MASX J18394935-7539006	14.36	12751		23
2MASX J18395164-7700326	12.66	5585		23
2MASX J18395297-7740446	14	21553	21480	23
2MASX J18395596-7555447	14.49	11728		23
2MASX J18395892-7737346	13.24	12592		23
2MASX J18400514-7736307	15.05	32447	32423	23
2MASX J18401812-7650126	14.68	11344		23
2MASX J18402280-7554216	14.91	12804		23
2MASX J18402360-7708586	14.75	5534		23
2MASX J18402926-7708005	11.98	5072		23
2MASX J18403957-7556025	14.23	12289		23
2MASX J18404428-7545432	14.63	43138		23
2MASX J18405544-7555373	11.53	12475		23
2MASX J18410692-7556194	14.01	13631		23
2MASX J18412248-7656435	14.79	30225		23
2MASX J18412836-7658246	12.55	5666		23
2MASX J18412967-7622386	14.72	35960		23
2MASX J18414619-7559176	14.34	12378		23
2MASX J18414927-7603156	14.9	35726	35777	23
2MASX J18420100-7713035	12.77	5196		23
2MASX J18420526-7552375	14.11	12039	11872	23
2MASX J18422359-7540540	13.74	10332	10259	23
2MASX J18422554-7555130	14.65	12004		23
2MASX J18422845-7630201	13.08	15515	15364	23
2MASX J18431484-7550023	14.92	12025	12064	23
2MASX J18431555-7622243	14.01	12481		23
2MASX J18433277-7558522	14.13	12709		23
2MASX J18433833-7618062	14.23	12490	12279	23
2MASX J18441415-7731044	14.27	32839		23
2MASX J18441577-7600214	14.7	12585		23
2MASX J18442093-7608235	14.73	42059		23
2MASX J18442238-7600494	12.44	12580		23
2MASX J18444454-7723534	15.06	51957		23

2MASX J18444583-7658274	14.5	21232		23
2MASX J18444843-7618394	13.61	12465		23
2MASX J18450340-7721563	15.09	42104	41869	23
2MASX J18450991-7621569	14.74	20664		23
2MASX J18451762-7611320	14.7	52314		23
2MASX J18453854-7659162	15.4	77220		23
2MASX J18454255-7600143	15.08	46612		23
2MASX J18461357-7625084	14.42	26631		23
2MASX J18463576-7600383	14.24	10721	10754	23
2MASX J18464114-7549192	14.94	21627	21555	23
2MASX J18470798-7634422	15.12	42062		23
2MASX J18471528-7700472	14.51	20219		23
2MASX J18472611-7553283	13.89	12415		23
2MASX J18475332-7648103	15.3	22034		23
2MASX J18475539-7607523	14.74	48987		23
2MASX J18480995-7729082	15.13	32672		23
2MASX J18481442-7656301	15.66	51652		23
2MASX J18482173-7633340	15.31	41636		23
2MASX J18483996-7648315	15.35	41329		23
2MASX J18490859-7648186	13.68	21004	20872	23
2MASX J18492234-7650486	14.65	22065		23
2MASX J18493494-7619555	14.45	21432		23
2MASX J18494530-7707155	13.98	35627		23
2MASX J18502225-7629001	14.45	50944		23
2MASX J18515903-7626023	14.95	21246	21222	23
2MASX J14013301-5045480	14.23	27095	27176	24
2MASX J14022699-5057138	12.64	28156		24
2MASX J14025101-5014594	14.35	27530	27422	24
2MASX J14031138-5103454	15.08	28291		24
2MASX J14033104-5006515	13.18	21603		24
2MASX J14033568-5118105	15.01		16893	24
2MASX J14035080-5114255	14.29	7612	7504	24
WKK 3858:14035529-5115410			16525	24
2MASX J14035980-4959520	14.3	21511	21471	24
2MASX J14042594-5104521	15.18	27910		24
2MASX J14043514-4956340	14.63	52685		24
2MASX J14044212-5128468	14.36	4230	4215	24
2MASX J14044752-5114328	14.24	9776	9761	24
2MASX J14050092-5059009	14.16	27593		24
2MASX J14051936-5034163	13.6	27503		24
2MASX J14053062-5050544	14.38	31562		24
2MASX J14053278-5038524	14.67	39159		24
2MASX J14054149-5102414	15.49	29227		24
2MASX J14054383-5105215	14.22	29829		24
2MASX J14055642-5057574	14.18	29206		24
2MASX J14055812-5059364	14.91	29123		24
2MASX J14060358-5106163	14.79	27552		24
2MASX J14060484-5103005	14.33	28423		24
2MASX J14060610-5103413	14.69	28567		24
2MASX J14060732-5112375	14.71	29718		24
2MASX J14061071-5055575	14.48	27393		24
2MASX J14061133-5059485	14.65	27156		24
2MASX J14062065-4954416	14.37	18776		24
2MASX J14062626-5109446	15.31	21513	21603	24
2MASX J14063082-5101596	14.76	28604		24
2MASX J14064078-5100405	14.79	27908		24
2MASX J14064108-5057035	15.11	26736		24
2MASX J14064356-5000125	14.25	22676		24
2MASX J14065608-5100409	14.85	27291		24
2MASX J14070339-5101060	15.17	28040		24
WKK 3868:14070511-5104188		31455		24
2MASX J14070900-5101200	13.21	27467		24
2MASX J14070975-5049570	14.2	28807		24
2MASX J14071401-5010280	14.13	21064	21027	24
2MASX J14071821-5056080	13.41	28295		24
2MASX J14072378-5006269	14.36	27654		24
2MASX J14072674-5016099	14.8	21685	21711	24
2MASX J14072789-5104049	14.8	26715		24
2MASX J14072804-5127349	15.01	23256		24
2MASX J14073358-5105438	13.55	28213		24
2MASX J14073722-5100429	14.86	28654		24
2MASX J14074186-5039559	14.98	24112	24001	24
2MASX J14074580-5059489	14.2	29277		24
2MASX J14075280-5101359	14.7	28193		24
2MASX J14075447-5013109	14.06	21496		24
2MASX J14075523-5059509	13.02	29133		24
2MASX J14080859-5101059	13.91	14160		24
2MASX J14080990-5108589	15.22	27845		24
2MASX J14081794-5116218	15.43	59914		24
2MASX J14081933-5043142	14.3	30139		24
2MASX J14084295-5059293	14.81	29553		24
2MASX J14085023-5029362	14.74	24175	24085	24
2MASX J14085151-5034312	14.82	27642		24
2MASX J14085476-5108202	14.71	31883		24
2MASX J14090220-5110078	12.51	4572		24
2MASX J14090223-5015059	13.97	21612		24
2MASX J14090788-5100169	15.46	29568		24
2MASX J14090856-5115039	13.61	14076		24
2MASX J14091413-5059349	13.5	30477		24
WKK 3882:14091579-5133439			4251	24
2MASX J14093619-5010179	14.25	2869	2902	24
2MASX J14094159-5116418	15.33	31769		24
2MASX J14094697-5110304	14.1	21540	21480	24
2MASX J14100178-5049305	14.14	28849		24
WKK 3889:14100994-5054209		21391	21408	24
2MASX J14102783-5056598	14.46	29042		24
2MASX J14102933-5053269	14.16	30012		24
2MASX J14104277-5037239	14.76	59575		24
2MASX J14110786-5100298	14.43	29015		24
2MASX J14110965-5101226	14.5	27710		24
2MASX J14111536-5047076	14.69	27501		24
DENIS J141121.3-504629		27434	27332	24
2MASX J14112213-5043517	15.01	28523		24
WKK 3899:14112772-5117596		14890	14936	24
2MASX J14113087-5042007	14.4	27323	27149	24
2MASX J14113118-5051107	14.72	29919		24
2MASX J14113725-5133007	14.87		14195	24
2MASX J14114047-5052407	14.44	27995		24
2MASX J14114291-5055057	15.38	29412		24
2MASX J14120530-5106552	14.56	27479		24
WKK 3903:14122101-5121248		21600	21747	24
2MASX J14122533-5055031	14.22	18090	18158	24
2MASX J14123581-5057121	14.87	28504		24
2MASX J14125956-5042140	15.14		28468	24
2MASX J14130503-5040290	14.97	28094	27953	24
2MASX J14131699-5034379	13.43	28720		24
2MASX J14345915-4535305	14.69	23540	23696	25
2MASX J14365201-4526547	13	15326	15337	25
2MASX J14365489-4438386	14.83	31637		25
2MASX J14365739-4520406	14.4	31349		25
2MASX J14370036-4524526	14.15	23569		25
2MASX J14370190-4545456	15.45	71768		25
2MASX J14370314-4527390	14.08	15176		25
2MASX J14370383-4425551	14.51	34105		25
2MASX J14370406-4533571	14.71	23720		25
2MASX J14371254-4533381	14.23	10891	10823	25
2MASX J14371368-4535341	14.36	23461		25
2MASX J14371626-4531051	14.27	23935		25
2MASX J14372859-4552261	15.07	35399		25
2MASX J14373015-4531451	15.02	24801		25
2MASX J14373487-4521431	14.98	34170		25
2MASX J14373978-4535080	14.87	24859		25
2MASX J14374188-4524294	13.4	34128		25
2MASX J14374194-4532194	14.66	23090		25
2MASX J14374307-4533244	14.01	21798		25
2MASX J14374646-4605574	14.88	23654	23660	25
2MASX J14375763-4542165	14.8	22859	22769	25
2MASX J14375793-4533465	14.5	23174		25
2MASX J14375832-4512405	15.45	35168	35109	25
2MASX J14380191-4457495	15.51	45934	45913	25
2MASX J14380241-4551465	14.54	23368		25
2MASX J14380314-4501465	14.86		22347	25
2MASX J14380374-4537085	14.13	23069		25
2MASX J14380611-4535024	13.87	22004		25
2MASX J14381059-4534514	14.64	23061		25
2MASX J14381082-4444134	14.24	21947	21846	25
2MASX J14381163-4531524	14.93	22410	22317	25
2MASX J14381258-4556524	14.25	33681		25
2MASX J14381271-4516384	14.67	23698		25
2MASX J14381389-4525464	13.96	23959		25
2MASX J14381502-4606374	14.67	23681	23732	25
2MASX J14381769-4523084	14.74	22706	22793	25
2MASX J14381845-4601254	14.58	31037		25
2MASX J14382352-4437365	14.97	24316	24253	25
2MASX J14382433-4504435	14.93	23530		25
2MASX J14382761-4535175	12.93	24337		25
2MASX J14383237-4537515	14.78	31101		25
2MASX J14383410-4443185	15.01	44538		25
2MASX J14383832-4452145	14.97	23408	23393	25
2MASX J14383849-4506265	15.3	23196		25
2MASX J14384048-4454425	13.31	10415	10319	25
2MASX J14384086-4531275	14.86	23381	23339	25
2MASX J14384599-4530195	14.64	15412	15220	25
2MASX J14384943-4534455	13.63	23195		25
2MASX J14385093-4455415	14.78	23447	23315	25
2MASX J14390132-4437392	14.4	21966	22089	25
2MASX J14390255-4532562	15.03	22952		25
2MASX J14390447-4446222	14.67	36394		25
2MASX J14390470-4457463	14.64	71945		25
2MASX J14390548-4452543	14.64	23863		25
2MASX J14390663-4603123	15.25	32467		25
2MASX J14390841-4516493	14.32	23563	23516	25
2MASX J14391323-4523053	14.41	23696	23486	25
2MASX J14391528-4433033	14.93	30842		25
2MASX J14391671-4604293	14.94	33049		25
2MASX J14392380-4432113	14.77	43968		25
2MASX J14393065-4508413	14.91	46046		25
2MASX J14393334-4519373	14.64	26224		25
2MASX J14393346-4439073	15.17	44376		25
2MASX J14393368-4531073	14.52	23638		25
2MASX J14393382-4604003	13.88	35357		25
2MASX J14393407-4555333	14.09	33037		25
2MASX J14393515-4501082	9.21	2818		25
2MASX J14393522-4517052	15.18	17506	17385	25
2MASX J14394636-4547156	14.89	26634		25
2MASX J14395190-4548356	14.93	26766		25
2MASX J14395414-4507536	14.74	23837		25
2MASX J14395879-4547256	14.05	26625		25

2MASX J14395924-4509106	13.84	23521	23435	25
2MASX J14395934-4501256	14.14	26095		25
2MASX J14400016-4432276	14.88	31020	30915	25
2MASX J14400241-4435366	15.15	31919		25
2MASX J14401087-4418526	10.36		2815	25
2MASX J14401107-4534586	14.87	31371		25
2MASX J14401390-4430215	14.89	31841	31589	25
2MASX J14401450-4537543	14.91	31098	30996	25
2MASX J14401521-4602325	14.98	23525	23636	25
2MASX J14401565-4536383	15.39	32251		25
2MASX J14401580-4436275	14.72	36011		25
2MASX J14401645-4526275	14.9	25432		25
2MASX J14401668-4607563	14.59	25440		25
2MASX J14401757-4604273	15.07	26991		25
2MASX J14402256-4603584	13.88	26598		25
2MASX J14402478-4602464	14.85	26273		25
2MASX J14402938-4432064	14.07	32225		25
2MASX J14402952-4553074	13.4	23831		25
2MASX J14403365-4449054	14.6	24274		25
2MASX J14403471-4536094	14.56	26730		25
2MASX J14403641-4551564	12.32	23572		25
2MASX J14403644-4522104	14.59	25902	25920	25
2MASX J14404120-4553004	15.33	23684		25
2MASX J14404137-4519194	13.43	31346		25
2MASX J14404164-4502274	14.18	26064		25
2MASX J14404735-4523054	14	25822		25
2MASX J14404756-4409514	14.14	25255		25
2MASX J14405262-4535154	14.64	31512	31541	25
2MASX J14405280-4555124	14.8	23881		25
2MASX J14405324-4523354	14.99	31688		25
2MASX J14405408-4520044	15.15	30890		25
2MASX J14405582-4422318	15.05	53021		25
2MASX J14405649-4540228	14.83	23789		25
2MASX J14405719-4444378	14.7	24265		25
2MASX J14405785-4426438	14.71	31829	31790	25
2MASX J14405827-4510468	15.01	31115		25
2MASX J14410110-4554398	15.02	23873		25
2MASX J14410191-4414379	14.33	25579		25
2MASX J14410383-4543259	14.75	31538		25
2MASX J14411329-4530519	14.12	17350		25
2MASX J14411438-4412249	15.38	24868		25
2MASX J14411653-4431329	14.58	36382		25
2MASX J14412226-4543569	14.4	31649		25
2MASX J14412390-4425389	14.26	21729		25
2MASX J14412804-4502419	14.88	25750		25
2MASX J14412822-4554349	15.09	23477		25
2MASX J14412831-4459509	15.17	31970		25
2MASX J14413261-4512048	15.16	25768	25581	25
2MASX J14413433-4456348	15.48	70695		25
2MASX J14413438-4447468	14.06	25723		25
2MASX J14413769-4537051	14.84	30836		25
2MASX J14413886-4532542	15.36	57918		25
2MASX J14414257-4427032	15.32	15748	15898	25
2MASX J14414285-4427552	14.98		25629	25
2MASX J14414615-4514562	14.89	25537		25
2MASX J14414908-4517282	14.93	31796		25
2MASX J14420531-4443192	14.27	35622		25
2MASX J14421152-4426102	14.19	25363		25
2MASX J14422275-4533340	15.21	54544		25
2MASX J14422427-4505570	14.5	17170		25
2MASX J14422513-4502270	15.88	34212		25
2MASX J14423306-4454051	14.87	24943	24796	25
2MASX J14423730-4508311	14.69	24916		25
2MASX J14424578-4456591	16.49	24928	24964	25
2MASX J14424709-4522540	14.83	57882		25
2MASX J14425201-4420540	15.15	37543		25
2MASX J14425252-4545518	14.91	39728		25
2MASX J14425392-4434378	14.75	23198		25
2MASX J14425861-4530189	15.46	55444	55453	25
2MASX J14430227-4520359	15.01	20823		25
2MASX J14430528-4530139	13.98	10469		25
2MASX J14430698-4452109	15.09	70920		25
2MASX J14430719-4522239	14.94	51345		25
2MASX J14432185-4452539	13.95	24955		25
2MASX J14433478-4442453	14.89	35684		25
2MASX J14433526-4440393	14.79	22268		25
2MASX J14434722-4500433	15.03	25012		25
2MASX J14435355-4438504	13.65	22019		25
2MASX J14435734-4544324	14.6	55516		25
2MASX J14440248-4451483	14.95	22769	22766	25
2MASX J14440358-4442463	14.71	24247		25
2MASX J14444244-4537474	15.06	31637	31574	25
2MASX J14451883-4524304	14.33	23741		25
2MASX J16440862-5930182	12.66	16046		26
2MASX J16444512-5919180	12.31	16243		26
2MASX J16445860-5936321	13.51	21351		26
2MASX J16450581-5951301	14.04	18497	18662	26
2MASX J16452293-5955252	11.46	5292	5204	26
2MASX J16454935-5908318	13.16	16034		26
2MASX J16460938-5935048	12.86	15491		26
2MASX J16463770-6013150	13.11	16067		26
2MASX J16464491-6024210	13.3	43860		26
WKK 7442:16465208-6016599			16204	26
2MASX J16465404-5914268	14.05	18167		26
2MASX J16472619-5943233	13.59	21399		26
2MASX J16474073-6008563	11.2	3304	3283	26
2MASX J16475728-5858212	13.95	14891		26
WKK 7480:16481819-5949494		14133		26
WKK 7482:16481891-5945410			30600	26
2MASX J16483097-5943293	14.69	48170		26
WKK 7498:16484501-5935341			15592	26
WKK 7509:16490505-5909464		17943		26
2MASX J16491749-6033435	13.26	16049		26
WKK 7517:16491798-5906072		21303		26
WKK 7527:16493754-5905017		34854		26
WKK 7530:16493805-5909482		14595	14555	26
2MASX J16495126-5925228	13.71	15059		26
2MASX J16495328-5936298	14.03	20991		26
2MASX J16495638-5950488	14.3	13656		26
2MASX J16500329-5942198	13.9	13953		26
2MASX J16501832-5954224	13.47	14288		26
2MASX J16502809-6020324	14.03	13731		26
WKK 7550:16502969-5910304		15116		26
2MASX J16504726-6035333	14.69	26840		26
2MASX J16505265-6005023	12.91	12448		26
2MASX J16510156-5953166	12.85	13623		26
2MASX J16510249-5921376	12.87	13437		26
2MASX J16510272-6048313	9.51	3068		26
2MASX J16510360-6001053	12.99	5852	5822	26
WKK 7578:16510521-5922199		13859	13829	26
2MASX J16510681-5859364	9.21	1646	1562	26
2MASX J16510768-6008063	13.36	14339	14240	26
2MASX J16510801-5944116	14.87	37403	37396	26
2MASX J16510933-6001203	14.65	14094		26
2MASX J16511114-6035204	14.3	24442	24349	26
WKK 7580:16511428-6008362		15086	15134	26
2MASX J16511520-6001494	12.96	15311		26
2MASX J16511947-6006464	13.43	14334	14303	26
2MASX J16512022-5914041	11.05	2542	2701	26
2MASX J16512454-5953224	14.91	13976		26
ESO 137-IG 047 NED02 :16513151-6035161			3316	26
2MASX J16513733-5958023	14.17	15365		26
2MASX J16514226-5900242	13.65	14861		26
2MASX J16514431-6015133	14.81		14132	26
2MASX J16514446-5903262	14.87	61358		26
2MASX J16514469-6037173	13.87	14379		26
2MASX J16514472-5912192	13.67	14882		26
2MASX J16514472-5925372	12.27	14301		26
2MASX J16514511-5928512	13.98	14493		26
2MASX J16514521-5959503	14.42	14067		26
WKK 7606:16514721-5922278		13737	13805	26
2MASX J16514817-5947503	14.54	15170		26
WKK 7610:16515189-5928098		14312	14372	26
2MASX J16515328-5936032	14.34	13887	13680	26
2MASX J16515376-6039082	14.53	14175		26
2MASX J16515387-5949042	13.77	13377		26
2MASX J16515442-6020112	14.28	14481		26
2MASX J16515765-5939022	14.43	14271		26
2MASX J16515883-5958462	13.15	15344	15199	26
WKK 7618:16515981-5916070		15263	15128	26
2MASX J16520132-5936032	13.77	13210		26
2MASX J16520477-5925251	13.44	13428		26
2MASX J16520540-5953243	12.68	14409	14282	26
2MASX J16521135-5959413	14.28	15125		26
2MASX J16521198-5948480	13.17	16174		26
2MASX J16521414-6048123	13.43	14532		26
2MASX J16521458-5940101	13.01	14322		26
2MASX J16521598-5928421	12.8	13251		26
2MASX J16522228-5930441	13.62	12397		26
2MASX J16522423-5934131	14.1	16591	16543	26
2MASX J16522498-5906341	13.73	14825		26
2MASX J16522655-5958523	13.56	15224		26
2MASX J16522685-6008363	13.45	15608		26
2MASX J16523004-5900181	14.05	17712	17682	26
2MASX J16523108-5854181	12.31	14804		26
2MASX J16523134-5939091	14.74	12519		26
2MASX J16523251-5917511	14.16	13884		26
2MASX J16523266-5938231	12.91	13779		26
2MASX J16523562-5959263	13.69	15356		26
2MASX J16523635-5934121	14.08	13470		26
2MASX J16523673-5929131	13.41	13872		26
2MASX J16523827-5957271	13.35	14403		26
2MASX J16523953-5940321	13.75	15071		26
2MASX J16524632-5913009	8.1		1340	26
WKK 7650:16524795-6001314		14328	14276	26
2MASX J16524840-5856461	11.38	2900	2905	26
2MASX J16524916-6023322	14.53	25240		26
2MASX J16525085-6008183	14.18	15511		26
2MASX J16525287-5940580	13.37	13680		26
2MASX J16525317-5954453	14.92	15383		26
2MASX J16525488-5920330	14.07	14975		26
2MASX J16525563-5951000	14.84	15170		26
2MASX J16525894-5941420	11.57	14310		26
2MASX J16530043-5950130	13.73	13344		26
2MASX J16530416-6034344	14.02	24578		26
2MASX J16530494-5944189	12.97	14454		26
2MASX J16530501-5942240	13.38	14343		26

2MASX J16530555-5941228	14.59	14738		26
2MASX J16530647-5853000	13.59	15451	15388	26
WKK 7662:16530727-6001214		15122		26
2MASX J16531101-5933581	14.03	13644		26
2MASX J16531220-5932471	14	13530		26
WKK 7673:16531337-5916541		13272		26
2MASX J16531742-5945441	14.3	15527		26
2MASX J16531748-6017145	14.66	26943		26
2MASX J16531868-6037265	12.9	14031		26
2MASX J16532485-6004175	14.34	26769		26
2MASX J16532530-6021345	13.85	25225		26
WKK 7680:16532801-5850038		13584	13611	26
2MASX J16532834-6009075	14.61	14438	14159	26
2MASX J16533213-6014184	15.57	16576		26
2MASX J16533499-6020214	13.39	37807		26
2MASX J16533508-5954451	14.52	14214		26
2MASX J16534095-6010304	14.58	13932		26
2MASX J16534313-5855370	13.23	15530		26
2MASX J16534541-6044433	14.58	14031		26
2MASX J16534789-5902577	12.97	13899		26
2MASX J16535337-5846408	9.23	2669		26
2MASX J16535367-5947008	13.99	14082		26
2MASX J16535436-5944228	14	14175		26
2MASX J16540337-5941299	13.61	13530		26
2MASX J16540625-5948019	14.24	13746		26
2MASX J16540963-6024084	14.26	15395		26
2MASX J16541486-5931119	14.21	13806		26
2MASX J16541500-5950509	13.15	15815		26
2MASX J16541827-6029564	14.64	16642		26
2MASX J16542058-6037254	14.86	13956		26
WKK 7707:16542352-5926323			2599	26
2MASX J16542755-6017194	14.45	14415		26
WKK 7709:16543079-5941463		14882		26
2MASX J16543129-5900408	14.78	26631		26
2MASX J16543422-5922368	14.69	15577	15619	26
2MASX J16543716-5956543	13.36	15361	15307	26
2MASX J16544904-6014473	13.72	15383		26
WKK 7719:16545169-5933569		14777		26
2MASX J16545978-5942043	14.76	14741		26
2MASX J16550124-5935343	14.13	21603	21384	26
2MASX J16550431-5959324	13.93	14684		26
WKK 7731:16551951-5926139		4938	4932	26
WKK 7732:16552101-5905481		14753		26
WKK 7747:16555508-5920190		14265		26
2MASX J16555846-5944538	14.2		26759	26
2MASX J16555951-5943338	13.56	13656		26
2MASX J16555971-5924378	12.96	4791	4725	26
2MASX J16560654-6029485	12.95	15014		26
2MASX J16561000-5955305	14.04	21712		26
2MASX J16561269-5926057	14.81	44238		26
2MASX J16563134-5950047	13.21	14334	14186	26
2MASX J16563558-5955507	13.56	13446	13314	26
2MASX J16564246-5925547	14.65	26784	26837	26
2MASX J16565456-5912086	13.99	25717	25584	26
2MASX J16570559-5951145	13.14	14681		26
2MASX J16571044-5928405	13.39	14720		26
2MASX J16571839-5916546	13.57	26751		26
2MASX J16572087-6017565	13.56	15011		26
2MASX J16573013-5959415	14.26	14457		26
2MASX J16575895-6001323	14.21	15353		26
2MASX J16580639-6013444	14.98	25120	25234	26
2MASX J16581938-5933123	13.73		21423	26
2MASX J16582767-5934183	14.44	14783		26
2MASX J16585305-6008300	13.25	14138		26
2MASX J16590295-6012576	9.08	1046	1037	26

B

Appendix B

B.1 SNIa predictions

Table B.1 lists the observed peculiar velocities of the SNIa sample described in section 3.4 as well as the velocities predicted from the PSCz, RBC and combined reconstructions. Column 1 is the SNIa identifier whilst columns 2 and 3 list the galactic coordinates of the source. The distance as calculated by Tonry et al. (2003) is given in column 4, whilst the Tonry et al. (2003) LG-frame peculiar velocity and error are given in columns 5 and 6. Columns 7 to 12 list the peculiar velocities and uncertainties predicted for the SNIa from the PSCz, RBC and combined reconstructions using the best fit values of $\beta_I = 0.55$ and $\beta_{\rm RBC} = 0.39$ and the best fit combination of the catalogues (78% PSCz, 22% RBC). As detailed in Section 2.5, the velocity uncertainty of the PSCz includes a 150 $\rm km\,s^{-1}$ estimate of the shot noise and reconstruction errors as well as an extra component to account for the greater uncertainties near galaxy clusters. The equivalent error for the RBC is the quadratic sum of the measured shot noise and an extra 150 $\rm km\,s^{-1}$ to account for additional errors in the reconstruction. Columns 13 to 20 list the equivalent values in the CMB reference frame, using the best fit values $\beta_I = 0.48$ and $\beta_{\rm RBC} = 0.51$ with the extra free dipoles of 206 $\rm km\,s^{-1}$ towards $l = 290°$, $b = 0°$ and 444 $\rm km\,s^{-1}$ towards $l = 250°$, $b = 0°$ for the PSCz and RBC respectively. The CMB frame fields are again combined in the ratio 78% PSCz, 22% RBC.

TABLE B.1: The observed peculiar velocities of the SNIa sample described in section 3.4 together with the velocities predicted from the PSCz, RBC and combined reconstructions.

SNIa	l	b	d	LG Frame (all in km s^{-1})								CMB Frame (all in km s^{-1})							
	(°)	(°)	(h^{-1} Mpc)	V_{SNIa}	σ_{SNIa}	V_{PSCz}	σ_{PSCz}	V_{RBC}	σ_{RBC}	$V_{Comb.}$	$\sigma_{Comb.}$	V_{SNIa}	σ_{SNIa}	V_{PSCz}	σ_{PSCz}	V_{RBC}	σ_{RBC}	$V_{Comb.}$	$\sigma_{Comb.}$
(1)	(2)	(3)	(4)	(5)	(6)	(7)	(8)	(9)	(10)	(11)	(12)	(13)	(14)	(15)	(16)	(17)	(18)	(19)	(20)
sn72E	314.84	30.08	2.5	-51	19	16	196	54	264	28	213	437	19	544	174	593	308	394	211
sn80N	240.16	-56.69	13.9	266	138	-179	306	78	227	-162	291	285	138	-47	302	109	262	-122	294
sn81B	292.97	64.74	12.1	463	114	-49	469	-168	288	-86	435	952	114	374	377	480	341	299	369
sn81D	240.16	-56.69	11.2	542	142	-147	306	66	231	-132	292	561	142	-11	302	94	267	-98	295
sn86G	309.54	19.40	2.8	29	22	4	184	53	264	16	204	531	22	576	167	602	307	393	206
sn89B	241.99	64.40	7.1	-111	49	-18	341	7	276	-16	328	374	49	381	269	531	323	326	282
sn90N	294.37	75.99	16.2	-710	130	-235	673	-383	277	-319	608	-297	130	59	635	16	330	-5	581
sn90O	37.65	28.36	95.8	-207	552	149	153	-159	249	114	179	-372	552	-69	153	-436	301	-33	196
sn90T	341.50	-31.53	127.4	-734	1234	314	158	390	215	400	172	-746	1234	480	158	530	253	408	183
sn90Y	232.65	-53.85	97.5	1916	877	-54	156	178	200	-14	167	1941	877	89	156	249	228	18	174
sn90af	330.82	-42.24	142.3	772	852	156	154	261	213	213	169	767	852	328	154	356	249	233	179
sn91M	30.39	45.90	25.2	-251	174	-259	191	-268	223	-318	198	-238	174	-365	171	-241	262	-265	195
sn91T	292.61	65.19	9.2	689	60	-49	480	100	284	-27	445	1176	60	370	388	735	335	353	377
sn91U	311.82	36.21	87.5	668	646	-106	160	-104	222	-129	176	1177	646	411	160	482	262	270	187
sn91ag	342.56	-31.64	42.7	-20	246	13	154	-48	231	2	174	-41	246	133	153	-30	276	18	187
sn91bg	278.23	74.46	11.7	-348	94	-140	705	-390	281	-225	637	89	94	191	694	513	333	198	633
sn92A	235.90	-54.06	13.4	361	71	-179	420	77	228	-162	386	394	71	-38	420	119	264	-115	391
sn92G	184.62	59.85	19.5	-379	135	-363	220	-474	239	-468	225	-93	135	-253	188	-280	281	-258	212
sn92J	263.54	23.55	126.8	491	965	-413	151	-460	189	-515	160	1121	965	205	151	166	213	-22	167
sn92K	306.27	16.31	27.3	115	227	-112	328	316	329	-42	329	627	227	466	292	1107	398	408	318
sn92P	295.62	73.11	87.7	-1263	546	-683	168	-458	218	-784	180	-831	546	-416	166	-63	256	-404	189
sn92ag	312.49	38.39	73.8	-35	527	-218	174	-378	222	-301	186	470	527	276	171	129	265	93	196
sn92al	347.34	-38.49	43.7	-44	262	15	151	35	222	23	169	-140	262	61	151	-24	264	-15	182
sn92bc	245.69	-59.63	60.4	-472	292	-168	154	253	210	-113	168	-470	292	-46	155	313	243	-75	178
sn92bg	274.61	-18.35	109.7	-616	758	-215	171	-108	226	-238	185	-180	758	334	170	418	266	122	195
sn92bl	344.13	-63.92	125.7	522	637	220	153	376	201	302	165	316	637	189	153	253	232	165	174
sn92bo	261.99	-80.35	56.1	-78	272	-44	164	336	214	30	176	-280	272	-114	165	178	250	-90	187
sn93H	318.22	30.34	70.7	-18	423	-98	235	-406	234	-187	235	450	423	394	226	69	282	170	240
sn93ae	144.63	-63.22	48.8	928	270	198	154	618	265	334	184	518	270	-127	154	194	324	14	204
sn93ah	25.88	-76.77	86.5	266	638	18	516	408	209	108	466	-83	638	-206	526	-41	243	-151	478
sn94C	174.63	29.92	139.1	1258	1154	-110	152	-42	207	-119	166	1370	1154	-134	152	24	240	-61	176
sn94D	290.15	70.14	10.2	-667	61	-51	628	13	283	-48	570	-208	61	326	563	684	335	325	522
sn94M	291.69	63.03	69.1	-95	414	-534	206	-504	224	-645	210	406	414	-153	198	-19	265	-228	215
sn94Q	64.38	39.68	91.0	-213	545	212	210	33	289	219	229	-414	545	-92	211	-349	355	13	250
sn94S	187.38	85.14	49.8	-454	275	-255	163	91	240	-235	183	-149	275	-107	161	502	286	26	196
sn94T	318.02	59.84	104.3	-82	601	-437	154	-305	204	-504	166	361	601	-94	154	158	235	-128	175
sn94U	308.73	54.77	14.2	-238	98	-116	291	1	295	-116	292	256	98	331	233	626	351	279	264
sn94ae	225.34	59.67	19.9	-836	128	-402	265	-501	256	-512	263	-374	128	-78	216	-98	301	-162	237
sn95D	230.03	39.66	23.8	-603	132	-446	204	-515	246	-559	214	-77	132	-21	178	-40	285	-158	207
sn95ac	58.69	-55.05	145.9	616	942	361	153	531	205	478	166	94	942	-49	153	58	239	87	176
sn95ak	169.66	-48.98	59.7	874	454	238	241	559	273	361	248	588	454	22	246	312	332	127	267
sn95al	192.18	50.83	21.5	-662	129	-383	205	-455	232	-483	211	-350	129	-236	179	-241	270	-256	202
sn95bd	187.11	-21.66	44.9	109	300	126	153	130	240	155	176	71	300	104	153	20	289	77	191
sn96C	99.62	65.04	98.4	-1604	590	-174	154	-254	212	-230	168	-1565	590	-314	154	-279	246	-204	178
sn96V	257.58	57.54	75.0	-551	987	-440	175	-482	217	-546	185	-3	987	-3	171	32	254	-119	193
sn96X	310.23	35.65	18.6	-41	103	-11	198	323	313	60	229	476	103	529	185	1057	373	484	240
sn96Z	253.61	22.56	24.6	-469	204	-319	186	-423	276	-412	209	145	204	283	176	269	321	71	216
sn96bk	111.25	54.88	20.1	206	190	-213	191	-337	224	-287	198	152	190	-460	171	-471	264	-328	195
sn96bl	116.99	-51.30	108.9	72	778	494	181	735	273	656	205	-471	778	32	183	180	339	205	227
sn96bo	144.46	-48.96	45.4	836	335	331	157	655	291	475	195	402	335	-43	158	165	361	106	219
sn96bv	157.34	17.97	46.5	470	386	141	152	33	235	148	174	365	386	-76	152	-159	278	13	187

Mapping the Local Density and Velocity Fields

...continued

SNIa	l	b	d	LG Frame (all in km s^{-1})								CMB Frame (all in km s^{-1})							
	(°)	(°)	(h^{-1} Mpc)	V_{SNIa}	σ_{SNIa}	V_{PSCz}	σ_{PSCz}	V_{RBC}	σ_{RBC}	$V_{Comb.}$	$\sigma_{Comb.}$	V_{SNIa}	σ_{SNIa}	V_{PSCz}	σ_{PSCz}	V_{RBC}	σ_{RBC}	$V_{Comb.}$	$\sigma_{Comb.}$
sn97E	140.20	25.81	42.5	-108	235	59	171	-114	216	34	182	-294	235	-275	160	-432	253	-155	185
sn97Y	124.77	62.37	54.2	-499	488	-185	153	-98	210	-206	167	-445	488	-317	153	-64	245	-163	177
sn97bp	301.16	51.21	26.3	-311	152	-290	165	-264	300	-348	203	220	152	184	161	375	361	90	221
sn97bq	136.29	39.48	30.8	-96	163	-90	178	-194	209	-133	185	-200	163	-371	164	-408	244	-238	185
sn97br	311.84	40.33	19.3	-41	116	-65	181	276	311	-4	216	466	116	443	172	995	371	417	231
sn97by	312.69	34.87	122.5	734	1102	172	672	379	267	256	607	1238	1102	722	669	1109	323	649	610
sn97cn	9.14	69.51	54.2	-420	325	-92	156	25	229	-87	175	-174	325	43	156	383	274	125	188
sn97dg	103.62	-33.98	108.9	-1365	728	435	502	413	263	526	460	-1982	728	-155	518	-265	322	20	481
sn97do	171.00	25.27	35.4	-479	228	-15	173	-75	216	-31	183	-423	228	-81	162	-105	251	-33	185
sn97dt	87.56	-39.12	23.9	57	237	335	151	707	233	491	172	-566	237	-247	151	253	294	50	192
sn98D	63.78	72.91	40.7	-250	649	-160	239	-44	215	-170	234	-113	649	-179	199	157	253	-43	212
sn98V	43.94	13.35	49.0	509	316	179	168	32	205	186	177	193	316	-169	159	-289	243	-46	181
sn98ab	124.86	75.19	75.9	574	437	-190	161	-140	248	-220	184	748	437	-188	160	21	298	-88	199
sn98aq	138.84	60.27	15.3	-503	81	-175	202	-410	241	-265	211	-423	81	-279	177	-408	286	-220	206
sn98bp	43.64	20.48	30.1	368	201	40	170	-101	205	18	179	104	201	-286	160	-366	240	-160	181
sn98co	41.52	-44.94	54.1	197	574	198	151	382	215	282	168	-281	574	-186	152	-70	258	-58	180
sn98cs	65.24	43.34	91.2	838	778	186	356	53	286	197	342	671	778	-93	360	-331	352	9	358
sn98de	122.03	-35.24	53.9	-119	298	193	165	141	311	224	206	-675	298	-367	168	-603	380	-242	232
sn98dh	82.83	-50.64	25.5	311	200	306	151	658	228	451	171	-274	200	-206	151	204	282	35	188
sn98dk	102.86	-62.16	37.6	356	243	361	152	748	246	526	177	-163	243	-58	153	314	306	136	197
sn98ec	166.29	20.71	63.9	-377	574	19	162	-15	245	15	183	-388	574	-111	162	-64	291	-28	198
sn98ef	125.88	-30.57	45.1	1122	291	430	181	664	337	576	225	583	291	-97	187	-22	422	99	258
sn98eg	76.46	-42.06	79.7	-344	772	351	152	422	247	444	177	-951	772	-194	153	-235	300	-32	195
sn98es	143.19	-55.18	27.7	516	198	350	152	939	254	557	180	83	198	-3	152	693	319	242	201
sn99X	186.59	39.59	78.0	-340	665	-279	152	-314	234	-348	173	-93	665	-181	152	-115	280	-172	188
sn99aa	202.73	30.31	48.8	-513	360	-291	182	-201	209	-335	188	-168	360	-58	166	97	238	-88	184
sn99ac	19.88	39.94	30.4	-110	161	-204	187	-219	219	-252	195	-70	161	-250	169	-139	257	-177	192
sn99by	166.91	44.12	11.8	-492	464	-172	186	-333	247	-246	201	-369	464	-214	169	-285	290	-176	202
sn99cc	59.67	48.74	97.1	-128	649	-72	187	-218	275	-120	209	-225	649	-308	188	-464	335	-211	228
sn99cp	334.85	52.71	33.8	-641	203	-333	243	-352	261	-411	247	-263	203	-34	202	91	314	-80	231
sn99cw	101.77	-67.91	29.7	867	233	311	152	708	231	467	173	384	233	-63	152	346	285	117	189
sn99da	89.73	32.65	42.4	-297	430	-37	173	-35	205	-45	180	-608	430	-503	161	-393	242	-275	182
sn99dk	137.35	-47.46	49.0	-201	441	259	158	467	294	362	196	-673	441	-169	160	-103	361	-33	221
sn99dq	152.84	-35.87	35.7	884	189	443	163	928	295	647	200	508	189	110	165	613	373	325	228
sn99ef	125.72	-50.09	141.6	-2244	1077	404	163	46	253	414	186	-2762	1077	-48	164	-609	304	-38	203
sn99ej	130.44	-28.95	48.8	-554	348	299	221	304	337	366	251	-1067	348	-221	233	-327	417	-71	284
sn99ek	189.40	-8.23	49.1	305	498	77	152	27	225	83	170	361	498	117	152	12	263	75	182
sn99gh	255.05	23.74	22.9	-274	121	-289	193	-347	281	-365	216	344	121	321	182	340	326	116	222
sn99gp	143.25	-19.50	86.5	-446	558	372	200	265	273	431	218	-855	558	-55	208	-174	334	71	242
sn00B	166.35	22.79	55.5	230	499	74	168	62	238	87	186	232	499	-40	168	25	281	46	199
sn00bk	295.29	55.23	82.3	-779	569	-593	171	-437	203	-690	178	-246	569	-165	168	78	234	-241	185
sn00cf	99.88	42.17	130.7	-2071	964	166	159	3	186	166	165	-2278	964	-186	159	-219	209	-13	171
sn00cn	53.45	23.32	71.0	183	376	117	153	153	224	150	171	-117	376	-259	153	-157	273	-69	186
sn00cx	136.51	-52.48	21.1	458	112	283	152	878	241	476	175	-11	112	-124	152	630	300	152	195
sn00dk	126.83	-30.34	48.0	654	254	359	186	447	335	458	227	121	254	-171	192	-178	416	5	259
sn00fa	194.17	15.48	69.4	-626	416	-144	152	-123	217	-171	169	-406	416	-6	152	63	249	-29	178
sn01V	218.93	77.73	46.4	-152	246	-301	207	-12	234	-304	213	216	246	-85	201	426	277	-1	220

C

Appendix C

C.1 Reconstructed RBC cluster positions and velocities

Table C.1 lists the reconstructed real-space positions and peculiar velocities for the number-weighted RBC catalogue in the LG frame as detailed in Section 4.3. If the bias between the density field, as traced by the RBC clusters, and the total underlying density field is fully corrected, β_{RBC} should be ~ 0.5. This value has been adopted for the reconstructed values presented here.

Column 1 of table C.1 lists the name of the catalogue from which the cluster was taken followed by the J2000 equatorial coordinates. The common name or identifier for the cluster is given in column 2. Columns 3 through 5 list the galactic coordinates and measured redshift of the source. Column 6 is the reconstructed distance to the source whilst the supergalactic Cartesian components of the associated peculiar velocity are listed in columns 7 to 9. The predicted radial peculiar velocity and uncertainty are given in columns 10 and 11. Finally, columns 12, 13 and 14 respectively list the flux, luminosity and luminosity-inferred mass recorded for the RBC sources.

TABLE C.1: The reconstructed real-space positions and peculiar velocities of the RBC clusters. Values are for the default reconstruction in the LG reference frame and with number-weighted sources.

ID	Alt.	l (°)	b (°)	z	d h^{-1} Mpc	v_x km s^{-1}	v_y km s^{-1}	v_z km s^{-1}	v_{pec} km s^{-1}	σ_v km s^{-1}	f_x $\times10^{-12}$ ergs cm^{-2} s^{-1}	l_x $\times10^{42}$ h_{50}^{-2} ergs s^{-1}	M $M_\odot$
(1)	(2)	(3)	(4)	(5)	(6)	(7)	(8)	(9)	(10)	(11)	(12)	(13)	(14)
CIZA J1712.4-2321	OPHIUCHUS CLUSTER	0.58	9.29	0.0280	87.5	525	-55	-24	-399	139	307.575	10.291	1.117E+15
REFLEX J1516.2+0005	ABELL 2050	1.12	45.96	0.1181	325.3	252	-128	123	-142	91	5.108	3.037	3.585E+14
REFLEX J2218.6-3854		2.74	-56.17	0.1411	383.1	17	-846	201	790	37	8.526	7.174	6.477E+14
REFLEX J1548.7-0300	ABELL 2128	4.85	37.72	0.1010	281.6	252	-15	81	-91	107	4.126	1.802	2.524E+14
REFLEX J1931.6-3355		5.15	-22.55	0.0972	289.3	151	-552	126	238	69	6.504	2.624	3.377E+14
BCS J1510.9+0544	ABELL 2029	6.47	50.55	0.0766	227.5	365	262	229	164	167	61.945	15.400	1.338E+15
REFLEX J2034.7-3549	ABELL 3695	6.69	-35.55	0.0894	265.2	157	-547	109	330	99	12.197	4.152	4.854E+14
BCS J1511.4+0620	ABELL 2033	7.35	50.80	0.0817	247.0	417	-131	11	-257	166	9.138	2.608	3.489E+14
REFLEX J2034.3-3429	ABELL 3693	8.28	-35.21	0.1240	340.7	61	-596	212	472	57	4.997	3.272	3.740E+14
REFLEX J1633.9-0739		8.38	25.94	0.0974	291.7	176	-80	183	8	94	3.508	1.427	2.138E+14
REFLEX J2217.8-3543	ABELL 3854	8.45	-56.35	0.1486	401.6	14	-939	265	906	30	6.783	6.334	5.799E+14
BCS J1509.4+0734	ABELL 2028	8.49	51.91	0.0777	232.4	168	-15	146	7	170	4.210	1.093	1.835E+14
REFLEX J2034.7-3404	ABELL 3694	8.80	-35.21	0.0936	279.2	165	-451	-16	197	91	10.572	3.945	4.624E+14
BCS J1518.7+0613	ABELL 2055	8.86	49.25	0.1021	284.5	381	-217	-22	-319	122	9.993	4.430	4.943E+14
BCS J1512.8+0725	ABELL 2040	9.08	51.15	0.0451	138.9	774	-201	50	-416	197	5.824	0.510	1.123E+14
BCS J1516.7+0700	ABELL 2052	9.41	50.12	0.0353	105.5	675	7	436	-6	223	49.430	2.636	3.946E+14
CIZA J1915.8-2656		10.82	-16.91	0.1360	370.7	-102	-570	489	629	36	3.803	2.998	3.406E+14
REFLEX J1958.2-3011		10.95	-26.77	0.1171	323.4	72	-538	181	366	70	11.154	6.480	6.345E+14
BCS J1521.8+0741	MKW 03S	11.38	49.45	0.0453	140.8	740	-67	-327	-528	193	29.588	2.599	3.807E+14
CIZA J1839.8-2108		12.75	-7.05	0.0680	204.3	283	-393	100	3	101	5.588	1.111	1.902E+14
BCS J1523.1+0836	ABELL 2063	12.83	49.68	0.0355	107.3	535	-14	141	-120	232	42.290	2.282	3.539E+14
REFLEX J2336.2-3136	ABELL S1136	13.15	-73.03	0.0643	190.8	369	-317	169	272	126	6.491	1.153	1.974E+14
CIZA J1910.1-2239		14.39	-14.04	0.0563	168.8	217	-405	54	62	109	5.292	0.722	1.417E+14
BCS J1451.0+1436		14.81	59.48	0.1460	395.1	105	209	369	332	42	3.801	3.449	3.697E+14
CIZA J1759.0-1333		14.86	5.12	0.0450	137.6	316	-235	-66	-224	97	17.129	1.487	2.506E+14
REFLEX J2149.1-3041	ABELL 3814	16.60	-50.21	0.1184	326.8	220	-586	156	483	60	7.002	4.172	4.546E+14
REFLEX J1657.7-0149		17.34	24.13	0.0313	99.2	570	-48	-276	-505	183	9.209	0.388	9.476E+13
CIZA J1735.7-0721		17.41	13.16	0.0239	72.0	172	60	106	16	174	13.141	0.323	8.410E+13
REFLEX J2101.8-2804	ABELL 3733	17.73	-39.61	0.0382	114.0	495	-455	23	147	161	8.026	0.504	1.132E+14
REFLEX J2227.8-3034	ABELL 3880	18.00	-58.50	0.0579	170.9	320	-459	91	362	127	14.071	2.021	3.055E+14
REFLEX J2043.6-2626	ABELL S0894	18.43	-35.29	0.0408	123.8	470	-498	-288	-47	145	3.573	0.257	6.780E+13
BCS J1454.4+1622		18.62	59.58	0.0454	140.2	269	-511	89	-431	205	5.949	0.528	1.151E+14
REFLEX J1706.3-0131	ZwCl 1703.8-0129	18.81	22.43	0.0912	273.6	172	-239	192	17	125	6.062	2.157	2.957E+14
BCS J1452.9+1642	ABELL 1983	18.91	60.05	0.0444	134.3	140	-344	324	-141	211	5.140	0.436	1.000E+14
REFLEX J2035.7-2513	ABELL 3698	19.25	-33.24	0.0200	59.0	269	-433	39	191	147	3.044	0.053	2.187E+13
REFLEX J0011.3-2851		19.57	-80.98	0.0620	183.9	326	-292	315	276	134	13.829	2.275	3.305E+14
CIZA J1726.9-0317		19.92	17.09	0.0880	263.4	220	-101	240	93	117	5.638	1.870	2.678E+14
CIZA J1720.6-0110	UGCl 424	21.05	19.51	0.0284	88.4	271	70	-196	-268	176	13.395	0.464	1.092E+14
REFLEX J2107.1-2527	ABELL 3744	21.42	-40.13	0.0381	114.2	238	-372	-122	112	163	7.750	0.484	1.099E+14
BCS J1454.5+1838	ABELL 1991	22.80	60.49	0.0586	176.9	321	-137	75	-137	158	11.814	1.739	2.725E+14
REFLEX J2022.8-2056	ABELL S0868	22.87	-29.07	0.0564	169.3	284	-496	-115	95	104	8.761	1.197	2.070E+14
CIZA J1930.0-1509		23.44	-15.26	0.0829	247.2	196	-360	225	243	106	7.897	2.322	3.188E+14
BCS J1715.2+0309		24.42	22.79	0.1317	360.5	67	-75	481	380	48	4.091	3.024	3.463E+14
REFLEX J2111.7-2309		24.69	-40.50	0.0333	97.8	281	-561	6	327	170	6.772	0.323	8.221E+13
REFLEX J2347.7-2808		25.13	-75.86	0.0300	87.5	410	-364	136	338	122	59.136	2.279	3.586E+14
CIZA J1757.7-0108		25.69	11.39	0.0728	217.0	134	-125	305	222	115	9.775	2.218	3.157E+14
BCS J1525.9+1814	ABELL 2072	27.18	53.42	0.1270	348.4	260	-76	195	16	79	6.675	4.570	4.771E+14
CIZA J1804.1+0042		28.12	10.83	0.0882	264.6	105	-102	134	84	106	11.934	3.956	4.695E+14
REFLEX J2139.8-2228	ABELL S0963	28.12	-46.53	0.0328	96.3	154	-348	173	339	160	4.162	0.193	5.593E+13
CIZA J1918.5-0842		28.18	-9.95	0.0900	269.2	125	-401	138	194	92	3.885	1.351	2.088E+14
BCS J1442.2+2218		28.19	64.42	0.0970	293.7	312	-368	119	-298	121	6.609	2.655	3.408E+14

...continued

ID	Alt.	l (°)	b (°)	z	d h^{-1} Mpc	v_x km s^{-1}	v_y km s^{-1}	v_z km s^{-1}	v_{pec} km s^{-1}	σ_v km s^{-1}	f_x $\times10^{-12}$ ergs cm^{-2} s^{-1}	l_x $\times10^{42}$ h_{50}^{-2} ergs s^{-1}	M $M_\odot$
BCS J1540.1+1754	ABELL 2108	28.65	50.15	0.0916	276.7	470	-122	-2	-183	143	5.913	2.123	2.919E+14
REFLEX J2048.2-1749	ABELL 2328	28.75	-33.56	0.1475	399.6	73	-814	552	898	28	3.949	3.654	3.848E+14
BCS J1602.3+1557	ABELL 2147	28.89	44.51	0.0353	107.7	372	127	-196	-151	242	57.185	3.048	4.400E+14
REFLEX J2201.7-2225		30.34	-51.38	0.0691	205.1	562	-480	91	347	131	4.250	0.874	1.585E+14
BCS J1604.5+1743	HERCULES CLUSTER	31.48	44.66	0.0370	116.2	252	-56	-522	-480	228	16.394	0.964	1.847E+14
BCS J1606.7+1746	ABELL 2151E	31.81	44.19	0.0321	93.7	241	315	200	300	240	4.933	0.219	6.160E+13
BCS J1341.8+2623	ABELL 1775	32.02	78.72	0.0724	218.8	162	-323	340	-216	167	12.083	2.708	3.671E+14
REFLEX J2158.2-2006		33.44	-49.91	0.0570	167.1	417	-638	111	524	142	4.857	0.680	1.352E+14
REFLEX J2152.4-1937	ABELL 2384	33.46	-48.45	0.0963	287.9	570	-363	40	227	106	13.421	5.289	5.724E+14
BCS J1348.9+2635	ABELL 1795	33.81	77.18	0.0622	185.8	112	-92	393	33	176	69.098	11.363	1.104E+15
CIZA J1947.6-0542		34.22	-15.09	0.0280	86.5	244	-418	-211	-93	120	3.878	0.131	4.242E+13
BCS J1539.6+2147	ABELL 2107	34.39	51.53	0.0411	127.8	-58	-314	-295	-419	209	12.899	0.936	1.788E+14
BCS J1431.1+2538	ABELL 1927	34.81	67.67	0.0908	274.2	145	-352	253	-202	137	5.228	1.846	2.634E+14
REFLEX J2101.4-1315		35.33	-34.75	0.0282	83.6	175	-543	-90	259	159	11.351	0.388	9.553E+13
BCS J1423.2+2615		35.75	69.51	0.0375	113.8	-91	-352	365	-146	174	4.991	0.302	7.735E+13
REFLEX J2151.9-1543	ABELL 2382	38.81	-46.94	0.0614	181.2	422	-653	-46	452	148	4.588	0.745	1.433E+14
REFLEX J2321.4-2312	ABELL 2580	38.86	-69.28	0.0890	265.7	372	-200	252	236	125	5.268	1.788	2.583E+14
REFLEX J2134.1-1328		39.24	-42.10	0.0897	268.6	589	-581	-258	203	134	12.803	4.386	5.054E+14
REFLEX J2243.0-2010	ABELL 2474	39.29	-59.88	0.1359	371.0	241	-766	256	786	44	3.607	2.841	3.272E+14
BCS J1604.9+2355		39.95	46.49	0.0318	93.9	-109	39	236	214	238	10.085	0.439	1.037E+14
REFLEX J2216.9-1725		39.97	-53.13	0.1301	356.8	275	-632	230	638	58	6.603	4.742	4.870E+14
BCS J1359.2+2758	ABELL 1831	40.10	74.95	0.0612	181.9	-20	61	213	134	173	11.580	1.859	2.846E+14
BCS J1349.3+2806		40.63	77.14	0.0748	227.6	58	-438	161	-363	160	10.565	2.528	3.467E+14
REFLEX J2058.0-0746	ABELL 2331	40.81	-31.63	0.0793	236.4	331	-761	-138	328	100	3.042	0.824	1.480E+14
REFLEX J2313.0-2138	ABELL 2556	41.32	-66.97	0.0871	259.5	368	-303	96	303	133	10.142	3.283	4.092E+14
REFLEX J2312.3-2130		41.52	-66.78	0.1108	307.7	280	-317	108	323	92	5.122	2.683	3.324E+14
BCS J1602.7+2520		41.79	47.31	0.0888	266.2	468	119	39	77	179	6.089	2.055	2.868E+14
BCS J1716.2+2021		42.03	29.68	0.1306	358.3	267	6	437	381	53	3.192	2.326	2.851E+14
REFLEX J0020.7-2543		42.78	-82.98	0.1410	383.1	238	-961	95	960	34	5.146	4.343	4.446E+14
BCS J1522.4+2742	ABELL 2065	42.84	56.62	0.0723	216.4	312	-37	201	87	180	21.297	4.745	5.592E+14
BCS J1558.3+2713	ABELL 2142	44.23	48.68	0.0894	268.7	194	-117	123	5	183	53.418	18.040	1.461E+15
REFLEX J2316.1-2027	ABELL 2566	44.83	-67.25	0.0822	242.5	315	-487	250	532	142	5.987	1.734	2.566E+14
REFLEX J2145.9-1005	ABELL 2377	45.10	-43.19	0.0808	238.8	526	-938	-244	540	173	5.026	1.408	2.203E+14
REFLEX J2210.3-1210	ABELL 2420	46.49	-49.46	0.0846	252.2	568	-302	152	329	182	13.978	4.262	5.008E+14
BCS J1524.1+2952	ABELL 2069	46.83	56.49	0.1145	317.2	169	-403	124	-231	132	9.525	5.300	5.490E+14
REFLEX J2158.5-0948	ABELL 2402	47.53	-45.78	0.0809	238.1	411	-862	-73	635	185	6.480	1.818	2.666E+14
REFLEX J2250.8-1623	ABELL 2496	47.72	-60.11	0.1221	336.7	272	-498	190	533	68	4.947	3.142	3.644E+14
BCS J1521.2+3037	ABELL 2061	48.11	57.17	0.0777	234.3	49	-237	160	-82	176	12.246	3.157	4.066E+14
REFLEX J2202.3-0950	ABELL 2410	48.15	-46.61	0.0809	237.2	314	-793	159	732	186	5.232	1.469	2.273E+14
BCS J1539.8+3042	ABELL 2110	48.78	53.19	0.0980	296.9	80	-418	106	-232	141	9.131	3.735	4.392E+14
BCS J1657.9+2751	NGC 6269 GROUP	49.02	35.94	0.0347	108.2	104	93	-374	-277	196	8.150	0.422	1.001E+14
BCS J1620.5+2953	ABELL 2175	49.32	44.37	0.0972	294.0	202	-167	-71	-154	155	6.647	2.681	3.432E+14
BCS J1533.3+3109	ABELL 2092	49.36	54.61	0.0670	199.3	137	117	207	228	178	4.021	0.778	1.459E+14
REFLEX J2214.5-1022	ABELL 2426	49.69	-49.49	0.0980	295.1	348	-136	-93	70	133	12.137	4.955	5.428E+14
REFLEX J2157.4-0747	ABELL 2399	49.81	-44.54	0.0579	170.2	297	-748	-71	545	149	7.101	1.023	1.834E+14
BCS J1432.5+3138		50.60	67.57	0.1313	359.2	196	30	295	172	61	4.130	3.035	3.475E+14
REFLEX J2216.2-0919	ABELL 2428	51.40	-49.33	0.0825	243.0	166	-548	312	636	188	7.864	2.290	3.159E+14
REFLEX J0015.2-2351	ABELL 0014	52.69	-81.20	0.0645	192.0	171	-227	283	241	128	3.093	0.555	1.140E+14
BCS J2113.8+0233		53.51	-29.83	0.0483	144.8	268	-618	-186	240	105	18.923	1.891	2.977E+14
BCS J1510.2+3331	ABELL 2034	53.59	59.53	0.1130	313.4	66	-333	186	-152	119	12.488	6.756	6.610E+14
REFLEX J2307.2-1513	ABELL 2533	53.79	-63.03	0.1110	308.5	233	-300	140	341	92	3.590	1.893	2.558E+14
REFLEX J2205.6-0535	ABELL 2415	53.98	-45.10	0.0582	171.5	106	-678	-37	515	147	16.123	2.337	3.405E+14
BCS J1659.7+3236	ABELL 2241	54.87	36.65	0.1013	284.0	287	17	92	117	151	4.082	1.794	2.514E+14
REFLEX J2135.3+0125	ABELL 2355	55.97	-34.90	0.1244	343.2	302	-677	243	662	54	3.177	2.103	2.682E+14
BCS J1702.6+3403	ABELL 2244	56.79	36.32	0.0970	293.2	56	-98	-44	-79	138	19.261	7.684	7.562E+14
REFLEX J2225.8-0635	ABELL 2442	56.93	-49.81	0.0897	268.3	116	-193	189	276	173	4.839	1.669	2.448E+14
BCS J1259.7+2755	COMA CLUSTER	56.99	88.00	0.0231	69.0	147	-63	170	-37	192	294.276	6.702	8.197E+14

...continued

ID	Alt.	l (°)	b (°)	z	d h^{-1} Mpc	v_x km s^{-1}	v_y km s^{-1}	v_z km s^{-1}	v_{pec} km s^{-1}	σ_v km s^{-1}	f_x $\times10^{-12}$ ergs cm^{-2} s^{-1}	l_x $\times10^{42}$ h_{50}^{-2} ergs s^{-1}	M $M_\odot$
REFLEX J2306.5-1319	ABELL 2529	57.12	-61.89	0.0659	193.6	232	-512	221	574	132	6.025	1.125	1.930E+14
CIZA J2017.4+1603		57.39	-10.81	0.1350	370.0	406	-486	641	815	39	3.800	2.952	3.375E+14
BCS J1709.7+3427	ABELL 2249	57.60	34.95	0.0802	240.3	230	-64	201	177	155	12.346	3.390	4.263E+14
BCS J1545.0+3606	ABELL 2124	57.77	52.29	0.0654	195.0	-91	108	202	206	162	9.942	1.823	2.775E+14
BCS J1744.2+3259	ZwCl 1742.1+3306	57.91	27.65	0.0757	227.7	369	-80	95	117	159	17.125	4.185	5.048E+14
CIZA J1824.1+3029		58.26	18.81	0.0720	217.1	479	5	1	88	160	5.267	1.174	1.963E+14
CIZA J1825.3+3026		58.31	18.55	0.0650	193.6	535	37	247	342	166	17.292	3.122	4.160E+14
REFLEX J2218.2-0349		58.65	-46.67	0.0901	269.4	93	-465	-146	297	169	7.813	2.709	3.518E+14
REFLEX J2218.8-0258		59.75	-46.28	0.0902	269.7	-124	-543	-194	297	165	4.135	1.443	2.193E+14
BCS J1740.5+3538		60.60	29.06	0.0430	131.4	208	-75	-78	-58	148	7.439	0.592	1.262E+14
REFLEX J2223.8-0137	ABELL 2440	62.41	-46.43	0.0906	271.1	-319	-469	-55	283	156	9.679	3.388	4.155E+14
BCS J1628.6+3932	ABELL 2199	62.93	43.70	0.0299	88.9	-22	-104	369	216	223	100.210	3.831	5.295E+14
BCS J1711.0+3941	ABELL 2250	63.98	35.57	0.0647	193.5	170	-120	293	226	141	3.367	0.608	1.220E+14
BCS J1629.6+4048	ABELL 2197E	64.68	43.53	0.0301	93.6	-258	-357	115	-185	218	5.502	0.215	6.101E+13
REFLEX J2325.3-1207	ABELL 2597	65.32	-64.85	0.0852	254.0	100	-275	173	325	131	24.336	7.503	7.642E+14
REFLEX J0028.6-2338		65.81	-83.77	0.1120	310.4	258	-528	208	535	76	5.009	2.682	3.313E+14
CIZA J1857.5+3540		66.02	14.27	0.1070	299.4	441	-116	145	257	96	3.050	1.498	2.166E+14
CIZA J1904.2+3626		67.29	13.35	0.0780	233.9	332	24	142	246	142	3.626	0.950	1.650E+14
CIZA J2042.1+2426		67.76	-10.81	0.1019	286.4	451	-340	251	477	72	13.795	6.079	6.270E+14
CIZA J1857.6+3800		68.24	15.17	0.0567	169.5	399	-80	193	302	173	12.811	1.766	2.769E+14
REFLEX J2235.6+0128	ABELL 2457	68.64	-46.58	0.0594	176.1	112	-565	-52	446	132	13.012	1.967	2.982E+14
BCS J1714.2+4341		68.95	35.43	0.0276	81.1	-73	263	303	355	207	16.113	0.527	1.204E+14
CIZA J2048.6+2515	ZwCl 2046.8+2506	69.34	-11.51	0.0482	145.4	297	-319	-8	197	100	11.144	1.112	1.999E+14
BCS J1733.0+4345		69.51	32.07	0.0330	102.3	-222	14	-83	-134	188	16.031	0.750	1.546E+14
REFLEX J0013.6-1930	ABELL 0013	72.26	-78.46	0.0940	278.9	215	-380	288	417	87	5.957	2.250	3.032E+14
BCS J1423.8+4015		73.36	66.83	0.0822	247.9	45	-221	193	-98	143	3.877	1.126	1.857E+14
BCS J1844.0+4533		74.70	20.22	0.0910	272.7	369	-311	213	265	144	4.493	1.595	2.359E+14
BCS J1334.4+3442		75.01	78.08	0.0240	72.6	-101	-79	29	-76	179	5.672	0.141	4.520E+13
BCS J2214.8+1350		75.16	-34.13	0.0263	78.8	421	-535	-326	287	161	7.687	0.229	6.464E+13
CIZA J1921.1+4357	ABELL 2319	75.70	13.51	0.0557	166.5	96	-170	345	323	171	91.412	12.063	1.173E+15
REFLEX J2315.7-0222		76.07	-56.28	0.0267	77.6	568	-366	-9	470	166	4.735	0.146	4.601E+13
CIZA J1959.5+4044	CYGNUS A Cluster	76.19	5.75	0.0561	168.2	163	66	239	288	152	52.826	7.085	7.862E+14
BCS J1810.9+4955		77.73	26.71	0.0473	142.4	9	-226	314	178	140	10.924	1.050	1.919E+14
BCS J2200.8+2058	ABELL 2409	77.89	-26.62	0.1470	399.7	597	-726	560	1057	34	6.619	6.052	5.624E+14
BCS J1320.2+3308		78.69	81.35	0.0362	111.5	-8	-373	169	-322	152	6.944	0.392	9.421E+13
CIZA J2106.2+3426		79.00	-8.60	0.0866	258.3	334	-328	231	442	102	4.042	1.302	2.047E+14
BCS J1520.8+4840	ABELL 2064	79.88	54.05	0.1076	300.1	151	-102	161	65	94	5.834	2.881	3.533E+14
CIZA J1926.1+4833		80.37	14.64	0.0980	294.3	272	-146	133	230	121	6.624	2.716	3.458E+14
BCS J2226.0+1722	ABELL 2443	80.40	-33.23	0.1072	300.0	324	-565	147	593	62	6.149	3.013	3.657E+14
BCS J2250.3+1054	ABELL 2495	81.21	-41.94	0.0768	228.6	140	-559	-46	443	106	12.156	3.063	3.983E+14
REFLEX J2354.2-1024	ABELL 2670	81.33	-68.53	0.0765	226.3	188	-388	354	481	131	9.120	2.284	3.199E+14
BCS J1413.7+4339	ABELL 1885	83.17	66.58	0.0890	269.3	-1	-319	209	-192	118	6.408	2.172	2.988E+14
BCS J1601.5+5355	ABELL 2149	84.01	46.26	0.0675	202.9	54	-118	255	106	113	3.677	0.722	1.379E+14
BCS J2310.5+0735	PEGASUS II CLUSTER	84.18	-47.55	0.0400	118.0	804	-361	-338	457	216	11.169	0.768	1.546E+14
BCS J1626.9+5528	ABELL 2201	84.69	42.30	0.1300	357.2	434	27	414	484	48	3.992	2.877	3.348E+14
CIZA J2138.3+3557		84.75	-12.21	0.1110	310.0	378	-383	314	573	78	3.149	1.663	2.321E+14
REFLEX J2344.3-0422		84.85	-62.18	0.0786	233.4	94	-393	157	431	130	13.013	3.432	4.319E+14
BCS J1718.1+5640		84.87	35.07	0.1135	315.9	361	-208	289	281	75	5.838	3.205	3.774E+14
BCS J1715.3+5724	NGC 6338 GROUP	85.80	35.40	0.0280	86.3	-379	-128	338	-21	164	9.482	0.320	8.267E+13
CIZA J2156.4+3318		85.82	-16.67	0.0780	232.3	293	-389	218	473	97	13.434	3.489	4.379E+14
BCS J1852.1+5711		87.03	22.45	0.1084	303.1	289	-361	153	176	132	3.816	1.919	2.600E+14
REFLEX J2347.3-0218		88.50	-60.82	0.0223	63.6	556	-373	83	540	169	8.339	0.179	5.419E+13
BCS J1629.7+5831	ABELL 2208	88.52	41.17	0.1329	364.5	493	45	432	546	44	3.644	2.746	3.212E+14
CIZA J2015.3+5609		90.87	11.62	0.0820	244.6	243	86	330	414	178	4.885	1.410	2.198E+14
CIZA J2012.7+5631		91.00	12.11	0.0810	238.2	472	-11	613	762	178	3.376	0.954	1.643E+14
CIZA J1957.2+5751	ZwCl 1956.0+5746	91.11	14.60	0.0884	266.0	127	-177	185	188	167	5.609	1.877	2.683E+14
BCS J1421.6+4932	ABELL 1907	91.30	61.68	0.0710	213.2	-18	-65	256	51	131	6.619	1.432	2.284E+14

...continued

ID	Alt.	l (°)	b (°)	z	d h^{-1} Mpc	v_x km s^{-1}	v_y km s^{-1}	v_z km s^{-1}	v_{pec} km s^{-1}	σ_v km s^{-1}	f_X $\times 10^{-12}$ ergs cm^{-2} s^{-1}	l_X $\times 10^{42}$ h_{50}^{-2} ergs s^{-1}	M M$_\odot$
CIZA J2215.6+3718		91.61	-15.92	0.0190	57.6	472	-603	-403	263	247	10.332	0.161	5.044E+13
CIZA J1931.2+6000		91.64	18.55	0.1080	302.2	187	-256	136	158	141	3.924	1.959	2.643E+14
CIZA J2212.6+3840		91.93	-14.45	0.0190	62.7	-5	-600	-663	-245	231	7.577	0.118	4.002E+13
BCS J2324.4+1439	ABELL 2593	93.47	-43.18	0.0428	131.3	57	-142	-355	-17	227	17.428	1.369	2.369E+14
BCS J1836.5+6344		93.58	25.76	0.0834	248.1	441	-278	387	444	160	4.629	1.382	2.158E+14
BCS J2317.1+1842	ABELL 2572A	93.87	-38.79	0.0422	128.4	-174	-682	-565	104	222	15.022	1.148	2.079E+14
BCS J1712.8+6404	ABELL 2255	93.94	34.92	0.0809	242.2	346	-347	357	252	120	15.990	4.459	5.227E+14
BCS J2318.4+1842	ABELL 2572	94.22	-38.92	0.0389	112.2	206	-1044	-220	729	232	13.022	0.846	1.668E+14
BCS J2323.9+1646	ABELL 2589	94.62	-41.24	0.0416	123.6	54	-639	-212	392	238	27.841	2.063	3.232E+14
BCS J2344.9+0911	ABELL 2657	96.71	-50.26	0.0400	117.6	457	-300	75	489	238	25.246	1.731	2.845E+14
BCS J2350.8+0609	ABELL 2665	96.94	-53.63	0.0562	167.9	220	-215	62	299	146	14.206	1.922	2.955E+14
CIZA J2237.9+4101		97.47	-15.16	0.0530	159.3	109	-577	20	282	98	7.588	0.916	1.709E+14
BCS J1853.9+6822	ABELL 2312	98.98	24.85	0.0928	277.9	310	-296	285	288	144	5.608	2.066	2.852E+14
BCS J1428.5+5652	ABELL 1925	99.49	55.60	0.1074	299.5	217	-55	242	159	65	3.249	1.606	2.281E+14
BCS J0003.8+0203	ABELL 2700	99.61	-58.63	0.0994	295.0	259	-431	161	523	72	4.168	1.763	2.493E+14
BCS J2336.4+2108	ABELL 2626	100.45	-38.43	0.0565	169.1	71	-474	-109	318	157	11.500	1.574	2.542E+14
BCS J1900.5+6958	ABELL 2315	100.82	24.60	0.0936	280.9	89	-286	451	227	135	5.027	1.886	2.658E+14
BCS J2355.7+1121	ABELL 2675	101.75	-49.21	0.0720	213.2	289	-440	60	521	146	6.697	1.490	2.347E+14
BCS J2336.6+2355	ABELL 2627	101.75	-35.85	0.1245	343.9	525	-576	138	767	70	5.358	3.534	3.958E+14
BCS J0000.1+0816		101.79	-52.48	0.0396	115.3	417	-354	323	585	230	9.396	0.634	1.340E+14
BCS J2334.9+2722	ABELL 2622	102.77	-32.49	0.0613	183.5	27	-620	-131	328	137	5.902	0.954	1.725E+14
BCS J2338.3+2659	ABELL 2634	103.46	-33.09	0.0309	91.2	-11	-804	-55	448	182	19.313	0.792	1.619E+14
BCS J0004.9+1142		105.22	-49.56	0.0761	227.0	188	-283	149	367	139	3.640	0.908	1.603E+14
CIZA J2320.2+4146		105.25	-17.94	0.1400	382.7	825	-597	363	1051	35	4.472	3.728	3.974E+14
CIZA J2318.6+4257		105.42	-16.73	0.0174	55.2	-151	-652	-173	18	264	19.701	0.256	7.185E+13
BCS J1311.1+3913		105.44	77.22	0.0720	217.4	-55	-235	369	-153	123	5.649	1.258	2.068E+14
CIZA J2319.7+4251		105.58	-16.91	0.0173	48.5	454	-849	-9	658	269	14.266	0.183	5.599E+13
BCS J1425.3+6311	ABELL 1918	106.40	50.82	0.1394	380.2	573	214	354	612	41	5.646	4.655	4.701E+14
BCS J0005.4+1613		107.15	-45.23	0.1164	323.1	448	-450	102	636	87	4.822	2.787	3.375E+14
BCS J2350.5+2930	ZwCl 2348.4+2908	107.38	-31.52	0.0950	282.2	401	-611	-223	561	130	4.546	1.757	2.513E+14
BCS J1905.7+7805		109.70	25.77	0.1405	383.6	799	-17	411	821	37	5.188	4.347	4.454E+14
BCS J1718.2+7801	ABELL 2271	110.04	31.27	0.0584	176.2	126	-130	187	118	121	4.905	0.720	1.408E+14
BCS J1703.7+7838	ABELL 2256	111.01	31.77	0.0581	173.3	246	-144	446	311	122	47.615	6.849	7.627E+14
BCS J1336.1+5912	ABELL 1767	112.45	57.00	0.0701	210.9	38	-92	268	30	105	13.258	2.786	3.771E+14
REFLEX J0034.1-0207		112.78	-64.66	0.0812	241.0	183	-363	376	434	104	5.091	1.441	2.238E+14
BCS J0011.7+3225	ABELL 0007	113.29	-29.71	0.1073	300.2	130	-639	-58	425	146	9.670	4.731	5.129E+14
CIZA J2302.7+7137		114.51	10.55	0.1450	394.8	968	-176	374	1002	32	5.810	5.177	5.026E+14
BCS J0020.5+2839	ABELL 0021	114.79	-33.72	0.0955	285.5	109	-498	-19	371	156	7.042	2.742	3.504E+14
BCS J0021.6+2802	IV Zw 015	114.96	-34.36	0.0943	279.2	375	-553	96	639	164	4.015	1.531	2.270E+14
REFLEX J0041.8-0918		115.22	-72.03	0.0555	166.3	146	-125	157	164	140	72.695	9.533	9.837E+14
BCS J0039.6+0651	ABELL 0076	117.69	-55.90	0.0395	114.2	320	-524	305	641	210	17.982	1.204	2.169E+14
BCS J0041.7+2123	ABELL 0084	119.93	-41.42	0.1014	284.6	363	-197	299	439	136	5.419	2.380	3.107E+14
BCS J0040.4+2933	ABELL 0077	120.08	-33.26	0.0712	209.1	310	-772	129	714	145	8.479	1.842	2.758E+14
BCS J0043.8+2424	ZwCl 0040.8+2404	120.72	-38.44	0.0830	245.5	380	-444	205	602	173	11.255	3.309	4.158E+14
BCS J0049.8+2426	ABELL 0104	122.46	-38.43	0.0815	239.3	449	-574	427	764	169	5.358	1.527	2.336E+14
CIZA J0055.4+5229		123.55	-10.37	0.1080	302.0	626	-340	23	672	122	9.650	4.782	5.162E+14
CIZA J0108.0+7558		123.96	13.14	0.0960	284.5	611	-196	205	591	52	7.760	3.051	3.791E+14
BCS J0058.9+2656	NGC 0326 GROUP	125.00	-35.90	0.0470	141.7	-199	-552	75	183	148	5.106	0.485	1.077E+14
CIZA J0107.7+5408		125.35	-8.65	0.1066	298.4	630	-459	135	714	53	11.233	5.419	5.688E+14
REFLEX J0056.2-0114	ABELL 0119	125.70	-64.09	0.0442	130.8	501	-161	152	358	202	32.418	2.710	3.939E+14
BCS J0107.3+3223	PISCES CLOUD	126.82	-30.36	0.0170	52.9	-1	-170	-73	80	263	34.271	0.424	1.051E+14
BCS J1155.9+7324	ABELL 1412	128.31	43.14	0.0833	249.2	321	-89	157	202	67	3.634	1.085	1.800E+14
BCS J0113.0+1529	ABELL 0160	130.59	-47.05	0.0442	132.4	-164	-478	288	241	184	3.324	0.280	7.180E+13
BCS J0123.6+3315		130.64	-29.14	0.0164	43.7	650	-508	-22	814	280	25.981	0.300	8.105E+13
BCS J0108.2+0210	ABELL 0147	131.45	-60.42	0.0447	133.4	100	-249	299	252	199	5.483	0.471	1.060E+14
BCS J1144.7+6724	ABELL 1366	132.50	48.46	0.1159	321.1	525	52	142	405	51	6.315	3.611	4.104E+14
BCS J1133.2+6622	ABELL 1302	134.71	48.92	0.1160	321.3	528	58	127	405	50	5.016	2.878	3.461E+14

...*continued*

ID	Alt.	l (°)	b (°)	z	d h^{-1} Mpc	v_x km s^{-1}	v_y km s^{-1}	v_z km s^{-1}	v_{pec} km s^{-1}	σ_v km s^{-1}	f_X $\times10^{-12}$ ergs cm^{-2} s^{-1}	l_X $\times10^{42}$ h_{50}^{-2} ergs s^{-1}	M $M_\odot$
REFLEX J0115.0+0021	ABELL 0168	135.55	-61.94	0.0450	135.2	197	-111	566	144	202	11.311	0.984	1.839E+14
CIZA J0214.2+5144	ZwCl 0210.2+5130	135.74	-9.05	0.0489	148.2	-3	-600	-65	92	107	11.617	1.192	2.103E+14
CIZA J0157.1+4120	ABELL 0276	135.98	-19.86	0.0811	239.4	398	-738	111	623	114	5.152	1.454	2.255E+14
BCS J0152.7+3608	ABELL 0262	136.57	-25.09	0.0163	44.3	434	-736	202	697	283	92.489	1.050	2.076E+14
BCS J0125.0+0841	ABELL 0193	136.92	-53.26	0.0491	149.6	-188	-137	458	-42	164	16.070	1.661	2.696E+14
BCS J0150.8+3304		137.03	-28.17	0.0363	110.0	-105	-452	-82	124	180	13.521	0.765	1.557E+14
BCS J0155.0+3354	ABELL 0272	137.73	-27.13	0.0872	257.7	402	-589	185	614	138	10.397	3.373	4.175E+14
BCS J0157.3+3213	ABELL 0278	138.80	-28.60	0.0894	266.1	318	-367	315	430	125	4.543	1.557	2.326E+14
REFLEX J0125.4+0146	NGC 0533 GROUP	140.12	-59.96	0.0174	46.9	697	-418	55	701	209	12.109	0.158	4.997E+13
REFLEX J0125.9-0121		142.19	-62.93	0.0180	51.5	644	-146	109	406	199	13.466	0.188	5.682E+13
REFLEX J0108.8-1524	ABELL 0151	142.85	-77.61	0.0533	159.1	251	-179	339	183	149	10.928	1.332	2.260E+14
REFLEX J0108.8-1537	ABELL 0151S	143.21	-77.81	0.0970	286.2	249	-563	191	573	59	4.159	1.677	2.414E+14
BCS J0708.1+7151		143.33	26.96	0.1053	294.2	587	-64	-119	496	85	3.674	1.745	2.439E+14
BCS J1132.3+5559	ABELL 1291	143.76	57.83	0.0527	159.2	46	-113	28	-71	106	5.394	0.645	1.314E+14
CIZA J0300.7+4427		145.95	-12.55	0.0300	91.9	-142	-809	16	22	179	56.552	2.179	3.468E+14
CIZA J0254.4+4134		146.35	-15.64	0.0172	50.0	201	-830	168	370	259	159.112	2.008	3.370E+14
BCS J0244.1+3731		146.45	-20.14	0.0320	97.3	-86	-561	144	76	203	3.701	0.164	4.949E+13
BCS J0209.5+1946	ABELL 0311	146.96	-39.43	0.0657	195.1	234	-398	215	381	109	6.707	1.243	2.082E+14
BCS J0246.0+3653	ABELL 0376	147.12	-20.54	0.0488	148.8	-152	-380	134	-41	155	13.389	1.367	2.331E+14
BCS J0228.1+2811		147.57	-30.02	0.0350	106.1	17	-295	329	88	187	7.966	0.420	9.956E+13
BCS J1058.4+5647	ABELL 1132	149.22	54.18	0.1363	371.8	644	292	27	607	32	7.365	5.796	5.580E+14
REFLEX J0102.7-2152		149.56	-84.16	0.0569	169.9	293	-183	376	160	133	23.876	3.304	4.428E+14
CIZA J0319.7+4130		150.57	-13.26	0.0179	55.6	-80	-772	347	-4	242	1000.800	13.637	1.415E+15
CIZA J0301.7+3549	ABELL 0407	150.61	-19.94	0.0470	141.9	31	-502	353	98	147	7.837	0.745	1.484E+14
BCS J1134.7+4905	ABELL 1314	151.76	63.53	0.0338	103.7	-228	-138	44	-223	146	8.734	0.429	1.015E+14
REFLEX J0120.9-1351		151.81	-75.05	0.0519	154.5	183	-272	510	218	149	13.965	1.613	2.618E+14
CIZA J0515.3+5845		151.85	11.65	0.1203	332.4	752	-67	-83	716	54	7.266	4.466	4.763E+14
REFLEX J0132.7-0804		151.99	-68.59	0.1489	402.7	538	-1067	-88	1184	24	4.380	4.124	4.200E+14
BCS J1053.7+5451		152.47	55.00	0.0704	211.7	80	-74	23	-19	104	4.511	0.962	1.698E+14
BCS J0819.4+6337		152.67	33.82	0.1190	328.8	629	-129	-88	443	88	3.373	2.043	2.658E+14
BCS J0704.3+6318	ABELL 0566	152.71	25.47	0.0980	290.3	540	-24	-108	480	112	7.291	2.987	3.714E+14
BCS J1143.5+4623	ABELL 1361	153.29	66.53	0.1167	322.3	360	103	55	232	52	9.001	5.202	5.387E+14
REFLEX J0137.2-0911		156.17	-69.06	0.0409	119.4	523	-400	487	438	161	7.609	0.547	1.197E+14
BCS J1205.2+3920		158.23	74.45	0.0370	114.6	-45	-395	66	-393	159	6.858	0.404	9.625E+13
REFLEX J0202.3-0107	ABELL 0295	159.06	-58.93	0.0427	127.6	149	-358	679	176	157	4.225	0.332	8.186E+13
CIZA J0602.0+5315		160.07	14.57	0.0510	152.8	149	-197	-143	124	114	6.107	0.684	1.378E+14
CIZA J0450.0+4501		160.52	0.27	0.0220	68.5	-6	-708	212	-122	180	91.313	1.890	3.181E+14
BCS J0721.4+5547	ABELL 0576	161.37	26.26	0.0381	117.0	-59	-332	-40	-195	143	26.582	1.654	2.762E+14
BCS J0740.9+5525		162.22	28.93	0.0341	103.7	95	-337	-107	-67	154	20.249	1.011	1.928E+14
REFLEX J0157.2-0551		162.25	-63.58	0.1289	353.3	487	-868	-88	976	32	3.130	2.223	2.767E+14
BCS J0714.3+5440	ABELL 0572	162.36	25.05	0.1043	291.0	510	-31	-10	408	117	3.558	1.659	2.353E+14
BCS J0716.6+5323	ZwCl 0712.9+5334	163.82	25.11	0.0644	192.5	271	-316	-174	134	118	3.232	0.578	1.176E+14
BCS J0759.6+5400	ZwCl 0755.8+5408	164.14	31.49	0.1038	289.5	646	-235	-53	378	106	3.668	1.693	2.393E+14
BCS J0258.9+1334	ABELL 0401	164.18	-38.87	0.0739	220.4	199	-341	206	252	112	38.218	8.869	8.905E+14
BCS J0257.8+1302	ABELL 0399	164.31	-39.47	0.0722	212.8	428	-432	115	502	117	23.236	5.161	5.957E+14
BCS J1023.7+4908	ABELL 0990	165.06	54.12	0.1440	390.4	653	369	-98	665	29	7.687	6.739	6.139E+14
CIZA J0612.6+4836	ABELL 0553	165.15	14.05	0.0670	200.1	165	-124	-139	164	114	9.877	1.900	2.852E+14
REFLEX J0231.9+0115		167.43	-52.71	0.0221	63.6	470	-243	127	381	207	5.107	0.108	3.712E+13
BCS J0751.4+5012		168.39	29.85	0.0220	66.9	167	-341	-48	-42	158	11.777	0.245	6.876E+13
CIZA J0629.1+4606	ZwCl 0625.6+4608	168.69	15.59	0.1290	353.5	734	-46	-215	690	54	3.738	2.654	3.159E+14
CIZA J0604.6+4257		169.69	10.29	0.1180	325.8	617	-87	-190	588	65	6.626	3.924	4.346E+14
BCS J0257.6+0600	ABELL 0400	170.26	-44.95	0.0238	70.9	147	-331	323	157	195	24.507	0.596	1.332E+14
BCS J0352.9+1940		171.04	-25.78	0.1090	302.9	509	-470	-226	681	58	6.963	3.523	4.095E+14
BCS J0913.6+4742	ABELL 0757	171.70	43.27	0.0514	155.4	56	-203	14	-119	118	5.210	0.593	1.237E+14
BCS J1109.2+4133	ABELL 1173	171.72	64.61	0.0770	230.3	253	-77	-9	20	141	5.162	1.315	2.111E+14
BCS J0341.2+1524		172.18	-30.79	0.0290	87.7	12	-466	363	23	179	21.557	0.778	1.606E+14
BCS J0822.1+4706	ABELL 0646	172.65	34.58	0.1303	356.5	701	59	-178	581	51	6.952	5.007	5.070E+14

...continued

ID	Alt.	l (°)	b (°)	z	d h^{-1} Mpc	v_x km s^{-1}	v_y km s^{-1}	v_z km s^{-1}	v_{pec} km s^{-1}	σ_v km s^{-1}	f_X $\times 10^{-12}$ ergs cm^{-2} s^{-1}	l_X $\times 10^{42}$ h_{50}^{-2} ergs s^{-1}	M $M_\odot$
BCS J0825.6+4708	ABELL 0655	172.65	35.17	0.1267	347.5	676	27	-151	529	56	6.636	4.522	4.737E+14
BCS J1111.6+4050	ABELL 1190	172.78	65.32	0.0794	240.1	254	-342	30	-236	132	6.418	1.735	2.584E+14
CIZA J0643.4+4214		173.42	16.47	0.0910	270.3	403	-145	-60	294	86	20.104	7.068	7.206E+14
BCS J0828.0+4445	ABELL 0667	175.60	35.43	0.1450	392.7	784	208	-298	764	32	5.087	4.538	4.553E+14
CIZA J0516.9+2925	ZwCl 0513.7+2922	176.17	-4.97	0.1300	355.8	768	-298	-408	859	34	5.939	4.263	4.497E+14
BCS J0338.6+0958		176.26	-35.05	0.0349	107.4	-96	-242	441	-190	150	85.612	4.456	5.856E+14
REFLEX J0252.8-0116		176.44	-51.07	0.0235	69.7	496	-151	390	165	198	14.443	0.343	8.808E+13
BCS J0726.1+4123	ABELL 0580	177.03	23.71	0.1118	309.6	575	-157	-61	366	87	3.354	1.795	2.453E+14
BCS J0747.0+4131		177.97	27.54	0.0294	90.1	173	-368	220	-191	155	7.159	0.267	7.183E+13
CIZA J0522.7+2806		177.98	-4.66	0.0580	171.7	177	-69	-195	262	125	14.850	2.139	3.187E+14
BCS J1020.0+4100	ABELL 0971	178.95	56.04	0.0926	277.2	248	-88	96	1	79	3.007	1.109	1.789E+14
BCS J1040.7+3957	ABELL 1068	179.10	60.13	0.1386	376.7	501	352	-111	528	34	9.183	7.454	6.704E+14
BCS J1032.2+4015	ABELL 1035	179.33	58.47	0.0733	219.3	217	-18	249	5	134	4.518	1.044	1.793E+14
CIZA J0603.8+2939		181.37	3.79	0.0300	91.9	93	-396	268	-172	132	16.791	0.649	1.398E+14
BCS J0413.4+1027	ABELL 0478	182.44	-28.28	0.0882	259.8	347	-337	-241	514	82	38.070	12.539	1.115E+15
BCS J1022.1+3831		183.24	56.90	0.0534	162.1	92	-289	106	-250	140	3.979	0.489	1.065E+14
CIZA J0711.7+3219		185.25	18.09	0.0672	201.4	140	-526	-153	-12	170	10.509	2.033	2.999E+14
CIZA J0516.3+1712		186.27	-11.99	0.1150	317.5	463	-419	-327	597	71	12.872	7.208	6.907E+14
CIZA J0602.1+2309		186.85	0.27	0.0654	193.4	223	112	-141	262	179	16.795	3.070	4.104E+14
CIZA J0632.0+2519		188.16	7.30	0.0750	224.7	141	-241	64	-10	183	7.038	1.698	2.570E+14
CIZA J0631.3+2500		188.37	7.02	0.0810	244.1	109	-271	221	-154	143	12.363	3.462	4.322E+14
REFLEX J0340.7-0239		189.22	-42.73	0.0352	106.9	82	-103	321	-108	153	10.876	0.579	1.267E+14
BCS J1031.7+3503	ABELL 1033	189.29	59.24	0.1259	344.9	404	201	-87	334	49	8.049	5.409	5.428E+14
CIZA J0707.0+2706		189.88	15.17	0.0620	182.0	469	-318	-246	346	193	6.827	1.128	1.952E+14
BCS J0419.6+0224		190.98	-31.85	0.0123	33.6	560	-585	283	336	159	55.995	0.362	9.445E+13
CIZA J0635.0+2231		191.00	6.66	0.0680	202.1	372	-145	60	143	207	30.869	6.079	6.806E+14
BCS J0919.7+3345	ABELL 0779	191.09	44.39	0.0230	70.4	195	-253	203	-211	144	10.750	0.245	6.848E+13
BCS J0459.1+0846	ABELL 0523	191.19	-20.15	0.1000	295.2	346	-402	-202	455	85	3.409	1.462	2.163E+14
BCS J0753.3+2921	ABELL 0602	191.46	25.51	0.0621	185.7	396	-543	-81	-12	152	6.211	1.030	1.823E+14
BCS J1016.3+3338	ABELL 0961	192.22	56.13	0.1241	340.3	406	182	-101	326	50	4.485	2.944	3.454E+14
BCS J0828.6+3025	ABELL 0671	192.74	33.15	0.0503	150.3	331	-272	13	-19	123	6.672	0.726	1.445E+14
REFLEX J0359.1-0319		193.37	-39.30	0.1220	335.1	488	-584	-379	806	42	3.148	2.005	2.602E+14
BCS J1002.6+3242		193.75	53.24	0.0500	151.2	204	-192	290	-214	142	7.023	0.755	1.489E+14
BCS J0503.1+0608		194.12	-20.73	0.0880	258.6	416	-411	-221	503	113	6.623	2.194	3.019E+14
CIZA J0524.4+0819		195.08	-15.08	0.0680	200.8	354	-211	-65	273	101	10.774	2.133	3.103E+14
CIZA J0516.6+0626	ABELL 0539	195.71	-17.72	0.0284	85.3	141	-552	279	-46	138	35.018	1.211	2.241E+14
CIZA J0649.3+1801		196.57	7.67	0.0640	188.8	686	-150	92	238	185	13.578	2.380	3.402E+14
BCS J1034.9+3041	ABELL 1045	197.89	60.04	0.1381	375.0	407	358	-171	483	34	4.275	3.470	3.782E+14
REFLEX J0501.9+0109		198.55	-23.58	0.1248	341.8	503	-443	-385	683	62	9.577	6.317	6.114E+14
REFLEX J0236.5-1922	ABELL 0367	200.71	-64.69	0.0907	267.5	168	-494	-26	468	60	3.388	1.197	1.904E+14
BCS J1116.5+2923		201.15	69.01	0.0471	144.0	195	-394	109	-373	142	7.535	0.719	1.446E+14
BCS J1110.6+2842	ABELL 1185	202.96	67.72	0.0314	96.0	-6	-222	322	-291	184	6.091	0.259	6.989E+13
REFLEX J0501.3-0332	ABELL 0531	202.98	-26.02	0.0913	268.9	432	-332	-175	426	91	3.111	1.115	1.802E+14
REFLEX J0425.8-0834		203.31	-36.17	0.0397	121.1	-126	-176	369	-247	137	25.090	1.695	2.802E+14
BCS J1206.5+2811	NGC 4104 GROUP	204.26	80.02	0.0283	86.7	179	-278	157	-273	192	3.497	0.121	3.987E+13
BCS J1006.6+2555	ABELL 0923	205.20	53.28	0.1162	319.9	321	112	-102	216	53	3.079	1.781	2.413E+14
REFLEX J0433.6-1314	ABELL 0496	209.57	-36.48	0.0326	95.0	69	-344	-20	208	172	82.178	3.734	5.159E+14
CIZA J0742.6+0922	ABELL 0592	210.24	15.59	0.0624	185.6	395	-273	9	3	117	6.366	1.066	1.869E+14
BCS J0907.3+1639	ABELL 0744	212.15	37.40	0.0733	218.2	261	-181	-98	-2	103	4.493	1.039	1.785E+14
BCS J0912.5+1556	ABELL 0763	213.58	38.27	0.0851	254.3	243	-226	-51	-78	85	7.476	2.316	3.165E+14
REFLEX J0445.1-1552		213.89	-34.95	0.0360	108.4	-37	-225	267	-127	168	10.124	0.564	1.239E+14
BCS J1048.7+2213	ABELL 1100	216.13	61.77	0.0458	139.6	302	-297	339	-370	138	4.146	0.375	8.894E+13
BCS J0924.0+1410	ABELL 0795	217.08	40.15	0.1357	368.4	339	224	-427	498	32	7.541	5.881	5.650E+14
REFLEX J0454.8-1807		217.45	-33.63	0.0335	97.0	163	-470	-2	242	175	6.117	0.296	7.684E+13
CIZA J0721.2-0220		218.43	5.54	0.0360	108.3	115	-383	155	-210	114	5.422	0.303	7.771E+13
REFLEX J0345.9-2416	ABELL 0458	218.84	-50.78	0.1057	292.9	227	-533	-160	508	48	5.007	2.389	3.084E+14
REFLEX J0448.2-2029		219.51	-35.90	0.0720	213.7	63	-358	86	110	99	8.056	1.790	2.694E+14

...continued

ID	Alt.	l (°)	b (°)	z	d h^{-1} Mpc	v_x km s^{-1}	v_y km s^{-1}	v_z km s^{-1}	v_{pec} km s^{-1}	σ_v km s^{-1}	f_x $\times 10^{-12}$ ergs cm^{-2} s^{-1}	l_x $\times 10^{42}$ h_{50}^{-2} ergs s^{-1}	M $M_\odot$
BCS J0823.3+0421		219.75	22.39	0.0293	88.5	180	-367	118	-257	122	13.150	0.485	1.126E+14
BCS J1109.7+2145	ABELL 1177	220.45	66.29	0.0319	98.0	338	-275	443	-377	173	8.568	0.375	9.223E+13
REFLEX J0438.8-2206	ABELL 0500	220.57	-38.49	0.0670	198.2	27	-361	26	173	108	6.076	1.172	1.985E+14
REFLEX J0311.3-2654	ABELL 3094	220.67	-58.93	0.0685	203.1	-102	-336	109	195	109	3.347	0.677	1.311E+14
CIZA J0818.2+0122		221.94	19.87	0.0879	262.2	188	-250	-34	-63	95	5.287	1.751	2.549E+14
REFLEX J0821.8+0113	ABELL 0653	222.54	20.59	0.0822	243.3	235	-221	-218	113	140	4.080	1.185	1.928E+14
CIZA J0640.1-1253		223.21	-8.31	0.1350	366.2	297	-335	-653	684	35	14.317	10.994	9.047E+14
REFLEX J0538.2-2037	ABELL 3358	224.36	-24.97	0.0915	268.7	147	-331	-310	407	106	5.675	2.033	2.827E+14
REFLEX J0225.1-2928		224.95	-69.28	0.0604	178.1	46	-323	-7	291	110	6.371	0.999	1.790E+14
CIZA J0717.4-1119		225.97	0.53	0.0750	222.6	164	-214	-40	18	103	18.108	4.343	5.199E+14
REFLEX J0552.8-2103	ABELL 0550	226.16	-21.95	0.0989	292.5	265	-436	-115	233	92	10.052	4.184	4.771E+14
BCS J1155.2+2324	ABELL 1413	226.20	76.78	0.1427	386.3	224	408	-21	409	34	12.199	10.463	8.564E+14
REFLEX J0548.7-2154		226.64	-23.16	0.0928	272.9	329	-458	-242	368	107	4.482	1.654	2.414E+14
BCS J1053.8+1650	ABELL 1126	227.52	60.95	0.0856	255.6	174	-8	129	-57	89	5.474	1.719	2.528E+14
BCS J1025.8+1241	ZwCl 1023.3+1257	228.63	53.05	0.1434	387.3	231	378	-323	487	29	4.802	4.193	4.307E+14
BCS J1123.2+1936		228.65	68.44	0.1042	289.0	165	-73	48	-84	75	5.258	2.439	3.143E+14
REFLEX J0249.6-3111	IC 1860 GROUP	229.02	-63.96	0.0230	66.7	437	-323	141	192	131	7.309	0.167	5.135E+13
CIZA J0817.4-0730	ABELL 0644	229.93	15.29	0.0704	208.6	296	-237	-126	17	117	29.302	6.183	6.853E+14
REFLEX J0408.3-3054	ABELL 3223	230.17	-47.13	0.0600	178.0	-133	-323	170	87	130	9.280	1.433	2.349E+14
REFLEX J0548.6-2527	ABELL 0548A	230.26	-24.42	0.0420	125.3	-165	-609	323	-110	177	14.827	1.123	2.045E+14
REFLEX J0542.1-2607	ABELL 0548-2	230.41	-26.02	0.0390	113.5	-111	-599	41	169	186	6.439	0.421	9.885E+13
REFLEX J0545.4-2556	ABELL 0548B	230.49	-25.25	0.0424	128.6	-143	-388	477	-318	174	5.420	0.419	9.764E+13
CIZA J0702.6-2240		234.46	-7.80	0.0650	193.5	235	-325	74	-94	107	4.757	0.865	1.589E+14
REFLEX J0230.7-3305		234.53	-67.76	0.0760	224.9	90	-285	-39	264	114	3.645	0.907	1.602E+14
BCS J1144.6+1945	ABELL 1367	235.08	73.02	0.0214	64.0	158	-54	349	-123	177	93.561	1.832	3.112E+14
REFLEX J0525.6-3135	ABELL 3341	235.17	-31.08	0.0380	109.5	55	-324	-158	272	188	14.764	0.916	1.773E+14
BCS J1127.0+1707	ABELL 1264	235.70	68.09	0.1267	346.2	198	163	-28	154	61	3.615	2.477	3.016E+14
REFLEX J0229.3-3332		235.81	-67.98	0.0792	236.2	161	-142	42	97	104	3.940	1.063	1.791E+14
CIZA J0747.5-1917	PKS 0745-19 Cluster	236.44	3.03	0.1028	284.1	232	-176	-183	114	82	45.729	20.365	1.549E+15
REFLEX J0547.6-3152	ABELL 3364	236.93	-26.64	0.1483	398.8	149	-592	-734	863	26	7.407	6.884	6.176E+14
CIZA J0802.1-1926		238.34	5.92	0.1400	378.1	136	-139	-664	581	39	3.075	2.573	3.009E+14
REFLEX J0909.1-0940	ABELL 0754	239.34	24.81	0.0542	162.6	131	-272	131	-275	124	55.281	6.922	7.762E+14
CIZA J0757.9-2157		239.99	3.77	0.0490	147.2	229	-424	180	-296	124	19.219	1.977	3.072E+14
REFLEX J0910.5-1034	ABELL 0761	240.37	24.54	0.0916	272.1	277	-209	-180	-13	79	5.237	1.882	2.667E+14
REFLEX J0413.9-3805		240.79	-46.52	0.0501	146.6	-120	-281	-40	230	151	11.531	1.242	2.162E+14
CIZA J0805.9-2251		241.72	4.86	0.1210	330.6	223	-198	-389	277	76	4.908	3.062	3.584E+14
REFLEX J0605.8-3518	ABELL 3378	241.79	-24.02	0.1392	376.3	115	-534	-642	732	30	9.132	7.476	6.709E+14
REFLEX J1013.7+0006	ABELL 0954	242.07	43.37	0.0927	276.1	166	-74	-44	-59	63	4.086	1.506	2.251E+14
CIZA J0826.7-2007	ABELL S0611	242.10	10.41	0.0876	259.4	358	-236	-226	52	98	5.652	1.858	2.667E+14
REFLEX J0500.7-3840	ABELL 3301	242.42	-37.41	0.0536	160.3	-2	-266	326	-132	155	8.860	1.093	1.948E+14
REFLEX J1013.6+0055	ABELL 0957	242.91	42.84	0.0445	134.0	112	-235	169	-305	121	9.012	0.767	1.528E+14
REFLEX J0918.1-1205		242.92	25.10	0.0539	161.8	344	-246	98	-291	124	48.167	5.968	6.951E+14
CIZA J0627.0-3529	ABELL 3392	243.46	-19.97	0.0554	167.2	165	-529	451	-338	135	13.362	1.758	2.769E+14
REFLEX J0557.2-3728	ABELL S0555	243.55	-26.30	0.0442	129.9	81	-538	123	55	191	7.921	0.666	1.374E+14
REFLEX J0521.4-4048	ABELL 3336	245.68	-33.76	0.0756	224.6	185	-393	142	14	106	4.386	1.078	1.826E+14
REFLEX J0345.7-4112	ABELL S0384	246.01	-51.76	0.0603	177.4	-68	-376	86	225	163	9.908	1.545	2.483E+14
REFLEX J0540.1-4050	ABELL S0540	246.42	-30.29	0.0358	101.2	186	-474	-302	404	178	17.690	0.973	1.867E+14
REFLEX J0601.7-3959		246.52	-26.09	0.0468	139.0	141	-521	247	-83	192	24.782	2.323	3.487E+14
REFLEX J0322.3-4120	ABELL 3122	247.56	-56.07	0.0643	189.9	-71	-207	-30	191	162	7.857	1.394	2.276E+14
CIZA J0826.4-2721	ABELL S0610	248.07	6.25	0.0410	122.8	322	-468	72	-277	134	11.902	0.860	1.678E+14
CIZA J0717.1-3621		248.34	-10.95	0.0320	92.5	164	-637	-84	77	144	19.750	0.868	1.730E+14
REFLEX J0540.1-4322	ABELL 3360	249.32	-30.74	0.0850	252.3	269	-463	81	39	93	4.061	1.260	2.006E+14
REFLEX J1020.4-0631	ABELL 0978	250.01	40.35	0.0540	161.9	113	-239	99	-268	125	4.449	0.559	1.176E+14
REFLEX J1058.4+0134	ABELL 1139	251.49	52.78	0.0398	120.6	237	-262	171	-360	119	6.762	0.461	1.055E+14
REFLEX J1027.9-0648	ABELL 1023	252.01	41.47	0.1176	322.2	126	48	-148	86	56	4.337	2.560	3.158E+14
REFLEX J0953.2-1558		252.50	28.96	0.0302	90.6	189	-296	83	-299	128	7.083	0.278	7.403E+13
REFLEX J0317.9-4414	ABELL 3112	252.94	-56.08	0.0752	226.0	173	-15	226	-164	139	36.270	8.715	8.760E+14

...continued

ID	Alt.	l (°)	b (°)	z	d h^{-1} Mpc	v_x km s^{-1}	v_y km s^{-1}	v_z km s^{-1}	v_{pec} km s^{-1}	σ_v km s^{-1}	f_x $\times10^{-12}$ ergs cm^{-2} s^{-1}	l_x $\times10^{42}$ h_{50}^{-2} ergs s^{-1}	M $M_\odot$
REFLEX J1017.3-1040	ABELL 0970	253.04	36.85	0.0586	176.5	239	-176	234	-355	121	12.047	1.773	2.765E+14
REFLEX J0938.0-2020	ABELL S0617	253.20	23.33	0.0344	104.3	301	-328	170	-412	130	6.805	0.347	8.637E+13
REFLEX J0340.8-4542		253.41	-51.78	0.0698	208.6	232	-301	329	-57	159	4.515	0.947	1.680E+14
REFLEX J0547.8-4724	ABELL S0547	254.17	-30.04	0.0515	153.8	166	-250	238	-158	191	3.442	0.393	9.096E+13
REFLEX J0545.4-4756	ABELL 3363	254.73	-30.52	0.1254	341.8	74	-559	-393	527	40	5.809	3.884	4.239E+14
REFLEX J0314.3-4525	ABELL 3104	255.33	-56.28	0.0718	214.1	219	-79	-9	10	154	11.568	2.551	3.516E+14
REFLEX J0514.6-4903	ABELL 3330	255.54	-35.69	0.0912	270.5	307	-384	-15	87	78	3.309	1.183	1.884E+14
REFLEX J0616.8-4748		255.66	-25.31	0.1164	318.9	123	-501	-305	372	48	4.281	2.476	3.089E+14
REFLEX J1044.5-0704	ABELL 1084	256.39	44.04	0.1342	364.0	24	216	-263	300	36	9.171	6.986	6.450E+14
REFLEX J1039.7-0840	ABELL 1069	256.60	42.04	0.0650	195.7	142	-257	198	-353	111	7.906	1.433	2.320E+14
REFLEX J0606.9-4928	ABELL 3380	257.11	-27.27	0.0553	168.7	431	-275	535	-525	177	4.435	0.584	1.212E+14
CIZA J0944.5-2634		259.08	19.99	0.1421	383.0	-119	64	-550	503	25	6.430	5.500	5.294E+14
REFLEX J1041.5-1123		259.35	40.24	0.0839	251.0	171	-107	141	-226	80	3.316	1.004	1.697E+14
REFLEX J0621.7-5242		261.16	-25.62	0.0511	151.0	314	-515	58	-24	197	6.826	0.767	1.502E+14
REFLEX J0626.3-5341	ABELL 3391	262.38	-25.15	0.0514	154.0	608	-504	128	-244	194	18.788	2.125	3.224E+14
REFLEX J0429.1-5350	ABELL S0463	262.45	-42.35	0.0400	114.2	185	-394	-342	390	161	8.988	0.618	1.314E+14
REFLEX J0627.2-5429	ABELL 3395	263.26	-25.19	0.0506	147.7	510	-608	-272	148	194	22.856	2.504	3.654E+14
REFLEX J0330.2-5233	ABELL 3128	264.73	-51.10	0.0624	186.1	379	-95	-46	-49	172	13.837	2.306	3.335E+14
REFLEX J0342.8-5337	ABELL 3158	265.04	-48.95	0.0590	173.3	312	-387	-103	204	176	30.731	4.564	5.613E+14
REFLEX J0631.4-5609		265.21	-24.96	0.0540	163.8	794	-348	163	-447	180	4.687	0.589	1.223E+14
REFLEX J0334.8-5342		265.90	-49.99	0.0619	184.3	554	-246	-40	-25	171	3.298	0.545	1.132E+14
REFLEX J0352.3-5453		266.01	-47.19	0.0447	128.7	213	-372	-343	368	161	4.484	0.386	9.119E+13
REFLEX J0322.2-5311		266.49	-51.91	0.0797	237.8	420	-229	57	-29	122	3.319	0.908	1.589E+14
CIZA J0745.1-5404		266.84	-14.36	0.0740	222.5	378	-366	228	-348	102	10.889	2.551	3.496E+14
CIZA J0757.7-5315	ABELL S0606	267.00	-12.33	0.0390	115.5	458	-660	-60	-154	140	11.728	0.767	1.548E+14
REFLEX J0600.9-5834	ABELL S0560	267.20	-29.37	0.0369	106.3	386	-428	-320	192	165	6.835	0.400	9.564E+13
REFLEX J0340.1-5504	ABELL S0377	267.29	-48.72	0.0464	135.2	270	-224	-337	238	159	4.160	0.386	9.079E+13
REFLEX J1038.4-2454		268.31	28.88	0.1230	335.5	-48	62	-209	188	41	4.956	3.194	3.681E+14
REFLEX J0346.2-5656	ABELL 3164	269.29	-47.15	0.0570	167.2	512	-427	-248	200	170	8.765	1.223	2.100E+14
REFLEX J0328.6-5542	ABELL 3126	269.31	-49.88	0.0853	254.6	452	-290	90	-40	96	10.019	3.112	3.949E+14
REFLEX J1036.6-2731	HYDRA CLUSTER	269.60	26.48	0.0126	41.9	137	-414	700	-723	188	122.740	0.831	1.760E+14
REFLEX J0712.0-6029		271.25	-20.95	0.0322	92.5	348	-494	-308	132	154	5.816	0.260	6.998E+13
CIZA J0812.5-5714		271.60	-12.51	0.0620	187.1	483	-390	193	-414	157	24.220	3.975	5.023E+14
CIZA J0820.9-5704		272.09	-11.45	0.0610	181.2	357	-611	-61	-129	158	9.746	1.556	2.491E+14
REFLEX J0431.4-6126	ABELL 3266	272.11	-40.13	0.0589	176.5	730	-391	41	-191	145	45.791	6.769	7.545E+14
CIZA J1029.7-3519	ANTLIA GROUP	272.90	19.16	0.0087	25.3	-189	-38	568	-241	213	39.443	0.128	4.371E+13
BCS J1200.3+0320	ABELL 1437	273.57	63.26	0.1339	363.8	52	215	0	182	43	8.387	6.365	6.020E+14
REFLEX J1107.3-2300	ABELL S0651	273.82	33.92	0.0639	191.7	163	-55	363	-315	109	4.300	0.756	1.440E+14
REFLEX J1130.3-1434	ABELL 1285	275.21	43.89	0.1068	294.5	127	-62	103	-156	63	9.262	4.490	4.938E+14
REFLEX J1135.4-1328	ABELL 1317	276.14	45.40	0.0722	217.1	83	-205	364	-338	122	3.319	0.746	1.397E+14
BCS J1210.3+0522	ZwCl 1207.5+0542	276.87	66.15	0.0770	231.2	-78	-191	468	-231	145	4.968	1.265	2.052E+14
REFLEX J1204.4+0153	ZwCl 1201.5+0205	276.90	62.36	0.0199	61.7	318	-257	332	-414	158	28.460	0.483	1.150E+14
REFLEX J1141.4-1216		277.36	47.09	0.1195	327.1	72	-16	17	-56	70	5.946	3.614	4.072E+14
BCS J1226.5+1243	VIRGO CLUSTER	279.68	74.46	0.0036	10.6	-250	-191	-22	-132	185	892.258	1.000	1.800E+14
CIZA J1024.5-5328		282.04	3.33	0.0720	215.9	259	-323	122	-319	76	3.744	0.836	1.522E+14
REFLEX J1202.9-0649	ABELL 1448	282.11	54.07	0.1268	345.7	38	78	38	38	54	4.026	2.761	3.271E+14
BCS J1217.6+0340	ZwCl 1215.1+0400	282.50	65.19	0.0750	223.1	16	34	346	-22	151	20.574	4.930	5.718E+14
REFLEX J1114.2-3811		282.68	20.83	0.1306	354.4	-205	17	-201	263	41	5.459	3.958	4.247E+14
REFLEX J1151.5-1619		282.72	44.19	0.0722	217.6	259	-179	310	-387	127	4.371	0.981	1.715E+14
BCS J1227.4+0849	ABELL 1541	284.62	70.84	0.0896	270.8	2	-385	274	-389	116	3.166	1.093	1.783E+14
REFLEX J0145.0-5300	ABELL 2941	285.50	-62.26	0.1168	321.1	63	-648	-10	531	47	7.132	4.136	4.534E+14
REFLEX J1139.4-3327		286.12	27.05	0.1076	296.2	61	-48	44	-89	53	4.960	2.452	3.131E+14
REFLEX J0738.1-7506		287.04	-23.23	0.1110	305.1	-57	-488	-99	261	42	3.235	1.708	2.368E+14
BCS J1241.3+1833		287.18	81.13	0.0718	216.4	-43	-251	335	-232	132	8.754	1.934	2.856E+14
REFLEX J1145.2-3425	ABELL 3490	287.73	26.49	0.0697	210.4	316	-37	474	-450	116	7.928	1.652	2.551E+14
REFLEX J1200.0-3124	ABELL 3497	290.24	30.19	0.0685	206.9	298	-179	377	-453	130	6.534	1.317	2.158E+14
REFLEX J1219.3-1315	ABELL 1520	291.01	48.87	0.0688	206.4	163	-166	227	-273	133	3.178	0.649	1.269E+14

...continued

ID	Alt.	l (°)	b (°)	z	d h^{-1} Mpc	v_x km s^{-1}	v_y km s^{-1}	v_z km s^{-1}	v_{pec} km s^{-1}	σv km s^{-1}	f_X $\times10^{-12}$ ergs cm^{-2} s^{-1}	l_X $\times10^{42}$ h_{50}^{-2} ergs s^{-1}	M M$_\odot$
CIZA J1040.7-7047		292.52	-10.61	0.0610	182.7	316	-346	90	-273	96	10.559	1.685	2.645E+14
REFLEX J0110.0-4554	ABELL 2877	293.04	-70.86	0.0238	68.7	352	-391	93	234	130	12.490	0.304	8.048E+13
CIZA J1201.0-4623		293.95	15.60	0.1180	322.8	-128	-83	-43	103	49	3.953	2.351	2.960E+14
REFLEX J1215.5-3901		295.35	23.31	0.1190	325.4	-57	-38	-37	43	57	5.132	3.097	3.631E+14
CIZA J1210.7-4644	ABELL S0689	295.71	15.56	0.0320	95.7	141	-68	429	-286	127	9.559	0.421	1.005E+14
REFLEX J0351.7-8213	ABELL S0405	296.42	-32.47	0.0613	182.5	283	-392	156	-83	99	16.717	2.687	3.751E+14
CIZA J1211.0-5405		296.96	8.31	0.1100	302.4	-87	-174	40	36	56	7.373	3.797	4.321E+14
REFLEX J1236.6-3354	ABELL S0700	299.44	28.86	0.0796	240.6	431	-167	205	-488	103	5.183	1.410	2.211E+14
REFLEX J1244.6-1159	ABELL 1606	300.30	50.84	0.0963	290.3	429	-132	295	-393	102	6.382	2.528	3.290E+14
REFLEX J0058.0-6648	ABELL S0112	301.92	-50.31	0.0661	195.9	224	-375	174	98	93	5.106	0.960	1.713E+14
REFLEX J1248.8-4118	CENTAURUS CLUSTER	302.40	21.57	0.0114	35.5	314	-79	566	-425	276	255.265	1.412	2.627E+14
REFLEX J0052.8-8015	ABELL 2837	302.86	-36.87	0.1141	313.6	22	-566	165	264	76	8.664	4.790	5.094E+14
REFLEX J1252.5-3116		303.22	31.60	0.0535	160.8	141	-175	690	-314	218	12.421	1.525	2.500E+14
REFLEX J1252.8-1522	ABELL 1631	303.45	47.50	0.0462	136.9	-379	-417	228	-83	160	8.886	0.815	1.592E+14
REFLEX J1254.5-2908	ABELL 3528	303.75	33.72	0.0542	165.3	121	-705	411	-557	210	24.317	3.054	4.202E+14
REFLEX J1255.5-3019	ABELL 3530	303.99	32.54	0.0541	165.0	323	-415	446	-556	213	6.905	0.869	1.638E+14
REFLEX J1257.0-3118		304.33	31.55	0.0561	175.8	858	-487	412	-1031	195	6.977	0.944	1.734E+14
REFLEX J1257.2-3023	ABELL 3532	304.43	32.47	0.0554	172.2	621	-600	333	-886	202	20.876	2.741	3.863E+14
REFLEX J1255.6-1239		304.54	50.20	0.0585	176.1	63	-332	102	-304	136	6.002	0.884	1.640E+14
REFLEX J1257.1-1723	ABELL 1644	304.89	45.45	0.0473	141.6	-197	-485	168	-228	172	36.571	3.498	4.733E+14
REFLEX J1258.7-2640	ABELL 1648	304.97	36.18	0.0767	232.4	438	-262	75	-512	109	5.635	1.423	2.242E+14
REFLEX J1305.9-3738	ABELL S0721	306.11	25.14	0.0497	148.9	305	224	746	-268	228	8.714	0.925	1.735E+14
REFLEX J1304.1-3030		306.17	32.29	0.0117	35.9	-23	-627	233	-349	271	19.421	0.114	3.983E+13
REFLEX J0040.0-5607	ABELL 2806	306.21	-60.93	0.0277	81.3	417	-370	92	101	119	8.529	0.282	7.522E+13
REFLEX J1303.7-2414	ABELL 3541	306.51	38.54	0.1288	350.6	-64	83	42	99	44	9.654	6.777	6.385E+14
REFLEX J1258.6-0145	ABELL 1650	306.67	61.06	0.0845	253.3	-3	-220	434	-189	186	24.285	7.366	7.550E+14
REFLEX J1259.3-0411	ABELL 1651	306.74	58.62	0.0845	252.9	400	60	468	-154	183	26.128	7.922	7.973E+14
CIZA J1324.7-5736		307.39	4.97	0.0190	59.9	527	-48	319	-574	168	63.275	0.977	1.954E+14
REFLEX J1301.5-0649	RXC J1301.6-0650	307.42	55.95	0.0898	272.6	641	-228	286	-545	156	3.078	1.068	1.751E+14
REFLEX J1539.8-8335	RXC J1539.5-8335	307.57	-22.30	0.0728	217.0	213	-474	378	-99	130	16.624	3.761	4.692E+14
CIZA J1321.2-4342		308.61	18.84	0.0114	30.4	-22	274	54	107	259	49.487	0.275	7.703E+13
REFLEX J1302.8-0230	ABELL 1663	308.67	60.24	0.0847	254.3	237	-132	230	-227	188	5.299	1.630	2.435E+14
REFLEX J1320.6-4102	ABELL S0727	308.85	21.49	0.0495	148.8	466	437	512	-313	222	4.170	0.440	9.940E+13
REFLEX J2105.0-8243	ABELL 3728	310.02	-30.96	0.0969	287.3	118	-518	161	132	85	3.612	1.454	2.171E+14
REFLEX J1705.7-8210	ABELL S0792	310.56	-23.44	0.0737	220.2	267	-360	212	-137	137	7.369	1.716	2.600E+14
REFLEX J1315.3-1623		311.22	46.10	0.0087	23.7	-394	-358	-162	12	250	41.183	0.134	4.514E+13
REFLEX J2319.7-7314		311.67	-42.30	0.0984	291.7	187	-560	297	189	98	4.975	2.060	2.808E+14
REFLEX J1328.0-3130	ABELL 3558	312.00	30.72	0.0480	140.1	-209	-101	-67	128	241	60.283	5.927	7.017E+14
REFLEX J1309.2-0137		312.12	60.94	0.0880	268.5	368	-543	62	-650	176	4.720	1.568	2.346E+14
REFLEX J1337.4-4119		312.15	20.72	0.0519	160.2	824	147	179	-723	210	6.346	0.735	1.453E+14
REFLEX J1329.8-3136		312.42	30.55	0.0488	146.8	156	-348	-196	-309	240	17.195	1.755	2.812E+14
REFLEX J1326.9-2710	ABELL 1736	312.58	35.04	0.0458	133.2	-464	-375	-170	163	223	29.041	2.607	3.811E+14
REFLEX J0027.3-5015	ABELL 2777	312.59	-66.42	0.1448	391.4	-42	-938	-5	868	32	3.552	3.173	3.483E+14
REFLEX J1332.4-3307	ABELL 3560	312.73	28.96	0.0487	145.4	272	68	-200	-200	242	16.198	1.647	2.681E+14
REFLEX J1331.4-3148		312.78	30.30	0.0448	127.8	-381	133	-40	396	230	11.346	0.978	1.831E+14
REFLEX J1333.6-3140	ABELL 3562	313.33	30.34	0.0490	150.7	493	-419	-424	-635	235	26.024	2.674	3.853E+14
REFLEX J0049.3-2931		313.51	-87.56	0.1084	300.8	221	-577	187	542	66	5.293	2.655	3.316E+14
REFLEX J1336.6-3357		313.54	27.98	0.0123	38.4	266	-357	-87	-403	268	9.102	0.060	2.439E+13
REFLEX J2358.7-6038	ABELL 4067	314.25	-55.31	0.0989	293.1	30	-391	348	259	97	5.531	2.312	3.058E+14
CIZA J1358.6-4746		314.46	13.58	0.0740	222.6	293	-186	210	-333	129	25.870	6.031	6.666E+14
REFLEX J1346.6-3753	ABELL 3570	314.80	23.70	0.0377	108.2	-130	275	61	230	193	5.527	0.366	8.921E+13
CIZA J1407.8-5100		315.01	10.06	0.0966	289.2	179	-198	176	-215	113	19.320	7.645	7.540E+14
REFLEX J1333.7-2316	ABELL 1757	315.39	38.57	0.1264	344.8	-29	60	97	64	46	6.595	4.473	4.702E+14
CIZA J1631.6-7507	ABELL 3628	315.72	-18.05	0.1050	290.1	76	-477	41	71	63	15.889	7.423	7.229E+14
REFLEX J1347.4-3251	ABELL 3571	316.32	28.56	0.0391	112.0	-282	78	-149	280	199	104.801	6.838	7.988E+14
REFLEX J1350.7-3343		316.83	27.54	0.1142	313.8	6	-125	83	-60	61	3.375	1.885	2.530E+14
REFLEX J1347.2-3025	ABELL 3574W	316.95	30.93	0.0145	48.7	518	-611	-42	-759	224	6.473	0.059	2.405E+13

...continued

ID	Alt.	l (°)	b (°)	z	d h^{-1} Mpc	v_x km s^{-1}	v_y km s^{-1}	v_z km s^{-1}	v_{pec} km s^{-1}	σ_v km s^{-1}	f_X $\times 10^{-12}$ ergs cm^{-2} s^{-1}	l_X $\times 10^{42}$ h_{50}^{-2} ergs s^{-1}	M $M_\odot$
CIZA J1420.0-4936		317.33	10.77	0.0915	272.5	29	-180	-16	-62	131	5.055	1.813	2.594E+14
CIZA J1645.4-7334		317.59	-17.82	0.0690	206.3	298	-462	39	-144	129	9.120	1.861	2.794E+14
REFLEX J2124.0-7446		317.68	-35.76	0.0586	172.9	176	-482	259	122	119	3.363	0.498	1.066E+14
CIZA J1410.4-4246		318.04	17.76	0.0490	147.1	361	290	-166	-263	193	9.355	0.965	1.794E+14
REFLEX J1348.9-2525	ABELL 1791	318.95	35.65	0.1269	346.1	-71	43	116	93	45	3.688	2.535	3.067E+14
REFLEX J1912.6-7517	ABELL S0810	319.49	-27.51	0.0726	216.7	264	-350	12	-72	130	12.384	2.791	3.753E+14
REFLEX J1403.5-3358	ABELL S0753	319.60	26.55	0.0132	42.8	460	-282	-319	-562	248	20.834	0.156	5.007E+13
CIZA J1432.8-4419	ABELL 3602	321.41	14.87	0.1180	323.5	-24	-228	14	-32	91	3.400	2.026	2.647E+14
REFLEX J1326.2+0013		321.63	61.82	0.0826	247.6	146	-101	-55	-164	190	5.326	1.559	2.367E+14
REFLEX J2249.9-6425	ABELL 3921	321.95	-47.97	0.0940	278.7	186	-467	379	212	143	11.960	4.497	5.096E+14
CIZA J1500.9-5134		322.50	6.31	0.0350	104.2	163	77	-20	-156	136	7.722	0.407	9.727E+13
REFLEX J1330.8-0151	ABELL 1750	322.61	59.49	0.0852	258.2	512	-186	-201	-446	177	7.514	2.333	3.182E+14
REFLEX J1407.4-2700	ABELL 3581	323.15	32.86	0.0230	70.7	297	-271	12	-390	156	34.038	0.772	1.621E+14
BCS J1303.7+1916	ABELL 1668	323.42	81.65	0.0634	189.2	99	-48	392	-13	147	9.889	1.705	2.652E+14
CIZA J1614.1-6307		323.65	-8.73	0.0620	187.2	385	-316	-23	-329	136	6.320	1.044	1.843E+14
REFLEX J2218.0-6511		324.53	-44.97	0.0951	282.9	426	-584	177	119	139	7.819	3.017	3.768E+14
CIZA J1638.2-6420		324.60	-11.51	0.0508	151.7	204	-235	154	-133	161	91.045	10.008	1.032E+15
CIZA J1614.3-6052	NORMA CLUSTER	325.26	-7.13	0.0157	49.6	439	64	-45	-446	176	220.170	2.313	3.762E+14
CIZA J1454.9-4312		325.62	14.16	0.0660	200.9	455	-235	-164	-517	151	5.800	1.086	1.880E+14
CIZA J1514.6-4558		327.30	10.01	0.0580	176.3	410	-92	-222	-454	178	23.125	3.325	4.437E+14
CIZA J1518.3-4632		327.56	9.18	0.0560	167.3	112	33	-197	-142	179	7.079	0.954	1.749E+14
CIZA J1501.6-4037		328.05	15.80	0.1240	338.9	-143	-147	116	122	60	7.215	4.708	4.914E+14
CIZA J1456.2-3826		328.21	18.23	0.1150	316.1	-12	-171	97	-18	75	4.882	2.755	3.357E+14
CIZA J1646.6-6023		328.32	-9.72	0.1480	398.4	-504	-456	160	600	28	5.700	5.290	5.073E+14
REFLEX J2228.8-6053		328.32	-48.61	0.0423	123.8	213	-460	315	224	124	7.723	0.594	1.269E+14
REFLEX J1435.0-2823	ABELL 3605	329.05	29.16	0.0689	208.9	336	-240	-151	-434	108	3.198	0.655	1.277E+14
REFLEX J1401.6-1107	ABELL 1837	329.24	48.12	0.0698	209.3	345	64	4	-178	120	5.953	1.246	2.064E+14
CIZA J1653.0-5943		329.35	-9.92	0.0480	142.2	33	-300	-137	1	157	40.924	4.028	5.253E+14
CIZA J1752.0-6348		329.58	-17.98	0.1330	361.6	-289	-539	112	464	40	7.083	5.312	5.267E+14
BCS J1323.5+1118	ABELL 1728	329.95	72.47	0.0911	276.0	36	-436	31	-416	116	4.439	1.580	2.342E+14
REFLEX J1421.9-2009		330.17	37.88	0.1208	331.1	93	12	170	-23	62	3.470	2.165	2.764E+14
REFLEX J1455.2-3325		330.65	22.70	0.1158	318.3	1	-148	152	-16	69	4.422	2.532	3.145E+14
BCS J1342.1+0213	ABELL 1773	331.07	62.30	0.0776	230.7	113	116	-11	47	172	5.412	1.399	2.209E+14
REFLEX J2158.3-6025	ABELL 3825	331.95	-45.76	0.0750	219.4	218	-789	419	470	170	7.762	1.871	2.765E+14
REFLEX J2201.9-5957	ABELL 3827	332.22	-46.38	0.0980	292.9	419	-406	-48	16	135	18.082	7.364	7.307E+14
REFLEX J1847.2-6320	ABELL S0805	332.25	-23.59	0.0146	44.5	216	50	36	-206	176	8.788	0.081	3.051E+13
REFLEX J1408.1-0904		332.76	49.31	0.0354	107.4	234	-233	102	-292	140	7.147	0.385	9.329E+13
CIZA J1813.3-6127		332.88	-19.28	0.1470	396.2	-429	-603	189	645	29	8.753	7.982	6.922E+14
REFLEX J1416.8-1158		333.63	45.75	0.0982	295.3	341	-91	128	-256	86	4.014	1.658	2.388E+14
REFLEX J2224.6-5632		334.28	-50.70	0.0860	255.2	90	-311	162	206	169	3.451	1.500	2.280E+14
REFLEX J2154.1-5751	ABELL 3822	335.57	-46.46	0.0760	222.8	103	-654	171	442	177	14.281	3.521	4.431E+14
REFLEX J2116.8-5930	ABELL S0927	335.91	-41.35	0.0602	177.6	222	-498	218	218	152	4.032	0.630	1.267E+14
REFLEX J2224.4-5515		336.03	-51.37	0.0791	232.7	-166	-347	221	400	171	5.969	1.602	2.436E+14
REFLEX J2246.3-5243	ABELL 3911	336.59	-55.43	0.0965	287.4	32	-203	109	163	130	11.189	4.433	5.012E+14
REFLEX J2146.3-5716	ABELL 3806 NED01	336.97	-45.74	0.0760	223.2	181	-735	-105	407	176	8.746	2.163	3.075E+14
REFLEX J1524.1-3154		337.05	20.67	0.1028	285.1	97	-157	134	-88	71	11.228	5.041	5.436E+14
REFLEX J2144.0-5637		338.00	-45.69	0.0824	245.6	402	-522	-173	94	170	11.875	3.441	4.288E+14
REFLEX J2151.3-5521	ABELL 3816	339.16	-47.12	0.0385	111.4	148	-565	152	359	130	6.661	0.425	9.957E+13
BCS J1353.0+0509		339.39	63.57	0.0790	237.6	92	-132	-186	-203	159	4.919	1.319	2.106E+14
REFLEX J2400.0-3928		340.58	-73.68	0.1024	285.1	139	-431	318	382	93	4.828	2.164	2.886E+14
CIZA J1802.4-5236		340.71	-14.34	0.1250	342.0	-202	-498	210	398	39	5.948	3.951	4.298E+14
REFLEX J2012.5-5650	ABELL 3667	340.85	-33.40	0.0556	165.4	345	-529	58	60	166	61.541	8.101	8.704E+14
REFLEX J2032.1-5626	ABELL 3685	341.19	-36.11	0.1380	374.6	-134	-712	156	582	43	3.381	2.747	3.175E+14
REFLEX J1436.8-0900		341.86	45.74	0.0842	252.7	346	32	90	-165	118	6.092	1.850	2.681E+14
REFLEX J2209.3-5149	ABELL 3836	342.54	-50.96	0.1065	295.4	180	-295	-194	98	120	6.236	3.016	3.666E+14
REFLEX J1952.1-5503	ABELL 3651	342.82	-30.49	0.0600	181.1	510	-488	-202	-194	146	7.969	1.232	2.097E+14
REFLEX J2009.1-5422	ABELL S0849	343.79	-32.89	0.0516	151.5	200	-715	-26	257	167	4.851	0.556	1.179E+14

...continued

ID	Alt.	l (°)	b (°)	z	d h^{-1} Mpc	v_x km s^{-1}	v_y km s^{-1}	v_z km s^{-1}	v_{pec} km s^{-1}	σ_v km s^{-1}	f_X $\times10^{-12}$ ergs cm^{-2} s^{-1}	l_X $\times10^{42}$ h_{50}^{-2} ergs s^{-1}	M $M_\odot$
REFLEX J1927.0-5342		343.80	-26.68	0.0570	170.8	421	-719	-250	-71	146	5.504	1.161	2.020E+14
REFLEX J0025.5-3302	ABELL S0041	344.81	-81.85	0.0491	144.0	240	-422	367	372	143	11.002	1.139	2.031E+14
REFLEX J2305.5-4512	ABELL 3970	345.32	-62.24	0.1253	343.5	81	-572	87	494	66	4.020	2.692	3.221E+14
REFLEX J2021.9-5258	ABELL 3675	345.52	-34.77	0.1383	375.5	-143	-709	194	599	42	3.235	2.641	3.081E+14
REFLEX J2018.8-5242	ABELL S0861	345.84	-34.29	0.0505	147.2	5	-677	-99	372	164	15.971	1.746	2.789E+14
CIZA J1626.3-3329		346.13	10.81	0.1098	303.5	125	-174	224	-21	102	16.376	8.355	7.811E+14
REFLEX J1953.0-5202	ABELL 3653	346.33	-30.32	0.1069	296.3	170	-583	50	209	64	6.308	3.073	3.715E+14
REFLEX J2104.9-5149		346.40	-41.38	0.0491	143.2	-11	-490	73	370	156	12.529	1.296	2.238E+14
REFLEX J2129.6-5048	ABELL 3771	346.84	-45.36	0.0796	236.6	137	-500	-411	180	148	5.322	1.447	2.255E+14
REFLEX J1928.1-5056	ABELL 3639	346.89	-26.33	0.1496	403.2	-329	-715	320	731	29	3.886	3.698	3.864E+14
REFLEX J1458.9-0843		348.17	42.67	0.1043	289.5	321	-68	86	-207	98	4.372	2.034	2.743E+14
REFLEX J2314.0-4243	ABELL S1101	348.32	-64.82	0.0564	166.5	305	-391	227	276	124	30.409	4.131	5.242E+14
REFLEX J2321.5-4153	ABELL 3998	348.33	-66.45	0.0894	264.2	164	-480	136	406	112	8.926	3.045	3.847E+14
CIZA J1640.4-3212		349.10	9.46	0.0870	259.2	81	-127	265	60	104	6.379	2.067	2.893E+14
REFLEX J0003.1-3555		349.33	-76.49	0.0490	144.1	418	-413	229	325	145	8.503	0.877	1.671E+14
REFLEX J0006.0-3443		352.19	-77.66	0.1147	316.9	135	-492	194	464	82	5.801	3.251	3.804E+14
REFLEX J2147.9-4600	ABELL S0974	352.84	-49.32	0.0593	174.5	104	-483	14	333	141	9.538	1.439	2.360E+14
REFLEX J1925.4-4257	ABELL 3638	355.35	-24.02	0.0774	231.0	251	-563	-5	80	86	6.902	1.773	2.639E+14
BCS J1440.6+0328		355.49	54.78	0.0276	81.7	287	-43	410	18	169	24.521	0.802	1.648E+14
CIZA J1655.0-2625		355.70	10.64	0.0940	281.0	61	-146	121	12	93	6.781	2.560	3.340E+14
REFLEX J2146.9-4355	ABELL 3809	356.04	-49.53	0.0620	184.4	140	-361	-157	168	134	11.181	1.842	2.821E+14
BCS J1354.0+1455	ABELL 1814	356.10	71.00	0.1251	342.9	154	-33	180	-14	65	3.108	2.080	2.656E+14
REFLEX J2356.9-3445		356.41	-76.07	0.0475	137.4	304	-621	88	557	144	33.823	3.263	4.491E+14
REFLEX J1558.3-1409		356.52	28.67	0.0970	290.3	203	-54	223	-26	88	14.511	5.799	6.123E+14
REFLEX J2103.4-4320	ABELL 3736	357.73	-41.73	0.1430	387.5	-107	-797	268	740	35	5.877	0.600	1.257E+14
REFLEX J0042.1-2832		358.03	-87.50	0.1082	300.4	227	-556	209	529	71	10.837	5.386	5.641E+14
REFLEX J2331.1-3630	ABELL 4010	359.06	-70.60	0.0957	284.1	170	-384	89	337	103	9.957	3.884	4.547E+14
REFLEX J2012.0-4128	ABELL 3668	359.08	-32.12	0.1496	403.7	-212	-779	394	792	29	3.655	3.481	3.692E+14
REFLEX J2018.4-4103		359.80	-33.24	0.0192	57.8	401	-306	87	-18	141	4.573	0.073	2.792E+13

References

Aaronson, M., Bothun, G., Mould, J., Huchra, J., Schommer, R. A., & Cornell, M. E., 1986, *ApJ*, **302**, 536

Aaronson, M., Bothun, G. D., Cornell, M. E., Dawe, J. A., Dickens, R. J., Hall, P. J., Sheng, H. M., Huchra, J. P., Lucey, J. R., Mould, J. R., Murray, J. D., Schommer, R. A., & Wright, A. E., 1989, *ApJ*, **338**, 654

Abell, G. O., 1958, *ApJS*, **3**, 211

Abell, G. O., Corwin, Jr., H. G., & Olowin, R. P., 1989, *ApJS*, **70**, 1

Aldering, G., Adam, G., Antilogus, P., Astier, P., Bacon, R., Bongard, S., Bonnaud, C., Copin, Y., Hardin, D., Henault, F., Howell, D. A., Lemonnier, J.-P., Levy, J.-M., Loken, S. C., Nugent, P. E., Pain, R., Pecontal, A., Pecontal, E., Perlmutter, S., Quimby, R. M., Schahmaneche, K., Smadja, G., & Wood-Vasey, W. M., 2002, in J. A. Tyson & S. Wolff (eds.), *Survey and Other Telescope Technologies and Discoveries.*, Vol. 4836 of *SPIE Conf. Ser.*, p. 61

Allen, D. A., Staveley-Smith, L., Meadows, V. S., Roche, P. F., & Norris, R. P., 1990, *Nat*, **343**, 45

Allen, S. W., Schmidt, R. W., Fabian, A. C., & Ebeling, H., 2003, *MNRAS*, **342**, 287

Bahcall, N. A., Gramann, M., & Cen, R., 1994, *ApJ*, **436**, 23

Baker, J. E., Davis, M., Strauss, M. A., Lahav, O., & Santiago, B. X., 1998, *ApJ*, **508**, 6

Bardelli, S., Zucca, E., Zamorani, G., Moscardini, L., & Scaramella, R., 2000, *MNRAS*, **312**, 540

Barnes, D. G., Staveley-Smith, L., de Blok, W. J. G., Oosterloo, T., Stewart, I. M., Wright, A. E., Banks, G. D., Bhathal, R., Boyce, P. J., Calabretta, M. R., Disney, M. J., Drinkwater, M. J., Ekers, R. D., Freeman, K. C., Gibson, B. K., Green, A. J., Haynes, R. F., te Lintel Hekkert, P., Henning, P. A., Jerjen, H., Juraszek, S., Kesteven, M. J., Kilborn, V. A., Knezek, P. M., Koribalski, B., Kraan-Korteweg, R. C., Malin, D. F., Marquarding, M., Minchin, R. F., Mould, J. R., Price, R. M., Putman, M. E., Ryder, S. D., Sadler, E. M., Schröder, A., Stootman, F., Webster, R. L., Wilson, W. E., & Ye, T., 2001, *MNRAS*, **322**, 486

Basilakos, S. & Plionis, M., 2006, *MNRAS*, **373**, 1112

Beichman, C. A., Neugebauer, G., Habing, H. J., Clegg, P. E., & Chester, T. J. (eds.), 1988, *Infrared astronomical satellite (IRAS) catalogs and atlases. Volume 1: Explanatory supplement*

Berlind, A. A., Narayanan, V. K., & Weinberg, D. H., 2000, *ApJ*, **537**, 537

Bernstein, G. M., Guhathakurta, P., Raychaudhury, S., Giovanelli, R., Haynes, M. P., Herter, T., & Vogt, N. P., 1994, *AJ*, **107**, 1962

Bertschinger, E. & Dekel, A., 1989, *ApJL*, **336**, L5

Binggeli, B., Popescu, C. C., & Tammann, G. A., 1993, *A&ASS*, **98**, 275

Binggeli, B., Tammann, G. A., & Sandage, A., 1987, *AJ*, **94**, 251

Blakeslee, J. P., Davis, M., Tonry, J. L., Dressler, A., & Ajhar, E. A., 1999, *ApJL*, **527**, L73

Boehringer, H., Voges, W., Fabian, A. C., Edge, A. C., & Neumann, D. M., 1993, *MNRAS*, **264**, L25

Böhringer, H., 1994, in W. C. Seitter (ed.), *Cosmological Aspects of X-Ray Clusters of Galaxies, NATO ASI Ser. C, 441*, p. 123

Böhringer, H., Briel, U. G., Schwarz, R. A., Voges, W., Hartner, G., & Trumper, J., 1994, *Nat*, **368**, 828

Bohringer, H., Guzzo, L., Collins, C. A., Neumann, D. M., Schindler, S., Schuecker, P., Cruddace, R., Degrandi, S., Chincarini, G., Edge, A. C., MacGillivray, H. T., Shaver, P., Vettolani, G., & Voges, W., 1998, *The Messenger*, **94**, 21

Böhringer, H., Schuecker, P., Guzzo, L., Collins, C. A., Voges, W., Cruddace, R. G., Ortiz-Gil, A., Chincarini, G., De Grandi, S., Edge, A. C., MacGillivray, H. T., Neumann, D. M., Schindler, S., & Shaver, P., 2004, *A&A*, **425**, 367

Böhringer, H., Schuecker, P., Guzzo, L., Collins, C. A., Voges, W., Schindler, S., Neumann, D. M., Cruddace, R. G., De Grandi, S., Chincarini, G., Edge, A. C., MacGillivray, H. T., & Shaver, P., 2001, *A&A*, **369**, 826

Böhringer, H., Voges, W., Huchra, J. P., McLean, B., Giacconi, R., Rosati, P., Burg, R., Mader, J., Schuecker, P., Simiç, D., Komossa, S., Reiprich, T. H., Retzlaff, J., & Trümper, J., 2000, *ApJS*, **129**, 435

Branchini, E., Freudling, W., Da Costa, L. N., Frenk, C. S., Giovanelli, R., Haynes, M. P., Salzer, J. J., Wegner, G., & Zehavi, I., 2001, *MNRAS*, **326**, 1191

Branchini, E. & Plionis, M., 1996, *ApJ*, **460**, 569

Branchini, E., Teodoro, L., Frenk, C. S., Schmoldt, I., Efstathiou, G., White, S. D. M., Saunders, W., Sutherland, W., Rowan-Robinson, M., Keeble, O., Tadros, H., Maddox, S., & Oliver, S., 1999, *MNRAS*, **308**, 1

Cappi, A., Zamorani, G., Zucca, E., Vettolani, G., Merighi, R., Mignoli, M., Stirpe, G. M., Collins, C., Guzzo, L., Chincarini, G., Maccagni, D., Balkowski, C., Cayatte, V., Maurogordato, S., Proust, D., Bardelli, S., Ramella, M., Scaramella, R., Blanchard, A., & MacGillivray, H., 1998, *A&A*, **336**, 445

Chincarini, G. & Rood, H. J., 1979, *ApJ*, **230**, 648

Colberg, J. M., Krughoff, K. S., & Connolly, A. J., 2005, *MNRAS,* **359**, 272

Colberg, J. M., White, S. D. M., MacFarland, T. J., Jenkins, A., Pearce, F. R., Frenk, C. S., Thomas, P. A., & Couchman, H. M. P., 2000, *MNRAS,* **313**, 229

Cole, S., Norberg, P., Baugh, C. M., Frenk, C. S., Bland-Hawthorn, J., Bridges, T., Cannon, R., Colless, M., Collins, C., Couch, W., Cross, N., Dalton, G., De Propris, R., Driver, S. P., Efstathiou, G., Ellis, R. S., Glazebrook, K., Jackson, C., Lahav, O., Lewis, I., Lumsden, S., Maddox, S., Madgwick, D., Peacock, J. A., Peterson, B. A., Sutherland, W., & Taylor, K., 2001, *MNRAS,* **326**, 255

Colless, M., Dalton, G., Maddox, S., Sutherland, W., Norberg, P., Cole, S., Bland-Hawthorn, J., Bridges, T., Cannon, R., Collins, C., Couch, W., Cross, N., Deeley, K., De Propris, R., Driver, S. P., Efstathiou, G., Ellis, R. S., Frenk, C. S., Glazebrook, K., Jackson, C., Lahav, O., Lewis, I., Lumsden, S., Madgwick, D., Peacock, J. A., Peterson, B. A., Price, I., Seaborne, M., & Taylor, K., 2001a, *MNRAS,* **328**, 1039

Colless, M., Saglia, R. P., Burstein, D., Davies, R. L., McMahan, R. K., & Wegner, G., 2001b, *MNRAS,* **321**, 277

Collins, C. A., Guzzo, L., Böhringer, H., Schuecker, P., Chincarini, G., Cruddace, R., De Grandi, S., MacGillivray, H. T., Neumann, D. M., Schindler, S., Shaver, P., & Voges, W., 2000, *MNRAS,* **319**, 939

Collins, C. A., Guzzo, L., Nichol, R. C., & Lumsden, S. L., 1995, *MNRAS,* **274**, 1071

Conklin, E. K., 1969, *Nat,* **222**, 971

Croft, R. A. C. & Efstathiou, G., 1994, *MNRAS,* **268**, L23

Crook, A. C., Huchra, J. P., Martimbeau, N., Masters, K. L., Jarrett, T., & Macri, L. M., 2007, *ApJ,* **655**, 790

Cutri, R. M., Skrutskie, M. F., van Dyk, S., Beichman, C. A., Carpenter, J. M., Chester, T., Cambresy, L., Evans, T., Fowler, J., Gizis, J., Howard, E., Huchra, J., Jarrett, T., Kopan, E. L., Kirkpatrick, J. D., Light, R. M., Marsh, K. A., McCallon, H., Schneider, S., Stiening, R., Sykes, M., Weinberg, M., Wheaton, W. A., Wheelock, S., & Zacarias, N., 2003, *VizieR Online Data Catalog,* **2246**, 0

da Costa, L. N., Bernardi, M., Alonso, M. V., Wegner, G., Willmer, C. N. A., Pellegrini, P. S., Rité, C., & Maia, M. A. G., 2000, *AJ,* **120**, 95

da Costa, L. N., Nusser, A., Freudling, W., Giovanelli, R., Haynes, M. P., Salzer, J. J., & Wegner, G., 1998, *MNRAS,* **299**, 425

Dale, D. A., Giovanelli, R., Haynes, M. P., Campusano, L. E., Hardy, E., & Borgani, S., 1999, *ApJL,* **510**, L11

Danese, L., de Zotti, G., & di Tullio, G., 1980, *A&A,* **82**, 322

Davis, M., Nusser, A., & Willick, J. A., 1996, *ApJ,* **473**, 22 de Lapparent, V., Geller, M. J., & Huchra, J. P., 1986, *ApJL,* **302**, L1

de Vaucouleurs, G., 1953, *AJ,* **58**, 30

de Vaucouleurs, G., de Vaucouleurs, A., & Corwin, J. R., 1976, in *Second reference catalogue of bright galaxies, 1976, Austin: University of Texas Press.*, p. 0

Dekel, A., Bertschinger, E., & Faber, S. M., 1990, *ApJ,* **364**, 349

Dekel, A., Bertschinger, E., Yahil, A., Strauss, M. A., Davis, M., & Huchra, J. P., 1993, *ApJ,* **412**, 1

Djorgovski, S. & Davis, M., 1987, *ApJ,* **313**, 59

Dressler, A. & Faber, S. M., 1990, *ApJ,* **354**, 13

Dressler, A., Faber, S. M., Burstein, D., Davies, R. L., Lynden-Bell, D., Terlevich, R. J., & Wegner, G., 1987, *ApJL,* **313**, L37

Ebeling, H., Edge, A. C., Allen, S. W., Crawford, C. S., Fabian, A. C., & Huchra, J. P., 2000, *MNRAS,* **318**, 333

Ebeling, H., Edge, A. C., Bohringer, H., Allen, S. W., Crawford, C. S., Fabian, A. C., Voges, W., & Huchra, J. P., 1998, *MNRAS,* **301**, 881

Ebeling, H., Mullis, C. R., & Tully, R. B., 2002, *ApJ,* **580**, 774

Ebeling, H., Voges, W., Bohringer, H., Edge, A. C., Huchra, J. P., & Briel, U. G., 1996, *MNRAS,* **281**, 799

Edge, A. C., Stewart, G. C., Fabian, A. C., & Arnaud, K. A., 1990, *MNRAS,* **245**, 559

Einasto, M., Einasto, J., Tago, E., Müller, V., & Andernach, H., 2001, AJ, **122**, 2222

Eke, V. R., Cole, S., & Frenk, C. S., 1996, *MNRAS,* **282**, 263

Erdoğdu, P., Huchra, J. P., Lahav, O., Colless, M., Cutri, R. M., Falco, E., George, T., Jarrett, T., Jones, D. H., Kochanek, C. S., Macri, L., Mader, J., Martimbeau, N., Pahre, M., Parker, Q., Rassat, A., & Saunders, W., 2006a, *MNRAS,* **368**, 1515

Erdoğdu, P., Lahav, O., Huchra, J. P., Colless, M., Cutri, R. M., Falco, E., George, T., Jarrett, T., Jones, D. H., Macri, L. M., Mader, J., Martimbeau, N., Pahre, M. A., Parker, Q. A., Rassat, A., & Saunders, W., 2006b, *MNRAS,* **373**, 45

Ettori, S., Fabian, A. C., & White, D. A., 1997, *MNRAS,* **289**, 787

Faber, S. M. & Burstein, D., 1988, *Motions of galaxies in the neighborhood of the local group*, p. 115, Large-Scale Motions in the Universe: A Vatican study Week

Faber, S. M., Dressler, A., Davies, R. L., Burstein, D., & Lynden-Bell, D., 1987, in S. M. Faber (ed.), *Nearly Normal Galaxies. From the Planck Time to the Present*, p. 175

Faber, S. M. & Jackson, R. E., 1976, *ApJ,* **204**, 668

Fabian, A. C., Arnaud, K. A., Bautz, M. W., & Tawara, Y., 1994, *ApJL,* **436**, L63

Fabian, A. C., Hu, E. M., Cowie, L. L., & Grindlay, J., 1981, *ApJ,* **248**, 47

Fabian, A. C., Sanders, J. S., Allen, S. W., Crawford, C. S., Iwasawa, K., Johnstone, R. M., Schmidt, R. W., & Taylor, G. B., 2003, *MNRAS,* **344**, L43

Fabian, A. C., Sanders, J. S., Ettori, S., Taylor, G. B., Allen, S. W., Crawford, C. S., Iwasawa, K., Johnstone, R. M., & Ogle, P. M., 2000, *MNRAS,* **318**, L65

Fairall, A. P., 1998, *Large-scale structures in the universe,* Wiley-Praxis series in Astronomy and A strophysics, New York

Fairall, A. P., Woudt, P. A., & Kraan-Korteweg, R. C., 1998, *A&ASS,* **127**, 463

Fisher, K. B., Huchra, J. P., Strauss, M. A., Davis, M., Yahil, A., & Schlegel, D., 1995a, *ApJS,* **100**, 69

Fisher, K. B., Lahav, O., Hoffman, Y., Lynden-Bell, D., & Zaroubi, S., 1995b, *MNRAS,* **272**, 885

Freedman, W. L. & Madore, B. F., 1990, *ApJ,* **365**, 186

Freedman, W. L., Madore, B. F., Gibson, B. K., Ferrarese, L., Kelson, D. D., Sakai, S., Mould, J. R., Kennicutt, Jr., R. C., Ford, H. C., Graham, J. A., Huchra, J. P., Hughes, S. M. G., Illingworth, G. D., Macri, L. M., & Stetson, P. B., 2001, *ApJ,* **553**, 47

Gao, L., Springel, V., & White, S. D. M., 2005, *MNRAS,* **363**, 66

Geller, M. J. & Huchra, J. P., 1989, *Science,* **246**, 897

Germany, L. M., 2001, *Ph.D. thesis,* Australian National University

Germany, L. M., Reiss, D. J., Schmidt, B. P., Stubbs, C. W., & Suntzeff, N. B., 2004, *A&A,* **415**, 863

Gibson, B. K., 2000, *Mem. Soc. Astron. Ital.* **71**, 693

Giovanelli, R., Dale, D. A., Haynes, M. P., Hardy, E., & Campusano, L. E., 1999, *ApJ,* **525**, 25

Giovanelli, R., Haynes, M. P., & Chincarini, G. L., 1986, *ApJ,* **300**, 77

Giovanelli, R., Haynes, M. P., Salzer, J. J., Wegner, G., da Costa, L. N., & Freudling, W., 1998, *AJ,* **116**, 2632

Gregory, S. A. & Thompson, L. A., 1978, *ApJ,* **222**, 784

Gregory, S. A. & Thompson, L. A., 1984, *ApJ,* **286**, 422

Gregory, S. A., Thompson, L. A., & Tifft, W. G., 1981, *ApJ,* **243**, 411

Guzzo, L., Bohringer, H., Schuecker, P., Collins, C. A., Schindler, S., Neumann, D. M., de Grandi, S., Cruddace, R., Chincarini, G., Edge, A. C., Shaver, P. A., & Voges, W., 1999, *The Messenger,* **95**, 27

Hamilton, A. J. S. & Tegmark, M., 2002, *MNRAS,* **330**, 506

Hamuy, M., Folatelli, G., Morrell, N. I., Phillips, M. M., Suntzeff, N. B., Persson, S. E., Roth, M., Gonzalez, S., Krzeminski, W., Contreras, C., Freedman, W. L., Murphy, D. C., Madore, B. F., Wyatt, P., Maza, J., Filippenko, A. V., Li, W., & Pinto, P. A., 2006, *PASP,* **118**, 2

Hamuy, M., Phillips, M. M., Maza, J., Suntzeff, N. B., Schommer, R. A., & Aviles, R., 1995, *AJ,* **109**, 1

Hamuy, M., Phillips, M. M., Suntzeff, N. B., Schommer, R. A., Maza, J., Antezan, A. R., Wischnjewsky, M., Valladares, G., Muena, C., Gonzales, L. E., Aviles, R., Wells, L. A., Smith, R. C., Navarrete, M., Covarrubias, R., Williger, G. M., Walker, A. R., Layden, A. C., Elias, J. H., Baldwin, J. A., Hernandez, M., Tirado, H., Ugarte, P., Elston, R., Saavedra, N., Barrientos, F., Costa, E., Lira, P., Ruiz, M. T., Anguita, C., Gomez, X., Ortiz, P., della Valle, M., Danziger, J., Storm, J., Kim, Y.-C., Bailyn, C., Rubenstein, E. P., Tucker, D., Cersosimo, S., Mendez, R. A., Siciliano, L., Sherry, W., Chaboyer, B., Koopmann, R. A., Geisler, D., Sarajedini, A., Dey, A., Tyson, N., Rich, R. M., Gal, R., Lamontagne, R., Caldwell, N., Guhathakurta, P., Phillips, A. C., Szkody, P., Prosser, C., Ho, L. C., McMahan, R., Baggley, G., Cheng, K.-P., Havlen, R., Wakamatsu, K., Janes, K., Malkan, M., Baganoff, F., Seitzer, P., Shara, M., Sturch, C., Hesser, J., Hartig, A. N. P., Hughes, J., Welch, D., Williams, T. B., Ferguson, H., Francis, P. J., French, L., Bolte, M., Roth, J., Odewahn, S., Howell, S., & Krzeminski, W., 1996, *AJ,* **112**, 2408

Han, M. & Mould, J. R., 1992, *ApJ,* **396**, 453

Hasegawa, T., Wakamatsu, K.-i., Malkan, M., Sekiguchi, K., Menzies, J. W., Parker, Q. A., Jugaku, J., Karoji, H., & Okamura, S., 2000, *MNRAS,* **316**, 326

Heisler, J., Tremaine, S., & Bahcall, J. N., 1985, *ApJ,* **298**, 8

Hendry, M., 2001, in B. A. Steves & A. J. Maciejewski (eds.), *The Restless Universe,* p. 191

Henning, P. A., Kraan-Korteweg, R. C., & Stavely-Smith, L., 2005, in A. P. Fairall & P. A. Woudt (eds.), *Nearby Large-Scale Structures and the Zone of Avoidance,* Vol. 329 of *ASP Conf. Ser.,* p. 199

Henry, P. S., 1971, *Nat,* **231**, 516

Hinshaw, G., Nolta, M. R., Bennett, C. L., Bean, R., Doré, O., Greason, M. R., Halpern, M., Hill, R. S., Jarosik, N., Kogut, A., Komatsu, E., Limon, M., Odegard, N., Meyer, S. S., Page, L., Peiris, H. V., Spergel, D. N., Tucker, G. S., Verde, L., Weiland, J. L., Wollack, E., & Wright, E. L., 2007, *ApJS,* **170**, 288

Høg, E., Fabricius, C., Makarov, V. V., Urban, S., Corbin, T., Wycoff, G., Bastian, U., Schwekendiek, P., & Wicenec, A., 2000, *A&A*, **355**, L27

Hubble, E., 1929, *Proceedings of the National Academy of Science*, **15**, 168

Huchra, J., Davis, M., Latham, D., & Tonry, J., 1983, *ApJS*, **52**, 89

Huchra, J., Jarrett, T., Skrutskie, M., Cutri, R., Schneider, S., Macri, L., Steining, R., Mader, J., Martimbeau, N., & George, T., 2005, in A. P. Fairall & P. A. Woudt (eds.), *Nearby Large-Scale Structures and the Zone of Avoidance*, Vol. 329 of *ASP Conf. Ser.*, p. 135

Huchra, J. P., Geller, M. J., Clemens, C. M., Tokarz, S. P., & Michel, A., 1992, *Bull. CDS*, **41**, 31

Hudson, M. J., 1993, *MNRAS*, **265**, 72

Hudson, M. J., 1994a, *MNRAS*, **266**, 468

Hudson, M. J., 1994b, *MNRAS*, **266**, 475

Hudson, M. J., 2003, *The Consistency of Cosmic Flows on 100 Mpc/h Scales*, astro-ph/0311072

Hudson, M. J., Lucey, J. R., Smith, R. J., & Steel, J., 1997, *MNRAS*, **291**, 488

Hudson, M. J., Smith, R. J., Lucey, J. R., & Branchini, E., 2004, *MNRAS*, **352**, 61

Hudson, M. J., Smith, R. J., Lucey, J. R., Schlegel, D. J., & Davies, R. L., 1999, *ApJL*, **512**, L79

Jarrett, T. H., Chester, T., Cutri, R., Schneider, S., Skrutskie, M., & Huchra, J. P., 2000, *AJ*, **119**, 2498

Jenkins, A., Frenk, C. S., Pearce, F. R., Thomas, P. A., Colberg, J. M., White, S. D. M., Couchman, H. M. P., Peacock, J. A., Efstathiou, G., & Nelson, A. H., 1998, *ApJ*, **499**, 20

Jha, S., 2002, *Ph.D. thesis*, Harvard University

Jing, Y. P., 1998, *ApJL*, **503**, 9

Jones, D. H., Saunders, W., Colless, M., Read, M. A., Parker, Q. A., Watson, F. G., Campbell, L. A., Burkey, D., Mauch, T., Moore, L., Hartley, M., Cass, P., James, D., Russell, K., Fiegert, K., Dawe, J., Huchra, J., Jarrett, T., Lahav, O., Lucey, J., Mamon, G. A., Proust, D., Sadler, E. M., & Wakamatsu, K.-i., 2004, *MNRAS*, **355**, 747

Jones, D. H., Saunders, W., Read, M., & Colless, M., 2005, *PASA*, **22**, 277

Jorgensen, I., Franx, M., & Kjaergaard, P., 1996, *MNRAS*, **280**, 167

Kaiser, N., 1987, *MNRAS*, **227**, 1

Kaiser, N., Aussel, H., Burke, B. E., Boesgaard, H., Chambers, K., Chun, M. R., Heasley, J. N., Hodapp, K.-W., Hunt, B., Jedicke, R., Jewitt, D., Kudritzki, R., Luppino, G. A., Maberry, M., Magnier, E., Monet, D. G., Onaka, P. M., Pickles, A. J., Rhoads, P. H. H., Simon, T., Szalay, A., Szapudi, I., Tholen, D. J., Tonry, J. L., Waterson, M., & Wick, J., 2002, in J. A. Tyson & S. Wolff (eds.), *Survey and Other Telescope Technologies and Discoveries.*, Vol. 4836 of *SPIE Conf. Ser.*, p. 154

Kaiser, N., Efstathiou, G., Saunders, W., Ellis, R., Frenk, C., Lawrence, A., & Rowan-Robinson, M., 1991, *MNRAS,* **252**, 1

Kaiser, N. & Lahav, O., 1988, *Theoretical implications of cosmological dipoles,* p. 339, Large-Scale Motions in the Universe: A Vatican study Week

Kaldare, R., Colless, M., Raychaudhury, S., & Peterson, B. A., 2003, *MNRAS,* **339**, 652

Kannappan, S. J., Fabricant, D. G., & Franx, M., 2002, *AJ,* **123**, 2358

Kocevski, D. D. & Ebeling, H., 2006, *ApJ,* **645**, 1043

Kocevski, D. D., Ebeling, H., Mullis, C. R., & Tully, R. B., 2005, *Mapping Large-Scale Structures Behind the Galactic Plane: The Second CIZA Subsample,* astro-ph/0512321

Kocevski, D. D., Ebeling, H., Mullis, C. R., & Tully, R. B., 2007, *ApJ,* **662**, 224

Kocevski, D. D., Mullis, C. R., & Ebeling, H., 2004, *ApJ,* **608**, 721

Kogut, A., Lineweaver, C., Smoot, G. F., Bennett, C. L., Banday, A., Boggess, N. W., Cheng, E. S., de Amici, G., Fixsen, D. J., Hinshaw, G., Jackson, P. D., Janssen, M., Keegstra, P., Loewenstein, K., Lubin, P., Mather, J. C., Tenorio, L., Weiss, R., Wilkinson, D. T., & Wright, E. L., 1993, *ApJ,* **419**, 1

Kolatt, T., Dekel, A., & Lahav, O., 1995, *MNRAS,* **275**, 797

Koribalski, B. S., 2005, in A. P. Fairall & P. A. Woudt (eds.), *Nearby Large-Scale Structures and the Zone of Avoidance,* Vol. 329 of *ASP Conf. Ser.*, p. 217

Koribalski, B. S., Staveley-Smith, L., Kilborn, V. A., Ryder, S. D., Kraan-Korteweg, R. C., Ryan-Weber, E. V., Ekers, R. D., Jerjen, H., Henning, P. A., Putman, M. E., Zwaan, M. A., de Blok, W. J. G., Calabretta, M. R., Disney, M. J., Minchin, R. F., Bhathal, R., Boyce, P. J., Drinkwater, M. J., Freeman, K. C., Gibson, B. K., Green, A. J., Haynes, R. F., Juraszek, S., Kesteven, M. J., Knezek, P. M., Mader, S., Marquarding, M., Meyer, M., Mould, J. R., Oosterloo, T., O'Brien, J., Price, R. M., Sadler, E. M., Schröder, A., Stewart, I. M., Stootman, F., Waugh, M., Warren, B. E., Webster, R. L., & Wright, A. E., 2004, *AJ,* **128**, 16

Kraan-Korteweg, R. C., Fairall, A. P., & Balkowski, C., 1995, *A&A,* **297**, 617

Kraan-Korteweg, R. C., Ochoa, M., Woudt, P. A., & Andernach, H., 2005a, in A. P. Fairall & P. A. Woudt (eds.), *Nearby Large-Scale Structures and the Zone of Avoidance,* Vol. 329 of *ASP Conf. Ser.*, p. 159

Kraan-Korteweg, R. C., Staveley-Smith, L., Donley, J., Koribalski, B., & Henning, P. A., 2005b, in M. Colless, L. Staveley-Smith, & R. A. Stathakis (eds.), *Maps of the Cosmos*, Vol. 216 of *IAU Symposium*, p. 203

Kraan-Korteweg, R. C. & Woudt, P. A., 1994, in C. Balkowski & R. C. Kraan-Korteweg (eds.), *Unveiling Large-Scale Structures Behind the Milky Way*, Vol. 67 of *ASP Conf. Ser.*, p. 89

Kraan-Korteweg, R. C. & Woudt, P. A., 1999, *PASA*, **16**, 53

Kraan-Korteweg, R. C., Woudt, P. A., Cayatte, V., Fairall, A. P., Balkowski, C., & Henning, P. A., 1996, *Nat*, **379**, 519

Lahav, O., Lilje, P. B., Primack, J. R., & Rees, M. J., 1991, *MNRAS*, **251**, 128

Lahav, O., Nemiroff, R. J., & Piran, T., 1990, *ApJ*, **350**, 119

Lahav, O., Santiago, B. X., Webster, A. M., Strauss, M. A., Davis, M., Dressler, A., & Huchra, J. P., 2000, *MNRAS*, **312**, 166

Lahav, O., Yamada, T., Scharf, C., & Kraan-Korteweg, R. C., 1993, *MNRAS*, **262**, 711

Lauer, T. R., Tonry, J. L., Postman, M., Ajhar, E. A., & Holtzman, J. A., 1998, *ApJ*, **499**, 577

Laustsen, S., Schuster, H.-E., & West, R. M., 1977, *A&A*, **59**, 3

Lewis, I. J., Cannon, R. D., Taylor, K., Glazebrook, K., Bailey, J. A., Baldry, I. K., Barton, J. R., Bridges, T. J., Dalton, G. B., Farrell, T. J., Gray, P. M., Lankshear, A., McCowage, C., Parry, I. R., Sharples, R. M., Shortridge, K., Smith, G. A., Stevenson, J., Straede, J. O., Waller, L. G., Whittard, J. D., Wilcox, J. K., & Willis, K. C., 2002, *MNRAS*, **333**, 279

Lilje, P. B., Yahil, A., & Jones, B. J. T., 1986, *ApJ*, **307**, 91

Lucey, J., Radburn-Smith, D., & Hudson, M., 2005, in A. P. Fairall & P. A. Woudt (eds.), *Nearby Large-Scale Structures and the Zone of Avoidance*, Vol. 329 of *ASP Conf. Ser.*, p. 21

Lucey, J. R., 1983, *MNRAS*, **204**, 33

Lucey, J. R. & Carter, D., 1988, *MNRAS*, **235**, 1177

Lynden-Bell, D., Faber, S. M., Burstein, D., Davies, R. L., Dressler, A., Terlevich, R. J., & Wegner, G., 1988, *ApJ*, **326**, 19

Lynden-Bell, D., Lahav, O., & Burstein, D., 1989, MNRAS, **241**, 325

Malmquist, K. G., 1920, *Medd. Lund. Astron. Obs., Ser. 2*, **22**, 1

Mandelbaum, R., Tasitsiomi, A., Seljak, U., Kravtsov, A. V., & Wechsler, R. H., 2005, *MNRAS*, **362**, 1451

Masters, K. L., 2007, *Mapping Mass in the Local Universe*, astro-ph/0708.2913

Masters, K. L., Haynes, M. P., & Giovanelli, R., 2004, *ApJL,* **607**, L115

Mathewson, D. S. & Ford, V. L., 1994, *ApJL,* **434**, L39

Mathewson, D. S., Ford, V. L., & Buchhorn, M., 1992, *ApJL,* **389**, L5

Melnick, J. & Moles, M., 1987, *Revista Mexicana de Astronomia y Astrofisica, vol. 14,* **14**, 72

Meyer, M. J., Zwaan, M. A., Webster, R. L., Staveley-Smith, L., Ryan-Weber, E., Drinkwater, M. J., Barnes, D. G., Howlett, M., Kilborn, V. A., Stevens, J., Waugh, M., Pierce, M. J., Bhathal, R., de Blok, W. J. G., Disney, M. J., Ekers, R. D., Freeman, K. C., Garcia, D. A., Gibson, B. K., Harnett, J., Henning, P. A., Jerjen, H., Kesteven, M. J., Knezek, P. M., Koribalski, B. S., Mader, S., Marquarding, M., Minchin, R. F., O'Brien, J., Oosterloo, T., Price, R. M., Putman, M. E., Ryder, S. D., Sadler, E. M., Stewart, I. M., Stootman, F., & Wright, A. E., 2004, *MNRAS,* **350**, 1195

Mills, B. Y., 1952, *Australian J. Sci. Res. series A 5, 5, 266-287 (1952),* **5**, 266

Mo, H. J. & White, S. D. M., 1996, *MNRAS,* **282**, 347

Mullis, C. R., Ebeling, H., Kocevski, D. D., & Tully, R. B., 2005, in A. P. Fairall & P. A. Woudt (eds.), *Nearby Large-Scale Structures and the Zone of Avoidance,* Vol. 329 of *ASP Conf. Ser.*, p. 183

Muriel, H., Quintana, H., Infante, L., Lambas, D. G., & Way, M. J., 2002, *AJ,* **124**, 1934

Nagayama, T., Nagata, T., Sato, S., Woudt, P. A., & Irsf/Sirius Team, 2005, in A. P. Fairall & P. A. Woudt (eds.), *Nearby Large-Scale Structures and the Zone of Avoidance,* Vol. 329 of *ASP Conf. Ser.*, p. 177

Nagayama, T., Woudt, P. A., Nagashima, C., Nakajima, Y., Kato, D., Kurita, M., Nagata, T., Nakaya, H., Tamura, M., Sugitani, K., Wakamatsu, K., & Sato, S., 2004, *MNRAS,* **354**, 980

Newsam, A., Simmons, J. F. L., & Hendry, M. A., 1995, *A&A,* **294**, 627

Nusser, A. & Davis, M., 1994, *ApJL,* **421**, L1

Peacock, J. A. & Dodds, S. J., 1994, *MNRAS,* **267**, 1020

Peebles, P. J. E., 1976, *ApJ,* **205**, 318

Peebles, P. J. E., 1980, *The Large-Scale Structure of the Universe,* Princeton Univ. Press, Princeton, NJ

Perlmutter, S., Aldering, G., Goldhaber, G., Knop, R. A., Nugent, P., Castro, P. G., Deustua, S., Fabbro, S., Goobar, A., Groom, D. E., Hook, I. M., Kim, A. G., Kim, M. Y., Lee, J. C., Nunes, N. J., Pain, R., Pennypacker, C. R., Quimby, R., Lidman, C., Ellis, R. S., Irwin, M., McMahon, R. G., Ruiz-Lapuente, P., Walton, N., Schaefer, B., Boyle, B. J., Filippenko, A. V., Matheson, T., Fruchter, A. S., Panagia, N., Newberg, H. J. M., Couch, W. J., & The Supernova Cosmology Project, 1999, *ApJ,* **517**, 565

Phillips, M. M., 1993, *ApJL,* **413**, L105

Pike, R. W. & Hudson, M. J., 2005, *ApJ,* **635**, 11

Pizagno, J., Prada, F., Weinberg, D. H., Rix, H.-W., Pogge, R. W., Grebel, E. K., Harbeck, D., Blanton, M., Brinkmann, J., & Gunn, J. E., 2007, *AJ,* **134**, 945

Plionis, M., Coles, P., & Catelan, P., 1993, *MNRAS,* **262**, 465

Plionis, M. & Kolokotronis, V., 1998, *ApJ,* **500**, 1

Plionis, M. & Valdarnini, R., 1991, *MNRAS,* **249**, 46

Proust, D., Quintana, H., Carrasco, E. R., Reisenegger, A., Slezak, E., Muriel, H., Dünner, R., Sodré, Jr., L., Drinkwater, M. J., Parker, Q. A., & Ragone, C. J., 2006, *A&A,* **447**, 133

Pskovskii, I. P., 1977, *Soviet Astronomy,* **21**, 675

Raychaudhury, S., 1989, *Nat,* **342**, 251

Reisenegger, A., Quintana, H., Carrasco, E. R., & Maze, J., 2000, *AJ,* **120**, 523

Riess, A. G., Davis, M., Baker, J., & Kirshner, R. P., 1997, *ApJL,* **488**, L1

Riess, A. G., Filippenko, A. V., Challis, P., Clocchiatti, A., Diercks, A., Garnavich, P. M., Gilliland, R. L., Hogan, C. J., Jha, S., Kirshner, R. P., Leibundgut, B., Phillips, M. M., Reiss, D., Schmidt, B. P., Schommer, R. A., Smith, R. C., Spyromilio, J., Stubbs, C., Suntzeff, N. B., & Tonry, J., 1998, *AJ,* **116**, 1009

Riess, A. G., Kirshner, R. P., Schmidt, B. P., Jha, S., Challis, P., Garnavich, P. M., Esin, A. A., Carpenter, C., Grashius, R., Schild, R. E., Berlind, P. L., Huchra, J. P., Prosser, C. F., Falco, E. E., Benson, P. J., Briceño, C., Brown, W. R., Caldwell, N., dell'Antonio, I. P., Filippenko, A. V., Goodman, A. A., Grogin, N. A., Groner, T., Hughes, J. P., Green, P. J., Jansen, R. A., Kleyna, J. T., Luu, J. X., Macri, L. M., McLeod, B. A., McLeod, K. K., McNamara, B. R., McLean, B., Milone, A. A. E., Mohr, J. J., Moraru, D., Peng, C., Peters, J., Prestwich, A. H., Stanek, K. Z., Szentgyorgyi, A., & Zhao, P., 1999, *AJ,* **117**, 707

Riess, A. G., Nugent, P. E., Gilliland, R. L., Schmidt, B. P., Tonry, J., Dickinson, M., Thompson, R. I., Budavári, T., Casertano, S., Evans, A. S., Filippenko, A. V., Livio, M., Sanders, D. B., Shapley, A. E., Spinrad, H., Steidel, C. C., Stern, D., Surace, J., & Veilleux, S., 2001, *ApJ,* **560**, 49

Riess, A. G., Press, W. H., & Kirshner, R. P., 1995, *ApJL,* **438**, L17

Riess, A. G., Strolger, L.-G., Tonry, J., Casertano, S., Ferguson, H. C., Mobasher, B., Challis, P., Filippenko, A. V., Jha, S., Li, W., Chornock, R., Kirshner, R. P., Leibundgut, B., Dickinson, M., Livio, M., Giavalisco, M., Steidel, C. C., Benítez, T., & Tsvetanov, Z., 2004, *ApJ,* **607**, 665

Rines, K., Geller, M. J., Kurtz, M. J., & Diaferio, A., 2003, *AJ,* **126**, 2152

Rowan-Robinson, M., Lawrence, A., Saunders, W., Crawford, J., Ellis, R., Frenk, C. S., Parry, I., Xiaoyang, X., Allington-Smith, J., Efstathiou, G., & Kaiser, N., 1990, *MNRAS,* **247**, 1

Rowan-Robinson, M., Sharpe, J., Oliver, S. J., Keeble, O., Canavezes, A., Saunders, W., Taylor, A. N., Valentine, H., Frenk, C. S., Efstathiou, G. P., McMahon, R. G., White, S. D. M., Sutherland, W., Tadros, H., & Maddox, S., 2000, *MNRAS,* **314**, 375

Royston, P., 1995, *Applied Statistics,* **44**, 547

Sako, M., Romani, R., Frieman, J., Adelman-McCarthy, J., Becker, A., DeJongh, F., Dilday, B., Estrada, J., Hendry, J., Holtzman, J., Kaplan, J., Kessler, R., Lampeitl, H., Marriner, J., Miknaitis, G., Riess, A., Tucker, D., Barentine, J., Blandford, R., Brewington, H., Dembicky, J., Harvanek, M., Hawley, S., Hogan, C., Johnston, D., Kahn, S., Ketzeback, B., Kleinman, S., Krzesinski, J., Lamenti, D., Long, D., McMillan, R., Newman, P., Nitta, A., Nichol, R., Scranton, R., Sheldon, E., Snedden, S., Stoughton, C., York, D., & the SDSS Collaboration, 2005, *The Fall 2004 SDSS Supernova Survey,* astro-ph/0504455

Santiago, B. X., Strauss, M. A., Lahav, O., Davis, M., Dressler, A., & Huchra, J. P., 1995, *ApJ,* **446**, 457

Saunders, W., D'Mellow, K. J., Valentine, H., Tully, R. B., Carrasco, B. E., Mobasher, B., Maddox, S. J., Hau, G. K. T., Sutherland, W. J., Clements, D. L., & Staveley-Smith, L., 2000a, in R. C. Kraan-Korteweg, P. A. Henning, & H. Andernach (eds.), *Mapping the Hidden Universe: The Universe behind the Mily Way - The Universe in HI,* Vol. 218 of *ASP Conf. Ser.*, p. 141

Saunders, W., Rowan-Robinson, M., & Lawrenequibce, A., 1992, *MNRAS,* **258**, 134

Saunders, W., Sutherland, W. J., Maddox, S. J., Keeble, O., Oliver, S. J., Rowan-Robinson, M., McMahon, R. G., Efstathiou, G. P., Tadros, H., White, S. D. M., Frenk, C. S., Carramiñana, A., & Hawkins, M. R. S., 2000b, *MNRAS,* **317**, 55

Scaramella, R., Baiesi-Pillastrini, G., Chincarini, G., Vettolani, G., & Zamorani, G., 1989, *Nature,* **338**, 562

Scaramella, R., Vettolani, G., & Zamorani, G., 1991, *ApJL,* **376**, L1

Schechter, P. L., 1980, *AJ,* **85**, 801

Schmoldt, I. M., Saar, V., Saha, P., Branchini, E., Efstathiou, G. P., Frenk, C. S., Keeble, O., Maddox, S., McMahon, R., Oliver, S., Rowan-Robinson, M., Saunders, W., Sutherland, W. J., Tadros, H., & White, S. D. M., 1999, *AJ,* **118**, 1146

Schröder, A. C., Kraan-Korteweg, R. C., Mamon, G. A., & Woudt, P. A., 2005, in A. P. Fairall & P. A. Woudt (eds.), *Nearby Large-Scale Structures and the Zone of Avoidance,* Vol. 329 of *ASP Conf. Ser.*, p. 167

Shapiro, S. S. & Wilk, M. B., 1965, *Biometrika,* **52**, 591

Shapley, H., 1930, *Harvard College Observatory Bulletin,* **874**, 9

Sheth, R. K., Mo, H. J., & Tormen, G., 2001, *MNRAS,* **323**, 1

Sigad, Y., Eldar, A., Dekel, A., Strauss, M. A., & Yahil, A., 1998, *ApJ,* **495**, 516

Smith, R. J., Hudson, M. J., Lucey, J. R., Schlegel, D. J., & Davies, R. L., 2000, in S. Courteau & J. Willick (eds.), *Cosmic Flows Workshop,* Vol. 201 of *ASP Conf. Ser.*, p. 39

Smith, R. J., Hudson, M. J., Nelan, J. E., Moore, S. A. W., Quinney, S. J., Wegner, G. A., Lucey, J. R., Davies, R. L., Malecki, J. J., Schade, D., & Suntzeff, N. B., 2004, *AJ,* **128**, 1558

Spergel, D. N., Bean, R., Doré, O., Nolta, M. R., Bennett, C. L., Dunkley, J., Hinshaw, G., Jarosik, N., Komatsu, E., Page, L., Peiris, H. V., Verde, L., Halpern, M., Hill, R. S., Kogut, A., Limon, M., Meyer, S. S., Odegard, N., Tucker, G. S., Weiland, J. L., Wollack, E., & Wright, E. L., 2007, *ApJS,* **170**, 377

Spergel, D. N., Verde, L., Peiris, H. V., Komatsu, E., Nolta, M. R., Bennett, C. L., Halpern, M., Hinshaw, G., Jarosik, N., Kogut, A., Limon, M., Meyer, S. S., Page, L., Tucker, G. S., Weiland, J. L., Wollack, E., & Wright, E. L., 2003, *ApJS,* **148**, 175

Stein, P., 1994, *Ph.D. thesis, University of Basel,*

Stein, P., 1996, *A&ASS,* **116**, 203

Stein, P., 1997, *A&A,* **317**, 670

Stewart, J. M. & Sciama, D. W., 1967, *Nat,* **216**, 748

Strauss, M. A. & Davis, M., 1988, *The peculiar velocity field predicted by the distribution of IRAS galaxies,* p. 255-274, Large-Scale Motions in the Universe: A Vatican study Week

Strauss, M. A., Davis, M., Yahil, A., & Huchra, J. P., 1992a, *ApJ,* **385**, 421

Strauss, M. A. & Willick, J. A., 1995, *Phy. Rep,* **261**, 271

Strauss, M. A., Yahil, A., Davis, M., Huchra, J. P., & Fisher, K., 1992b, *ApJ,* **397**, 395

Tammann, G. A. & Sandage, A., 1985, *ApJ,* **294**, 81

Tamura, T., Fukazawa, Y., Kaneda, H., Makishima, K., Tashiro, M., Tanaka, Y., & Bohringer, H., 1998, *PASJ,* **50**, 195

Tashiro, M., Kaneda, H., Makishima, K., Iyomoto, N., Idesawa, E., Ishisaki, Y., Kotani, T., Takahashi, T., & Yamashita, A., 1998, *ApJ,* **499**, 713

Tonry, J. & Davis, M., 1979, *AJ,* **84**, 1511

Tonry, J. & Schneider, D. P., 1988, *AJ,* **96**, 807

Tonry, J. L., Blakeslee, J. P., Ajhar, E. A., & Dressler, A., 1997, *ApJ,* **475**, 399

Tonry, J. L., Blakeslee, J. P., Ajhar, E. A., & Dressler, A., 2000, *ApJ,* **530**, 625

Tonry, J. L. & Davis, M., 1981, *ApJ,* **246**, 680

Tonry, J. L., Schmidt, B. P., Barris, B., Candia, P., Challis, P., Clocchiatti, A., Coil, A. L., Filippenko, A. V., Garnavich, P., Hogan, C., Holland, S. T., Jha, S., Kirshner, R. P., Krisciunas, K., Leibundgut, B., Li, W., Matheson, T., Phillips, M. M., Riess, A. G., Schommer, R., Smith, R. C., Sollerman, J., Spyromilio, J., Stubbs, C. W., & Suntzeff, N. B., 2003, *ApJ,* **594**, 1

Trümper, J., 1983, *Adv. Space Res.* **2**, 241

Tully, R. B. & Fisher, J. R., 1977, *A&A,* **54**, 661

Tully, R. B., Shaya, E. J., Karachentsev, I. D., Courtois, H., Kocevski, D. D., Rizzi, L., & Peel, A., 2007, *Our Peculiar Motion Away from the Local Void,* astro-ph/0705.4139

Udalski, A., Szymanski, M., Kubiak, M., Pietrzynski, G., Soszynski, I., Wozniak, P., & Zebrun, K., 1999, *Acta Astronomica,* **49**, 201

van den Bergh, S. & Pazder, J., 1992, *ApJ,* **390**, 34

Voges, W., 1992, *The ROSAT all-sky X ray survey,* Technical report, Max-Planck-Institut für Extraterrestrische Physik

Voges, W., Aschenbach, B., Boller, T., Bräuninger, H., Briel, U., Burkert, W., Dennerl, K., Englhauser, J., Gruber, R., Haberl, F., Hartner, G., Hasinger, G., Kürster, M., Pfeffermann, E., Pietsch, W., Predehl, P., Rosso, C., Schmitt, J. H. M. M., Trümper, J., & Zimmermann, H. U., 1999, *A&A,* **349**, 389

Vowles, G., 2007, *Master's thesis,* Durham University

Wakamatsu, K., Malkan, M. A., Nishida, M. T., Parker, Q. A., Saunders, W., & Watson, F. G., 2005, in A. P. Fairall & P. A. Woudt (eds.), *Nearby Large-Scale Structures and the Zone of Avoidance,* Vol. 329 of *ASP Conf. Ser.,* p. 189

Webster, M., Lahav, O., & Fisher, K., 1997, *MNRAS,* **287**, 425

West, R. M. & Tarenghi, M., 1989, *A&A,* **223**, 61

Westerlund, B. E., 1997, *The Magellanic Clouds,* Cambridge Univ. Press

White, S. D. M., Efstathiou, G., & Frenk, C. S., 1993, *MNRAS,* **262**, 1023

Willick, J. A., 1990, *ApJL,* **351**, L5

Willick, J. A., 1999, *ApJ,* **522**, 647

Willick, J. A., 2000, *Cosmic Velocities 2000: A Review,* astro-ph/0003232

Willick, J. A., Courteau, S., Faber, S. M., Burstein, D., Dekel, A., & Strauss, M. A., 1997a, *ApJS*, **109**, 333

Willick, J. A. & Strauss, M. A., 1998, *ApJ*, **507**, 64

Willick, J. A., Strauss, M. A., Dekel, A., & Kolatt, T., 1997b, *ApJ*, **486**, 629

Woudt, P. A., 1998, *Ph.D. Thesis*,

Woudt, P. A., Fairall, A., Kraan-Korteweg, R. C., Lucey, J., Schröder, A., Burstein, D., & McCall, M. L., 2005, in A. P. Fairall & P. A. Woudt (eds.), *Nearby Large-Scale Structures and the Zone of Avoidance*, Vol. 329 of *ASP Conf. Ser.*, p. 147

Woudt, P. A., Fairall, A. P., & Kraan-Korteweg, R. C., 1997, in M. Persic & P. Salucci (eds.), *ASP Conf. Ser. Vol. 117, Dark and Visible Matter in Galaxies and Cosmological Implications*, Vol. 117 of *ASP Conf. Ser.*, p. 373-379

Woudt, P. A., Kraan-Korteweg, R. C., Cayatte, V., Balkowski, C., & Felenbok, P., 2004, *A&A*, **415**, 9

Woudt, P. A., Kraan-Korteweg, R. C., & Fairall, A. P., 1999, *A&A*, **352**, 39

Yahil, A., Sandage, A., & Tammann, G. A., 1980, *ApJ*, **242**, 448

Yahil, A., Strauss, M. A., Davis, M., & Huchra, J. P., 1991, *ApJ*, **372**, 380

York, D. G., Adelman, J., Anderson, Jr., J. E., Anderson, S. F., Annis, J., Bahcall, N. A., Bakken, J. A., Barkhouser, R., Bastian, S., Berman, E., Boroski, W. N., Bracker, S., Briegel, C., Briggs, J. W., Brinkmann, J., Brunner, R., Burles, S., Carey, L., Carr, M. A., Castander, F. J., Chen, B., Colestock, P. L., Connolly, A. J., Crocker, J. H., Csabai, I., Czarapata, P. C., Davis, J. E., Doi, M., Dombeck, T., Eisenstein, D., Ellman, N., Elms, B. R., Evans, M. L., Fan, X., Federwitz, G. R., Fiscelli, L., Friedman, S., Frieman, J. A., Fukugita, M., Gillespie, B., Gunn, J. E., Gurbani, V. K., de Haas, E., Haldeman, M., Harris, F. H., Hayes, J., Heckman, T. M., Hennessy, G. S., Hindsley, R. B., Holm, S., Holmgren, D. J., Huang, C.-h., Hull, C., Husby, D., Ichikawa, S.-I., Ichikawa, T., Ivezić, Ž., Kent, S., Kim, R. S. J., Kinney, E., Klaene, M., Kleinman, A. N., Kleinman, S., Knapp, G. R., Korienek, J., Kron, R. G., Kunszt, P. Z., Lamb, D. Q., Lee, B., Leger, R. F., Limmongkol, S., Lindenmeyer, C., Long, D. C., Loomis, C., Loveday, J., Lucinio, R., Lupton, R. H., MacKinnon, B., Mannery, E. J., Mantsch, P. M., Margon, B., McGehee, P., McKay, T. A., Meiksin, A., Merelli, A., Monet, D. G., Munn, J. A., Narayanan, V. K., Nash, T., Neilsen, E., Neswold, R., Newberg, H. J., Nichol, R. C., Nicinski, T., Nonino, M., Okada, N., Okamura, S., Ostriker, J. P., Owen, R., Pauls, A. G., Peoples, J., Peterson, R. L., Petravick, D., Pier, J. R., Pope, A., Pordes, R., Prosapio, A., Rechenmacher, R., Quinn, T. R., Richards, G. T., Richmond, M. W., Rivetta, C. H., Rockosi, C. M., Ruthmansdorfer, K., Sandford, D., Schlegel, D. J., Schneider, D. P., Sekiguchi, M., Sergey, G., Shimasaku, K., Siegmund, W. A., Smee, S., Smith, J. A., Snedden, S., Stone, R., Stoughton, C., Strauss, M. A., Stubbs, C., SubbaRao, M., Szalay, A. S., Szapudi, I., Szokoly, G. P., Thakar, A. R., Tremonti, C., Tucker, D. L., Uomoto, A., Vanden Berk, D., Vogeley, M. S., Waddell, P., Wang, S.-i., Watanabe, M., Weinberg, D. H., Yanny, B., & Yasuda, N., 2000, *AJ*, **120**, 1579

Zaroubi, S., 2000, in R. C. Kraan-Korteweg, P. A. Henning, & H. Andernach (eds.), *Mapping the Hidden Universe: The Universe behind the Mily Way - The Universe in HI*, Vol. 218 of *ASP Conf. Ser.*, p. 173

Zaroubi, S., 2002, in L. M. Celnikier & J. Trân Thanh Vân (eds.), *Frontiers of the universe : proceedings of the XIIIrd Rencontres de Blois*, p. 65

Zaroubi, S., Branchini, E., Hoffman, Y., & da Costa, L. N., 2002, *MNRAS*, **336**, 1234

Zel'Dovich, Y. B., 1970, *A&A*, **5**, 84

Zwicky, F., Herzog, E., & Wild, P., 1961, *Catalogue of galaxies and of clusters of galaxies*, Pasadena: California Institute of Technology (CIT)